

**UCSF**

**UC San Francisco Electronic Theses and Dissertations**

**Title**

Discovery and Characterization of Inhibitory Mechanisms of Drugs and Antibodies Against Viral, Fungal, and Amoebic Human Pathogens, Including SARS-CoV-2, Zika Virus, Balamuthia mandrillaris, and Candida auris

**Permalink**

<https://escholarship.org/uc/item/8ps1z42p>

**Author**

Laurie, Matthew Thomas

**Publication Date**

2022

Peer reviewed|Thesis/dissertation

Discovery and Characterization of Inhibitory Mechanisms of Drugs and Antibodies Against Viral, Fungal, and Amoebic Human Pathogens, Including SARS-CoV-2, Zika Virus, Balamuthia mandrillaris, and Candida auris  
by  
Matthew Laurie

DISSERTATION

Submitted in partial satisfaction of the requirements for degree of  
DOCTOR OF PHILOSOPHY

in

Biochemistry and Molecular Biology

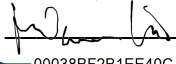
in the

GRADUATE DIVISION

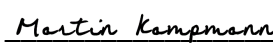
of the

UNIVERSITY OF CALIFORNIA, SAN FRANCISCO

Approved:

DocuSigned by:  
  
00038BF2B1EE40C... Melanie Ott  
Chair

DocuSigned by:  
  
00038BF2B1EE40C... Joseph DeRisi

DocuSigned by:  
  
03BA4012CC044AF... Martin Kampmann

Committee Members

**Copyright 2022**

**by**

**Matthew Thomas Laurie**

*To Inne and Mina, for bringing me the greatest joy I can imagine and the motivation to do  
whatever I can to make the world a better place for you to live in*

## Acknowledgements

I would first like to thank my Ph.D advisor and mentor Dr. Joseph DeRisi for teaching me so much about how to be a thoughtful and creative scientist. When I entered graduate school at UCSF I was looking for an exciting, fast-paced, and unique research experience and there is no doubt that your lab was the right place for that. Something I have told every prospective student thinking about joining the DeRisi lab is that there will never be a shortage of opportunities to lead great projects and make a real impact. That was certainly true for me and I am very grateful to you for providing the environment that facilitated those opportunities. I truly appreciate that you have always led from the front and even though everyone works extremely hard in your lab, you're always there with us working tirelessly as well. I admire that you have consistently practiced and advocated for a strong set of principles in the research your lab produces and the academic work environment that we all create. As annoying as it can be for your students when you keep asking for one more experiment or pitching another big spin-off project, I do still admire your attitude that science is never truly finished and there are always ways to keep improving our research. Lastly, I want to thank you for always believing in me and pushing me to try my hardest on everything, I know my work and development as a scientist is much better for it.

My research and education also benefited greatly from the guidance of my thesis committee members Dr. Melanie Ott and Dr. Martin Kampmann. Your expert advice, constructive commentary, and thoughtful encouragement were critical for my success at every stage of my graduate work. Thank you very much for your support through all of the ups and downs of my research and everything you have done to help with my career development.

All of the work throughout my graduate career was made possible by collaboration with many talented and thoughtful co-authors. To Sara Sunshine, Jamin Liu, Dr. Hanna Retallack, Dr.

Matthew Lohse, Dr. Corin White, Dr. Alexander Johnson, Sophia Levan, Kelsey Zorn, Dr. Diane Havlir, James Peng, Dr. Genay Pilarowski, Dr. Luis Rubio, Douglas Black, Dr. Eric Chow, Sabrina Mann, Anthea Mitchell, Dr. Kristeene Knopp, Dr. Carolina Arias, Dr. Elizabeth Di Lullo, Dr. Jayant Rajan, Dr. Vida Ahyong, Dr. Emily Crawford, Dr. Amy Kistler, Dr. Joseph Sabatino Jr., Dr. Judy Sakanri, Dr. Wesley Wu, Matthew Moser, Dr. Michael Wilson, and Dr. Joseph DeRisi, thank you all so much for making the body of work that is presented here possible by sharing your skills, knowledge, and effort. Thank you also to Armando Mis and Joselin Payan for bringing me so much blood (and donuts).

By far the best part of my Ph.D has been the time spent working with and getting to know an amazing group of people in the DeRisi lab and at the Biohub. Thank you so much to Manny De Vera, Jennifer Mann, and Brittany Worth for everything you've done to support me and everyone else in the lab, for solving all of the crazy problems that come up, and for somehow making it all look easy by keeping the lab running smoothly. To the past and present post-docs that have taught me so much, Dr. Corin White, Dr. Kristeene Knopp, Dr. Carolina Arias, Dr. Wesley Wu, Dr. Jayant Rajan, Dr. Caleigh Mandel-Brehm, Dr. Madhura Raghavan, Dr. Chuka Didigu, and Dr. Sharline Madera, thank you for being so patient and encouraging as you helped guide my research. To the amazing technicians Sabrina Mann, Anthea Mitchell, and Grace Wang, thank you for being incredibly dedicated, helpful, and flexible despite the immense amount of work thrown at you from all sides. To the fearless and tireless CLIAhub leaders Dr. Emily Crawford and Dr. Vida Ahyong, your effort and selflessness was truly inspiring and I am so grateful for what you accomplished. To the Biohub group leaders that graciously and frequently assisted me, Dr. Manu Leonetti, Dr. Andreas Puschnik, Dr. Leslie Goo, Dr. Amy Kistler, Dr. Ivan Ivanov, thank you for being so generous with your time and going out of your way to help me so often. To Dr. Eric Chow, thank

you for being the best person to talk to for troubleshooting equipment and protocols and when looking for creative solutions to experimental problems, your help was consistently invaluable.

My fellow graduate students in the DeRisi lab made my time in the lab so enjoyable. Thank you so much to Sara Sunshine, Jamin Liu, Dr. Valentina Garcia, Dr. Hanna Retallack, Andrew Kung, Isobel Hawes, and Robert Puccinelli for all of your help and advice and for making the lab a fun and supportive environment. Sara and Jamin, I am so happy to have had the chance to work so closely with you on Covid projects throughout the pandemic, the stress and frustration of working on endless urgent projects was made so much better by your support and friendship. I consider myself incredibly fortunate to have been surrounded with such a kind and talented group of people in the DeRisi lab.

I would also like to thank the generous donors who are responsible for funding the work presented in this manuscript. This work was made possible by the Ruth L. Kirschstein National Research Service Award, the University of California San Francisco COVID Fund, Marc and Lynne Benioff, Howard Hughes Medical Institute, the Chan Zuckerberg Biohub, and the Chan Zuckerberg Initiative.

I am immensely grateful to my family and friends for their support throughout my Ph.D. You have all been so patient and understanding despite me often not being able to devote the time that you deserve. To my mother- and father-in-law, thank you for everything you have done for me, Inne, and Mina. You have worked tirelessly to support us in every situation from moving across the country three times, to having a baby in the middle of a pandemic, and of course for finishing the long and difficult road to my Ph.D. To my parents, thank you for all of the love and support you've given me throughout my life. Neither of you had easy lives or many advantages growing up, but I did. That is entirely thanks to your hard work and the sacrifices you've made for

me. I know that I would not be where I am today without the advantages you provided for me, so I hope you know that my accomplishments are your accomplishments as well.

To Mina, thank you for being such a bright light in my life and the lives of the many people who love you. Already you are such a sweet, intelligent, funny, and loving child and I have no doubt you will grow into an amazing person. The work you see in this dissertation came at the enormous cost of time that I would otherwise have spent with you. I am sorry that you had to share in this sacrifice, but I want you to know that I did this all with the belief that it would help make a better world for you. Being your dad is the thing I am most proud of and I hope that you will be proud of me too.

Inne, no part of the work presented here would have been possible without you. I have had many difficult days in graduate school and life in general, but coming home to you never fails to instantly make everything alright. Thank you for believing in me more than I believed in myself. Thank you for all of your sacrifices that made it possible to meet all the challenges over the course of my Ph.D. Thank you for always standing up for what is right, giving your all to everything you do, and pushing me to do the same. Your love and support means everything to me. Thank you for being the best partner I could ever ask for.



## Contributions

### Chapter 2

Includes content previously published in:

Retallack H\*, Di Lullo E\*, Arias C, Knopp KA, Laurie MT, Sandoval-Espinosa C, Mancía Leon WR, Krencik R, Ullian EM, Spatazza J, Pollen AA, Mandel-Brehm C, Nowakowski TJ, Kriegstein AR, DeRisi JL. Zika virus cell tropism in the developing human brain and inhibition by azithromycin. *Proc Natl Acad Sci U S A*. 2016;113(50):14408-14413.

doi:10.1073/pnas.1618029113

### Chapter 3

Includes contributions by Dr. Hanna Retallack, Dr. Kristeene Knopp, Dr. Carolina Arias, and Dr. Joseph DeRisi.

### Chapter 4

Includes content previously published in:

Laurie MT\*, White CV\*, Retallack H, Wu W, Moser MS, Sakanari JA, Ang K, Wilson C, Arkin MR, DeRisi JL. Functional Assessment of 2,177 U.S. and International Drugs Identifies the Quinoline Nitroxoline as a Potent Amoebicidal Agent against the Pathogen *Balamuthia mandrillaris*. *mBio*. 2018; Oct 30;9(5):e02051-18. doi: 10.1128/mBio.02051-18

### Chapter 5

Includes contributions by Dr. Matthew Lohse, Sophia Levan, Dr. Naomi Ziv, Dr. Craig Ennis, Dr. Clarissa Nobile, Dr. Alexander Johnson, and Dr. Joseph DeRisi.

### Chapter 6

Includes content previously published in:

Pilarowski G, Lebel P, Sunshine S, Liu J, Crawford E, Marquez C, Rubio L, Chamie G, Martinez J, Peng J, Black D, Wu W, Pak J, Laurie MT, Jones D, Miller S, Jacobo J, Rojas S, Rojas S, Nakamura R, Tulier-Laiwa V, Petersen M, Havlir DV; CLIAHUB Consortium, DeRisi J. Performance Characteristics of a Rapid Severe Acute Respiratory Syndrome Coronavirus 2 Antigen Detection Assay at a Public Plaza Testing Site in San Francisco. *J Infect Dis.* 2021; Apr 8;223(7):1139-1144. doi: 10.1093/infdis/jiaa802.

## **Chapter 7**

Includes content previously published in:

Peng J\*, Liu J\*, Mann SA\*, Mitchell AM\*, Laurie MT\*, Sunshine S\*, Pilarowski G\*, Ayscue P\*, Kistler A, Vanaerschot M, Li LM, McGeever A, Chow ED, Marquez C, Nakamura R, Rubio L, Chamie G, Jones D, Jacobo J, Rojas S, Rojas S, Tulier-Laiwa V, Black D, Martinez J, Naso J, Schwab J, Petersen M, Havlir D, DeRisi J; IDseq Team. Estimation of Secondary Household Attack Rates for Emergent Spike L452R Severe Acute Respiratory Syndrome Coronavirus 2 (SARS-CoV-2) Variants Detected by Genomic Surveillance at a Community-Based Testing Site in San Francisco. *Clin Infect Dis.* 2022; Jan 7;74(1):32-39. doi: 10.1093/cid/ciab283.

## **Chapter 8**

Includes content previously published in:

Sabatino JJ Jr, Mittl K, Rowles WM, McPolin K, Rajan JV, Laurie MT, Zamecnik CR, Dandekar R, Alvarenga BD, Loudermilk RP, Gerungan C, Spencer CM, Sagan SA, Augusto DG, Alexander JR, DeRisi JL, Hollenbach JA, Wilson MR, Zamvil SS, Bove R. Multiple sclerosis therapies differentially affect SARS-CoV-2 vaccine-induced antibody and T cell immunity and function. *JCI Insight.* 2022; Feb 22;7(4):e156978. doi:10.1172/jci.insight.156978.

## **Chapter 9**

Includes content previously published in:

Liu J, Laurie MT, Rubio L, Vazquez SE, Sunshine S, Mitchell AM, Hapte-Selassie M, Mann SA, Pilarowski G, Black D, Marquez C, Rojas S, Lionakis MS, Petersen M, Whitman JD, Jain V, Anderson M, Havlir D, DeRisi J. SARS-CoV-2 transmission dynamics and immune responses in a household of vaccinated persons. *Clin Infect Dis.* 2022; Jan 17:ciac029. doi: 10.1093/cid/ciac029.

## **Chapter 10**

Includes content previously published in:

Laurie MT, Liu J, Sunshine S, Peng J, Black D, Mitchell AM, Mann SA, Pilarowski G, Zorn KC, Rubio L, Bravo S, Marquez C, Sabatino JJ Jr, Mittl K, Petersen M, Havlir D, DeRisi J. SARS-CoV-2 variant exposures elicit antibody responses with differential cross-neutralization of established and emerging strains including Delta and Omicron. *J Infect Dis.* 2022; Jan 3:jiab635. doi: 10.1093/infdis/jiab635.

**Discovery and Characterization of Inhibitory Mechanisms of Drugs and Antibodies  
Against Viral, Fungal, and Amoebic Human Pathogens, Including  
SARS-CoV-2, Zika Virus, *Balamuthia mandrillaris*, and *Candida auris***

Matthew Thomas Laurie

**Abstract**

The development of effective approaches to prevent, diagnose, and treat infectious diseases is made possible through a strong basis in the fundamental biology of pathogen lifecycles as well as methods for direct discovery and validation of tools to fight infectious diseases. In this dissertation, I discuss work that was performed with the primary goal of identifying actionable countermeasure strategies against specific infectious diseases, while contributing to understanding aspects of basic pathogen biology where possible. Chapters 2 through 5 of this dissertation discuss efforts utilizing high-throughput small molecule screening to repurpose existing clinically-approved compounds as potential inhibitors of specific human pathogens. Chapters 2 and 3 describe discovery, validation, and mechanistic investigation for the novel antiviral effect of azithromycin. Chapter 4 describes a similar discovery pipeline for identification of the 8-hydroxyquinoline nitroxoline as a novel inhibitor of the brain-eating amoeba *Balamuthia mandrillaris*. In chapter 5, we apply a similar drug repurposing approach to validate the potent antifungal effect of another 8-hydroxyquinoline, clioquinol, against the fungal pathogen *Candida auris*. Chapters 6 through 10 describe studies pertaining to our team's response to the SARS-CoV-2 pandemic. Chapter 6 details a large team effort to validate the field performance of the Abbott BinaxNOW rapid SARS-CoV-2 antigen test that is now in widespread over the counter use. This antigen test was used extensively for the study described in chapter 7, which measured the transmission dynamics of specific SARS-CoV-2 variants. Chapters 8, 9, and 10 investigate the

magnitude and specificity of neutralizing antibody responses produced by individuals with prior exposure to SARS-CoV-2 variants and/or vaccines.

## Table of Contents

Chapter 1: An Introduction.....	1
Chapter 1 references.....	9
Chapter 2: Zika virus cell tropism and inhibition by azithromycin.....	12
Chapter 2 references.....	31
Chapter 3: Preliminary investigation of the antiviral mechanism of azithromycin.....	35
Chapter 3 references.....	53
Chapter 4: Identification and characterization of nitroxoline as a novel inhibitor of the amoebic pathogen <i>Balamuthia mandrillaris</i> .....	56
Chapter 4 references.....	87
Chapter 5: Identification and characterization of clioquinol as a potent inhibitor of <i>Candida</i> <i>Auris</i> .....	99
Chapter 5 references.....	132
Chapter 6: Real-world performance testing of a SARS-CoV-2 rapid antigen test in San Francisco, California.....	147
Chapter 6 references.....	160
Chapter 7: Differential secondary attack rates of SARS-CoV-2 variants measured by local viral genomic surveillance.....	162
Chapter 7 references.....	180
Chapter 8: Neutralizing antibody responses to SARS-CoV-2 vaccination in Multiple Sclerosis patients.....	184
Chapter 8 references.....	215

Chapter 9: Transmission dynamics of SARS-CoV-2 among vaccinated household members and related immune responses.....	220
Chapter 9 references.....	229
Chapter 10: Cross-neutralization of SARS-CoV-2 variants by immune sera elicited by a range of infection and vaccination exposures.....	231
Chapter 10 references.....	242

## List of Figures

### Chapter 2

- Figure 2.1 Tropism of ZIKV for radial glia in the developing human brain.....26
- Figure 2.2 ZIKV infects astrocytes in later stages of human brain development.....28
- Figure 2.3 Azithromycin (AZ) treatment inhibits ZIKV infection in glial cells.....30

### Chapter 3

- Figure 3.1 Antiviral activity of azithromycin and timing of inhibition.....48
- Figure 3.2 Characterization of azithromycin-resistant ZIKV mutants.....49
- Figure 3.3 Genetic modifiers of azithromycin anti-ZIKV activity.....50
- Figure 3.4 Synergistic activity of azithromycin in combination with entry inhibitors.....52

### Chapter 4

- Figure 4.1 Primary drug repurposing screen against *B. mandrillaris*.....78
- Figure 4.2 Activity of compounds structurally related to nitroxoline.....79
- Figure 4.3 Comparison of nitroxoline potency and selectivity to standard of care  
drugs.....80
- Figure 4.4 Drug-induced encystment and killing of *B. mandrillaris* cysts.....81
- Figure 4.5 Nitroxoline prevention of brain explant destruction by *B. mandrillaris*.....82
- Figure 4.6 Example brightfield images of *B. mandrillaris* trophozoites and cysts.....83
- Figure 4.7 Efficacy of nitroxoline in combination with miltefosine and pentamidine  
isethionate for inhibition of *B. mandrillaris*.....84
- Figure 4.8 Inhibition of *B. mandrillaris*-mediated brain tissue explant destruction in  
the presence of nitroxoline.....85



## Chapter 5

- Figure 5.1 A screen of 1990 clinically approved and investigational compounds for *in vitro* inhibition of *C. auris* identified 89 candidates for further evaluation.....128
- Figure 5.2 Secondary screening and selectivity measurement identified five promising compounds, including three hydroxyquinolines.....129
- Figure 5.3 Evolution of clioquinol resistance in a serial passaging selection experiment.....130
- Figure 5.4 Dihalogenated 8-hydroxyquinolines are the most effective inhibitors of *C. auris* and this activity is abrogated by the presence of Iron or Copper.....131

## Chapter 6

- Figure 6.1 Titration of in vitro grown severe acute respiratory syndrome coronavirus 2 and detection with Binax-CoV2 assay.....157
- Figure 6.2 Comparison of Binax-CoV2 test with quantitative reverse-transcription polymerase chain reaction (RT-PCR) test.....158
- Figure 6.3 Variability of signal intensity in Binax-CoV2 card lots.....159

## Chapter 7

- Figure 7.1 Testing catchment area.....176
- Figure 7.2 Variants observed at 24th & Mission.....177

## Chapter 8

- Figure 8.1 Analysis of total spike and spike RBD IgG before and after SARS-CoV-2 vaccination of patients with MS receiving different DMTs.....210

Figure 8.2 VirScan analysis of postvaccination Ab reactivity against the SARS-CoV-2 spike proteome by MS DMT status.....	211
Figure 8.3 SARS-CoV-2 pseudovirus neutralization in seropositive patients treated with S1P receptor modulators or anti-CD20 mAbs.....	212
Figure 8.4 Evaluation of spike antigen-specific CD4 <sup>+</sup> and CD8 <sup>+</sup> T cells in patients with MS treated with different DMTs.....	213
Figure 8.5 Ex vivo analysis of postvaccination spike-specific CD8 <sup>+</sup> T cells of patients with MS treated with different DMTs, by pMHC I tetramer.....	214
 Chapter 9	
Figure 9.1 Serum samples from household individuals reveal diverse neutralization capabilities as well as presence of anti-IFN- $\alpha$ 2 auto-antibodies in Individual 1.....	227
Figure 9.2 Sequencing depth and coverage of recovered SARS-CoV-2 genomes.....	228
 Chapter 10	
Figure 10.1 Neutralization of D614G and B.1.429 pseudoviruses by serum from individuals with different exposures.....	240
Figure 10.2 Change in variant pseudovirus neutralization titer relative to D614G.....	241

## List of Tables

### Chapter 4

Table 4.1 Recrudescence time of active <i>B. mandrillaris</i> following drug treatment.....	86
---	----

### Chapter 7

Table 7.1 Characteristics of households included in the household attack rate analysis, stratified by strain.....	178
Table 7.2 Secondary household attack rates for West Coast Variants, combined and disaggregated by B.1.427 and B.1.429.....	178
Table 7.3 Secondary attack rate disaggregated by covariates.....	179

## List of Abbreviations

AZ – Azithromycin

CC<sub>50</sub> – Half-maximal cytotoxic concentration

CNS – Central nervous system

Covid-19 – Coronavirus disease 2019

EC<sub>50</sub> – Half-maximal effective concentration

hpi – Hours post-infection

IC<sub>50</sub> – Half-maximal inhibitory concentration

MOI – Multiplicity of infection

NT<sub>50</sub> – 50% neutralization titer

NX – Nitroxoline

qRT-PCR – Quantitative reverse transcriptase polymerase chain reaction

SARS-CoV-2 – Severe Acute Respiratory Syndrome Coronavirus 2

## **Chapter 1:**

### **An Introduction**

Science has afforded humanity the incredible ability to treat and prevent infectious diseases through understanding the fundamental biology underlying pathogenesis and through empirical discovery and validation of specific interventions. Although incredible medical advancements have prevented and cured many terrible infectious diseases, there exists an equally incredible diversity of endemic and emerging human and animal pathogens that present constant challenges to our ability to develop effective countermeasures [1,2]. These challenges are apparent at every level of infectious disease medicine, including the basic science research that supports development of diagnostic tools and novel vaccine and treatment options. The available research tools, experimental procedures, and existing bodies of literature vary greatly between different pathogens. Furthermore, vast differences in the biology of diverse pathogens in terms of structure, lifecycle, and mechanism of pathogenesis lead to inherently different opportunities for diagnostic methods and treatment targets. Less common pathogens, particularly those with poorly understood lifecycles, are highly unlikely to attract investment in commercial drug discovery programs and even less likely to be studied in clinical trials. Finally, the evolution of drug resistance and immune evasion creates a constant arms race between pathogens and strategies to mitigate their impact [3,4]. Factors such as these heavily influence the ability to turn laboratory research studies into medically useful outcomes and lead to large differences in the availability of tools to fight different types of pathogens. A stark example of this is the very large number of antibiotic drugs that have been discovered relative to the number of antiviral drugs [5,6]. Difficulties presented by the lack of research tools and limitations of biology certainly do not mean that there is no viable way to

fight certain pathogens, rather than it is necessary to invest effort to adapt our approaches to the biological context of each pathogen.

Much of the work presented in this dissertation was performed with the goal of identifying opportunities to produce clinically relevant and potentially actionable findings through empirical drug screening studies. These opportunities have presented themselves in the DeRisi lab in large part due to the lab's pioneering of metagenomic sequencing techniques for identifying mystery pathogens and due to close associations with clinical scientists. As discussed here across multiple chapters, these opportunities have presented themselves for pathogens ranging from the brain-eating amoeba *Balamuthia mandrillaris*, a very rare infection, to SARS-CoV-2, which will continue to affect the lives of nearly every person on Earth for decades to come. Studying Zika virus during the 2016 outbreak presented the first way for me to contribute to infectious disease research with a team of fantastic scientists in the DeRisi lab. Because the threat of Zika as a pathogen was largely due to its effects *in utero*, our team focused our efforts on understanding the virus in that context and searching for potential treatment options that would be safe in pregnancy. For *Balamuthia*, the opportunity to make a significant impact in the study and clinical approach towards this pathogen was apparent, as *Balamuthia* brain infections result in a greater than 95% mortality rate even with treatment, reflective of a very poor standard of care and lack of specifically effective treatment options [7]. For the fungal pathogen *Candida auris*, effective treatments currently exist, but the recent emergence of strains that are resistant to all three major classes of antifungals is a cause for concern and led us to design a study to address the need for novel treatment options outside of the established classes of antifungal drugs [8,9]. Finally, although an unprecedented number of researchers have focused their efforts on SARS-CoV-2 since the beginning of the Covid-19 pandemic, our group has found several additional important ways to

contribute through verification of diagnostic test performance, viral genome surveillance, and analysis of humoral immune responses to vaccination and infection with variants.

For certain highly prevalent pathogens such as SARS-CoV-2, significant investment has been made to fast-track efforts to develop diagnostics, therapies, and vaccines [10,11]. However, this is very much the exception within infectious disease research as for most pathogens, the traditional drug and vaccine development pipelines are prohibitively costly and time consuming. Several of the pathogens that I have studied fall under this category as they are either too rare or emerged too rapidly for typical development timelines to be practical, resulting in unmet needs for therapeutic options. Several of the studies described in this manuscript attempted to subvert some of these issues using a strategy to identify clinically-approved compounds that are candidates for repurposing using high-throughput screening. The primary advantage of this general approach is that clinically-approved drugs have already undergone substantial testing to rigorously establish pharmacological and safety profiles, which eliminates a significant hurdle in therapeutic development. Repurposed drugs that have already been shown to be safe in humans can theoretically be deployed much more rapidly against a novel indication compared to newly discovered compounds with unknown safety profiles. For extremely rare pathogens, drug repurposing may, in fact, be the only option available for finding new treatments. The most significant limitation to drug repurposing screens is the relatively small set of approximately 2000 drugs that are currently approved for clinical use, which reduces the likelihood of finding inhibitors with activity specific pathogens. Nevertheless, *in vitro* drug repurposing strategies have been successfully employed by several groups and we have attempted to add to this field by adapting screening and validation techniques to different pathogens by addressing the unique challenges specific to each biological context [12–14].

A thorough and specific introduction for each study is included within each chapter, but a broad overview will be provided here for context and to connect common themes and methods used across different studies. Chapters 2 and 3 discuss efforts to identify inhibitors of the arthropod-borne flavivirus Zika that would be safe for use in pregnancy [15]. We performed a screen of nearly 2000 FDA- and internationally-approved drugs for inhibition of the cytopathic effect caused by Zika virus in a human glioma cell line, selected to be somewhat representative of one of the cell types observed to be infected in the developing brain. The lead candidate that we identified from this screen was the macrolide antibiotic azithromycin, which is extremely widely used, well-tolerated, and safe for use in pregnancy. Our *in vitro* studies with azithromycin showed that the antiviral effect exists in multiple cell types in the low micromolar range and occurs at concentrations that are not toxic to host cells. Preliminary investigations into the antiviral mechanism of action of azithromycin are discussed in Chapter 3. Although these studies did not definitively identify the antiviral mechanism, we produced circumstantial evidence that azithromycin inhibits the entry of Zika virus into host cells by preventing the normal migration of viral particles through host endosomes.

Chapter 4 details a drug repurposing study designed to identify inhibitors of the brain-eating amoeba *Balamuthia mandrillaris* [16]. Although *Balamuthia* infections are extremely rare with only a handful of documented cases per year, nearly all past cases have been fatal [7]. One drug discovery challenge that is specific to *Balamuthia* is that this pathogen has both an active trophozoite form as well as a highly robust cyst form that is resistant to many types of damage including many drug treatments. The existing standard of care for *Balamuthia* infections recommended by the CDC includes several drugs with significant side effects and a lack of proven activity against *Balamuthia*, even *in vitro* [17]. Our drug repurposing screen identified nitroxoline,



an 8-hydroxyquinoline antibiotic approved for clinical use in Europe, as a potent inhibitor of *Balamuthia*. We showed that nitroxoline, unlike the current standard of care drugs, inhibits *Balamuthia* at concentrations below cytotoxicity to human cells. Importantly, we also showed that nitroxoline inhibits both the trophozoite and cyst forms of *Balamuthia* and that nitroxoline treatment prevented the recrudescence of *Balamuthia* trophozoites for at least one month. Finally, we performed brain tissue explant experiments to show that nitroxoline treatment prevented *Balamuthia*-mediated destruction of tissue. The publication of our study directly led to an emergency investigational new drug authorization being granted for the use of nitroxoline in patients with *Balamuthia* infection of the brain and, at the time of this writing, at least one patient is currently being treated for *Balamuthia* with nitroxoline.

Chapter 5 describes another drug repurposing study, this time aimed at discovering novel inhibitors of the fungal pathogen *Candida auris*, which is noteworthy for the frequent isolation of highly drug-resistant strains, including those resistant to all three major classes of antifungal drugs [8,9]. Because different *C. auris* strains have evolved a variety of mechanisms of resistance to different drugs, we designed our drug repurposing pipeline to identify inhibitors that were broadly effective against a wide range of genetically diverse strains. Our primary screen identified several hit compounds that inhibited *C. auris* growth at sub-micromolar concentrations. Subsequent experiments to determine the breadth of drug effects across many *C. auris* strains and the toxicity to human cells narrowed the list of candidates down to a small handful of highly selective inhibitors. Because the evolution of resistance even to novel drugs is a concern, we performed *in vitro* selections for drug resistance for the lead compounds. We found that for clioquinol, an 8-hydroxyquinoline antibiotic, *C. auris* gained only a very moderate 2- to 6- fold increase in resistance after almost 200 generations of selection, a much lower magnitude of resistance

compared to other drugs [18–20]. Due to its potency, selectivity, and relatively low propensity for resistance evolution, clioquinol was the clear lead compound identified in our study. Interestingly, the mutations that confer resistance to clioquinol in our *in vitro* selection experiments increase susceptibility to certain other antifungals including posaconazole, which is used frequently in the current standard of care. We also provide strong evidence that clioquinol inhibits *C. auris* growth through a metal chelation mechanism and structurally related compounds behave similarly to clioquinol.

In addition to the drug repurposing studies mentioned above, this dissertation also describes a separate set of projects focused on epidemiology, viral evolution, and host immune response related to SARS-CoV-2. Because several members of the DeRisi lab already had significant expertise in virology and interest in public health collaborations, we had several opportunities to assist in rapid response efforts aiming to help mitigate aspects of the Covid-19 pandemic. One such opportunity is detailed in Chapter 6, in which we evaluated the real-world performance of a SARS-CoV-2 diagnostic rapid antigen test, the Abbott BinaxNOW test, in comparison to established qRT-PCR tests [21]. Close collaboration with the Unidos en Salud community health program in San Francisco enabled the validation study for BinaxNOW and opened the door for subsequent efforts to utilize rapid testing at community Covid-19 testing sites in San Francisco to support sequencing of SARS-CoV-2 samples from positive individuals for genomic surveillance of viral variants. In chapter 7, we used this data to characterize the diversity of circulating variants and to calculate the differential attack rate of certain variants relative to the wild-type virus [22].

Chapters 8 through 10 describe studies that examine aspects of humoral immunity acquired by exposure to SARS-CoV-2 infection or vaccination. Neutralizing antibodies that are produced in response to vaccination or natural infection strongly correlate with protective immunity against

SARS-CoV-2 infection and severe illness. To study neutralizing antibody responses in different exposure contexts and understand the specificity of polyclonal responses, we used a pseudovirus reporter assay that expresses different versions of the SARS-CoV-2 spike glycoprotein on the outside of virus-like particles. In the work described in Chapter 8, we assessed neutralizing antibody titers in healthy donors as well as patients undergoing multiple sclerosis treatment to show that specific MS drugs, which are known to affect immune function, interfere with production of neutralizing antibodies targeting SARS-CoV-2 [23]. In Chapter 9 we show that, despite normal levels of anti-SARS-CoV-2 neutralizing antibodies, breakthrough infections of vaccinated individuals can occur and may be exacerbated in several circumstances, including infection with viral variants and underlying autoimmune disorders [24].

In Chapter 10, we address questions related to how the neutralizing antibody response changes based on the SARS-CoV-2 variant that an individual was exposed to and how this determines the specificity of cross-neutralization towards the landscape of circulating variants [25]. The opportunity to perform this study came from a community testing and viral genome surveillance partnership that was previously mentioned in Chapter 8. Since viral genomes were sequenced for variant surveillance, we were able to acquire convalescent serum samples from donors with known exposure to specific SARS-CoV-2 variants. Access to exposure-matched serum allowed us to design a cross-reactivity matrix study in which the neutralization efficiency of different serum exposure groups was tested against pseudoviruses representative of different SARS-CoV-2 variants. The results of this study showed that polyclonal anti-sera is most efficient at neutralizing variants sharing key spike mutations with the variant that the donor was exposed to. Additionally, we showed that serial exposure to SARS-CoV-2 spike in the form of natural

infection and/or vaccination resulted in not only higher overall antibody titers, but also an increased breadth of cross-reactive neutralization.

The ideas and study findings presented in this dissertation are products of the dedication and creativity of many talented scientists that worked together in the collaborative, multi-disciplinary environment of the DeRisi lab and the Chan Zuckerberg Biohub. It was a great privilege to be a part of projects that successfully identified novel drug candidates against three different pathogens, Zika virus, *Candida auris*, and *Balamuthia Mandrillaris* and may one day contribute to the development of viable therapies. As a basic scientist, it has also been an important experience to contribute to the understanding of pathogen lifecycles and identification of pathway vulnerabilities that suggest potential treatment options. To study infectious disease during a global pandemic was a unique challenge and call to action. I am very proud of the work that our team did in helping to support Covid-19 diagnostics, track the transmission of viral variants, and characterize the immune responses to different types of exposures. I am thankful for all of these opportunities, but I hope there are far fewer of them in the future.

## Chapter 1 References:

1. Dunn RR, Davies TJ, Harris NC, Gavin MC. Global drivers of human pathogen richness and prevalence. *Proc Biol Sci.* 2010; 277(1694):2587–2595.
2. Murray KA, Preston N, Allen T, Zambrana-Torrel C, Hosseini PR, Daszak P. Global biogeography of human infectious diseases. *Proceedings of the National Academy of Sciences.* *Proceedings of the National Academy of Sciences*; 2015; 112(41):12746–12751.
3. Nabel KG, Clark SA, Shankar S, et al. Structural basis for continued antibody evasion by the SARS-CoV-2 receptor binding domain. *Science.* 2022; 375(6578):eabl6251.
4. Antimicrobial Resistance Collaborators. Global burden of bacterial antimicrobial resistance in 2019: a systematic analysis. *Lancet.* 2022; 399(10325):629–655.
5. Purssell E. Antimicrobials. *Understanding Pharmacology in Nursing Practice.* 2019; :147–165.
6. Adalja A, Inglesby T. Broad-Spectrum Antiviral Agents: A Crucial Pandemic Tool. *Expert Rev Anti Infect Ther.* 2019; 17(7):467–470.
7. Martínez DY, Seas C, Bravo F, et al. Successful treatment of *Balamuthia mandrillaris* amoebic infection with extensive neurological and cutaneous involvement. *Clin Infect Dis.* 2010; 51(2):e7-11.
8. *Candida auris* Clinical Update - September 2017 | *Candida auris* | Fungal Diseases | CDC [Internet]. 2019 [cited 2022 Apr 12]. Available from: <https://www.cdc.gov/fungal/candida-auris/c-auris-alert-09-17.html>
9. Forsberg K, Woodworth K, Walters M, et al. *Candida auris*: The recent emergence of a multidrug-resistant fungal pathogen. *Med Mycol.* 2019; 57(1):1–12.

10. Kyriakidis NC, López-Cortés A, González EV, Grimaldos AB, Prado EO. SARS-CoV-2 vaccines strategies: a comprehensive review of phase 3 candidates. *NPJ Vaccines*. 2021; 6(1):28.
11. Research C for DE and. Coronavirus Treatment Acceleration Program (CTAP). FDA [Internet]. FDA; 2022 [cited 2022 Apr 12]; . Available from: <https://www.fda.gov/drugs/coronavirus-covid-19-drugs/coronavirus-treatment-acceleration-program-ctap>
12. Sleigh SH, Barton CL. Repurposing Strategies for Therapeutics. *Pharm Med*. 2010; 24(3):151–159.
13. Ashburn TT, Thor KB. Drug repositioning: identifying and developing new uses for existing drugs. *Nat Rev Drug Discov*. 2004; 3(8):673–683.
14. Firth A, Prathapan P. Broad-spectrum therapeutics: A new antimicrobial class. *Curr Res Pharmacol Drug Discov*. 2021; 2:100011.
15. Retallack H, Di Lullo E, Arias C, et al. Zika virus cell tropism in the developing human brain and inhibition by azithromycin. *Proc Natl Acad Sci U S A*. 2016; 113(50):14408–14413.
16. Laurie MT, White CV, Retallack H, et al. Functional Assessment of 2,177 U.S. and International Drugs Identifies the Quinoline Nitroxoline as a Potent Amoebicidal Agent against the Pathogen *Balamuthia mandrillaris*. *mBio*. 2018; 9(5):e02051-18.
17. Treatment | Balamuthia | Parasites | CDC [Internet]. 2019 [cited 2022 Apr 12]. Available from: <https://www.cdc.gov/parasites/balamuthia/treatment.html>
18. Rybak JM, Muñoz JF, Barker KS, et al. Mutations in TAC1B: a Novel Genetic Determinant of Clinical Fluconazole Resistance in *Candida auris*. *mBio*. 2020; 11(3):e00365-20.

19. Bing J, Hu T, Zheng Q, Muñoz JF, Cuomo CA, Huang G. Experimental Evolution Identifies Adaptive Aneuploidy as a Mechanism of Fluconazole Resistance in *Candida auris*. *Antimicrob Agents Chemother*. 2020; 65(1):e01466-20.
20. Carolus H, Pierson S, Muñoz JF, et al. Genome-Wide Analysis of Experimentally Evolved *Candida auris* Reveals Multiple Novel Mechanisms of Multidrug Resistance. *mBio*. 2021; 12(2):e03333-20.
21. Pilarowski G, Lebel P, Sunshine S, et al. Performance Characteristics of a Rapid Severe Acute Respiratory Syndrome Coronavirus 2 Antigen Detection Assay at a Public Plaza Testing Site in San Francisco. *J Infect Dis*. 2021; 223(7):1139–1144.
22. Peng J, Liu J, Mann SA, et al. Estimation of secondary household attack rates for emergent spike L452R SARS-CoV-2 variants detected by genomic surveillance at a community-based testing site in San Francisco. *Clin Infect Dis*. 2021; :ciab283.
23. Sabatino JJ, Mittl K, Rowles WM, et al. Multiple sclerosis therapies differentially affect SARS-CoV-2 vaccine-induced antibody and T cell immunity and function. *JCI Insight*. 2022; 7(4):e156978.
24. Liu J, Laurie MT, Rubio L, et al. SARS-CoV-2 transmission dynamics and immune responses in a household of vaccinated persons. *Clin Infect Dis*. 2022; :ciac029.
25. Laurie MT, Liu J, Sunshine S, et al. SARS-CoV-2 variant exposures elicit antibody responses with differential cross-neutralization of established and emerging strains including Delta and Omicron. *J Infect Dis*. 2022; :jiab635.

## Chapter 2:

### Zika virus cell tropism and inhibition by azithromycin

This chapter is a reprint of:

Retallack H\*, Di Lullo E\*, Arias C, Knopp KA, Laurie MT, Sandoval-Espinosa C, Mancia Leon WR, Krencik R, Ullian EM, Spatazza J, Pollen AA, Mandel-Brehm C, Nowakowski TJ, Kriegstein AR, DeRisi JL. Zika virus cell tropism in the developing human brain and inhibition by azithromycin. *Proc Natl Acad Sci U S A*. 2016;113(50):14408-14413.

doi:10.1073/pnas.1618029113

\*These authors contributed equally to this work

Supplemental files that are not figures can be found with the original work.



## ***Abstract***

The rapid spread of Zika virus (ZIKV) and its association with abnormal brain development constitute a global health emergency. Congenital ZIKV infection produces a range of mild to severe pathologies, including microcephaly. To understand the pathophysiology of ZIKV infection, we used models of developing brain that faithfully recapitulate the tissue architecture in early- to mid-gestation. We identify the brain cell populations that are most susceptible to ZIKV infection in primary human tissue, provide evidence for a mechanism of viral entry, and show that a commonly used antibiotic protects cultured brain cells by reducing viral proliferation. In the brain, ZIKV preferentially infected neural stem cells, astrocytes, oligodendrocyte progenitor cells, and microglia, whereas neurons were less susceptible to infection. These findings suggest mechanisms for microcephaly and other pathologic features of infants with congenital ZIKV infection that are not explained by neural stem cell infection alone, such as calcifications in the cortical plate. Furthermore, we find that blocking the glia-enriched putative viral entry receptor, AXL, reduced ZIKV infection of astrocytes *in vitro* and genetic knockdown of AXL in a glial cell line nearly abolished infection. Finally, we evaluate 2,177 compounds, focusing on drugs safe in pregnancy. We show the macrolide antibiotic, azithromycin, reduced viral proliferation and viral-induced cytopathic effects in glial cell lines and human astrocytes. Our characterization of infection in developing human brain clarifies the pathogenesis of congenital ZIKV infection and provides the basis for investigating possible therapeutic strategies to safely alleviate or prevent the most severe consequences of the epidemic.

### ***Significance statement***

Zika virus is a mosquito-borne flavivirus that has rapidly spread through the Americas and has been associated with fetal abnormalities, including microcephaly. To understand how microcephaly develops, it is important to identify which cell types of the developing brain are susceptible to infection. We use primary human tissue to show that radial glia and astrocytes are more susceptible to infection than neurons, a pattern that correlates with expression of a putative viral entry receptor, AXL. We also perform a screen of FDA-approved compounds, with an emphasis on drugs known to be safe in pregnancy. We identify an antibiotic, azithromycin, that reduces viral proliferation in glial cells, and compare its activity to daptomycin and sofosbuvir, two additional drugs with anti-ZIKV activity.

### ***Main Text***

A correlation between congenital exposure to the mosquito-borne and sexually transmitted Zika flavivirus (ZIKV) and the increased incidence of severe microcephaly suggests a causal relationship between ZIKV infection and neurodevelopmental abnormalities (1, 2). However, the mechanisms of infection and specifically which cell populations are vulnerable to ZIKV during the course of human brain development remain unclear. Major insights have been drawn from in vitro models of human brain development and primary mouse tissues. In the developing mouse brain, ZIKV has been shown to infect radial glia and neurons (3), whereas studies in human pluripotent stem cell (hPSC)-derived neural cells have highlighted widespread infection and apoptosis of neural progenitor cells (4, 5). Because these models do not fully recapitulate the developmental events and cell types present during human brain development, these results may not faithfully represent ZIKV-induced pathology in vivo.

During human brain development, radial glial cells, the neural stem cells, give rise to diverse types of neuronal and glial cells, including neurons, oligodendrocytes, and astrocytes, in a temporally controlled pattern. We reasoned that identifying cell types that are especially vulnerable to viral infection would facilitate studies of the viral life cycle, including entry mechanisms and host cell requirements. Building on studies that suggested that enriched expression of the candidate entry factor AXL could confer vulnerability to ZIKV entry (6–8), we used AXL expression levels to predict that radial glia, astrocytes, microglia, and endothelial cells would be particularly vulnerable to infection (9). A recent study highlighted the utility of *ex vivo* models using primary human tissue samples to analyze the consequences of ZIKV infection in the human prenatal brain (7). Here we further use primary tissue samples from distinct stages of brain development corresponding to periods of peak neurogenesis and early gliogenesis.

Determining the tropism of ZIKV for specific cell types will help identify suitable cellular models for investigating potential therapeutic interventions. Although development of a vaccine could provide a long-term solution to the current ZIKV epidemic, there remains an unmet clinical need to identify drugs that can limit or prevent the consequences of congenital infection. A recent screen of a subset of Food and Drug Administration (FDA)-approved compounds against ZIKV in hepatic cells identified several anticancer, antimicrobial, antiparasitic, and antifungal drugs with anti-ZIKV activity (10). Another screen, based on human neural progenitor cells, identified an antifungal drug and several scaffold compounds for further development (11). However, the majority of compounds with anti-ZIKV activity from these screens are contraindicated or of unknown safety during pregnancy. Furthermore, two promising candidates that might be safe during pregnancy, daptomycin and sofosbuvir, showed variable effectiveness by cell type (7, 10, 12). Combining unbiased screens of approved compounds with comparisons of top

candidates with known antiviral activity may quickly narrow the search for drugs that could mitigate the effects of congenital ZIKV infection.

Here we assessed ZIKV cell tropism in the developing human brain and performed a drug screen on relevant cell types targeted by the virus with an emphasis on drugs known to be safe in pregnancy. We found that radial glia and, later in development, astrocytes were especially vulnerable to ZIKV infection. By screening FDA-approved compounds for anti-ZIKV activity in a glial cell line with features of both cell types, we also found that the common antibiotic azithromycin prevented viral production and virus-mediated cell death, which we further validated in human astrocytes.

## ***Results***

To determine the cell populations most susceptible to ZIKV infection we investigated the infectivity of ZIKV in the developing human brain using organotypic cultures from primary human tissue. We exposed human cortical tissue slices to three strains of ZIKV: Cambodia 2010 (ZIKV-CAM), Brazil 2015 (ZIKV-BR), and Puerto Rico 2015 (ZIKV-PR), cultured them for 72 hours (h), and detected infection by immunostaining for the flavivirus envelope protein (ENV), an approach that we validated in cultured cells (Fig. S1). Infection in tissue was confirmed by immunostaining for the viral RNA- dependent RNA polymerase, nonstructural protein 5 (NS5), present only during viral replication. In samples from mid-neurogenesis (13-16 post-conception weeks (pcw)), we observed high rates of infection in the ventricular and subventricular zones (Figure 2.1, and Fig. S2). We found that the virus preferentially infected both ventricular (vRG) and outer radial glia (oRG) cells (Figure 2.1, A to F, and Fig. S2). Interestingly, we observed clusters of infected radial glia (Fig. S2B), which may reflect local viral spread. A minor fraction

of cells positive for ENV at these stages included postmitotic neurons (Fig. 1H), and microglia (Figure 2.1 I). We observed similar patterns of infection across ZIKV strains (Fig. S2). We also observed a small but significant increase in cell death of ENV+ cells as compared to ENV- cells in ZIKV-infected tissue or mock-infected tissue (Fig. S3).

At later stages of development (after 17 pcw), we observed infection and viral replication throughout the developing cortex, including the cortical plate and subplate, with production of infectious virus by 48 hpi (Figure 2.2, and Fig. S4). Among cortical plate cells, we observed a high rate of infection in astrocytes as distinguished by their location, morphology, and immunoreactivity with the glial markers GFAP and SOX2 (Figure 2.2, A, B and D, and Fig. S4, A, B, C, and D). We also observed cells immunoreactive for both ENV and the microglial marker IBA1, indicating microglial infection or phagocytosis of other ZIKV infected cells (Figure 2.2, and Fig. S4 G and H). This ENV+/IBA1+ microglial population was quantified at  $7\pm 1\%$  of ENV+ cells, and represented  $7\pm 2\%$  of the total IBA1+ population ( $n = 4$ , 15-22 pcw, see Methods). We further observed infection of oligodendrocyte precursor cells (OPCs) (Figure 2.2G and Fig. S4I), but limited infection of neurons (Figure 2.2, B and D, and Fig. S4, A and J). This pattern of infectivity was consistent across ZIKV strains (Fig. S4) and matched viral tropism predicted by AXL receptor expression (9).

To test the possible role of AXL in mediating ZIKV entry into human astrocytes, we infected hPSC-derived astrocytes (13, 14) in the presence of a nonactivating antibody specific for the extracellular domain of AXL. Blocking the AXL receptor substantially reduced infection (Fig. 2 I and J and Fig. S5A). To further test the requirement of AXL for ZIKV infection of glial cells, we used the U87 glioblastoma line that expresses high levels of astrocyte marker genes and AXL

(15). U87 cells were readily infected with ZIKV, with strong virus production at 48 hpi (Fig. S1) and robust cytopathic effect at 72 hpi (Fig. 3C and Fig. S6D). We then used CRISPR interference (CRISPRi) to knock down AXL in this cell line (*SI Materials and Methods*; validated by Western blot in Fig. S5B) and observed a substantial decrease in infection (Fig. 2K), confirming the importance of this receptor for ZIKV infection in this cell type. Given that AXL is a receptor tyrosine kinase with signaling pathways that could be involved in innate immune responses (16), we tested whether the kinase activity of AXL was relevant for the decrease in infection observed in the knockdown line. After pretreatment with a small-molecule inhibitor, R428, we observed no decrease in infection at up to 1  $\mu\text{M}$ , which is >70-fold the half-maximal effective concentration ( $\text{EC}_{50}$ ) for AXL kinase inhibition (Fig. S5C) (17). Although we did observe a decrease in infection at 3  $\mu\text{M}$  R428, this high concentration of >200-fold the  $\text{EC}_{50}$  likely created off-target effects. Together, these results suggest that AXL has an important role in glial cell infection that depends more on its extracellular domain than on its intracellular kinase activity.

There is a pressing need to identify pharmacological compounds that can diminish the effects of ZIKV infection in relevant human cell types. We performed a screen of 2177 clinically approved compounds (2016 unique) by monitoring inhibition of virus-dependent cell death at 72 hpi in Vero cells. While our screen revealed compounds that rescued cell viability, including antibiotics and inhibitors of nucleotide and protein synthesis, many showed toxicity in Vero or U87 cells, or are contraindicated during pregnancy (Tables S1, S2, S3, S4). We focused on further characterization of the macrolide antibiotic azithromycin (AZ), which rescued ZIKV-induced cytopathic effect with low toxicity in our primary screens, and is generally safe during pregnancy (18). AZ dramatically reduced ZIKV infection of U87 cells at an  $\text{EC}_{50}$  of 2-3  $\mu\text{M}$  at multiplicities of infection (MOIs) of 0.01-0.1, as evaluated by ENV staining (Figure 2.3, A and B, and Fig. S6A).

We further established a relationship between EC<sub>50</sub> and baseline infection rate (Fig. S6B), and showed that even at >60% infection, AZ consistently reduced infection at concentrations ten- to twenty-fold below the half-maximal toxicity concentration (TC<sub>50</sub>) of 53 μM (Fig. S6, A and C). AZ treatment also rescued cell viability (Figure 2.3C, Fig. S6D) and decreased viral production (Figure 2.3D). Finally, we found that AZ substantially reduced infection in hPSC-derived astrocytes without toxicity at the effective concentration (EC<sub>50</sub> 15 μM at 72% baseline infection) (Fig. S6, E to G). To compare AZ with compounds identified in previous screens, we evaluated the anti-ZIKV activity of daptomycin and sofosbuvir in U87 cells (EC<sub>50</sub> 2.2 μM and 12.4 μM respectively) (Fig. S6H). We observed that treatment with daptomycin was insufficient to lower the percentage of infected cells below 46% even at the highest dose in this cell type (20 μM) (Fig. S6H), whereas AZ and sofosbuvir treatment decreased ZIKV infection from 78% to below 5% infection at 20 μM and 50 μM respectively. These results highlight AZ as a potential tool compound against ZIKV infection in glial cells.

### ***Discussion***

The rapid spread of ZIKV and its link to fetal abnormalities, including microcephaly, have created a global health crisis. Understanding viral tropism for specific cell types in the developing brain furthers our understanding of the pathophysiology of ZIKV-associated microcephaly and provides a basis for investigating antiviral drugs in a relevant cell type. Our findings offer several novel aspects. In particular, we show ZIKV tropism for astrocytes in addition to radial glia in the primary developing human brain, demonstrate the importance of AXL for ZIKV infection of glial cells, and identify a common antibiotic with anti-ZIKV activity, AZ, which we compare with two other drugs with anti-ZIKV activity that may be safe in pregnancy.

Our finding that radial glia are preferentially infected during early neurogenesis is consistent with experiments in cultured primary human brain cells (19), developing mouse cortex (3, 20), and primary human organotypic brain slice culture (7). These studies also reported overall survival of infected radial glia, in contrast to in vitro derived neural stem cells that undergo apoptotic cell death following infection (4, 5, 21). Cell lines derived from primary neural progenitors have variably shown infection with substantial apoptosis (7) or persistence (19). In our organotypic slice culture, we observe a small increase in apoptosis of infected cells. The discrepancy in levels of apoptosis in dissociated versus tissue cell culture may reflect differences in gene expression, maturation, or experimental conditions. Besides causing cell death, ZIKV infection could also affect cell-cycle progression (3, 21), differentiation, or the migration and survival of newborn neurons—mechanisms thought to underlie genetic causes of microcephaly and lissencephaly (22). Tissue disorganization in organotypic slice culture suggests these non-cell death-mediated mechanisms may contribute to clinical phenotypes (7), but this remains to be confirmed by directly analyzing cell behavior.

The high rate of infection in astrocytes at later developmental ages, many of which contact microcapillaries, could link our understanding of initial infection with clinical findings of cortical plate damage. For example, after prolonged infection, viral production in astrocytes could lead to a higher viral load in the cortical plate, causing infection of additional cortical cell types, and astrocyte loss could lead to inflammation and further damage, even in uninfected cells. Widespread cell death in vivo, which may take days to weeks to occur and is therefore outside the time frame of our experimental paradigm, is expected, given clinical reports of band-like calcifications in the cortical plate, cortical thinning, and hydrocephalus (2, 23). On the basis of their susceptibility to ZIKV infection and a central role in brain tissue homeostasis, human astrocytes provide a good



cellular model for further investigation of mechanisms of viral entry and a platform for testing the efficacy of candidate therapeutic compounds.

Our observation that blocking or knocking down the AXL receptor prevents infection of human astrocytes, but that blocking intracellular kinase activity does not, suggests that the extracellular domain of AXL contributes to ZIKV infection whereas AXL signaling is dispensable. This extends comparable findings in endothelial cells to a cell type relevant for understanding microcephaly (6, 8) but does not address other viral receptors that may be important for ZIKV infectivity in other cell types or rule out a role for AXL signaling in the context of a full immune response *in vivo*. Although AXL knockout mice can be readily infected with ZIKV, disruption of the blood–brain barrier in these mice could lead to atypical routes for infection of the brain (24).

In addition to characterizing brain cell tropism, we also sought to identify possible therapeutic candidates with known safety profiles, especially in pregnancy. Several compounds expected to inhibit ZIKV were identified by our drug screen. These positive controls include the protein synthesis inhibitor cycloheximide, nucleic acid synthesis inhibitors such as mycophenolate derivatives, and intercalating compounds such as doxorubicin and homidium bromide. We additionally identified compounds that are known to be safe in pregnancy, including AZ. AZ is recommended for the treatment of pregnant women with sexually transmitted infections or respiratory infections due to AZ-susceptible bacteria (25, 26). Adverse events have not been observed in animal reproduction studies, and studies in pregnant women show no negative effects on pregnancy outcome or fetal health associated with AZ (18, 27). Orally administered AZ has been shown to reach concentrations of  $\sim 2.8 \mu\text{M}$  in the placenta, and is rapidly transported to amniotic fluid and umbilical cord plasma in humans (28, 29). Moreover, AZ accumulates in fetal

tissue and in the adult human brain at concentrations from 4 to 21  $\mu\text{M}$  (30, 31). Together, these pharmacokinetic studies suggest that AZ could rapidly accumulate in fetal tissue, including the placenta *in vivo*, at concentrations comparable to those that inhibit ZIKV proliferation in culture. Nonetheless, it remains unknown whether these *in vitro* results would be recapitulated in humans.

We further compared AZ with two promising drug candidates that might be safe in pregnancy and have reported anti-ZIKV activity in cell culture: daptomycin and sofosbuvir. Our dose–response curves are in agreement with the documented activity of sofosbuvir in human neuroepithelial stem cells (7), and extend the activity of daptomycin previously seen in HuH-7 and HeLa cells (10) to glial cells. We noted that daptomycin would not have been highly ranked in our initial screen due to the limited maximum effect of the drug as observed in dose–response curves. Unlike sofosbuvir, which likely targets the ZIKV RNA-dependent RNA polymerase (NS5) based on its mechanism against hepatitis C virus, daptomycin and AZ have unknown mechanisms of action against ZIKV. Nonetheless, the difference in *in vitro* dose–response between AZ and daptomycin is intriguing, and suggests different mechanisms of inhibition. Another important factor for a drug candidate for ZIKV treatment is accessibility. Access to sofosbuvir and its derivatives may be limited by its current price whereas AZ and daptomycin are available as generic forms, although daptomycin is not available in oral formulation due to poor oral bioavailability. Our comparison adds new data to consider alongside other antiviral activity data, safety, cost, and accessibility in moving forward with further exploration of these and related compounds. In parallel with direct comparisons *in vitro*, follow-up studies in animal models can be useful for prioritizing candidates. However, as with *in vitro* studies, there are caveats in interpreting animal models, such as substantial differences between human and mouse immune systems, placental structure, and fetal brain development.

Together, our work identifies cell type-specific patterns of ZIKV infection in second-trimester human developing brain, provides experimental evidence that AXL is important for ZIKV infection of relevant human brain cell types, and highlights a common antibiotic with inhibitory activity against ZIKV in glial cells. Ongoing studies will be required to determine whether AZ, daptomycin, sofosbuvir, and other inhibitors or combinations are capable of reducing ZIKV infection in the critical cell types identified here in vivo. Although preventative measures such as mosquito abatement and a ZIKV vaccine are imperative for long-term control of this pathogen, the study of ZIKV infection of primary human tissues and identification of inhibitors with therapeutic potential remain important components of a global response to this emerging threat.

### ***Materials and Methods***

Detailed Materials and Methods are available in SI Materials and Methods.

#### *Cells and Viruses*

Cell lines were Vero cells, U87 cells, and human astrocytes derived from human pluripotent stem cells (13). ZIKV strains were SPH2015 (Brazil 2015; ZIKV-BR), PRVABC59 (Puerto Rico 2015; ZIKV-PR), and FSS13025 (Cambodia 2010; ZIKV-CAM).

#### *Brain Samples*

Deidentified primary tissue samples were collected with previous patient consent in strict observance of the legal and institutional ethical regulations. Protocols were approved by the Human Gamete, Embryo and Stem Cell Research Committee (institutional review board) at the University of California, San Francisco (UCSF). Slices in organotypic culture were inoculated

with ZIKV or mock-infected, fixed at 72 hpi or 5 d postinfection, and processed for immunohistochemistry. Quantification was performed on 13- to 22-pcw slices.

### *AXL*

For 1 h before infection, cells were treated with AXL-blocking antibody or goat IgG control at 100  $\mu\text{g}/\text{mL}$ , or with 1 to 3  $\mu\text{M}$  R428 or vehicle ( $<0.1\%$  DMSO). For AXL knockdown, U87 cells stably expressing dCas9-KRAB (15) were transduced with lentiviral particles expressing a pool of gRNAs targeting AXL or a gRNA targeting GFP as a control.

### *Drug Screen*

A collection of 2,177 FDA-approved compounds, provided by the UCSF Small Molecule Discovery Center, was tested at 2  $\mu\text{M}$  in Vero cells infected with ZIKV-BR (MOIs of 1, 3, and 10) and in U87 cells (MOI of 3). Toxicity screens in uninfected cells were performed in parallel. Cells were pretreated for 2 h before addition of ZIKV-BR or media, and cell viability was assessed at 72 hpi using the CellTiter-Glo 2.0 assay (Promega). Candidates with cell viability  $>2.5$ -fold that of untreated cells in every Vero cell screen were identified for follow-up.

### *Drug Validation*

U87 cells or hPSC-derived astrocytes were treated with azithromycin, daptomycin, sofosbuvir, or vehicle for  $>1$  h, and then infected with ZIKV-PR. Cell-viability assays were performed using CellTiter-Glo as above. To assess viral envelope production, cells were fixed and

stained at 48 hpi using anti-flavivirus envelope protein, and then quantified by plate imaging with automated cell counting or by flow cytometry.

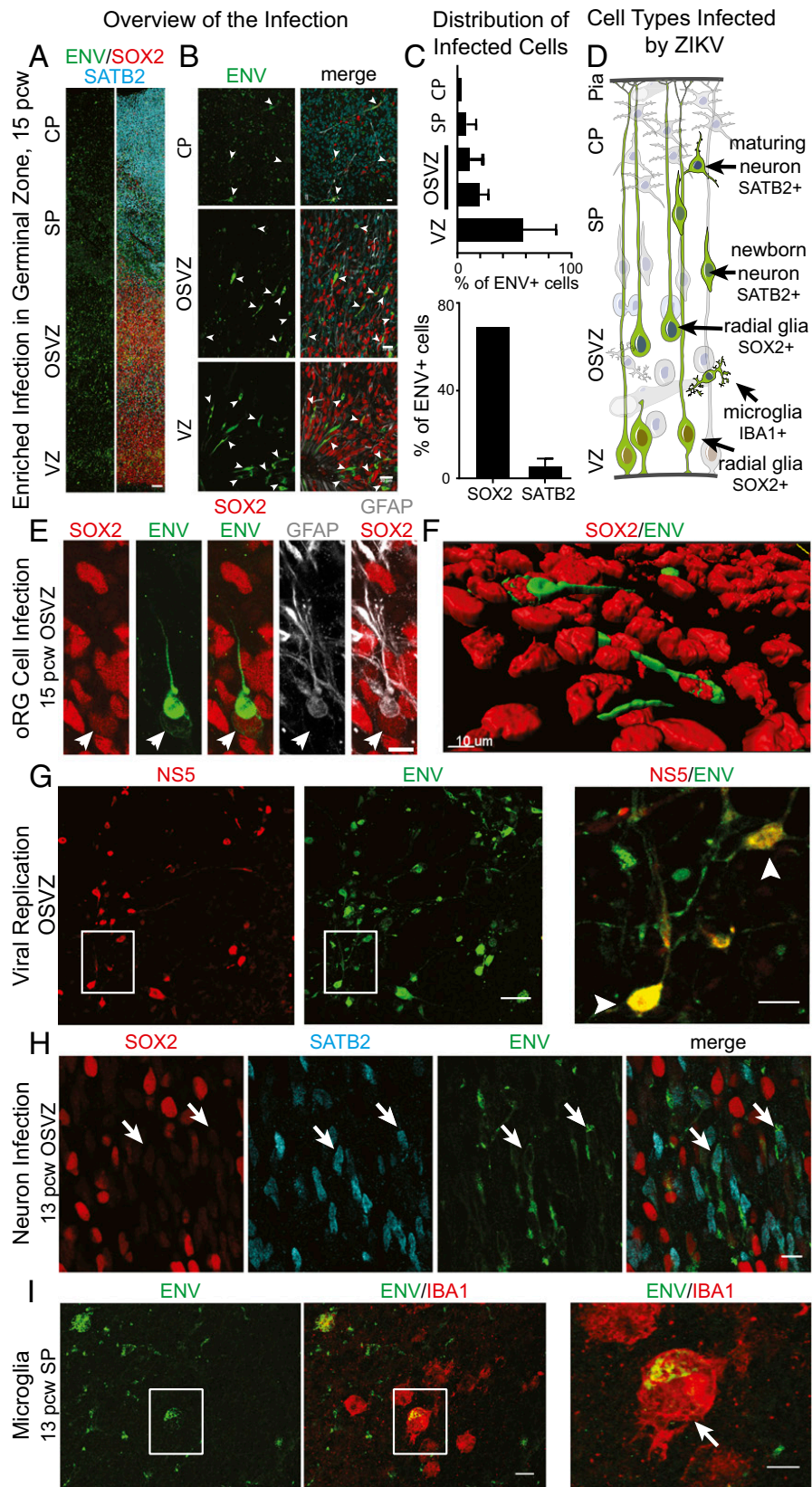


## Figure 2.1 Tropism of ZIKV for radial glia in the developing human brain.

Human cortical organotypic brain slices were infected with ZIKV-BR and cultured for 72 h. (A to B) Low magnification overview of ZIKV infection detected by ENV (green) within the cortex. (A) ENV staining was analyzed with respect to region and cell type. Scale bar 100  $\mu\text{m}$ . (B) High magnification of (A). Notably, ENV staining (arrowheads) appears to be preferentially enriched in the ventricular zone (VZ) and outer subventricular zone (OSVZ). SP – subplate, CP – cortical plate, pcw – post-conception weeks. Scale bar 20  $\mu\text{m}$ . (C) Quantification of ENV positive cells by region (top) and cell type (bottom) at 13-14 pcw.  $n = 2$ . mean  $\pm$  SD (see Methods, error bar not shown where shorter than line thickness (top panel, CP, and bottom panel, SOX2)). (D) Schematic summary of cell types observed to be susceptible to ZIKV infection (green) in the developing human brain during mid- neurogenesis. (E) High magnification overview of a ZIKV-infected radial glial cell in the OSVZ. Scale bar 10  $\mu\text{m}$ . (F) Three dimensional reconstruction of (E), highlighting intracellular presence of ENV signal. Scale bar 10  $\mu\text{m}$ . (G) ENV and NS5 signal in OSVZ cells (arrowheads) suggested replicating ZIKV-PR. Scale bar 20  $\mu\text{m}$ . (H) Immature neurons (SATB2+, blue) infected with ZIKV (arrows). Scale bar 20  $\mu\text{m}$ . (I) Microglia (IBA1+) immunopositive for ENV. High magnification panel (right) shows ENV+ microglia with amoeboid morphology (arrow), typical of activated microglia. Scale bar 10  $\mu\text{m}$ .

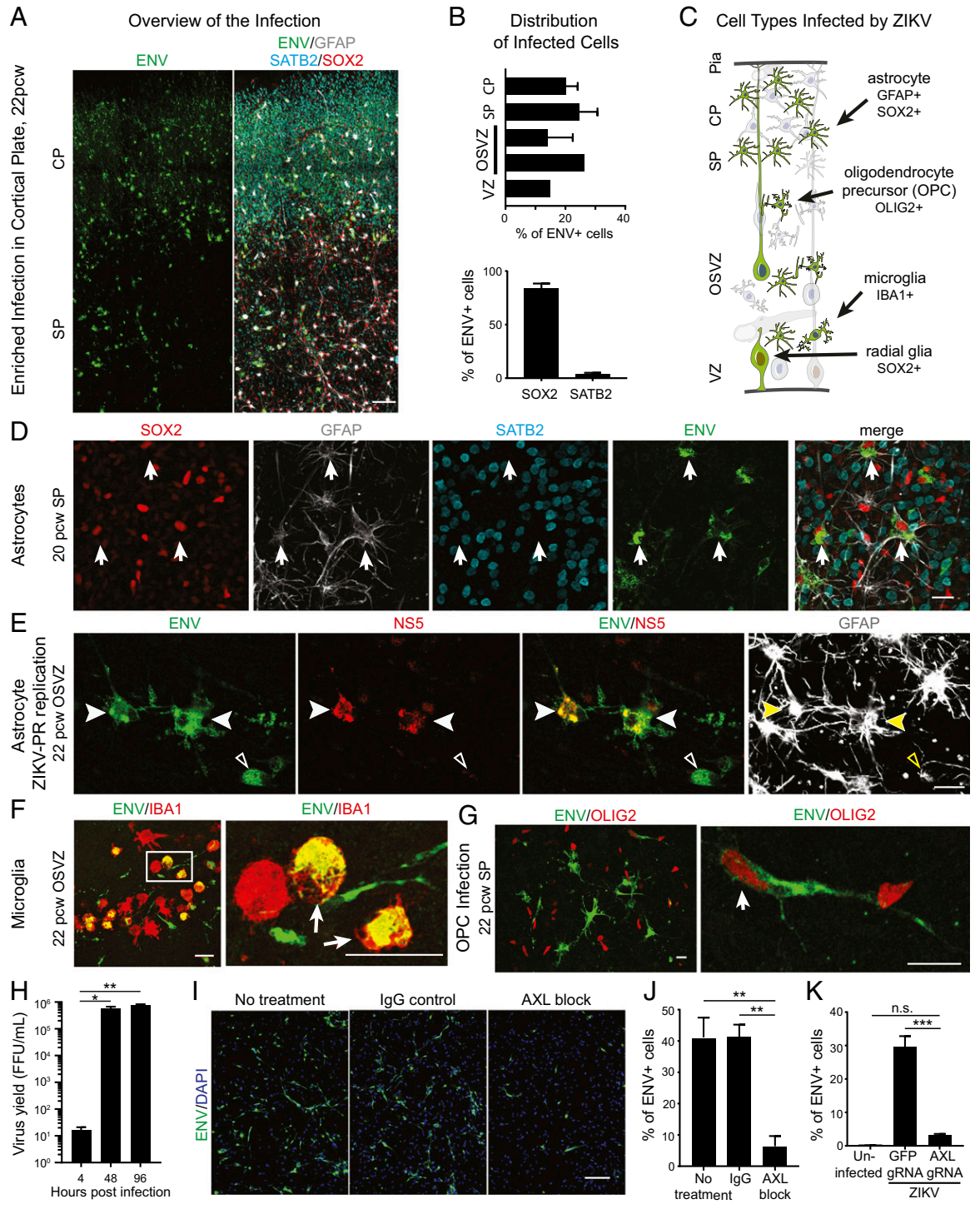




## Figure 2.2. ZIKV infects astrocytes in later stages of human brain development.

(A) Low-magnification overview of ZIKV infection detected by ENV (green) within human organotypic cortical slices during late neurogenesis/gliogenesis. (Scale bar, 100  $\mu\text{m}$ .) (B) Quantification of ENV<sup>+</sup> cells by region (Top) and cell type (Bottom) at 20 to 22 pcw.  $n = 2$ ; mean  $\pm$  SD [SI Materials and Methods; an error bar is not shown where shorter than the line thickness (Top, VZ and second OSVZ)]. (C) Schematic summary of cell types observed to be susceptible to ZIKV infection (green). (D and E) Immunohistochemical analysis reveals ZIKV infection in astrocytes by positivity for ENV (arrows, D; arrowheads, E) or ENV and nonstructural protein NS5, indicating active viral replication (filled arrowheads, E). (Scale bars, 20  $\mu\text{m}$ .) (F) Microglia colabeled with ENV (arrows). (Scale bars, 50  $\mu\text{m}$ .) (G) ZIKV infection of oligodendrocyte precursor cells (OPCs, arrow). (Scale bars, 20  $\mu\text{m}$ .) (H) Viral production in 19-pcw cortical slices, quantified by focus-forming assay from combined homogenized tissue and conditioned media at 4, 48, and 96 h postinfection. FFU, focus-forming units. Two independent biological replicates with two technical replicates for each time point; mean  $\pm$  SEM; one-way ANOVA with Tukey's multiple comparisons test, \* $P \leq 0.05$ , \*\* $P \leq 0.01$ ; see also Fig. S4F. (I and J) Analysis of ZIKV-BR infection in the presence of AXL-blocking antibody in hPSC-derived astrocytes (SI Materials and Methods). Note the reduced ENV staining with AXL block compared with IgG control. (Scale bar, 100  $\mu\text{m}$ .) (J) Quantification of the experiment represented in I; see also Fig. S5A;  $n = 3$ ; mean  $\pm$  SEM; one-way ANOVA with Tukey's multiple comparisons test, \*\* $P \leq 0.01$ . (K) ZIKV-PR infection after knockdown of AXL using U87-dCas9 lines expressing either GFP guide (g) RNA (nontargeting control) or AXL gRNAs (dCas9-mediated knockdown); see also Fig. S5B; two biological replicates in cell lines generated with independent transductions; mean  $\pm$  SEM; two-way ANOVA with Tukey's multiple comparisons test, n.s. (not significant), \*\*\* $P \leq 0.001$ .

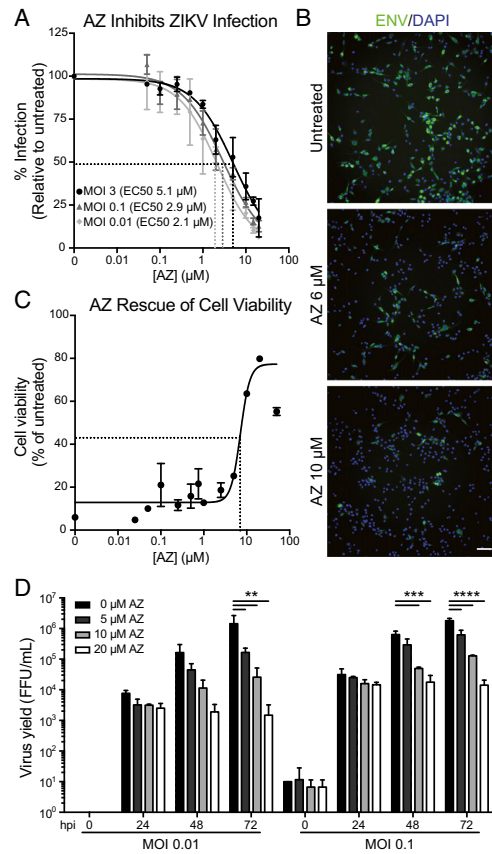


**Figure 2.3. Azithromycin treatment inhibits ZIKV infection in glial cells.**

(A) U87 cells were treated with increasing concentrations of AZ and infected with ZIKV-PR at varying MOIs (0.01, 0.1, and 3, as indicated). The percentage of infected cells at 48 hpi was determined by flow cytometry of cells immunostained for ENV and normalized to untreated cells (for raw data, see Fig. S6A).  $EC_{50}$  values for AZ-mediated reduction of ZIKV infection were 5.1  $\mu$ M for an MOI of 3 ( $n = 2$ ), 2.9  $\mu$ M for an MOI of 0.1 ( $n=2$ ), and 2.1  $\mu$ M for an MOI of 0.01 ( $n=2$ ); mean  $\pm$  SD. (B) Representative images of U87 cells treated with AZ and infected with ZIKV-PR at an MOI of 3 (as in A). At 48 hpi, cells were immunostained for ENV protein (green) and cellular DNA (DAPI, blue). (Scale bar, 100  $\mu$ m.) (C) Rescue of cell viability with AZ. U87 cells were pretreated with AZ for 1 h and then infected with ZIKV-PR at an MOI of 10 in the presence of AZ. Cell viability was measured at 72 hpi using the CellTiter-Glo luminescence assay. The  $EC_{50}$  value for the AZ-mediated rescue of cell viability was 7.1  $\mu$ M. The data point at the highest concentration of AZ (50  $\mu$ M) showed reduced cell viability, likely due to drug toxicity (Fig. S6C).  $n = 2$ ; mean  $\pm$  SD. (D) Decrease of virus production with AZ treatment. U87 cells were pretreated with AZ for 1 h and then infected with ZIKV-PR at an MOI of 0.1 or 0.01 in the presence of AZ. Quantification of virus yield in conditioned media was performed by focus-forming assay at 0, 24, 48, and 72 hpi;  $n = 2$  for each MOI; mean  $\pm$  SD; two-way ANOVA with Tukey's multiple comparisons testing,  $**P \leq 0.01$ ,  $***P \leq 0.001$ ,  $****P \leq 0.0001$ .

## Chapter 2 References

1. Brasil P, et al. (March 4, 2016) Zika virus infection in pregnant women in Rio de Janeiro—Preliminary report. *N Engl J Med*, 10.1056/NEJMoa1602412.
2. Mlakar J, et al. (2016) Zika virus associated with microcephaly. *N Engl J Med* 374(10):951–958.
3. Li C, et al. (2016) Zika virus disrupts neural progenitor development and leads to microcephaly in mice. *Cell Stem Cell* 19(1):120–126.
4. Tang H, et al. (2016) Zika virus infects human cortical neural progenitors and attenuates their growth. *Cell Stem Cell* 18(5):587–590.
5. Qian X, et al. (2016) Brain-region-specific organoids using mini-bioreactors for modeling ZIKV exposure. *Cell* 165(5):1238–1254.
6. Hamel R, et al. (2015) Biology of Zika virus infection in human skin cells. *J Virol* 89(17):8880–8896.
7. Onorati M, et al. (2016) Zika virus disrupts phospho-TBK1 localization and mitosis in human neuroepithelial stem cells and radial glia. *Cell Reports* 16(10):2576–2592.
8. Liu S, DeLalio LJ, Isakson BE, Wang TT (September 20, 2016) AXL-mediated productive infection of human endothelial cells by Zika virus. *Circ Res*, 10.1161/CIRCRESAHA.116.309866.
9. Nowakowski TJ, et al. (2016) Expression analysis highlights AXL as a candidate Zika virus entry receptor in neural stem cells. *Cell Stem Cell* 18(5):591–596.
10. Barrows NJ, et al. (2016) A screen of FDA-approved drugs for inhibitors of Zika virus infection. *Cell Host Microbe* 20(2):259–270.

11. Xu M, et al. (2016) Identification of small-molecule inhibitors of Zika virus infection and induced neural cell death via a drug repurposing screen. *Nat Med* 22(10):1101–1107.
12. Sacramento CQ, et al. (2016) The clinically approved antiviral drug sofosbuvir impairs Brazilian Zika virus replication. *bioRxiv*. Available at [biorxiv.org/content/early/2016/07/06/061671](https://www.biorxiv.org/content/early/2016/07/06/061671).
13. Krencik R, et al. (2015) Dysregulation of astrocyte extracellular signaling in Costello syndrome. *Sci Transl Med* 7(286):286ra66.
14. Krencik R, Weick JP, Liu Y, Zhang Z-J, Zhang S-C (2011) Specification of transplantable astroglial subtypes from human pluripotent stem cells. *Nat Biotechnol* 29(6):528–534.
15. Liu SJ, et al. (2016) Single-cell analysis of long non-coding RNAs in the developing human neocortex. *Genome Biol* 17:67.
16. Rothlin CV, Ghosh S, Zuniga EI, Oldstone MBA, Lemke G (2007) TAM receptors are pleiotropic inhibitors of the innate immune response. *Cell* 131(6):1124–1136.
17. Holland SJ, et al. (2010) R428, a selective small molecule inhibitor of Axl kinase, blocks tumor spread and prolongs survival in models of metastatic breast cancer. *Cancer Res* 70(4):1544–1554.
18. Lin KJ, Mitchell AA, Yau W-P, Louik C, Hernández-Díaz S (2013) Safety of macrolides during pregnancy. *Am J Obstet Gynecol* 208(3):221.e1–221.e8.
19. Hanners NW, et al. (2016) Western Zika virus in human fetal neural progenitors persists long term with partial cytopathic and limited immunogenic effects. *Cell Reports* 15(11):2315–2322.
20. Brault JB, et al. (2016) Comparative analysis between flaviviruses reveals specific neural stem cell tropism for Zika virus in the mouse developing neocortex. *EBioMedicine* 10:71–76.

21. Cugola FR, et al. (2016) The Brazilian Zika virus strain causes birth defects in experimental models. *Nature* 534(7606):267–271.
22. Thornton GK, Woods CG (2009) Primary microcephaly: Do all roads lead to Rome? *Trends Genet* 25(11):501–510.
23. Hazin AN, et al.; Microcephaly Epidemic Research Group (2016) Computed tomographic findings in microcephaly associated with Zika virus. *N Engl J Med* 374(22): 2193–2195.
24. Miner JJ, et al. (2016) Zika virus infection in mice causes panuveitis with shedding of virus in tears. *Cell Reports* 16(12):3208–3218.
25. Workowski KA, Bolan GA; Centers for Disease Control and Prevention (2015) Sexually transmitted diseases treatment guidelines, 2015. *MMWR Recomm Rep* 64(RR-03):1–137.
26. DHHS Panel on Opportunistic Infections in HIV-Infected Adults and Adolescents (2016) Guidelines for the Prevention and Treatment of Opportunistic Infections in HIV-Infected Adults and Adolescents: Recommendations from the Centers for Disease Control and Prevention, the National Institutes of Health, and the HIV Medicine Association of the Infectious Diseases Society of America. Available at [https://aidsinfo.nih.gov/contentfiles/lvguidelines/adult\\_oi.pdf](https://aidsinfo.nih.gov/contentfiles/lvguidelines/adult_oi.pdf). Accessed October 7, 2016.
27. Sarkar M, Woodland C, Koren G, Einarson ARN (2006) Pregnancy outcome following gestational exposure to azithromycin. *BMC Pregnancy Childbirth* 6:18.
28. Ramsey PS, Vaules MB, Vasdev GM, Andrews WW, Ramin KD (2003) Maternal and transplacental pharmacokinetics of azithromycin. *Am J Obstet Gynecol* 188(3):714–718.
29. Sutton AL, et al. (2015) Perinatal pharmacokinetics of azithromycin for cesarean prophylaxis. *Am J Obstet Gynecol* 212(6):812.e1–812.e6.

30. Jaruratanasirikul S, Hortiwakul R, Tantisarasart T, Phuenpathom N, Tussanasunthornwong S (1996) Distribution of azithromycin into brain tissue, cerebrospinal fluid, and aqueous humor of the eye. *Antimicrob Agents Chemother* 40(3):825–826.
31. Kemp MW, et al. (2014) Maternal intravenous administration of azithromycin results in significant fetal uptake in a sheep model of second trimester pregnancy. *Antimicrob Agents Chemother* 58(11):6581–6591.
32. Stenglein MD, et al. (2014) Ball python nidovirus: A candidate etiologic agent for severe respiratory disease in *Python regius*. *MBio* 5(5):e01484–e14.

### **Chapter 3:**

#### **Preliminary investigation of the antiviral mechanism of azithromycin**

The work presented in this chapter includes contributions from: Dr. Hanna Retallack, Dr. Kristeene Knopp, Dr. Carolina Arias, and Dr. Joseph DeRisi

## ***Abstract***

Zika virus (ZIKV), a mosquito-borne flavivirus, was responsible for a rapid outbreak in South America and elsewhere in 2015 and 2016 and remains in circulation at low levels. Gestational exposure to ZIKV is the likely cause of many thousands of birth defects, including thousands of cases of severe microcephaly. Efforts to develop therapeutics for ZIKV and related viruses have identified several promising candidates, including the macrolide antibiotic azithromycin. Because azithromycin is FDA-approved, is in widespread use, is generally well-tolerated, and is one of relatively few drugs that are safe for use in pregnancy, its potential activity against ZIKV warrants further investigation. Here, we present preliminary findings related to the mechanism of ZIKV inhibition by azithromycin. We show that inhibition of ZIKV by azithromycin occurs early in the viral lifecycle. We also demonstrate that mutations in the ZIKV envelope glycoprotein, which has several roles in the viral lifecycle including facilitating entry into host cells, confer resistance to azithromycin inhibition. Furthermore, through CRISPR genetic screening, we identify gene-drug interactions that augment or mitigate the anti-ZIKV effect of azithromycin. We observe that several genes that affect azithromycin efficacy are involved in lipid biosynthesis or vesicular trafficking. Although we do not establish a definitive antiviral mechanism for azithromycin, the circumstantial evidence we present here suggests a role in inhibition of viral entry into host cells.

## ***Introduction***

Zika virus (ZIKV) is a single-strand positive-sense RNA virus in the flavivirus family transmitted primarily by the *Aedes aegypti* mosquito [1]. A large outbreak of ZIKV infections in 2015 and 2016 spread across over 30 countries and caused millions of infections [2]. While most



ZIKV cases are asymptomatic or cause mild symptoms, exposure of pregnant women to ZIKV has been associated with cases of abnormal infant brain development ranging from mild to severe birth defects [3]. The most severe of these effects is microcephaly, which is defined as a head circumference at least two standard deviations below average in infants. Microcephaly associated with congenital ZIKV infection has been reported in at least 5000 cases and remains a cause for concern as ZIKV remains in circulation despite a large drop in incidence [4].

With no known treatment for ZIKV infection, previous studies have attempted to identify novel therapeutic candidates that may help prevent the consequences of congenital ZIKV infection. Previously, we reported on the identification and validation of the macrolide antibiotic azithromycin as an inhibitor of ZIKV infection *in vitro* [5]. Azithromycin is an ideal candidate for repurposing as a potential therapeutic for ZIKV as it has a long history of safe use in humans and is one of relatively few drugs that is safe for use in pregnancy [6]. Azithromycin has in fact been used in clinical trials for treatment of Covid-19, despite the lack of clear evidence for an *in vitro* effect against the causative virus Severe Acute Respiratory Syndrome Coronavirus 2 [7]. To facilitate the development of azithromycin as a potential therapeutic for ZIKV and other viruses, it will be critical to understand the antiviral mechanism of action.

The putative mechanism of action of azithromycin against bacteria is direct binding to the 50S subunit of the bacterial ribosome, which would not be expected to be relevant to viral inhibition [8]. The antiviral mechanism of azithromycin has been investigated in several studies (reviewed in [7]), but perhaps due to the pleiotropic effects of azithromycin in human cells, no definitive mechanism has been established. Li *et al.* report evidence that azithromycin inhibits ZIKV infection by upregulating type I and type III interferon responses [9]. A separate report presents evidence that azithromycin, as well as several other drugs of related classes, may exert an

antiviral effect through a shared mechanism of induction of phospholipidosis in host cells [10]. Azithromycin and other drugs with similar properties are found to accumulate within mammalian cell endosomes and lysosomes and may affect vesicular pH as well as disrupt lipid homeostasis, potentially affecting vesicle composition [10–12]. Induction of phospholipidosis may therefore be a non-specific antiviral mechanism that disrupts the host cell entry process for viruses such as ZIKV that require the presence of specific factors in endosomes and lysosomes such as pH. Mechanisms proposed by previous studies are not mutually exclusive with other potential antiviral effects of azithromycin, and there remains a clear need to fully understand the breadth of drug effects on host cells and viral pathways.

In this study, we investigate azithromycin's mechanism using two primary approaches which differ from previous studies: 1) selection of ZIKV for mutations that confer resistance to azithromycin to identify viral genes related to the effect and 2) CRISPR-interference (CRISPRi) gene knockdown screening to identify host genes that modulate the antiviral effect of azithromycin. Selection for azithromycin resistance in ZIKV produced mutations in the viral envelope protein adjacent to the fusion loop peptide, which is responsible for insertion into host cell endosomal membranes to initiate the deposition of the viral genome into the host cytoplasm [13]. Azithromycin-resistant ZIKV mutants were found to be more susceptible to neutralization by antibodies that bind to cryptic epitopes near the envelope fusion loop, indicating that the conformational dynamics of resistant mutants may differ from wild-type [13,14]. These viral mutants are also significantly less stable at 37°C, again indicating potential changes to the outer coat of the virion [15].

The CRISPRi genetic screen for host factors affecting ZIKV susceptibility to azithromycin revealed several genes that reduce ZIKV-mediated cell death when knocked down, including

several that do so only in the presence of azithromycin. Many genes that appear to potentially enhance the antiviral effect of azithromycin have likely roles in pathways related to lipid metabolism or vesicular trafficking, indicating that those pathways may be related to the azithromycin mechanism. Finally, we show that azithromycin exhibits synergistic activity with two potential entry inhibitors: orlistat, a lipase and lipid synthesis inhibitor that interacts with multiple genes found in our genetic screen, and the anti-flavivirus envelope protein monoclonal antibody 4G2, which binds to and blocks parts of the envelope protein to prevent viral entry.

## ***Results***

We first assessed the antiviral activity of azithromycin against three different flaviviruses: ZIKV, Dengue Virus (DENV), Yellow Fever Virus (YFV), as well as the alphavirus Chikungunya virus (CHIKV). Azithromycin inhibition was strongest in ZIKV with a half-maximal effective concentration ( $EC_{50}$ ) of  $4.7\mu\text{M}$  (Fig. 3.1A). Lower potency was observed against other viruses with  $EC_{50}$  values of  $15.9\mu\text{M}$ ,  $21.7\mu\text{M}$ , and  $29.4\mu\text{M}$  for YFV, CHIKV, and DENV, respectively. A time course experiment to examine when inhibition of ZIKV replication and protein translation occurs was performed by staining for the presence of ZIKV envelope protein (Env) at 8, 12, 16, and 24 hours post infection (hpi) in the presence and absence of azithromycin treatment. The inhibitory effect of azithromycin is apparent as early as 12hpi, the earliest timepoint at which viral protein production is observed (Fig. 3.1B).

Selection for resistance to azithromycin was carried out with ZIKV in two parallel lineages by serial passaging of virus in the presence of highly inhibitory concentrations of azithromycin (roughly  $EC_{80}$  and  $EC_{90}$ ). Sequencing of resistant strains revealed one mutation in the viral membrane protein in one lineage and four mutations in the viral envelope protein, including M68I and H401Y, which were found in both azithromycin-selected lineages, but not in virus passaged

in the absence of azithromycin (Fig. 3.2A). The azithromycin-resistant strains had moderate shifts in  $EC_{50}$  compared to wild-type, with 4.3-fold and 7.2-fold increases in  $EC_{50}$  for strains selected in 10 $\mu$ M and 20 $\mu$ M azithromycin, respectively (Fig. 3.2B). Because mutations in the viral envelope glycoprotein may affect the conformational dynamics of the outer virion coat, we performed assays to assess neutralization by monoclonal antibodies E53 and E60, which bind to cryptic epitopes in envelope and measured the intrinsic decay rate of infectivity at 37°C. While wild-type ZIKV is not neutralized effectively by E53 or E60, azithromycin-resistant ZIKV is neutralized partially at 0.4 $\mu$ g/mL and significantly at 40 $\mu$ g/mL (Fig. 3.2C). Infectivity of azithromycin-resistant ZIKV was also considerably less stable at 37°C with a half-life 5.3-fold lower than wild-type ZIKV (Fig. 3.2D).

A CRISPRi genetic knockdown screen to identify interactions between host cell genes and the anti-ZIKV effect of azithromycin was performed in K562-dCas9-KRAB cells using the H1 sub-library of sgRNAs targeting kinase, phosphatase, and known drug-target genes. The genetic screen used selection for resistance to the cytopathic effect of ZIKV and was performed in the presence and absence of azithromycin to differentiate gene knockdowns that promote resistance to ZIKV infection in general versus gene knockdowns that enhance the survival effect of azithromycin. Rho, a measurement of resistance phenotype of genetic perturbations, was calculated for each gene and compared between screening conditions with and without azithromycin (Fig. 3.3A). Genes with high rho resistance phenotype in the presence of azithromycin but low or average rho in the absence of azithromycin are potential candidates for gene-drug interactions. Several genes with potential functions in lipid synthesis or vesicular trafficking pathways were among the genes with greater effect in the azithromycin treatment condition. Follow-up validation of hit genes was performed by generating individual K562-dCas9-

KRAB cell lines expressing individual sgRNAs targeting hit genes. Validation of gene-drug interactions showed the strongest augmentation of azithromycin effect with PTPN1, CES1, and SPTLC2, which are involved in antiviral innate immune response, fatty acyl/cholesterol ester metabolism, and sphingolipid biosynthesis, respectively [16].

Orlistat, a lipase and fatty acid synthase inhibitor that has previously characterized interactions with pathways implicated in our genetic screen, was tested in combination with azithromycin for inhibitory effect against ZIKV [17]. A potentially synergistic interaction between orlistat and azithromycin was observed, as similar inhibition levels could be achieved with lower concentrations of a combination of the drugs compared to each drug individually (Fig. 3.4A). Similarly, azithromycin exhibited a potentially synergistic relationship with the anti-flavivirus envelope monoclonal antibody 4G2. Increasing concentrations of 4G2 neutralized ZIKV and inhibited infection when used individually. The combination of 4G2 neutralization and azithromycin treatment achieved inhibition levels with lower concentrations of each agent compared to treatment with the agents individually (Fig. 3.4B).

## ***Discussion***

Together, our results point to an antiviral mechanism of action of azithromycin related to inhibiting the entry of virions into host cells. First, we observe that the timing of inhibition occurs within the first 12 hours of the viral lifecycle, which suggests that inhibition likely occurs within the timeframe of viral entry or early replication and translation. This does not rule out potential additional effects at later stages of the viral lifecycle including host anti-viral defense, virion assembly, or egress and is not mutually exclusive with other proposed mechanisms [9,10].

Next, we find that mutations that confer resistance to azithromycin are largely clustered in the ZIKV envelope glycoprotein, which is responsible for virion stability, attachment to host cell

adhesion molecules, initiation of fusion between host endosome and viral membranes, and assembly of nascent virions [18]. While the role of the specific residues mutated in azithromycin-resistant strains is not known, the mutations cluster adjacent to the fusion loop peptide of the protein. The H401Y mutation is of particular interest due to its location directly adjacent to the fusion loop in the protein dimer and the potential role of histidine residues as pH sensors for the envelope protein in the acidic environment of the host cell endosome [19]. We also made the interesting observations that mutations conferring azithromycin resistance increase ZIKV neutralization by antibodies that bind to cryptic envelope epitopes and also increase the rate of intrinsic decay. These physical phenotypes are potentially indicative of changes to the conformational dynamics of the mutant envelope proteins, which could conceivably affect the efficiency of host cell entry in different contexts and may underly an ability to subvert the inhibitory mechanism of azithromycin [14,15,20]. The observed mutant envelope phenotypes would likely not be fit in the context of wild transmission, but in the context of azithromycin treatment in cell culture they appear to promote more efficient infection, likely indicating a fitness tradeoff that exists within envelope protein structure and dynamics.

Our genetic interaction screen in the context of azithromycin treatment and ZIKV infection produced a set of potential gene-drug interaction targets. Several of the hit genes which increased resistance to ZIKV-mediated cytotoxicity are potentially involved in vesicular trafficking or lipid biosynthesis, which are pathways that could potentially affect viral entry or viral assembly and egress [21]. The strongest validated gene-drug interactions were in the genes PTPN1, CES1, and SPTLC2. Tyrosine-protein phosphatase nonreceptor type 1 (PTPN1) has been implicated in the innate antiviral immune response, potentially supporting a previously suggest immunomodulatory mechanism of azithromycin [22]. Carboxylesterase 1 (CES1) does not have a known antiviral

mechanism, but is involved in fatty acyl and cholesterol ester metabolism, pathways that are known to play an important role for flavivirus infection. CES1 may also have roles in drug metabolism, so knockdown of CES1 may impact azithromycin intracellular concentrations [23]. Serine Palmitoyltransferase Long Chain Base Subunit 2 (SPTLC) is similarly involved in lipid biosynthesis and is a likely host dependency factor for other viruses, likely suggesting a role in maintenance of endosomal membranes required for viral entry [24].

Finally, the observation of potentially synergistic effects of azithromycin in combination with the lipid biosynthesis inhibitor orlistat and with the neutralizing antibody 4G2 suggest a potential convergence of mechanism. It is expected that neutralizing antibodies primarily inhibit the entry steps of the viral lifecycle and the lipid pathway involvement of orlistat suggests a possible effect on viral entry as well. The mechanistic insight provided by these interactions is limited, but may suggest an avenue for future drug development.

The collection of observations presented here provides only circumstantial and preliminary evidence in support of an antiviral mechanism of action of azithromycin related to entry and endosomal escape. There is ambiguity within each result presented here, making it critical to consider alternative interpretations. The results of our study do not directly contradict previous studies that have suggested different mechanisms and in fact is likely consistent with a non-specific host cell effect such as induction of phospholipidosis [10]. Future work may seek to provide more direct evidence of the cellular compartments of azithromycin's action and the specific viral factors with which azithromycin interacts. Additional studies should attempt to reconcile the multiple potential mechanisms for which evidence exists and focus on factors related to the potential use of azithromycin as an antiviral therapeutic.

## **Methods**

### *Cells lines*

U87 (gift of Dr. Jonathan Weissman, University of California, San Francisco), H4 (ATCC HTB-148), Vero (ATCC CCL-81) were cultured in Dulbecco's modified Eagle's medium (Gibco) containing 10% (vol/vol) fetal bovine serum (FBS) (Gibco), 2 mM l-glutamine, 100 U/ml penicillin/streptomycin (Gibco), and 10 mM HEPES buffer. K562-dCas9-KRAB cells (gift of Dr. James Nunez, University of California, San Francisco), were cultured in RPMI 1640 (Gibco) containing 10% (vol/vol) fetal bovine serum (FBS) (Gibco), 2 mM l-glutamine, 100 U/mL penicillin/streptomycin (Gibco), and 10 mM HEPES buffer. For infection experiments, cells were seeded at specific densities using the Accuri C6 cytometer (BD) for cell counting. All cells were cultured at 37°C and 5% CO<sub>2</sub>. Cells were seeded into culture dishes 1 day prior to infection. For all infection experiments, extra wells were seeded to be resuspended and counted on the day of infection for MOI calculations. All cell lines were verified to be free of mycoplasma contamination by MycoAlert (Lonza).

### *Virus propagation, selection, and titering*

ZIKV strain PRVAB59 (Puerto Rico 2015; ZIKV-PR) was propagated in Vero cells infected at an MOI of 0.01. Virus in the supernatant was harvested at 72 hpi, cell debris was removed by centrifugation, viral supernatant was filtered through a 0.22µm PES syringe filter (Millipore), and aliquots were frozen at -80°C to avoid freeze-thaw cycles.

Selection for azithromycin was carried out in H4 glial cells. Parallel cultures for untreated, 10 µM, and 20 µM azithromycin selection conditions were cultured simultaneously. For the initial round of selection, large cultures of 1x10<sup>8</sup> cells were infected with ZIKV-PR at an MOI of 0.5.



Each passage was cultured for 72-96h depending on the rate of cytopathic effect in the cells. For subsequent passages, supernatant from the previous passage was transferred at a 1/50 dilution for treated cultures and a 1/500 dilution for untreated. Selections were stopped when significant cytopathic effect was observed within 48h following transfer of supernatant in treated cultures (25 passages, roughly 100 generations). All strains were sequenced using a previously published protocol [25]. All viral stocks were verified to be free of mycoplasma contamination by MycoAlert (Lonza).

Viral stocks were titered by focus assay in Vero cells. Briefly, viral stocks were serially diluted in triplicate, added to Vero cells and allowed to infect for 24h before cells were fixed with 3.7% paraformaldehyde (PFA) for 15 minutes at room temperature. Fixed cells were stained with a mouse monoclonal antibody against flavivirus envelope protein (clone D1-4G2-4-15).

#### *Drug and antibody inhibition experiments*

U87 cells were seeded into 12-well tissue culture treated plates (Corning 3513) 1 day prior to treatment and infection. Cells were treated with azithromycin (Selleck) or vehicle only (water) at various concentrations to create a concentration series. ZIKV-PR was added directly to cells 2 hours after drug treatment and allowed to infect cells for 24 hours (or specified times for time course experiments). Following infection, cells were resuspended using trypsin (Gibco), pelleted to remove supernatant, fixed in 3.7% PFA for 15 minutes at room temperature, and then stained with mouse anti-flavivirus envelope primary antibody 4G2 and Alexa 488 goat anti-mouse antibody (Invitrogen). Fluorescent (infected) and non-fluorescent (uninfected) cells were counted using the LSRII flow cytometer (BD). Dose-response curves were generated in GraphPad Prism 7 using four parameter logistic regression and  $EC_{50}$  was calculated these curves.

For antibody neutralization experiments, anti-flavivirus envelope antibodies E53 and E60 (Dr. Leslie Goo, Chan Zuckerberg Biohub) and 4G2 (clone D1-4G2-4-15) were diluted in complete media to specified concentrations and incubated with ZIKV-PR WT or azithromycin-resistant ZIKV at 37°C for 1h. Following incubation, the antibody-virus mixture was added directly to either treated or untreated U87 cells. Infection, staining, and cell counting was performed as described above.

#### *Virus intrinsic decay experiments*

ZIKV-PR or azithromycin-resistant ZIKV was diluted to a concentration of  $1 \times 10^5$  ffu/mL in complete media and aliquoted into separate tubes which were incubated at 37°C. At specified time points, individual aliquots were removed from 37°C and transferred to -80°C storage. After all time points were transferred and allowed to freeze fully, all aliquots were thawed and used to infect Vero cells. Infected cells were cultured for 24h, fixed, stained, and counted by flow cytometry as described above. Decay curves were generated in GraphPad Prism 7 using four parameter logistic regression and infectivity half-life was calculated these curves.

#### *CRISPRi screening and gene validation*

K562 cells stably expressing dCas9-KRAB [26] were transduced with lentiviral particles expressing a pool single-guide (sg)RNAs representing the CRISPRi V2 H1 sub-library (gift of Ryan Pak, Innovative Genomics Institute) at an MOI of 0.3. The CRISPRi H1 sublibrary consists of 5 different sgRNAs targeting each of 2555 human genes as well as 250 non-targeting sgRNAs. Transduced K562-dCas9-KRAB cells were selected with Puromycin (Sigma) at  $1 \mu\text{g/mL}$  for 5 days and allowed to recover from selection for 2 days. Transduced and selected cells were split into 4

parallel cultures for the following conditions: uninfected with no treatment, uninfected with 25 $\mu$ M azithromycin treatment, ZIKV-PR-infected with no treatment, ZIKV-PR-infected with 25 $\mu$ M azithromycin treatment. All cultures were split daily, fresh drug (or vehicle) was added, and aliquots of cells were frozen for subsequent analysis. The experiment was carried out over 8 days, at the end of which all remaining cells were harvested and genomic DNA was extracted using the Machery Nagel NucleoSpin Blood kit. The sgRNA locus was amplified using primers TruSeq5'A:

AATGATACGGCGACCACCGAGATCTACACGATCGGAAGAGCACACGTCTGAACTCC  
AGTCACCTTGTAGCACAAAAGGAAACTCACCCCT                      and                      TruSeq3'A':

CAAGCAGAAGACGGCATAACGAGATCGACTCGGTGCCACTTTTTTC or TruSeq5'B:

AATGATACGGCGACCACCGAGATCTACACGATCGGAAGAGCACACGTCTGAACTCC  
AGTCACGCCAATCGACTCGGTGCCACTTTTTTC                      and                      TruSeq3'B:

CAAGCAGAAGACGGCATAACGAGATGCACAAAAGGAAACTCACCCCT. Libraries were sequenced on the Illumina HiSeq using single-end 50 sequencing. Counts for each sgRNA were extracted and analyzed using a previously published screen analysis pipeline [27]. Gene functions were characterized using the KEGG pathway database [21]. Validation of hit genes was performed by cloning and transducing individual sgRNAs into K562-dCas9-KRAB, selecting with puromycin, verifying gene expression knockdown by qRT-PCR, and performing drug treatments and infections as described above. The top 3 performing sgRNAs for each hit gene were cloned and expressed individually for follow-up.

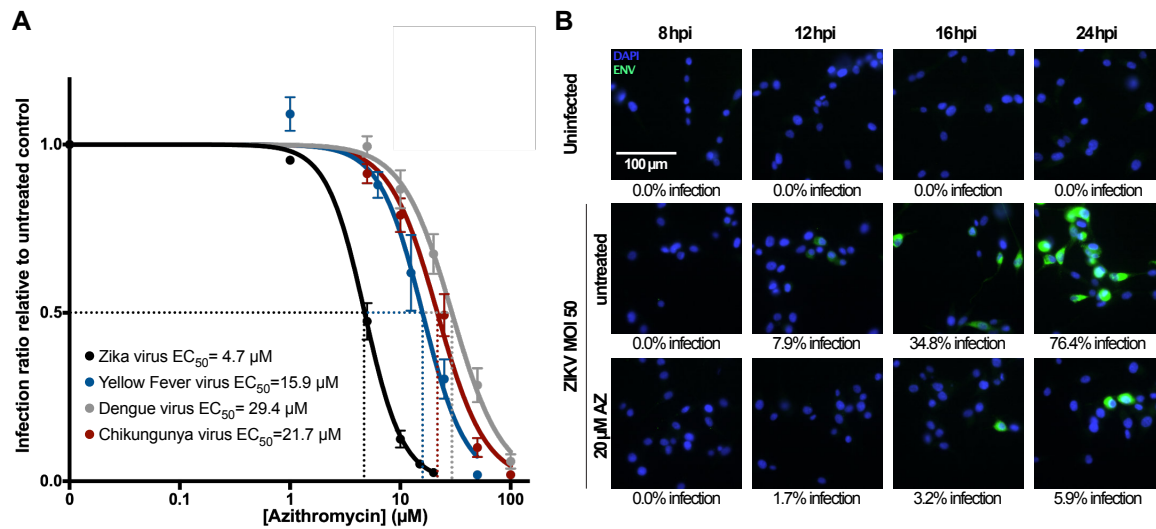


**Figure 3.1. Antiviral activity of azithromycin and timing of inhibition.** (A) Dose-response curves for azithromycin inhibition of Zika virus, Dengue virus, Yellow Fever virus, and Chikungunya virus infection in K562 cells. Cells were pre-treated for 2h prior to virus infection and incubated with virus for 24h. Values are the mean of three biological replicates and error bars show the standard error of the mean. (B) Representative images for time course of ZIKV infection in untreated and azithromycin-treated U87 cells. Cells were infected simultaneously, fixed at the indicated time points, and stained for DAPI (blue) and ZIKV envelope protein (green). The percentage of envelope positive (ZIKV infected) cells at each time point was counted and averaged across three biological replicate wells for each condition.

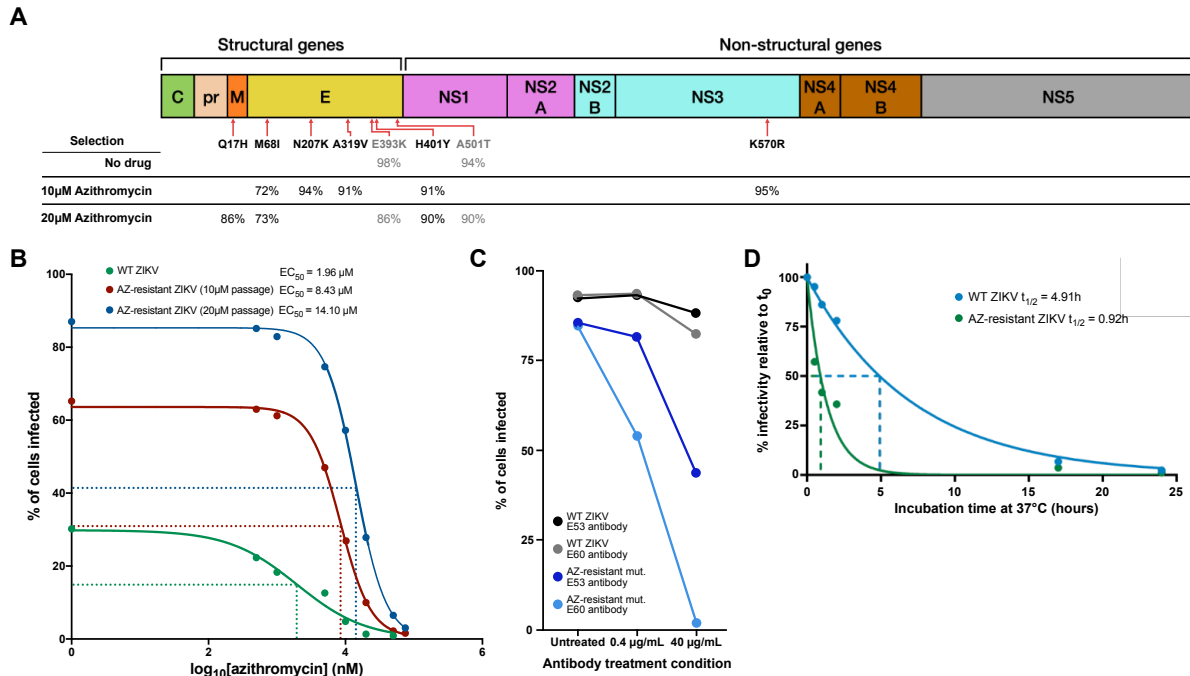
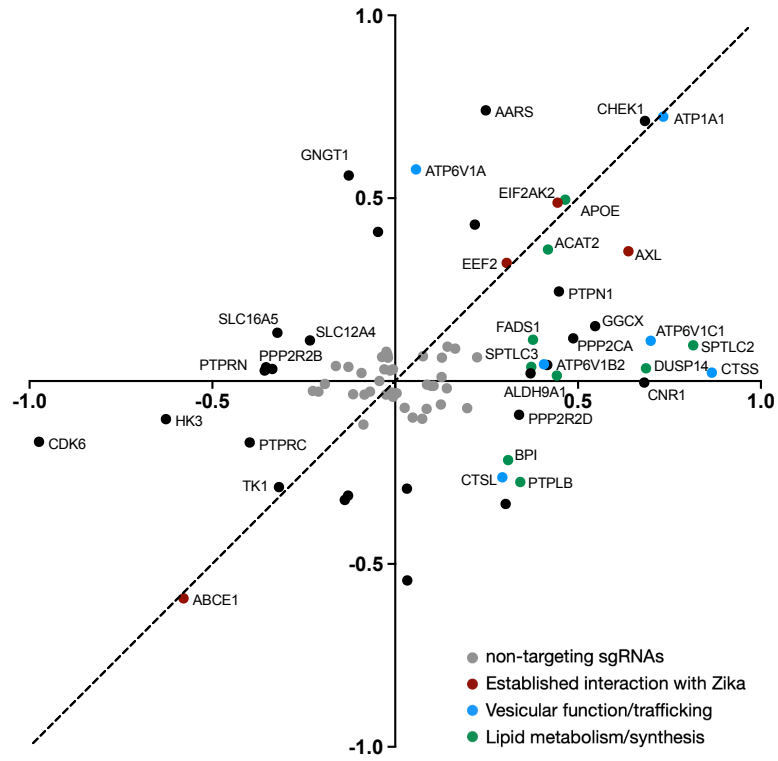


**Figure 3.2 Characterization of azithromycin-resistant ZIKV mutants.** (A) Schematic of ZIKV genome labeled with location and identity of mutations observed in ZIKV strains selected for azithromycin resistance. Strains were serially passaged in the presence of no drug, 10µM azithromycin, or 20µM azithromycin for approximately 100 viral lifecycle generations. The prevalence of each observed mutation at the final passage is reported for each strain, where no number indicates the absence of the mutation in that strain. Envelope (E) mutations that were found in the no drug selection condition are colored in grey. (B) Dose-response curves for azithromycin inhibition of wild-type and azithromycin-resistant ZIKV strains. (C) Infectivity of wild-type and azithromycin-resistant ZIKV in the presence of 0, 0.4, and 40µg/mL of monoclonal antibodies E53 and E60. Lower infectivity indicates greater antibody neutralization of ZIKV. (D) Intrinsic decay rate of wild-type and azithromycin resistant ZIKV at 37°C. The infectivity of ZIKV at each time point is calculated relative to  $t_0$  and the half-life of infectivity is reported.

**A**

Rho gene knockdown resistance phenotype in untreated, ZIKV-infected K562 cells



Rho gene knockdown resistance phenotype in AZ-treated, ZIKV-infected K562 cells

**B**

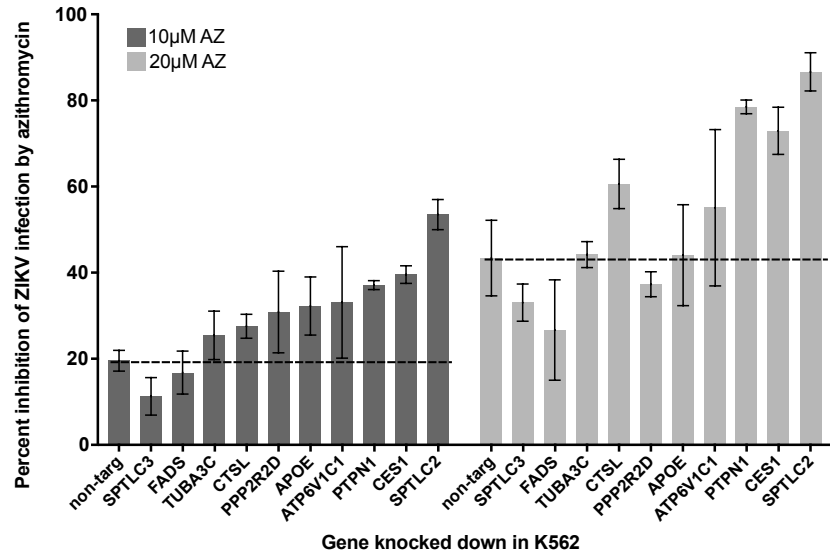


**Figure 3.3 Genetic modifiers of azithromycin anti-ZIKV activity.** (A) Comparison of CRISPRi gene knockdown resistance phenotype ( $\rho$ ) in ZIKV-infected K562 cells with (horizontal axis) and without (vertical axis) azithromycin treatment. Potential gene-drug interaction candidate genes are labeled with the gene name and categorized by previously reported involvement in ZIKV infection (red), vesicular function and trafficking (blue), lipid metabolism and synthesis (green). Non-targeting control sgRNAs are shown in grey. (B) Follow-up validation of top candidate genes in individual knockdown K562 cell lines. Percent inhibition of 10 $\mu$ M (dark grey) and 20 $\mu$ M (light grey) azithromycin-treated cells is shown for individual K562 gene knockdown cell lines and compared to cells expressing non-targeting sgRNAs. Dashed lines indicate the baseline infection percentage in non-targeting (no gene knockdown) cell lines. Values below the dashed lines indicate a reduction in the effect of azithromycin, whereas values above the dashed lines indicate enhancement of azithromycin inhibition. Values are the mean of the top three sgRNAs against each indicated gene, except for non-targeting, which is the mean of 6 sgRNAs. Error bars show the standard deviation.

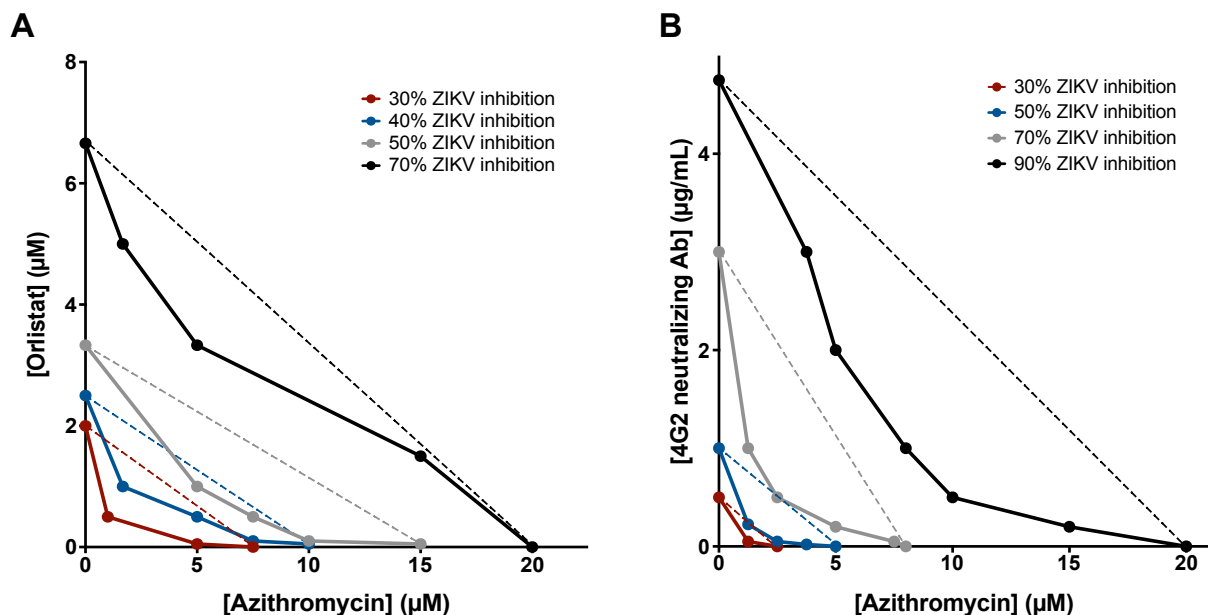


**Figure 3.4 Synergistic activity of azithromycin in combination with entry inhibitors.** (A) Isobologram of anti-ZIKV effect of azithromycin in combination with orlistat. Points on the horizontal axis indicate azithromycin treatment only, while points on the vertical axis indicate orlistat treatment only, and points off the axis were treated with the indicated concentration of each drug. Points show the concentration of each drug in the combination needed to achieve 30% (red), 40% (blue), 50% (grey), or 70% (black) inhibition of ZIKV infection. Dashed lines show the expected concentration of each drug required to achieve the indicated inhibition assuming simple additivity of drug effects. Points to the bottom-left of the dashed lines indicate efficacy beyond additive interactions and potential drug synergy. (B) Isobologram of anti-ZIKV effect of azithromycin in combination with neutralization by anti-envelope monoclonal antibody (mAb) 4G2. ZIKV was incubated in the presence of the indicated concentrations of 4G2 mAb prior to adding to azithromycin treated cells. Points show the concentration of each drug in the combination needed to achieve 30% (red), 50% (blue), 70% (grey), or 90% (black) inhibition of ZIKV infection.



### Chapter 3 References

1. Du S, Liu Y, Liu J, et al. Aedes mosquitoes acquire and transmit Zika virus by breeding in contaminated aquatic environments. *Nat Commun.* 2019; 10(1):1324.
2. Plourde AR, Bloch EM. A Literature Review of Zika Virus. *Emerg Infect Dis.* 2016; 22(7):1185–1192.
3. Oliveira WK de, França GVA de, Carmo EH, Duncan BB, Souza Kuchenbecker R de, Schmidt MI. Infection-related microcephaly after the 2015 and 2016 Zika virus outbreaks in Brazil: a surveillance-based analysis. *Lancet.* 2017; 390(10097):861–870.
4. Epidemiological Update Dengue, Chikungunya and Zika in the context of COVID-19: 23 December 2021 - PAHO/WHO | Pan American Health Organization [Internet]. [cited 2022 Apr 14]. Available from: <https://www.paho.org/en/documents/epidemiological-update-dengue-chikungunya-and-zika-context-covid-19-23-december-2021>
5. Retallack H, Di Lullo E, Arias C, et al. Zika virus cell tropism in the developing human brain and inhibition by azithromycin. *Proc Natl Acad Sci U S A.* 2016; 113(50):14408–14413.
6. Wehbeh HA, Ruggeirio RM, Shahem S, Lopez G, Ali Y. Single-dose azithromycin for Chlamydia in pregnant women. *J Reprod Med.* 1998; 43(6):509–514.
7. Oliver ME, Hinks TSC. Azithromycin in viral infections. *Rev Med Virol.* 2020; :e2163.
8. Parnham MJ, Erakovic Haber V, Giamarellos-Bourboulis EJ, Perletti G, Verleden GM, Vos R. Azithromycin: mechanisms of action and their relevance for clinical applications. *Pharmacol Ther.* 2014; 143(2):225–245.
9. Li C, Zu S, Deng Y-Q, et al. Azithromycin Protects against Zika Virus Infection by Upregulating Virus-Induced Type I and III Interferon Responses. *Antimicrob Agents Chemother.* 2019; 63(12):e00394-19.

10. Tummino TA, Rezelj VV, Fischer B, et al. Drug-induced phospholipidosis confounds drug repurposing for SARS-CoV-2. *Science*. 2021; 373(6554):541–547.
11. Abu-Farha M, Thanaraj TA, Qaddoumi MG, Hashem A, Abubaker J, Al-Mulla F. The Role of Lipid Metabolism in COVID-19 Virus Infection and as a Drug Target. *Int J Mol Sci*. 2020; 21(10):3544.
12. Breiden B, Sandhoff K. Emerging mechanisms of drug-induced phospholipidosis. *Biol Chem*. 2019; 401(1):31–46.
13. Chao LH, Klein DE, Schmidt AG, Peña JM, Harrison SC. Sequential conformational rearrangements in flavivirus membrane fusion. *Elife*. 2014; 3:e04389.
14. Goo L, DeMaso CR, Pelc RS, et al. The Zika virus envelope protein glycan loop regulates virion antigenicity. *Virology*. 2018; 515:191–202.
15. Goo L, VanBlargan LA, Dowd KA, Diamond MS, Pierson TC. A single mutation in the envelope protein modulates flavivirus antigenicity, stability, and pathogenesis. *PLoS Pathog*. 2017; 13(2):e1006178.
16. Reimer E, Stempel M, Chan B, Bley H, Brinkmann MM. Protein tyrosine phosphatase 1B is involved in efficient type I interferon secretion upon viral infection. *J Cell Sci*. 2020; 134(5):jcs246421.
17. Kridel SJ, Axelrod F, Rozenkrantz N, Smith JW. Orlistat is a novel inhibitor of fatty acid synthase with antitumor activity. *Cancer Res*. 2004; 64(6):2070–2075.
18. Zhang X, Jia R, Shen H, Wang M, Yin Z, Cheng A. Structures and Functions of the Envelope Glycoprotein in Flavivirus Infections. *Viruses*. 2017; 9(11):338.
19. Bressanelli S, Stiasny K, Allison SL, et al. Structure of a flavivirus envelope glycoprotein in its low-pH-induced membrane fusion conformation. *EMBO J*. 2004; 23(4):728–738.

20. Dowd KA, Pierson TC. The Many Faces of a Dynamic Virion: Implications of Viral Breathing on Flavivirus Biology and Immunogenicity. *Annu Rev Virol.* 2018; 5(1):185–207.
21. Kanehisa M, Goto S. KEGG: Kyoto Encyclopedia of Genes and Genomes. *Nucleic Acids Res.* 2000; 28(1):27–30.
22. Xia T, Yi X-M, Wu X, Shang J, Shu H-B. PTPN1/2-mediated dephosphorylation of MITA/STING promotes its 20S proteasomal degradation and attenuates innate antiviral response. *Proc Natl Acad Sci U S A.* 2019; 116(40):20063–20069.
23. CES1 carboxylesterase 1 - NIH Genetic Testing Registry (GTR) - NCBI [Internet]. [cited 2022 Apr 14]. Available from: <https://www.ncbi.nlm.nih.gov/gtr/genes/1066/><https://pubmed.ncbi.nlm.nih.gov/30450339/>
24. Orchard RC, Wilen CB, Virgin HW. Sphingolipid biosynthesis induces a conformational change in the murine norovirus receptor and facilitates viral infection. *Nat Microbiol.* 2018; 3(10):1109–1114.
25. Stenglein MD, Jacobson ER, Wozniak EJ, et al. Ball python nidovirus: a candidate etiologic agent for severe respiratory disease in *Python regius*. *mBio.* 2014; 5(5):e01484-01414.
26. Liu SJ, Nowakowski TJ, Pollen AA, et al. Single-cell analysis of long non-coding RNAs in the developing human neocortex. *Genome Biol.* 2016; 17:67.
27. Horlbeck MA, Gilbert LA, Villalta JE, et al. Compact and highly active next-generation libraries for CRISPR-mediated gene repression and activation. *Elife.* 2016; 5:e19760.

## Chapter 4:

### **Identification and characterization of nitroxoline as a novel inhibitor of the amoebic pathogen *Balamuthia mandrillaris***

This chapter is a reprint of:

Laurie MT\*, White CV\*, Retallack H, Wu W, Moser MS, Sakanari JA, Ang K, Wilson C, Arkin MR, DeRisi JL. Functional Assessment of 2,177 U.S. and International Drugs Identifies the Quinoline Nitroxoline as a Potent Amoebicidal Agent against the Pathogen *Balamuthia mandrillaris*. *mBio*. 2018; Oct 30;9(5):e02051-18. doi: 10.1128/mBio.02051-18

\*These authors contributed equally to this work

Supplemental files that are not figures can be found with the original work.

## ***Abstract***

*Balamuthia mandrillaris* is a pathogenic free-living amoeba that causes a rare but almost always fatal infection of the central nervous system called granulomatous amoebic encephalitis (GAE). Two distinct forms of *B. mandrillaris*—a proliferative trophozoite form and a nonproliferative cyst form, which is highly resistant to harsh physical and chemical conditions—have been isolated from environmental samples worldwide and are both observed in infected tissue. Patients suffering from GAE are typically treated with aggressive and prolonged multidrug regimens that often include the antimicrobial agents miltefosine and pentamidine isethionate. However, survival rates remain low, and studies evaluating the susceptibility of *B. mandrillaris* to these compounds and other potential therapeutics are limited. To address the need for more-effective treatments, we screened 2,177 clinically approved compounds for *in vitro* activity against *B. mandrillaris*. The quinoline antibiotic nitroxoline (8-hydroxy-5-nitroquinoline), which has safely been used in humans to treat urinary tract infections, was identified as a lead compound. We show that nitroxoline inhibits both trophozoites and cysts at low micromolar concentrations, which are within a pharmacologically relevant range. We compared the *in vitro* efficacy of nitroxoline to that of drugs currently used in the standard of care for GAE and found that nitroxoline is the most potent and selective inhibitor of *B. mandrillaris* tested. Furthermore, we demonstrate that nitroxoline prevents *B. mandrillaris*-mediated destruction of host cells in cultured fibroblast and primary brain explant models also at pharmacologically relevant concentrations. Taken together, our findings indicate that nitroxoline is a promising candidate for repurposing as a novel treatment of *B. mandrillaris* infections.

## ***Introduction***

The opportunistic protist pathogen *Balamuthia mandrillaris* causes rare but life-threatening infections of the central nervous system (CNS), termed balamuthia or granulomatous amoebic encephalitis (GAE) (1, 2). Onset of the disease is gradual and chronically develops over a few weeks to months in both immunocompromised and immunocompetent individuals worldwide (1, 3). Presenting clinical symptoms include but are not limited to fever, vomiting, neck stiffness, headache, nausea, personality changes, and seizures (1, 3). These symptoms are nonspecific and overlap symptoms caused by more common brain infections such as bacterial and viral meningitis as well as noninfectious neuroinflammatory syndromes. Cutaneous presentation is less common and can produce symptoms ranging from painless swelling to ulceration and formation of large lesions (4,–6). Infections involving other organs ranging from the lungs to the eye have also been documented (7, 8). Thus, *B. mandrillaris*-induced encephalitis often goes unrecognized and diagnosis is frequently only made postmortem. Several hundred cases have been reported; however, the actual disease burden is likely underestimated (2, 9).

While systematic ecological studies of *B. mandrillaris* have not been performed, free-living *B. mandrillaris* amoebae have been isolated from water, soil, and dust across all continents (10,–18). Cases of human and animal infections are also reported on all continents but are most common in South America and the southern United States (19,–35) (reviewed in references 31, 32, and 33). *B. mandrillaris* is thought to be transmitted by inhalation of contaminated aerosols or exposure via broken skin (36). Fatal amoebic encephalitis has also occurred after solid-organ transplantation (37, 38). Pathogenesis is believed to involve hematogenous spread to the CNS through penetration of the blood-brain barrier, and amoebae are frequently observed around blood vessels (3, 36).

Free-living amoebae such as *Sappinia pedata*, *Acanthamoeba* spp., and *Naegleria fowleri* can also cause infection of the CNS with very poor prognosis (2, 39). *Acanthamoeba* and *Balamuthia* are the most similar and are classified in the same eukaryote supergroup (*Amoebozoa: Acanthamoebidae*) (40). The mode of infection employed by *Sappinia pedata* and *Acanthamoeba* spp. is thought to be similar to that used by *Balamuthia*, as encephalitis caused by these genera progresses over several weeks to months and is associated with water or soil contact. Acute encephalitis caused by *N. fowleri* is specifically associated with recreation in warm freshwater environments, with presumed neuroinvasion of the amoeba by passing up the nose through the cribriform plate to the brain (41). All of these pathogenic amoebae have a proliferative trophozoite form and a dormant, thick-walled cyst form, while *N. fowleri* also has a motile flagellate form. The cyst form of free-living amoebae is notoriously more resistant to antimicrobials (42,–47) and to a variety of abiotic stressors such as UV light (48,–50). Such attributes, along with the fact that drug sensitivities differ among genera, species, and strains of free-living amoebae, have complicated studies in drug discovery (51).

Infection of the CNS by *B. mandrillaris* is almost always fatal, and no specific and highly successful treatment regimen is known (45, 52). The CDC recommends the following drugs for treatment of *B. mandrillaris* CNS infection: pentamidine isethionate, miltefosine, fluconazole, flucytosine, sulfadiazine, azithromycin, and/or clarithromycin (53). *In vitro* studies performed with the CDC-recommended drugs have shown little to no inhibition of amoebic growth by fluconazole, sulfadiazine, and flucytosine, while azithromycin, pentamidine isethionate, miltefosine, and voriconazole (a fluconazole derivative) exhibit amoebicidal or amoebistatic activity (11, 42, 51). Current treatments for *B. mandrillaris* CNS infections employing experimental combinations of these drugs have produced inconsistent outcomes, including

survival in some cases and fatality in others (7, 19, 23, 27, 29, 30, 34, 54,–62). As the efficacy and specificity of current treatments remain uncertain, there is a clear need to identify additional drugs that can improve patient outcomes.

The goal of this study was to identify, from a set of clinically approved compounds, candidates that have the potential to be repurposed for treatment of *B. mandrillaris* infections. Here, we screened a library of 2,177 clinically approved compounds and found that the quinoline antibiotic nitroxoline (8-hydroxy-5-nitroquinoline) exhibits amoebicidal activity at low micromolar concentrations, well within the range of the estimated plasma concentrations achieved with recommended oral dosing (63,–65). Through direct *in vitro* comparisons, we found that nitroxoline is a substantially more potent and selective inhibitor of *B. mandrillaris* than three commonly used GAE treatments currently recommended by the CDC. In addition to killing *B. mandrillaris* trophozoites, nitroxoline treatment also causes encystment and substantially delays recrudescence of active amoebae, which is significant considering the rapid decompensation of patients suffering from GAE. Nitroxoline, with its ease of delivery and favorable pharmacodynamic properties, has the potential to be used as an effective treatment for GAE in singularity or in combination with drugs in the current standard of care.

## **Results**

### *Identification of nitroxoline as an inhibitor of B. mandrillaris trophozoites in vitro.*

Due to the extremely high mortality rate associated with *Balamuthia mandrillaris* infections and the limited efficacy of current treatments, there is a clear need to identify additional therapeutic strategies to improve patient outcomes in these rare but deadly infections. Here, we established replicating axenic cultures of *B. mandrillaris* (ATCC PRA-291)



and screened 2,177 clinically approved compounds for reduction of trophozoite viability following 72 h of treatment at 20  $\mu$ M. Compounds with high percent inhibition ( $\sim$ 40% or above) and B-score ( $\sim$ 5 or above) were nominated for secondary screening (Fig. 4.1A; see also Table S1A in the supplemental material). The remaining compounds were annotated by class and delivery method to eliminate drugs approved only for topical delivery or veterinary use, which have low therapeutic potential (Table S1B). The selected candidate drugs were tested in dose-response assays with *B. mandrillaris* trophozoites as well as HFF-1 and H4 human cell cultures to confirm their activity and evaluate toxicity to human cells (Table S1C). Half-maximal inhibitory concentration ( $IC_{50}$ ) values indicated that only two compounds, pentamidine isethionate and nitroxoline, demonstrated adequate potency against *B. mandrillaris* without high toxicity to human cells. Since the amoebistatic activity of pentamidine has previously been described (46), we focused on further characterizing the novel activity of nitroxoline as the lead compound identified by this screen.

#### *Nitroxoline structure-activity relationship (SAR) experiments.*

Nitroxoline is currently in clinical use as an antimicrobial drug in certain European and Asian countries. The hypothesized mechanism of action (MoA) is as a metal chelator that disrupts biofilm formation (66). Nitroxoline and other 8-hydroxyquinolines have also previously demonstrated *in vitro* anticancer activity, and free-radical metabolites are thought to be involved in cell death (67). To test which of these mechanisms is applicable in killing *B. mandrillaris*, we tested 19 commercially available analogs of nitroxoline for amoebicidal activity. While nitroxoline itself remained the most potent compound tested, there was a clear necessity for the 8-position hydroxyl group on the quinoline ring to retain high activity (Fig. 4.2; see also Table S2). As demonstrated by the activity of 8-hydroxyquinoline (compound 2), the 5-position nitro group is not necessary for activity, while in contrast, retaining the nitro group without the hydroxy group

(compound 3) significantly decreases activity. Replacing the nitro group at the 5 position of the 8-hydroxyquinoline core with a variety of other functional groups, along with dual 5,7-position functionalization (compounds 4 to 13) results in several active but less potent analogs with no clear trend due to aromatic electronic effects. The sulfonic acid functionalized variant (compound 13) was the sole inactive compound among compounds 4 to 13, which we speculate may have been due to differences in uptake or permeability. Lastly, phenanthroline (compound 14), a structurally similar bidentate metal binding ligand, also demonstrated activity against *B. mandrillaris*. Taken together, these results indicate a likely metal binding mechanism for the original nitroxoline compound.

#### *Direct comparison of nitroxoline to standard-of-care drugs for GAE treatment.*

To evaluate nitroxoline as a potential drug to treat *B. mandrillaris* infections, we compared the *in vitro* performance of nitroxoline to that of pentamidine isethionate, miltefosine, and azithromycin, three drugs recommended by the CDC and commonly used in treatment of GAE (53). We performed side-by-side dose-response experiments to measure the efficacy of each drug against *B. mandrillaris* trophozoites and the toxicity to different human cell types using the following cell lines: HFF-1 (fibroblast), H4 (glial), U87 (glial), HEK-293T (kidney), and Hep-G2 (liver). Nitroxoline was the most potent inhibitor of *B. mandrillaris* trophozoites, with an  $IC_{50}$  of 2.84  $\mu$ M compared to  $IC_{50}$  values of 9.14  $\mu$ M, 63.23  $\mu$ M, and 244.10  $\mu$ M for pentamidine, miltefosine, and azithromycin, respectively (Fig. 4.3A). Nitroxoline was also the only drug with an  $IC_{50}$  against *B. mandrillaris* that was lower than the half-maximal cytotoxic concentration ( $CC_{50}$ ) for all cell lines tested. The average  $\text{Log}_{10}$  selectivity index ( $CC_{50}$  for human cell toxicity/ $IC_{50}$  for *B. mandrillaris* inhibition) of nitroxoline across all cell lines was 0.832, compared to 0.049, -0.102, and -0.409 for pentamidine, miltefosine, and azithromycin, respectively

(Fig. 4.3B [summarized in Table S3]). Combinations of nitroxoline with miltefosine and with pentamidine isethionate showed generally additive inhibitory effects on *B. mandrillaris* viability, suggesting that nitroxoline can be combined with other amoebicidal drugs to produce greater inhibition (see Fig. 4.7 in the supplemental material).

#### *Encystment response of B. mandrillaris.*

In addition to a dose-dependent reduction in *B. mandrillaris* trophozoite viability, we also observed a general increase in the ratio of cysts to trophozoites correlated with increasing concentrations of some drugs. We investigated the propensity of nitroxoline, pentamidine isethionate, miltefosine, and azithromycin to induce encystment of *B. mandrillaris* by counting the number of cysts and trophozoites in culture samples following 72 h of treatment with different drug concentrations. We observed a dose-dependent reduction in the number of trophozoites in the population for all four drugs. Nitroxoline and pentamidine isethionate caused an increase in both the total number and the proportion of cysts in the population, while no substantial number of cysts was observed at any concentration of miltefosine or azithromycin (Fig. 4.4A to D). Because encystment appears to occur as a response to certain drug treatments, we also assessed the ability of each drug to inhibit the viability of preformed *B. mandrillaris* cysts. We induced encystment by sustained exposure to 12% galactose and conducted dose-response viability measurements for each drug. Nitroxoline was again the most potent inhibitor of cysts, with an  $IC_{50}$  of 15.48  $\mu$ M compared to  $IC_{50}$  values of 26.26  $\mu$ M, 76.48  $\mu$ M, and 788.4  $\mu$ M for pentamidine, miltefosine, and azithromycin, respectively (Fig. 4.4E). While nitroxoline, pentamidine, and azithromycin were considerably less potent inhibitors of cyst viability than of trophozoite viability, miltefosine inhibited the two forms of *B. mandrillaris* at similar concentrations (Table S3).

*Delayed recrudescence of B. mandrillaris treated with nitroxoline.*

Nitroxoline and the tested standard-of-care drugs induce various combinations of distinct and intermediate *B. mandrillaris* phenotypes, including death and encystment. Though it is assumed that drug-induced phenotypes such as encystment affect the rate of amoeba population growth and host cell destruction, the magnitude and duration of these effects are unknown. To assess how rapidly amoeba populations recover and proliferate following drug treatment, we developed a recrudescence assay wherein we treated *B. mandrillaris* trophozoite cultures with various concentrations of nitroxoline, pentamidine, or miltefosine for 72 h, removed drug, and then added the remaining amoebae to a monolayer of HFF-1 cells in the absence of drug. The posttreatment recovery time was measured as the number of days required for each *B. mandrillaris* population to clear 100% of the host cells. Treatments that completely eliminated *B. mandrillaris* populations were determined by observing no live trophozoites or destruction of host cells at any point during the 28-day experiment. We found that 7  $\mu$ M and 14  $\mu$ M pentamidine delayed recovery of *B. mandrillaris* by 1 to 2 weeks but that increasing the dose from 14  $\mu$ M to 56  $\mu$ M delayed recovery by only an additional 3 days (Table S1). Consistent with the steep Hill slope observed in dose-response experiments, miltefosine caused very little delay in clearance time at 56  $\mu$ M but completely eliminated *B. mandrillaris* populations at 112  $\mu$ M. In contrast, nitroxoline delayed amoeba recovery by 2 to 3 weeks at low micromolar concentrations and completely eliminated *B. mandrillaris* populations at 28  $\mu$ M.

*Protective effect of nitroxoline in a primary human brain tissue model.*

Findings from the recrudescence assays suggest that nitroxoline treatment may significantly impede destruction of host cells in the context of *B. mandrillaris* infection. To further

explore this possibility, we performed experiments modeling *B. mandrillaris* infection and nitroxoline treatment in primary human brain tissue. Human cortical tissue slices were exposed to *B. mandrillaris* trophozoites and simultaneously treated with nitroxoline or vehicle (dimethyl sulfoxide [DMSO]) for 20 h before media were changed to remove drug or vehicle. Tissues were cultured for 4 days and then evaluated for damage by microscopic examination (Fig. 4.5; see also Fig. 4.8). Untreated tissues showed widespread damage following *B. mandrillaris* exposure, including loss of distinct tissue edges and reduction of cell density (Fig. 4.5B). Large numbers of highly motile *B. mandrillaris* trophozoites were present at the edges of tissues and were intermixed with human cells (see Movies S1 to S3 in the supplemental material). In contrast, nitroxoline-treated tissues did not show signs of *B. mandrillaris*-mediated destruction and appeared to be similar to uninfected tissues (Fig. 4.5A and C). Cysts with little to no motility were observed outside the boundaries of tissues (Movie S4). While these findings are qualitative, the large-scale differences in tissue morphology observed in this experiment are consistent with the possibility that nitroxoline has a protective effect on host tissue in the context of *B. mandrillaris* infection.

## **Discussion**

GAE caused by *Balamuthia mandrillaris* is almost always fatal (19,–34). Because there is no established treatment for GAE, patients commonly receive experimental combinations of antimicrobial agents in aggressive and prolonged treatment regimens with mixed outcomes (7, 19, 23, 27, 29, 30, 34, 54,–62). In the present study, we aimed to address the critical need for new treatments of GAE by identifying novel amoebicidal compounds. Because our goal was to identify candidate drugs with established safety and pharmacodynamic profiles, we chose to screen a library of 2,177 clinically approved compounds. Based on the criteria of B-score and percent

inhibition of *B. mandrillaris* viability, we selected 12 compounds from the primary screen for follow-up screening (Fig. 4.1A; see also Table S1B in the supplemental material). Secondary screening eliminated all candidate compounds on the basis of low potency for inhibition of *B. mandrillaris* or high toxicity to human cells, with the exception of the quinoline antibiotic nitroxoline. Nitroxoline demonstrated promising potency and selectivity for *B. mandrillaris* inhibition, which led us to focus our efforts on further investigating its novel amoebicidal activity.

We performed side-by-side experiments to directly compare the *in vitro* efficacy of nitroxoline with respect to *B. mandrillaris* inhibition to the efficacy of pentamidine isethionate, miltefosine, and azithromycin, three drugs recommended by the CDC for treatment of GAE and commonly used in case reports (29, 30, 53,–55, 57). We found that nitroxoline was the most potent inhibitor of *B. mandrillaris* trophozoite viability, with an  $IC_{50}$  of 2.84  $\mu$ M and  $IC_{99}$  of 7.54  $\mu$ M (Fig. 4.3A). To estimate the selectivity of each drug, we also measured the toxicity of each compound to five different human cell lines. For pentamidine, miltefosine, and azithromycin, drug concentrations that reduced *B. mandrillaris* viability also caused significant toxicity to human cells, giving very small selectivity indices (Fig. 4.3B). In contrast, nitroxoline had an  $IC_{50}$  for *B. mandrillaris* inhibition that was lower than the  $CC_{50}$  for all cell lines tested and had the highest mean selectivity index value (Fig. 4.3B; see also Table S3).

*B. mandrillaris* and other free-living amoebae have a dormant, thick-walled cyst form which is highly resistant to several types of environmental stress, including exposure to some compounds that are toxic to the trophozoite form (44, 46, 48, 50). A previous study postulated that the transition from the trophozoite form to the cyst form can be triggered under a variety of conditions, including chemical stress (68), raising the possibility that treatment with amoebicidal

or amoebistatic drugs may induce encystment. To investigate this possibility, we quantified the frequency of cysts observed in *B. mandrillaris* populations treated with different drug concentrations. We observed that low micromolar concentrations of nitroxoline and pentamidine isethionate caused increases in the total number and proportion of cysts in *B. mandrillaris* populations (Fig. 4.4A and B). In contrast, miltefosine and azithromycin were not observed to induce encystment at any concentration (Fig. 4.4C and D). These data support the possibility that *B. mandrillaris* encystment occurs as a response to some but not all compounds that are toxic to trophozoites. We suggest that compounds which promote encystment in addition to killing trophozoites may provide additional benefit in the context of infection by slowing or halting the rapid tissue destruction by trophozoites.

Because it is common for both cysts and trophozoites to be found in *B. mandrillaris*-infected tissue, it is important to understand the efficacy of amoebicidal drugs against both stages (69). To address this issue, we performed side-by-side dose-response experiments with homogenous populations of cysts or trophozoites treated with nitroxoline, pentamidine isethionate, miltefosine, and azithromycin. We found that cysts were less sensitive than the trophozoites to all four drugs (Table S3). The difference in sensitivity was marginal for miltefosine and greatest for nitroxoline, which had an  $IC_{50}$  for cyst inhibition 6-fold higher than the  $IC_{50}$  for trophozoite inhibition. Nevertheless, nitroxoline remained the most potent inhibitor of preformed *B. mandrillaris* cysts, with an  $IC_{50}$  of 15.48  $\mu$ M.

Viability measurements of drug-treated *B. mandrillaris* cultures reflect a complex population phenotype that includes various degrees of both death and encystment. These measurements are not sufficient to predict the rate at which populations recrudescence following treatment, which is an important factor in evaluating the overall efficacy of different treatments.

We chose to address this aspect of treatment efficacy by performing recovery assays in which *B. mandrillaris* populations were exposed to various drug treatments, removed from drug, and then cocultured with monolayers of human cells until the host cells were fully consumed. As predicted, increasing drug concentrations caused greater delays to *B. mandrillaris* recrudescence and host cell destruction (Table 4.1). Surprisingly, even low micromolar concentrations of nitroxoline near the IC<sub>50</sub> for trophozoite inhibition delayed *B. mandrillaris*-mediated host cell destruction by 2 to 3 weeks. This assay also served as a sensitive method to detect very low numbers of surviving amoebae due to the large population expansion occurring over the 28-day experiment duration. Importantly, this sensitive assay allowed us to infer that *B. mandrillaris* populations had been completely eliminated by drug treatment when we observed no signs of amoeba population recovery after 28 days of coculture with host cells.

Using this method, we determined that concentrations of 28  $\mu$ M nitroxoline and 112  $\mu$ M miltefosine completely eliminated *B. mandrillaris* populations. These data are consistent with viability inhibition experiments in indicating that nitroxoline is the most potent inhibitor of *B. mandrillaris* tested. The promising results of this experiment suggest that nitroxoline may be able to fully eliminate *B. mandrillaris* infection if sufficiently high concentrations are reached and is likely to cause substantial delays with respect to host tissue damage even at lower concentrations. This is supported by our findings indicating that nitroxoline prevented *B. mandrillaris* activity and tissue destruction in a primary human brain tissue model (Fig. 4.5; see also Movie S1 to S4 in the supplemental material). Together, these findings suggest that nitroxoline substantially impedes host tissue destruction by *B. mandrillaris in vitro*. Given the rapid progression of pathogenesis that is characteristic of GAE, any impediment to tissue destruction could significantly improve patient prognosis.



The known safety and pharmacokinetic properties of nitroxoline suggest further promise for its therapeutic value as an inhibitor of *B. mandrillaris*. Nitroxoline has been safely used for over 50 years in the treatment of urinary tract infections, with minimal adverse effects reported (70). Nitroxoline is available in oral and intravenous administration forms and is typically dosed at 600 to 800 mg/day for adults, resulting in maximal plasma concentrations ( $C_{\max}$ ) of up to approximately 30  $\mu\text{M}$  (5.6 mg/liter) (63,–65), which is 10-fold higher than the  $\text{IC}_{50}$  for *B. mandrillaris* trophozoites *in vitro* (Fig. 4.3A; see also Table S3). Although the extent to which nitroxoline crosses the blood brain barrier is unknown, a recent study showed that systemically delivered nitroxoline exhibits efficacy against gliomas in mice, implying that efficacious concentrations reached the brain in that model (71). In addition, we previously noted that *B. mandrillaris* frequently causes necrotizing vasculitis in the CNS with extensive blood-brain barrier (BBB) breakdown, which may affect the bioavailability of systemically administered drugs in the CNS of patients actively suffering from GAE (3, 36, 57). Furthermore, given the extreme severity of GAE, intrathecal drug delivery can be performed to maximize drug concentrations reaching the brain (2, 72). While many variables may affect the *in vivo* efficacy of nitroxoline as well as the concentrations that can be achieved in relevant compartments, the literature suggests that the *in vitro* efficacious concentrations that we demonstrated are well within a pharmacologically relevant range.

The *in vitro* results presented in this study strongly indicate that nitroxoline warrants further investigation as a potential treatment for *B. mandrillaris* infections. As there were many variables that were untested in our study that may affect the efficacy of nitroxoline *in vivo*, future work will ideally focus on providing *in vivo* validation of the amoebicidal activity of nitroxoline. In particular, *in vivo* studies will determine if efficacious concentrations of nitroxoline reach the

relevant tissues as well as provide comparative evidence for amoebicidal activity with respect to currently recommended compounds. We note that nitroxoline is an approved compound in several countries, with an established safety profile (70), and it is possible that it could be considered as an emergency experimental treatment in dire cases of GAE. In particular, since the current standard of care generally consists of experimental combinations of several antimicrobial agents, adding nitroxoline to these regimens may be a reasonable step in the effort to improve patient prognosis. Although our SAR experiments did not identify any analog that matched the potency of nitroxoline, medicinal chemistry optimization may still be beneficial for a better understanding of possible mechanisms of action and efforts to improve drug specificity. The similarity of *B. mandrillaris* to other free-living amoebae such as *Acanthamoeba* spp. and *Naegleria fowleri* raises the intriguing possibility that nitroxoline or related compounds may also have activity against these pathogens.

## ***Materials and Methods***

### *Human cell lines.*

Hep-G2 (ATCC HB-8065), U87 (gift of Jonathan Weissman, University of California, San Francisco [UCSF]), H4 (ATCC HTB-148), and HEK-293T (ATCC CRL-3216) cells were cultured in Dulbecco's modified Eagle's medium (Gibco) containing 10% (vol/vol) fetal bovine serum (FBS) (Gibco), 2 mM l-glutamine, 100 U/ml penicillin/streptomycin (Gibco), and 10 mM HEPES buffer. HFF-1 cells (ATCC SCRC-1041) were cultured in DMEM containing 15% (vol/vol) FBS, 2 mM l-glutamine, 100 U/ml penicillin/streptomycin, and 10 mM HEPES buffer (Gibco). All mammalian-cell incubation steps were carried out at 37°C with 5% CO<sub>2</sub>. All cell lines were tested for mycoplasma contamination using a Lonza Mycoalert mycoplasma detection kit (Lonza).

*Balamuthia mandrillaris* propagation, handling, and encystment.

*Balamuthia mandrillaris* (ATCC PRA-291) was maintained axenically in 150-cm<sup>2</sup> flasks (Corning) containing modified Cerva's medium (axenic medium) with the following formulation: 20 g of Bacto Casitone (Difco), 68 ml of 10× Hanks' balanced salt solution (Gibco), 10% fetal bovine serum, and 1× penicillin-streptomycin (200 IU/ml to 200 µg/ml) (73). Axenic growth of *B. mandrillaris* resulted in  $2 \times 10^5$  to  $3 \times 10^5$  amoebae/ml in log phase. Routine subculturing was performed every 3 to 4 days by transferring 5 ml of amoebae into 15 ml of fresh axenic media.

Following the findings of a previous study, encystment of *B. mandrillaris* was induced by galactose exposure (74). *B. mandrillaris* trophozoites were grown to log phase in axenic media, and galactose was added to reach a final concentration of 12% (vol/vol). Amoebae were cultured in the induction medium until trophozoites were no longer observed (approximately 10 days). Galactose-induced cysts transition back to trophozoites after approximately 3 days of incubation in galactose-free axenic medium. Therefore, all assays with cysts were completed in the induction medium. To quantify amoebae for use in experiments, actively growing trophozoites or recently induced cysts were centrifuged at 3,000 rpm for 5 min, resuspended in axenic medium, and counted with a disposable hemocytometer (SKC, Inc.). All incubation steps for *B. mandrillaris* growth were carried out at 37°C with 5% CO<sub>2</sub>.

*Primary drug screening of Balamuthia mandrillaris* trophozoites *in vitro*.

Screening of a clinically approved library of compounds, compiled by the Small Molecule Discovery Center (SMDC) at the UCSF, was completed at 20 µM in 0.2% DMSO. All 2,177 drugs in the library were stored as 10 mM stocks dissolved in 100% DMSO (Sigma-Aldrich) at -20°C. *B. mandrillaris* amoebae were resuspended in axenic medium and distributed into opaque 384-well

plates (Corning) at a density of 3,000 amoebae per well using a BioMek NX liquid handler. Negative-control wells were treated with vehicle only (0.2% DMSO in axenic medium), and positive-control wells simulating total destruction of amoebae were seeded with amoeba lysate generated by 3 consecutive freeze-thaw cycles. Following 72 h of incubation, 30  $\mu$ l of CellTiter Glo reagent (CTG; Promega) was added to each well. The luminescence was measured with a Promega GloMax-Multi+ plate reader at 2, 4, and 8 h after CTG addition. The percent inhibition of *B. mandrillaris* was calculated based on the CTG luminescence measurements of treated wells relative to both positive and negative controls using the following equation: percent inhibition =  $100 - 100 * [(test\ well\ intensity - positive-control\ intensity) / (negative-control\ intensity - positive-control\ intensity)]$ . The B-score, representing a plate-based statistical approach for correcting row, column, and edge effects, was also calculated for each compound in the library (75). Raw luminescence measurements and computed inhibition values are displayed in Table S1A in the supplemental material. Hits represented compounds with a B-score of approximately 5 or above and percent inhibition of approximately 40% or above (Table S1B). Hit compounds that are approved only for topical administration or veterinary use were not tested in secondary screening (highlighted in yellow in Table S1B and Fig. 4.1B). Compounds identified in the primary screen that did not exhibit activity upon repurchase of fresh compound were removed from consideration in the screening funnel.

*Secondary drug screening against B. mandrillaris trophozoites and HFF-1 and H4 human cells in vitro.*

Secondary screening of hit compounds consisted of dose-response experiments to measure the toxicity of each compound to *B. mandrillaris* trophozoites, HFF-1 human fibroblast cells, and

H4 human neuroglioma cells. Four 384-well plates were prepared prior to addition of drug as follows: one opaque plate (Corning) seeded with 3,000 HFF-1 cells per well in 60  $\mu$ l complete media, one opaque plate seeded with 2,000 H4 cells per well in 60  $\mu$ l complete media, one opaque plate containing 30  $\mu$ l axenic media, and one clear plate (Corning) containing 30  $\mu$ l axenic media. Opaque plates were used to measure the viability of trophozoites in the CTG assay, and clear plates were used for microscopic examination of cyst formation. HFF-1 and H4 plates were seeded 24 h prior to drug addition. The selected primary screen hits were added from 10 mM DMSO stocks into wells of all four test plates to reach final concentrations ranging from 0.06  $\mu$ M to 30  $\mu$ M (10 concentrations, 2-fold serial dilution). Negative-control wells received concentrations of DMSO corresponding to the amount of DMSO in each tested drug well (reaching a maximum of 0.3% DMSO). *B. mandrillaris* trophozoites were resuspended in axenic media and added to the plates containing drug dilutions in axenic media at a density of 3,000 amoebae per well in a final volume of 60  $\mu$ l media. All plates were incubated for 72 h. Throughout the incubation period, the clear-bottom *B. mandrillaris* plate was monitored for large-scale changes to population encystment in response to drug treatment. After the 72-h incubation, 30  $\mu$ l of CTG reagent was added to all wells of the opaque assay plates and luminescence was measured with a Promega GloMax-Multi+ plate reader at 2, 4, and 8 h after CTG addition. IC<sub>50</sub> values for inhibition of *B. mandrillaris* viability were determined using the GraphPad Prism 4-parametric sigmoidal curve-fitting model, with the bottom and top constraints set to 0 and 1, respectively (Table S1C).

#### *Nitroxoline structure-activity relationship experiments.*

Nineteen commercially available analogs of nitroxoline were selected for structure-activity relationship (SAR) experiments based on variances in functional groups that may play a role in

the observed mechanism of action (compound sourcing and data are presented in Table S2). *B. mandrillaris* was grown to log phase axenically and plated at 4,000 amoebae per well in opaque 96-well plates. Each nitroxoline analog was dissolved in 100% DMSO at 10 mM. Analog stocks were serially diluted in water to generate 8-point dilution series, which were then used to treat assay wells containing *B. mandrillaris* trophozoites at final concentrations ranging from 0.14  $\mu\text{M}$  to 300  $\mu\text{M}$  (8 concentrations, 3-fold serial dilution) in a final volume of 100  $\mu\text{l}$ . After incubation for 72 h, 50  $\mu\text{l}$  of CTG was added to all assay wells. Luminescence was measured using a Promega GloMax Multi+ luminometer 2, 4, and 8 h after CTG addition.  $\text{IC}_{50}$  values were determined using the GraphPad Prism 4-parametric sigmoidal curve-fitting model with bottom and top constraints of 0 and 1, respectively.

*Dose-response experiments with HFF-1, H4, U87, Hep-G2, and HEK 293T cells and Balamuthia mandrillaris trophozoites and cysts.*

*B. mandrillaris* trophozoites were seeded at 4,000 amoebae per well into opaque and clear-bottom 96-well plates (Corning). Homogenous populations of *B. mandrillaris* cysts generated by galactose induction were seeded at 4,000 amoebae per well into opaque 96-well plates. HFF-1 (fibroblast), H4 (glial), U87 (glial), HEK-293T (kidney), and Hep-G2 (liver) cells were seeded at 3,000 cells per well in opaque 96-well plates 24 h prior to addition of drug. Stocks of nitroxoline (Selleck Chemicals) were dissolved in 100% DMSO at 10 mM. Stocks of azithromycin (Selleck Chemicals), pentamidine isethionate (Selleck Chemicals), and miltefosine (Selleck Chemicals) were dissolved in water at 10 mM. Drug stocks were serially diluted in water to generate 12-point dilution series, which were then used to treat assay wells containing *B. mandrillaris* or human cells at final concentrations ranging from 0.39  $\mu\text{M}$  to 400  $\mu\text{M}$  in 100- $\mu\text{l}$  total well volumes. Control

wells were treated with vehicle (DMSO or water) at concentrations corresponding to the final vehicle concentrations in each drug dilution series. After incubation for 72 h, 50  $\mu$ l of CTG was added to all assay wells. Luminescence was measured with a Promega GloMax-Multi+ plate reader 2, 4, and 8 h after CTG addition. All dose-response experiments were performed with at least three independent biological replicates. IC<sub>50</sub> values were determined as previously described. To quantify encystment under treated and untreated conditions, amoebae in individual assay wells were resuspended thoroughly and the number of cysts and number of trophozoites in 10- $\mu$ l samples were counted by the use of a hemocytometer (SKC, Inc.). Cysts and trophozoites are morphologically distinct, making them simple to distinguish with bright-field microscopy (example images are shown in Fig. 4.6 in the supplemental material). Encystment assays were performed with three independent biological replicates.

Experiments measuring the effect of drug combinations were carried out similarly to the dose-response experiments described above. *B. mandrillaris* trophozoites were seeded into opaque 96-well plates (Corning) at a density of 4,000 amoebae per well and then treated with concentrations of nitroxoline that differed across the rows of each plate and with concentrations of either miltefosine or pentamidine isethionate that differed down the columns to generate 7-by-7 dose combination matrices. Final drug concentrations ranged from 0.5 to 10  $\mu$ M, from 10 to 100  $\mu$ M, and from 1 to 100  $\mu$ M for nitroxoline, miltefosine, and pentamidine isethionate, respectively. After incubation with drug or vehicle was performed for 72 h, CTG was added to all assay wells and luminescence was measured with a Promega Glomax-Multi+ plate reader. The percent effect of each drug combination was calculated as the reduction in luminescence value relative to vehicle-only controls. The additive effect of drug combinations was assessed using the excess over highest single agent (EOHSA) model (76, 77). EOHSA values were calculated using

the equation  $EOHSA = E_{\text{combo}} - E_{\text{HSA}}$ , where  $E_{\text{combo}}$  is the percent effect of a given dose combination and  $E_{\text{HSA}}$  is the percent effect of the most active (highest) single agent in the drug pair. Drug combination experiments were performed with three independent replicates.

*Balamuthia mandrillaris* recrudescence assays.

Populations of *B. mandrillaris* were diluted to  $2.5 \times 10^5$  amoebae in 10 ml media and were treated with 3.5, 7, 14, 28, 56, 84, and 112  $\mu\text{M}$  nitroloxine, pentamidine isethionate, or miltefosine and incubated for 72 h. Following incubation, all remaining amoebae in each population (various mixtures of cysts and trophozoites) were pelleted at 3,000 rpm for 5 min and resuspended in drug-free HFF-1 medium. Each resuspended *B. mandrillaris* population was placed on a monolayer of HFF-1 cells that were seeded at  $10^6$  cells per flask in 10 ml at 24 h prior to inoculation. At that cell density, untreated amoebae typically consume 100% of HFF-1 monolayers within 24 h. Coculture flasks containing amoebae and HFF-1 cells were incubated until 100% of the HFF-1 monolayer was consumed as observed by daily microscopic inspection or until the predetermined endpoint of the experiment at 28 days post-*B. mandrillaris* inoculation was reached. The day on which complete clearance of the HFF-1 monolayer occurred was recorded for all conditions. All recrudescence assays were performed with three independent biological replicates. These methods were adapted from a minimum trophozoite amoebicidal concentration (MTAC) assay that was conducted with monolayers of MA104 monkey kidney cells (42).

*Primary brain tissue model.*

Deidentified tissue samples were collected with previous patient consent in strict observance of the legal and institutional ethical regulations. Protocols were approved by the Human Gamete, Embryo, and Stem Cell Research Committee (institutional review board) at the



University of California, San Francisco. Primary brain tissue samples were sectioned perpendicularly to the ventricle to obtain slices 300  $\mu\text{m}$  thick and  $\sim 2.5 \text{ mm}^2$  in surface area, using a Leica VT1200S vibrating blade microtome and artificial cerebrospinal fluid containing 125 mM NaCl, 2.5 mM KCl, 1 mM  $\text{MgCl}_2$ , 1 mM  $\text{CaCl}_2$ , and 1.25 mM  $\text{NaH}_2\text{PO}_4$ . Explants were transferred to slice culture insertions (Millicell) in 6-well culture plates and were cultured with media containing 66% Eagle's basal medium, 25% Hanks balanced salt solution, 5% fetal bovine serum, 1% N-2 supplement,  $1\times$  penicillin-streptomycin, and glutamine in a  $37^\circ\text{C}$  incubator with 5%  $\text{CO}_2$ . At 12 h after plating, slices were inoculated with  $10^4$  *B. mandrillaris* trophozoites in 20  $\mu\text{l}$  of complete media containing vehicle (DMSO) or 35  $\mu\text{M}$  nitroxoline, which was added dropwise to the slice surface. Media below the cell culture insert was adjusted to matching vehicle or nitroxoline concentrations. At 20 h postinoculation, media below the cell culture insertion were replaced with fresh media containing no drug. At that time, amoebae on top of the insertion surrounding and within the tissue were left undisturbed. Bright-field and phase contrast images were captured during the live culture experiment at magnifications of  $\times 4$ ,  $\times 10$ , and  $\times 20$  using an Evos FL Cell Imaging System. At 4 days postinoculation, slices were gently fixed in 3.7% paraformaldehyde (PFA) for 4 h at  $4^\circ\text{C}$  and then rinsed with phosphate-buffered saline (PBS), stained for 2 h at room temperature with DAPI (4',6-diamidino-2-phenylindole) (0.3  $\mu\text{M}$ )–PBS–1% Triton X-100, and then mounted with ProLong Gold antifade mountant (Thermo). Images of stained tissue were obtained with a Nikon Ti spinning disk confocal microscope at  $\times 20$  magnification. Confocal z-stacks were projected and adjusted in ImageJ (78). Bright-field images were stitched together using photomerge in Photoshop (Adobe). Bright-field time-lapse images were processed as movies in ImageJ.

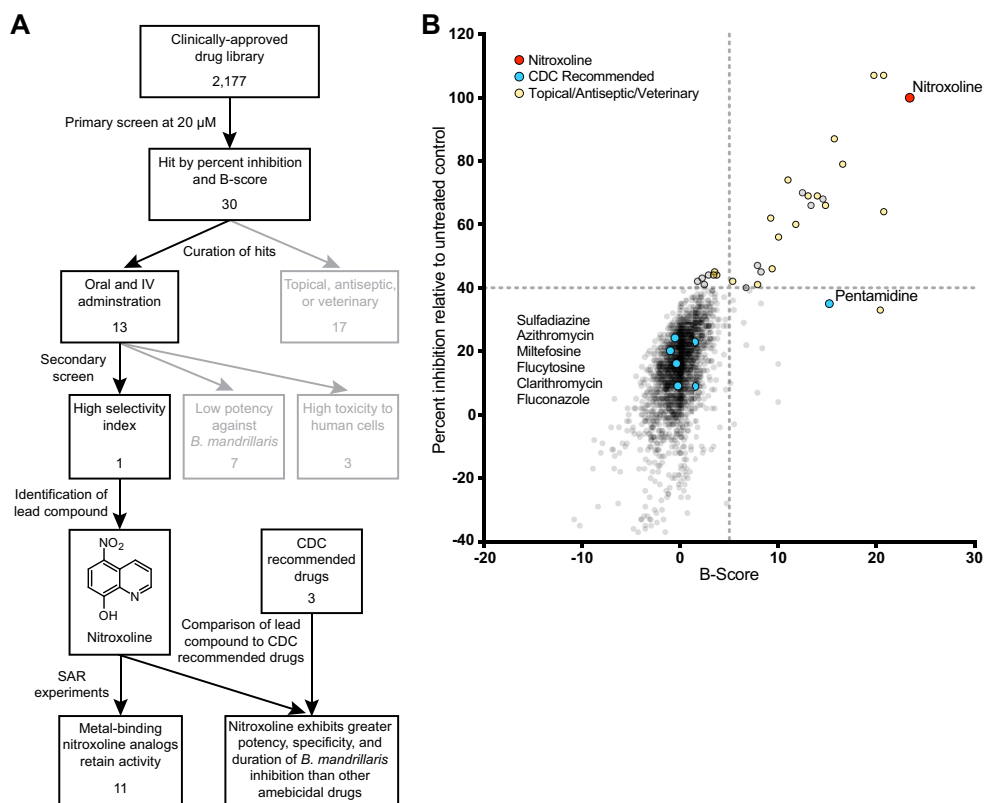


**Figure 4.1. Primary drug repurposing screen against *B. mandrillaris*.** (A) Workflow for screening of clinically approved compounds for *in vitro* activity against *B. mandrillaris*. A primary screen of 2,177 clinically approved compounds yielded 30 hits meeting the percent inhibition and B-score criteria, among which only 13 candidates were available for oral or intravenous (IV) administration (see panel B). Secondary screening identified only one novel lead compound, nitroxoline, which displayed high selectivity for inhibition of *B. mandrillaris* viability (Table S1C). Structure-activity relationship (SAR) experiments showed that 11 of 12 nitroxoline analogs tested with potential metal binding domains remained active against *B. mandrillaris*, suggesting that metal binding plays a role in the mechanism of inhibition by nitroxoline (Fig. 4.2). Comparison of nitroxoline to three drugs recommended by the CDC for treatment of *B. mandrillaris* CNS infections (pentamidine isethionate, miltefosine, and azithromycin) indicates that nitroxoline is the most potent and specific inhibitor of *B. mandrillaris* among the compounds tested (Fig. 4.3 and 4.4; see also Table S1). (B) Plot of percent inhibition relative to untreated controls and B-score measured for each compound in a library of 2,177 clinically approved compounds. Raw data used to calculate these values are compiled in Table S1A. Drugs recommended by the CDC for treatment of GAE are highlighted in blue. Drugs that are classified as antiseptic or topical and/or have not been used in humans are shown in yellow. The quinoline antibiotic nitroxoline, which was the top hit identified in this screen, is highlighted in red.

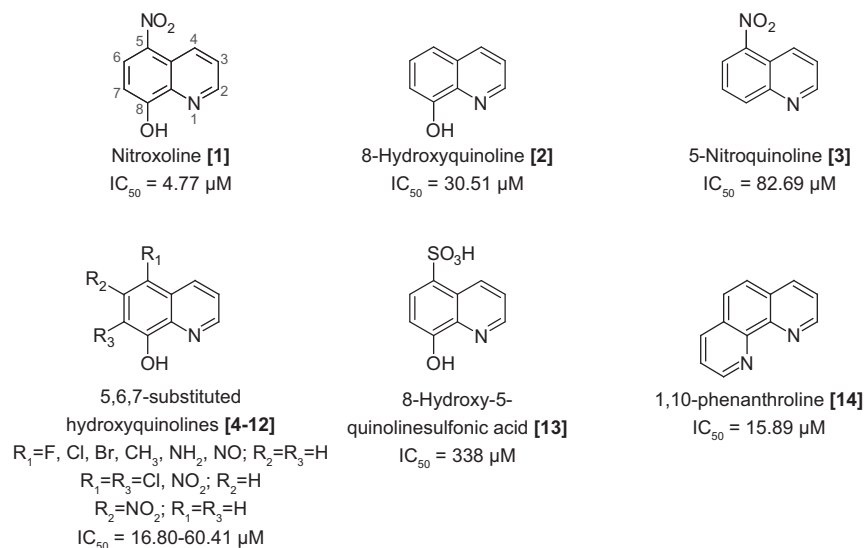


**Figure 4.2. Activity of compounds structurally related to nitroxoline.** Structure-activity relationship experiments suggest that nitroxoline inhibits *B. mandrillaris* through a mechanism related to metal binding. Structures and  $IC_{50}$  values are shown for nitroxoline and select analogs; additional compounds are shown in Table S2. Nitroxoline is made up of a quinoline core with a nitro group at the 5 position and a hydroxyl group at the 8 position. Analogs lacking the 8-position hydroxyl group were generally inactive, with  $IC_{50}$  values greater than  $80 \mu M$  (e.g., 5-nitroquinoline [compound 3]). Twelve nitroxoline analogs with predicted metal binding activity were tested, and of these, 1,10-phenanthroline (compound 14) and 10 of 11 compounds with an 8-position hydroxyl group (e.g., 8-hydroxyquinoline [compound 2]) were active, with  $IC_{50}$  values ranging from 17 to  $60 \mu M$ . The only inactive analog with an 8-position hydroxyl group was 8-hydroxy-5-quinolinesulfonic acid (compound 13). Variance of the 5-position nitro group reduced potency compared to nitroxoline, but no trend related to aromatic electronic effects is apparent.

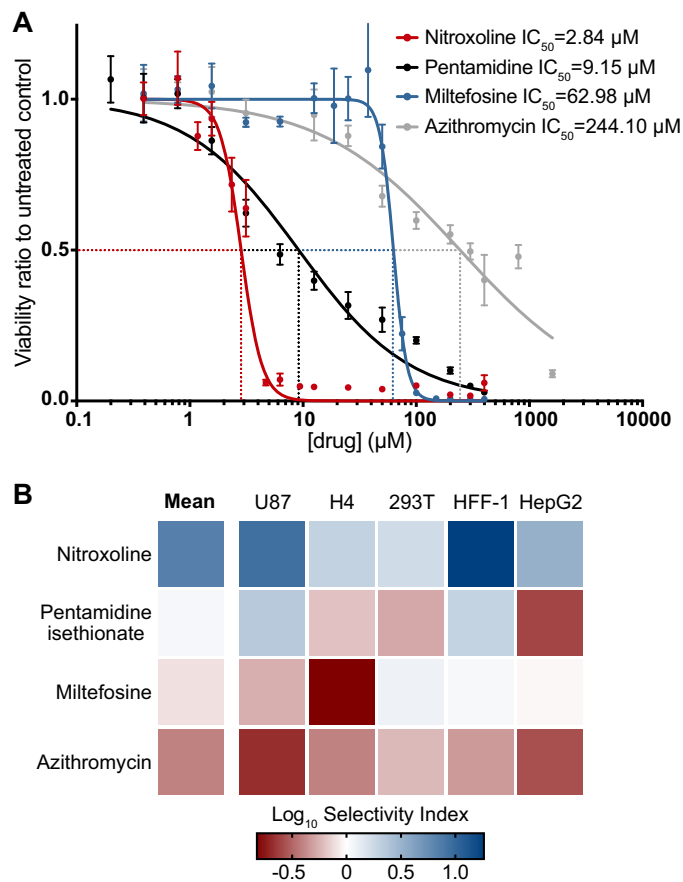


**Figure 4.3. Comparison of nitroxoline potency and selectivity to standard of care drugs.** Potency and selectivity for inhibition of *B. mandrillaris* viability by nitroxoline, pentamidine isethionate, miltefosine, and azithromycin. (A) Dose-response curves show the effect of nitroxoline (red), pentamidine isethionate (black), miltefosine (blue), and azithromycin (gray) on the viability of *B. mandrillaris* trophozoite populations following 72 h of treatment. Data points represent means and standard errors of results from at least three independent biological replicates. Nitroxoline was the most potent inhibitor of *B. mandrillaris* viability, with an  $\text{IC}_{50}$  of 2.84  $\mu\text{M}$ . (B) Heat map showing the  $\text{Log}_{10}$  selectivity index (human cell  $\text{CC}_{50}/B. mandrillaris \text{IC}_{50}$ ) for nitroxoline, pentamidine, isethionate, miltefosine, and azithromycin calculated from the ratio of human cell  $\text{CC}_{50}$  to *B. mandrillaris*  $\text{IC}_{50}$ . Nitroxoline exhibited the greatest mean  $\text{Log}_{10}$  selectivity index at 0.832 and was the only drug with a positive  $\text{Log}_{10}$  selectivity index (comparing *B. mandrillaris* inhibition to the results from all cell lines tested).

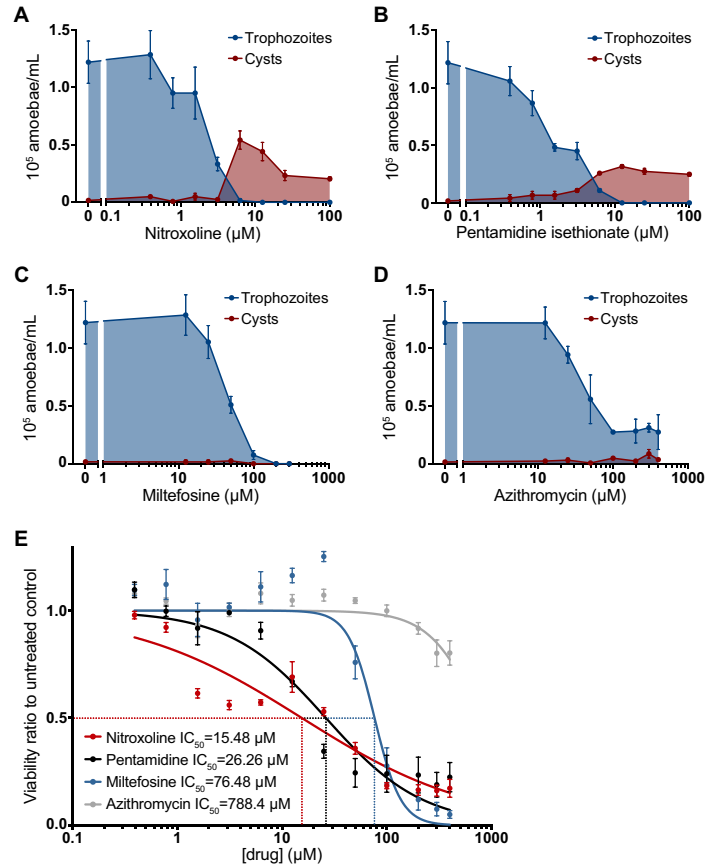


**Figure 4.4. Drug-induced encystment and killing of *B. mandrillaris* cysts.** Relationship of drug treatment to *B. mandrillaris* encystment. (A to D) Changes in the number of trophozoites (blue) and cysts (red) in *B. mandrillaris* populations following 72 h of treatment with various concentrations of nitroxoline (A), pentamidine isethionate (B), miltefosine (C), and azithromycin (D). Low micromolar concentrations of nitroxoline and pentamidine isethionate caused an increase in the total number of cysts observed in *B. mandrillaris* populations and an increase in the ratio of cysts to trophozoites. No increase in encystment was observed in *B. mandrillaris* populations treated with miltefosine or azithromycin. (E) Dose-response curve showing the effect of nitroxoline (red), pentamidine isethionate (black), miltefosine (blue), and azithromycin (gray) on the viability of preformed *B. mandrillaris* cysts. Nitroxoline was the most potent inhibitor of cysts, with an  $\text{IC}_{50}$  of  $15.48 \mu\text{M}$ . Cysts were substantially less sensitive than trophozoites (Fig. 4.2A) to all drugs except for miltefosine, which had similar  $\text{IC}_{50}$  values for inhibition of both *B. mandrillaris* forms.

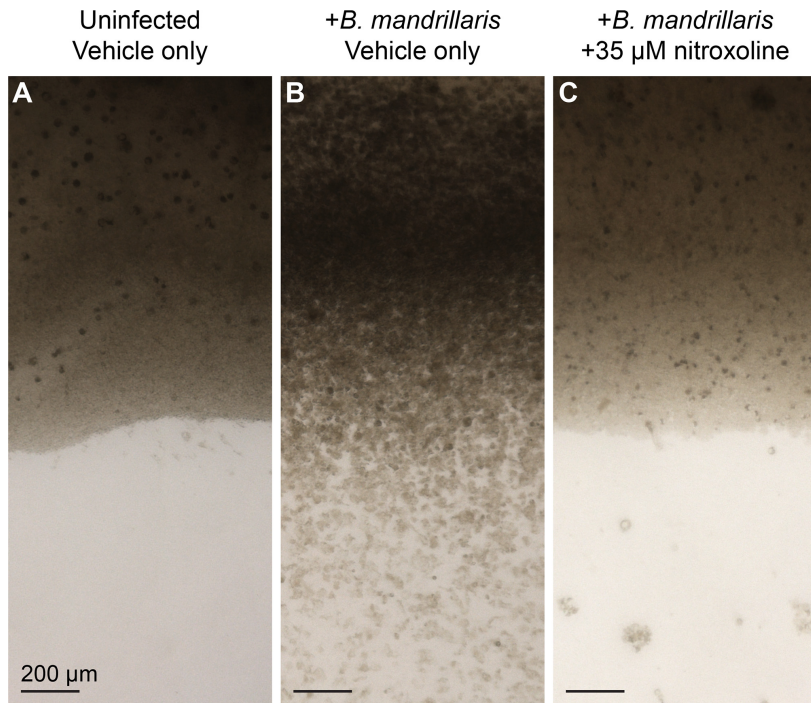


**Figure 4.5. Nitroxoline prevention of brain explant destruction by *B. mandrillaris*.** Nitroxoline prevents *B. mandrillaris*-mediated destruction of human brain tissue explants. Each panel shows an image representative of two tissues 96 h after exposure to the indicated conditions. Media were changed at 20 h postinfection to remove nitroxoline or vehicle. (A) Uninfected, untreated (vehicle only) tissues had distinct edges and maintained cell density throughout culture. (B) *B. mandrillaris*-infected, untreated (vehicle only) tissues show widespread damage, particularly at edges, where loss of cell density and disorder of tissue structure are apparent. Large numbers of *B. mandrillaris* trophozoites are observed intermixed with human cells and outside the tissue (lower half of image). (C) *B. mandrillaris*-infected tissues treated with 35 μM nitroxoline simultaneously with inoculation do not show signs of tissue damage or loss of cell density and maintain distinct edges similar to those of uninfected tissues. Clusters of *B. mandrillaris* cysts are observed outside the boundaries of the tissue.

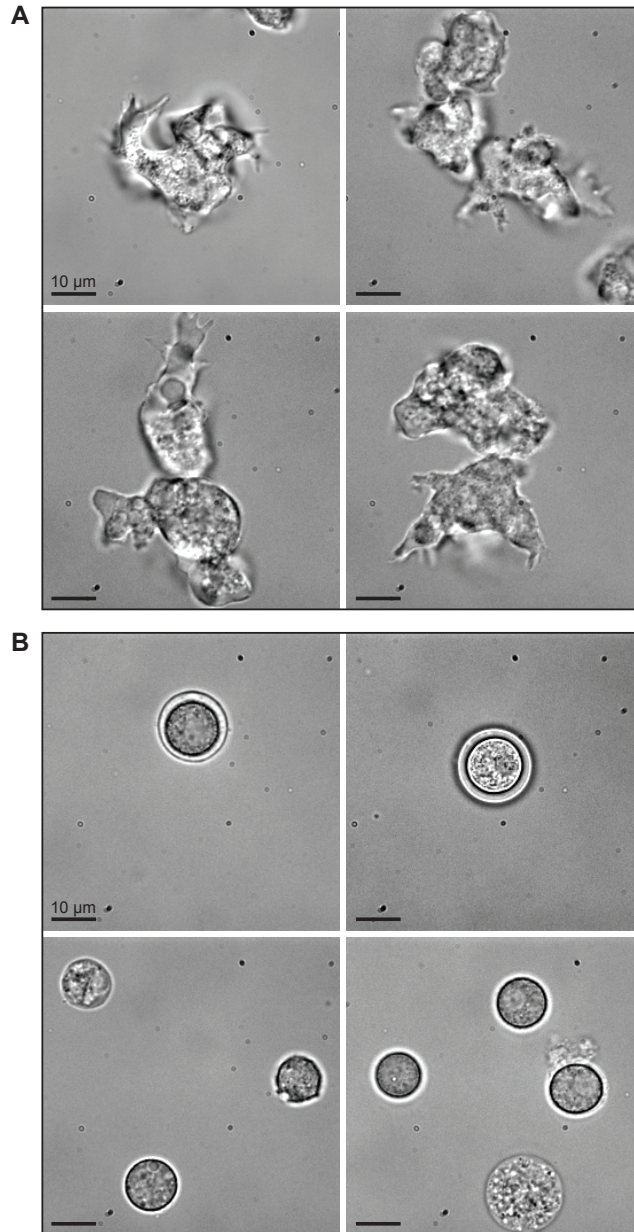


**Figure 4.6. Example brightfield images of *B. mandrillaris* trophozoites and cysts.** (A) Example images show *B. mandrillaris* trophozoites in log-phase growth. Trophozoites are pleomorphic and can be elongated or generally rounded, often with highly branched pseudopodia. (B) Example images show *B. mandrillaris* cysts induced by galactose exposure. Cysts are spherical, generally smaller in diameter than trophozoites, and can have visibly distinct layers. Some cysts show signs of vacuolization that may be indicative of cell death.

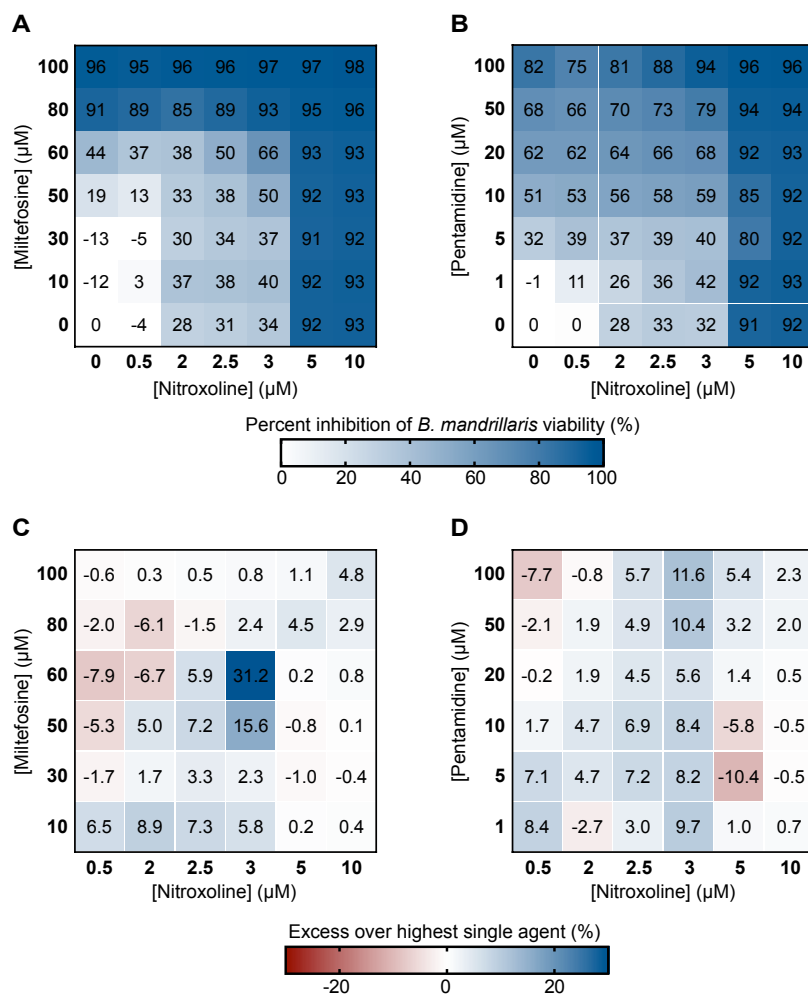


**Figure 4.7. Efficacy of nitroxoline in combination with miltefosine and pentamidine isethionate for inhibition of *B. mandrillaris*.** (A and B) Heat maps show mean treatment effect (percent inhibition of *B. mandrillaris* population viability relative to untreated control) across dose matrices for nitroxoline in combination with miltefosine (A) and pentamidine isethionate (B). The viability of *B. mandrillaris* trophozoite populations was measured following 72 hours of drug treatment in three independent replicates. (C and D) Heat maps of excess effect over highest single agent (EOHSA) showing the additional effect of dose combinations beyond the effect of the most active single agent in the combination ( $EOHSA = E_{\text{Combo}} - E_{\text{HSA}}$ ) across dose matrices for nitroxoline in combination with miltefosine (C) and pentamidine isethionate (D). For both drug pairs, mild antagonism (negative values colored in red) is observed for a small number of combinations, whereas most combinations produce a modest additive effect (positive values colored in blue). No strong antagonism or synergy is observed between nitroxoline and miltefosine or pentamidine isethionate. For reference, the reported  $C_{\text{max}}$  values for nitroxoline, miltefosine, and pentamidine are approximately  $30\mu\text{M}$ ,  $78\mu\text{M}$ , and  $2.5\mu\text{M}$ , respectively [63, 65, 79].



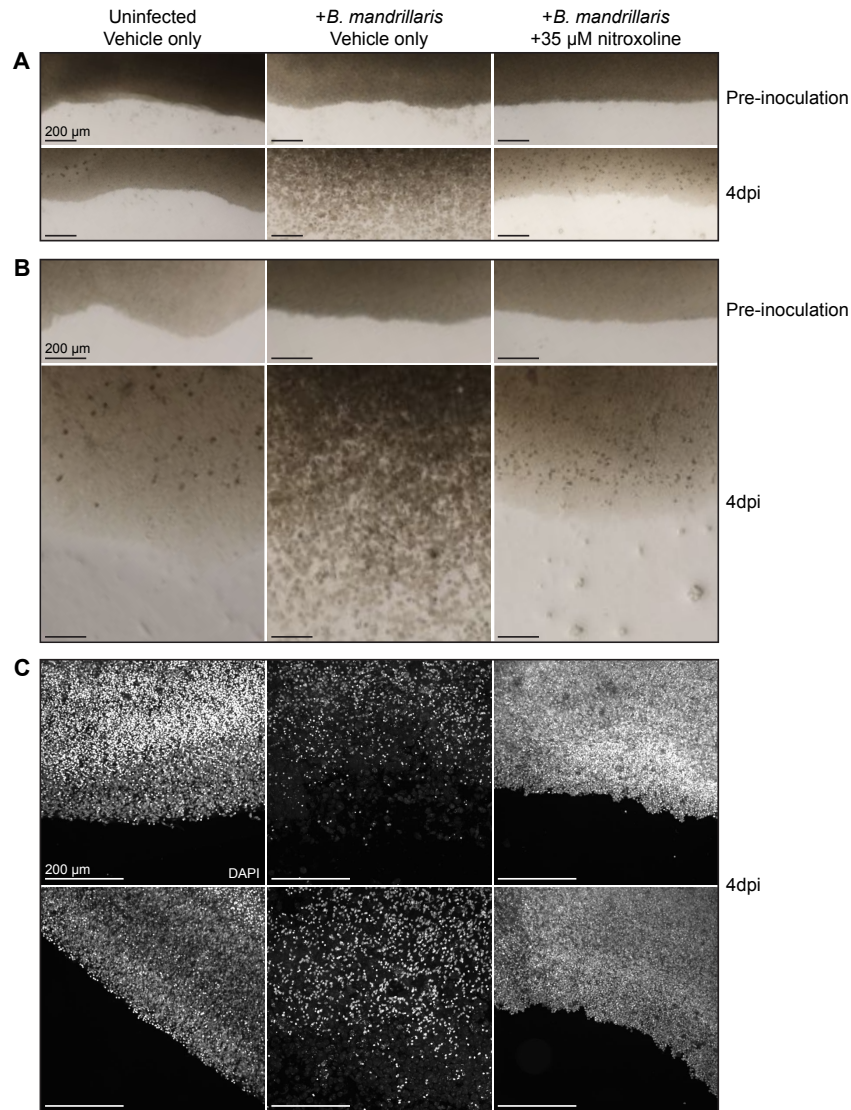


**Figure 4.8. Inhibition of *B. mandrillaris*-mediated brain tissue explant destruction in the presence of nitroxoline.** (A and B) Brightfield images representative of two biological replicates for human brain tissue explants before and after exposure to the indicated conditions. Nitroxoline or vehicle was added simultaneously with *B. mandrillaris* trophozoites and removed after 20 hours. Four days after exposure to *B. mandrillaris*, untreated tissues show wide- spread damage and loss of cell density while nitroxoline treated tissues remain intact and appear similar to uninfected tissues. Large numbers of *B. mandrillaris* trophozoites can be seen at the edges of untreated tissues, while only clusters of cysts are observed in nitroxoline-treated tissues. (C) Images representative of two biological replicates of human brain tissue explants fixed and stained with DAPI four days after exposure to the indicated conditions (two images per condi- tion). The number of host cell nuclei is dramatically reduced in untreated, *B. mandrillaris*-infected tissues compared to uninfected tissues, whereas *B. mandrillaris*-infected tissues treated with nitroxoline show no apparent loss of nuclei.

**Table 4.1. Recrudescence time of active *B. mandrillaris* following drug treatment.**

Treatment	Mean no. of days for host cell clearance $\pm$ SE
Vehicle only	
0.28% (vol/vol) DMSO	1.33 $\pm$ 0.33
1.12% (vol/vol) water	1.67 $\pm$ 0.67
Nitroxoline (in DMSO)	
3.5 $\mu$ M	15.33 $\pm$ 0.67
7 $\mu$ M	19 $\pm$ 0.58
14 $\mu$ M	22 $\pm$ 2.08
28 $\mu$ M	NRT <sup>a</sup>
Pentamidine isethionate (in water)	
3.5 $\mu$ M	1.33 $\pm$ 0.33
7 $\mu$ M	7 $\pm$ 1.15
14 $\mu$ M	13 $\pm$ 2.51
28 $\mu$ M	15.33 $\pm$ 2.56
56 $\mu$ M	16 $\pm$ 2
Miltefosine	
28 $\mu$ M	1.5 $\pm$ 0.33
56 $\mu$ M	3.5 $\pm$ 2.64
84 $\mu$ M	>28 <sup>b</sup>
112 $\mu$ M	NRT <sup>a</sup>

<sup>a</sup>NRT, no recovery of trophozoites or host cell destruction observed through 28 days.

<sup>b</sup>Incomplete recovery of trophozoites and destruction of host cells on day 28.

## Chapter 4 References

1. Schuster FL, Yagi S, Gavali S, Michelson D, Raghavan R, Blomquist I, Glastonbury C, Bollen AW, Scharnhorst D, Reed SL, Kuriyama S, Visvesvara GS, Glaser CA. 2009. Under the radar: *Balamuthia* amoebic encephalitis. *Clin Infect Dis* 48:879–887. doi:10.1086/597260.
2. Visvesvara GS, Moura H, Schuster FL. 2007. Pathogenic and opportunistic free-living amoebae: *Acanthamoeba* spp., *Balamuthia mandrillaris*, *Naegleria fowleri*, and *Sappinia diploidea*. *FEMS Immunol Med Microbiol* 50:1–26. doi:10.1111/j.1574-695X.2007.00232.x.
3. Visvesvara GS. 2011. *Pathogenic and Opportunistic Free-Living Amebae Manual of Clinical Microbiology*, 10th ed American Society of Microbiology, Washington, DC.
4. Bravo FG, Alvarez PJ, Gotuzzo E. 2011. *Balamuthia mandrillaris* infection of the skin and central nervous system: an emerging disease of concern to many specialties in medicine. *Curr Opin Infect Dis* 24:112–117. doi:10.1097/QCO.0b013e3283428d1e.
5. Lehmer LM, Ulibarri GE, Ragsdale BD, Kunkle J. 2017. Cutaneous *Balamuthia mandrillaris* infection as a precursor to *Balamuthia* amoebic encephalitis (BAE) in a healthy 84-year-old Californian. *Dermatol Online J* 23.
6. Chang OH, Liu F, Knopp E, Muehlenbachs A, Cope JR, Ali I, Thompson R, George E. 2016. Centrofacial Balamuthiasis: case report of a rare cutaneous amoebic infection. *J Cutan Pathol* 43:892–897. doi:10.1111/cup.12748.
7. Bodi I, Dutt N, Hampton T, Akbar N. 2008. Fatal granulomatous amoebic meningoencephalitis due to *Balamuthia mandrillaris*. *Pathol Res Pract* 204:925–928. doi:10.1016/j.prp.2008.06.005.
8. Wilson MR, Shanbhag NM, Reid MJ, Singhal NS, Gelfand JM, Sample HA, Benkli B, O'Donovan BD, Ali IKM, Keating MK, Dunnebacke TH, Wood MD, Bollen A, DeRisi JL.

2015. Diagnosing *Balamuthia mandrillaris* encephalitis with metagenomic deep sequencing. *Ann Neurol* 78:722–730. doi:10.1002/ana.24499.
9. da Rocha-Azevedo B, Tanowitz HB, Marciano-Cabral F. 2009. Diagnosis of infections caused by pathogenic free-living amoebae. *Interdiscip Perspect Infect Dis* 2009:251406. doi:10.1155/2009/251406.
10. Cabello-Vílchez AM, Reyes-Batlle M, Montalbán-Sandoval E, Martín-Navarro CM, López-Arencibia A, Elias-Letts R, Guerra H, Gotuzzo E, Martínez-Carretero E, Piñero JE, Maciver SK, Valladares B, Lorenzo-Morales J. 2014. The isolation of *Balamuthia mandrillaris* from environmental sources from Peru. *Parasitol Res* 113:2509–2513. doi:10.1007/s00436-014-3900-2.
11. Dunnebacke TH, Schuster FL, Yagi S, Booton GC. 2004. *Balamuthia mandrillaris* from soil samples. *Microbiology* 150:2837–2842. doi:10.1099/mic.0.27218-0.
12. Lares-Jiménez LF, Booton GC, Lares-Villa F, Velázquez-Contreras CA, Fuerst PA. 2014. Genetic analysis among environmental strains of *Balamuthia mandrillaris* recovered from an artificial lagoon and from soil in Sonora, Mexico. *Exp Parasitol* 145:S57–S61. doi:10.1016/j.exppara.2014.07.007.
13. Latifi AR, Niyiyati M, Lorenzo-Morales J, Haghghi A, Seyyed Tabaei SJ, Lasjerdi Z. 2016. Presence of *Balamuthia mandrillaris* in hot springs from Mazandaran province, northern Iran. *Epidemiol Infect* 144:2456–2461. doi:10.1017/S095026881600073X.
14. Niyiyati M, Lorenzo-Morales J, Rezaeian M, Martín-Navarro CM, Haghi AM, Maciver SK, Valladares B. 2009. Isolation of *Balamuthia mandrillaris* from urban dust, free of known infectious involvement. *Parasitol Res* 106:279–281. doi:10.1007/s00436-009-1592-9.

15. Schuster FL, Dunnebacke TH, Booton GC, Yagi S, Kohlmeier CK, Glaser C, Vugia D, Bakardjiev A, Azimi P, Maddux-Gonzalez M, Martinez AJ, Visvesvara GS. 2003. Environmental isolation of *Balamuthia mandrillaris* associated with a case of amebic encephalitis. *J Clin Microbiol* 41:3175–3180. doi:10.1128/JCM.41.7.3175-3180.2003.
16. Saburi E, Rajaii T, Behdari A, Kohansal MH, Vazini H. 2017. Free-living amoebae in the water resources of Iran: a systematic review. *J Parasit Dis* 41:919–928. doi:10.1007/s12639-017-0950-2.
17. Taravaud A, Ali M, Lafosse B, Nicolas V, Féliers C, Thibert S, Lévi Y, Loiseau PM, Pomel S. 2018. Enrichment of free-living amoebae in biofilms developed at upper water levels in drinking water storage towers: an inter- and intra-seasonal study. *Sci Total Environ* 633:157–166. doi:10.1016/j.scitotenv.2018.03.178.
18. Baquero RA, Reyes-Batlle M, Nicola GG, Martín-Navarro CM, López-Arencibia A, Guillermo Esteban J, Valladares B, Martínez-Carretero E, Piñero JE, Lorenzo-Morales J. 2014. Presence of potentially pathogenic free-living amoebae strains from well water samples in Guinea-Bissau. *Pathog Glob Health* 108:206–211. doi:10.1179/2047773214Y.0000000143.
19. Schafer KR, Shah N, Almira-Suarez MI, Reese JM, Hoke GM, Mandell JW, Roy SL, Visvesvara G. 2015. Disseminated *Balamuthia mandrillaris* infection. *J Clin Microbiol* 53:3072–3076. doi:10.1128/JCM.01549-15.
20. van der Beek NA, van Tienen C, de Haan JE, Roelfsema J, Wismans PJ, van Genderen PJJ, Tanghe HL, Verdijk RM, Titulaer MJ, van Hellemond JJ. 2015. Fatal *Balamuthia mandrillaris* meningoencephalitis in the Netherlands after travel to The Gambia. *Emerg Infect Dis* 21:896–898. doi:10.3201/eid2105.141325.

21. Shirabe T, Monobe Y, Visvesvara GS. 2002. An autopsy case of amebic meningoencephalitis. The first Japanese case caused by *Balamuthia mandrillaris*. *Neuropathology* 22:213–217. doi:10.1046/j.1440-1789.2002.00444.x.
22. Sangruchi T, Martinez AJ, Visvesvara GS. 1994. Spontaneous granulomatous amebic encephalitis: report of four cases from Thailand. *Southeast Asian J Trop Med Public Health* 25:309–313.
23. Tavares M, Correia da Costa JM, Carpenter SS, Santos LA, Afonso C, Aguiar A, Pereira J, Cardoso AI, Schuster FL, Yagi S, Sriram R, Visvesvara GS. 2006. Diagnosis of first case of *Balamuthia* amoebic encephalitis in Portugal by immunofluorescence and PCR. *J Clin Microbiol* 44:2660–2663. doi:10.1128/JCM.00479-06.
24. Kodet R, Nohýnková E, Tichý M, Soukup J, Visvesvara GS. 1998. Amebic encephalitis caused by *Balamuthia mandrillaris* in a Czech child: description of the first case from Europe. *Pathol Res Pract* 194:423–429. doi:10.1016/S0344-0338(98)80033-2.
25. Deol I, Robledo L, Meza A, Visvesvara GS, Andrews RJ. 2000. Encephalitis due to a free-living amoeba (*Balamuthia mandrillaris*): case report with literature review. *Surg Neurol* 53:611–616. doi:10.1016/S0090-3019(00)00232-9.
26. Riestra-Castaneda JM, Riestra-Castaneda R, Gonzalez-Garrido AA, Moreno PP, Martinez AJ, Visvesvara GS, Careaga FJ, Alba JLO, de Cornejo SG. 1997. Granulomatous amebic encephalitis Due to *Balamuthia mandrillaris* (Leptomyxiidae): report of four cases from Mexico. *Am J Trop Med Hyg* 56:603–607. doi:10.4269/ajtmh.1997.56.603.
27. Galarza M, Cuccia V, Sosa FP, Monges JA. 2002. Pediatric granulomatous cerebral amebiasis: a delayed diagnosis. *Pediatr Neurol* 26:153–156. doi:10.1016/S0887-8994(01)00360-5.

28. Hill CP, Damodaran O, Walsh P, Jevon GP, Blyth CC. 2011. *Balamuthia* amoebic meningoencephalitis and mycotic aneurysms in an infant. *Pediatr Neurol* 45:45–48. doi:10.1016/j.pediatrneurol.2011.05.003.
29. Moriarty P, Burke C, McCrossin D, Campbell R, Cherian S, Shahab MS, Visvesvara GS, Nourse C. 2014. *Balamuthia mandrillaris* encephalitis: survival of a child with severe meningoencephalitis and review of the literature. *J Pediatr Infect Dis Soc* 3:e4–e9. doi:10.1093/jpids/pit033.
30. Krasaelap A, Prechawit S, Chansaenroj J, Punyahotra P, Puthanakit T, Chomtho K, Shuangshoti S, Amornfa J, Poovorawan Y. 2013. Fatal *Balamuthia* amoebic encephalitis in a healthy child: a case report with review of survival cases. *Korean J Parasitol* 51:335–341. doi:10.3347/kjp.2013.51.3.335.
31. Bravo FG, Seas C. 2012. *Balamuthia Mandrillaris* amoebic encephalitis: an emerging parasitic infection. *Curr Infect Dis Rep* 14:391–396. doi:10.1007/s11908-012-0266-4.
32. Diaz JH. 2011. The public health threat from *Balamuthia mandrillaris* in the southern United States. *J La State Med Soc* 163:197–204.
33. Centers for Disease Control and Prevention (CDC). 2008. *Balamuthia* amoebic encephalitis—California, 1999–2007. *MMWR Morb Mortal Wkly Rep* 57:768–771.
34. Khurana S, Hallur V, Goyal MK, Sehgal R, Radotra BD. 2015. Emergence of *Balamuthia mandrillaris* meningoencephalitis in India. *Indian J Med Microbiol* 33:298–300. doi:10.4103/0255-0857.154887.
35. Cabello-Vílchez AM, Rodríguez-Zaragoza S, Piñero J, Valladares B, Lorenzo-Morales J. 2014. *Balamuthia mandrillaris* in South America: an emerging potential hidden pathogen in Perú. *Exp Parasitol* 145:S10–S19. doi:10.1016/j.exppara.2014.05.007.

36. Martinez AJ, Visvesvara GS. 1997. Free-living, amphizoic and opportunistic amebas. *Brain Pathol* 7:583–598. doi:10.1111/j.1750-3639.1997.tb01076.x.
37. Farnon EC, Kokko KE, Budge PJ, Mbaeyi C, Lutterloh EC, Qvarnstrom Y, da Silva AJ, Shieh W-J, Roy SL, Paddock CD, Sriram R, Zaki SR, Visvesvara GS, Kuehnert MJ, Weiss J, Komatsu K, Manch R, Ramos A, Echeverria L, Moore A, Zakowski P, Kittleson M, Kobashigawa J, Yoder J, Beach M, Mahle W, Kanter K, Geraghty P, Navarro E, Hahn C, Fujita S, Stinson J, Trachtenberg J, Byers P, Cheung M, Jie T, Kaplan B, Gruessner R, Bracamonte E, Viscusi C, Gonzalez-Peralta R, Lawrence R, Fratkin J, Butt F. 2016. Transmission of *Balamuthia mandrillaris* by organ transplantation. *Clin Infect Dis* 63:878–888. doi:10.1093/cid/ciw422.
38. Gupte AA, Hocevar SN, Lea AS, Kulkarni RD, Schain DC, Casey MJ, Zendejas-Ruiz IR, Chung WK, Mbaeyi C, Roy SL, Visvesvara GS, da Silva AJ, Tallaj J, Eckhoff D, Baddley JW. 2014. Transmission of *Balamuthia mandrillaris* through solid organ transplantation: utility of organ recipient serology to guide clinical management. *Am J Transplant* 14:1417–1424. doi:10.1111/ajt.12726.
39. Qvarnstrom Y, da Silva AJ, Schuster FL, Gelman BB, Visvesvara GS. 2009. Molecular confirmation of *Sappinia pedata* as a causative agent of amoebic encephalitis. *J Infect Dis* 199:1139–1142. doi:10.1086/597473.
40. Adl SM, Simpson AGB, Farmer MA, Andersen RA, Anderson OR, Barta JR, Bowser SS, Brugerolle G, Fensome RA, Fredericq S, James TY, Karpov S, Kugrens P, Krug J, Lane CE, Lewis LA, Lodge J, Lynn DH, Mann DG, McCourt RM, Mendoza L, Moestrup O, Mozley-Standridge SE, Nerad TA, Shearer CA, Smirnov AV, Spiegel FW, Taylor MFJR. 2005. The



- new higher level classification of eukaryotes with emphasis on the taxonomy of protists. *J Eukaryot Microbiol* 52:399–451. doi:10.1111/j.1550-7408.2005.00053.x.
41. Siddiqui R, Ali IKM, Cope JR, Khan NA. 2016. Biology and pathogenesis of *Naegleria fowleri*. *Acta Trop* 164:375–394. doi:10.1016/j.actatropica.2016.09.009.
42. Ahmad AF, Heaselgrave W, Andrew PW, Kilvington S. 2013. The in vitro efficacy of antimicrobial agents against the pathogenic free-living amoeba *Balamuthia mandrillaris*. *J Eukaryot Microbiol* 60:539–543. doi:10.1111/jeu.12062.
43. Turner NA, Russell AD, Furr JR, Lloyd D. 2000. Emergence of resistance to biocides during differentiation of *Acanthamoeba castellanii*. *J Antimicrob Chemother* 46:27–34. doi:10.1093/jac/46.1.27.
44. Varga JH, Wolf TC, Jensen HG, Parmley VC, Rowsey JJ. 1993. Combined treatment of *Acanthamoeba* keratitis with propamidine, neomycin, and polyhexamethylene biguanide. *Am J Ophthalmol* 115:466–470. doi:10.1016/S0002-9394(14)74448-4.
45. Siddiqui R, Khan NA. 2015. *Balamuthia mandrillaris*: morphology, biology, and virulence. *Trop Parasitol* 5:15–22. doi:10.4103/2229-5070.149888.
46. Schuster FL, Visvesvara GS. 1996. Axenic growth and drug sensitivity studies of *Balamuthia mandrillaris*, an agent of amebic meningoencephalitis in humans and other animals. *J Clin Microbiol* 34:385–388.
47. González-Robles A, Lares-Villa F, Lares-Jiménez LF, Omaña-Molina M, Salazar-Villatoro L, Martínez-Palomo A. 2015. *Balamuthia mandrillaris*: further morphological observations of trophozoites by light, scanning and transmission electron microscopy. *Exp Parasitol* 157:150–155. doi:10.1016/j.exppara.2015.08.011.

48. Siddiqui R, Ortega-Rivas A, Khan NA. 2008. *Balamuthia mandrillaris* resistance to hostile conditions. *J Med Microbiol* 57:428–431. doi:10.1099/jmm.0.47694-0.
49. Aksozek A, McClellan K, Howard K, Niederkorn JY, Alizadeh H. 2002. Resistance of *Acanthamoeba castellanii* cysts to physical, chemical, and radiological conditions. *J Parasitol* 88:621–623. doi:10.1645/0022-3395(2002)088[0621:ROACCT]2.0.CO;2.
50. Fouque E, Trouilhé M-C, Thomas V, Hartemann P, Rodier M-H, Hécharde Y. 2012. Cellular, biochemical, and molecular changes during encystment of free-living amoebae. *Eukaryot Cell* 11:382–387. doi:10.1128/EC.05301-11.
51. Schuster FL, Guglielmo BJ, Visvesvara GS. 2006. In-vitro activity of miltefosine and voriconazole on clinical isolates of free-living amebas: *Balamuthia mandrillaris*, *Acanthamoeba* spp., and *Naegleria fowleri*. *J Eukaryot Microbiol* 53:121–126. doi:10.1111/j.1550-7408.2005.00082.x.
52. Perez MT, Bush LM. 2007. Fatal amebic encephalitis caused by *Balamuthia mandrillaris* in an immunocompetent host: a clinicopathological review of pathogenic free-living amoebae in human hosts. *Ann Diagn Pathol* 11:440–447. doi:10.1016/j.anndiagpath.2006.04.003.]
53. Centers for Disease Control and Prevention (CDC). 2017. Treatment | Balamuthia | Parasites. Centers for Disease Control and Prevention, Atlanta, GA.
54. Deetz TR, Sawyer MH, Billman G, Schuster FL, Visvesvara GS. 2003. Successful treatment of *Balamuthia* amoebic encephalitis: presentation of 2 cases. *Clin Infect Dis* 37:1304–1312. doi:10.1086/379020.
55. Vollmer ME, Glaser C. 2016. A *Balamuthia* survivor. *JMM Case Rep* 3:e005031. doi:10.1099/jmmcr.0.005031.

56. Jung S, Schelper RL, Visvesvara GS, Chang HT. 2004. *Balamuthia mandrillaris* meningoencephalitis in an immunocompetent patient: an unusual clinical course and a favorable outcome. *Arch Pathol Lab Med* 128:466–468.
57. Roy SL, Atkins JT, Gennuso R, Kofos D, Sriram RR, Dorlo TP, Hayes T, Qvarnstrom Y, Kucerova Z, Guglielmo BJ, Visvesvara GS. 2015. Assessment of blood-brain barrier penetration of miltefosine used to treat a fatal case of granulomatous amoebic encephalitis possibly caused by an unusual *Balamuthia mandrillaris* strain. *Parasitol Res* 114:4431–4439. doi:10.1007/s00436-015-4684-8.
58. Martínez DY, Seas C, Bravo F, Legua P, Ramos C, Cabello AM, Gotuzzo E. 2010. Successful treatment of *Balamuthia mandrillaris* amoebic infection with extensive neurological and cutaneous involvement. *Clin Infect Dis* 51:e7–e11. doi:10.1086/653609.
59. Doyle JS, Campbell E, Fuller A, Spelman DW, Cameron R, Malham G, Gin D, Lewin SR. 2011. *Balamuthia mandrillaris* brain abscess successfully treated with complete surgical excision and prolonged combination antimicrobial
60. Prasad K, Bhatia R, Srivastava MVP, Pardasani V, Garg A, Rishi A. 2008. Fatal subacute necrotising brainstem encephalitis in a young man due to a rare parasitic (*Balamuthia*) infection. *Pract Neurol* 8:112–117. doi:10.1136/jnnp.2007.142547.
61. Pritzker AS, Kim BK, Agrawal D, Southern PM, Pandya AG. 2004. Fatal granulomatous amoebic encephalitis caused by *Balamuthia mandrillaris* presenting as a skin lesion. *J Am Acad Dermatol* 50:S38–S41. doi:10.1016/S0190.
62. Bakardjiev A, Azimi PH, Ashouri N, Ascher DP, Janner D, Schuster FL, Visvesvara GS, Glaser C. 2003. Amoebic encephalitis caused by *Balamuthia mandrillaris*: report of four cases. *Pediatr Infect Dis J* 22:447–453. doi:10.1097/01.inf.0000066540.18671.f8.

63. Bergogne-Berezin E, Berthelot G, Muller-Serieys C. 1987. Present status of nitroxoline. *Pathol Biol (Paris)* 35:873–878.
64. Mrhar A, Kopitar Z, Kozjek F, Presl V, Karba R. 1979. Clinical pharmacokinetics of nitroxoline. *Int J Clin Pharmacol Biopharm* 17:476–481.
65. Sorel RH, Snelleman C, Hulshoff A. 1981. High-performance liquid chromatographic analysis of nitroxoline in plasma and urine. *J Chromatogr* 222:241–248. doi:10.1016/S0378-4347(00)81056-7.
66. Sobke A, Klinger M, Hermann B, Sachse S, Nietzsche S, Makarewicz O, Keller PM, Pfister W, Straube E. 2012. The urinary antibiotic 5-nitro-8-hydroxyquinoline (nitroxoline) reduces the formation and induces the dispersal of *Pseudomonas aeruginosa* biofilms by chelation of iron and zinc. *Antimicrob Agents Chemother* 56:6021–6025. doi:10.1128/AAC.01484-12.
67. Prachayasittikul V, Prachayasittikul S, Ruchirawat S, Prachayasittikul V. 2013. 8-Hydroxyquinolines: a review of their metal chelating properties and medicinal applications. *Drug Des Devel Ther* 7:1157–1178. doi:10.2147/DDDT.S49763.
68. Lee X, Reimann C, Greub G, Sufrin J, Croxatto A. 2012. The *Pseudomonas aeruginosa* toxin L-2-amino-4-methoxy-trans-3-butenoic acid inhibits growth and induces encystment in *Acanthamoeba castellanii*. *Microbes Infect* 14:268–272. doi:10.1016/j.micinf.2011.10.004.
69. Bando Y, Takahashi T, Uehara H, Kagegi T, Nagahiro S, Izumi K. 2012. Autopsy case of amebic granulomatous meningoencephalitis caused by *Balamuthia mandrillaris* in Japan. *Pathol Int* 62:418–423. doi:10.1111/j.1440-1827.2012.02816.x.
70. Naber KG, Niggemann H, Stein G, Stein G. 2014. Review of the literature and individual patients' data meta-analysis on efficacy and tolerance of nitroxoline in the treatment of

- uncomplicated urinary tract infections. *BMC Infect Dis* 14:628. doi:10.1186/s12879-014-0628-7.
71. Lazovic J, Guo L, Nakashima J, Mirsadraei L, Yong W, Kim HJ, Ellingson B, Wu H, Pope WB. 2015. Nitroxoline induces apoptosis and slows glioma growth in vivo. *Neuro Oncol* 17:53–62. doi:10.1093/neuonc/nou139.
72. Seidel JS, Harmatz P, Visvesvara GS, Cohen A, Edwards J, Turner J. 1982. Successful treatment of primary amebic meningoencephalitis. *N Engl J Med* 306:346–348. doi:10.1056/NEJM198202113060607.
73. Lares-Jiménez LF, Gámez-Gutiérrez RA, Lares-Villa F. 2015. Novel culture medium for the axenic growth of *Balamuthia mandrillaris*. *Diagn Microbiol Infect Dis* 82:286–288. doi:10.1016/j.diagmicrobio.2015.04.007.
74. Siddiqui R, Jarroll EL, Khan NA. 2010. *Balamuthia mandrillaris*: role of galactose in encystment and identification of potential inhibitory targets. *Exp Parasitol* 126:22–27. doi:10.1016/j.exppara.2009.09.013.
75. Brideau C, Gunter B, Pikounis B, Liaw A. 2003. Improved statistical methods for hit selection in high-throughput screening. *J Biomol Screen* 8:634–647. doi:10.1177/1087057103258285.
76. Borisy AA, Elliott PJ, Hurst NW, Lee MS, Lehar J, Price ER, Serbedzija G, Zimmermann GR, Foley MA, Stockwell BR, Keith CT. 2003. Systematic discovery of multicomponent therapeutics. *Proc Natl Acad Sci U S A* 100:7977–7982. doi:10.1073/pnas.1337088100.
77. Geary N. 2013. Understanding synergy. *Am J Physiol Endocrinol Metab* 304:E237–E253. doi:10.1152/ajpendo.00308.2012.
78. Schindelin J, Arganda-Carreras I, Frise E, Kaynig V, Longair M, Pietzsch T, Preibisch S, Rueden C, Saalfeld S, Schmid B, Tinevez J-Y, White DJ, Hartenstein V, Eliceiri K, Tomancak

P, Cardona A. 2012. Fiji: an open-source platform for biological-image analysis. *Nat Methods* 9:676–682. doi:10.1038/nmeth.2019.

79. Kip AE, Schellens JHM, Beijnen JH, Dorlo TPC. Clinical Pharmacokinetics of Systemically Administered Antileishmanial Drugs. *Clin Pharmacokinet*. 2018; 57(2):151–176.

## **Chapter 5:**

### **Identification and characterization of clioquinol as a potent inhibitor of *Candida auris***

The work presented in this chapter includes contributions from:

Dr. Matthew Lohse, Sophia Levan, Dr. Naomi Ziv, Dr. Craig Ennis, Dr. Clarissa Nobile, Dr.

Joseph DeRisi, and Dr. Alexander Johnson

## ***Abstract***

The rapidly emerging fungal pathogen *C. auris* represents a growing threat to hospitalized patients due to its frequent resistance to multiple classes of antifungal drugs and its ability to spread and resist decontamination in health care settings. We screened two libraries with 1990 clinically-approved and late stage investigational compounds for the potential to be repurposed as antifungal drugs targeting *C. auris*. From the 89 candidate compounds identified in the initial screen, we identified five FDA-approved compounds with inhibitory concentrations under 10  $\mu$ M and at least an order of magnitude lower than their toxicity to three human cell lines. These hits include the dihalogenated 8-hydroxyquinolines broxyquinoline, chloroxine, and clioquinol. A structure-activity relationship study of 32 quinoline derivatives found that 8-hydroxyquinolines, especially those dihalogenated at the C5 and C7 positions, were the most effective quinoline inhibitors of *C. auris*. Consistent with previous studies in *Saccharomyces cerevisiae*, we show that these compounds are fungistatic, rather than fungicidal, and inhibit *C. auris* via chelation of divalent metal ions. *C. auris* developed only 2- to 5- fold resistance to clioquinol in an extended experimental evolution assay; the mechanism of resistance involved mutations in the transcriptional regulator Cap1 (causing up-regulation of the drug transporter Mdr1) and the drug transporter Cdr1. These mutations had only modest effects on resistance to traditional antifungal agents and the Cdr1 mutation left *C. auris* more sensitive to posaconazole; this raises the possibility that a combination treatment involving an 8-hydroxyquinoline and posaconazole might prevent *C. auris* from developing resistance to this established antifungal agent.



## ***Introduction***

*Candida auris* is a rapidly emerging multi-drug resistant pathogen responsible for invasive fungal infections in hospitalized patients. Similar to other *Candida* species, *C. auris* predominately induces candidemia in the immunocompromised and those subjected to prolonged hospitalization in ICU wards or long-term care facilities. In untreated patients, invasive candidemia has a mortality rate of approximately 60%, which only improves to approximately 40% with antifungal therapy [1,2]. The threat of *C. auris* is compounded by persistent colonization in previously exposed patients and pervasive spread through hospital wards despite multiple rounds of decontamination [3,4]. Furthermore, *C. auris* can spread through long term care and skilled nursing facilities with older and ventilator-dependent patients especially at risk of developing infections; several *C. auris* outbreaks associated with COVID-19 treatment units have been reported [5–9]. This pervasive colonization, in combination with frequent resistance to one, two, or even all three major classes of antifungals, cements *C. auris* as a growing threat to our most vulnerable patients (CDC) [10].

*C. auris* represents a relatively new threat to hospitalized patients. It was first reported in Japan in 2009 [11], and was subsequently found to have five clades (I-V) that localize to distinct geographic locations [12,13]. The five clades, which are geographically represented by South Asia (I), East Asia (II), Africa (III), South America (IV), and Iran (V), have unique mechanisms of antifungal resistance and two distinct mating types [12–15]. Clades I, III, IV, and V have been linked to outbreaks of invasive infections while Clade II is more commonly associated with ear infections [16,17]. While specific clades are predominant in much of the world, the US, Canada, UK, and Kenya have identified infections associated with a range of isolates from multiple clades [15,18–20]. Nearly all *C. auris* isolates are highly resistant to fluconazole; more than half demonstrate resistance to voriconazole; a third are resistant to amphotericin B; and some isolates

have demonstrated resistance to all three major classes of antifungal drugs [15,21–25]. Given the high mortality, limited treatment options, and growing threat to vulnerable patient populations, there is an urgent need to mobilize new antifungals to combat *C. auris*.

Several approaches have been taken to identify new antifungals effective against *C. auris* (for more detail on this topic and the current state of the antifungal drug development pipeline, see [26–32]). The most straightforward approach has focused on the evaluation of the effectiveness of the newest members of common antifungal classes (e.g. the echinocandin Rezafungin (CD101)) [33,34]. A closely related line of investigation has focused on testing the lead compound(s) from new classes of potential antifungal agents in development and/or in the clinical testing pipeline (e.g. the fungal inositol acylase inhibitor Fosmanogepix / APX001 [35–37] and the glucan synthesis inhibitor Ibrexafungerp / SCY-078 as well as the second generation Fungerp analog SCY-247 [38–42]). A broader approach, and one less dependent on existing antifungal drug development pipelines, involves screening libraries of FDA-approved compounds and/or drug like compounds in order to repurpose existing clinical compounds for use against *C. auris*. These types of screens have identified a number of promising compounds, including Ebselen, miltefosine, and alexidine dihydrochloride. Interestingly, three of these screens were conducted with the same library (the Prestwick Chemical Library with 1280 compounds) but the hits from these screens were not always concordant (49 different compounds were identified in these screens: 3 in all three, 18 in two, and 28 in only one) [43–48].

To identify potential drug repurposing candidates, our team conducted a broad primary drug screen that examined the effect of 1990 clinically-approved or late stage investigational compounds on three *C. auris* strains from the clades most associated with invasive infections (I, III, and IV). From the 89 candidate compounds identified during this preliminary screen, five

FDA-approved compounds were identified with half-maximal inhibitory concentrations (IC<sub>50</sub>) that were both less than 10 μM and at least an order of magnitude lower than their toxicity to three human cell lines. For one of these compounds, the 8-hydroxyquinoline clioquinol, a secondary screen was implemented to test for synergy or antagonism with other commonly used antifungal drugs. In addition to an investigation of mechanism of action, two *C. auris* isolates were grown for an extended period in the presence of clioquinol to identify possible determinants of resistance through whole genome sequencing and reintroduction and testing of mutants.

## **Results**

### *The hydroxyquinolines broxyquinoline, chloroxine, and clioquinol inhibit C. auris growth at sub-micromolar concentrations*

A primary screen of 1990 compounds, consisting of clinically approved drugs, late stage investigational compounds, and drug-like compounds, was performed using three strains of *C. auris* that were selected based on their range of resistance to the three main classes of antifungal agents and to represent the three clades most associated with invasive infections (Figure 5.1A). Strain AR-387 (B8441 / MLY1543) originated in Pakistan, belongs to the South Asian Clade, and is sensitive to fluconazole, caspofungin, and amphotericin B. Strain AR-386 (B11245 / MLY1542) originated in Venezuela, belongs to the South American Clade, is sensitive to both caspofungin and amphotericin B , and is resistant to fluconazole. Strain AR-384 (B11222 / MLY1540) originated in South Africa, belongs to the African Clade, is sensitive to amphotericin B , and is resistant to both fluconazole and caspofungin. Antifungal resistance to nine commonly used antifungal agents was verified for these three strains and these results are summarized in Supplemental Table 1.

These three strains were screened for growth inhibition at two concentrations (1  $\mu\text{M}$  and 10  $\mu\text{M}$ ) of drugs from a FDA-Approved Drug Library (Selleck Chemical, 1591 compounds) and the Pandemic Drug Library (Medicines for Malaria Venture, 399 compounds) (Figure 5.1A). Compounds with a B-score greater than 0.1 and greater than 50 percent inhibition ( $\text{OD}_{600}$ ) were considered hits (Figure 5.1B). Of the 89 compounds that met both of these criteria, 59 did not have known antifungal activity and 61 were not topical formulations (Figure 5.1B). The 89 hits include 10 established standard of care compounds, 48 compounds active against only two *C. auris* strains, and 32 compounds active against all three *C. auris* strains. A secondary screen was then performed to confirm the antifungal activity observed in the primary screen and to estimate the  $\text{IC}_{50}$  for these compounds (Figure 5.1C). All 89 compounds were screened at 8 concentrations ranging from 0.3 to 100  $\mu\text{M}$  against the same three strains (AR-387, AR-386, and AR-384) (Figure 5.2A). Based on the results of this secondary screen, 11 non-topical compounds were selected that did not belong to the three main known classes of antifungal drugs and that had estimated  $\text{IC}_{50}$ s less than 10  $\mu\text{M}$ . Three additional drugs (sirolimus, everolimus, temsirolimus) that met these criteria were not selected for further investigation because of their known immunosuppressive activity.

An optimal drug candidate would have antifungal activity against a wide range of *C. auris* isolates at concentrations that are not toxic to human cells. To determine if any of the 11 non-topical hits fulfilled both of these criteria,  $\text{IC}_{50}$ s were determined for 16 *Candida* strains, including 13 *C. auris* strains, covering all five clades, and one strain each of *Candida albicans*, *Candida glabrata*, and *Candida dubliniensis*. The  $\text{IC}_{50}$ s of these 11 compounds were also determined for three common human cell lines, HEK293 (kidney), HEPG2 (liver) and HFF1 (fibroblast) (Figure 5.1C). Of the 11 compounds, five had  $\text{IC}_{50}$ s that were at least 10-fold less than their lowest  $\text{IC}_{50}$  for human cells, suggesting the possibility of a wider therapeutic window (Figure 5.2B). These

five compounds included three hydroxyquinolines, broxyquinoline, chloroxine, and clioquinol, and two anti-protozoals, miltefosine and triclabendazole (Figure 5.2B). Unlike many of the traditional antifungal agents, there was minimal variation in the IC<sub>50</sub>s observed for miltefosine, broxyquinoline, chloroxine, and clioquinol across all 13 *C. auris* strains tested (Figure 5.2B). These results are broadly consistent with previous repurposing screens, which have reported effectiveness by miltefosine [45], several different hydroxyquinolines including chloroxine, and clioquinol [44–46,48,49], as well as Pentamidine (one of the six compounds that performed poorly in the human cell toxicity tests) [43,45].

#### *C. auris* develops only moderate resistance to clioquinol despite extended exposure

*C. auris* has repeatedly demonstrated a propensity for rapid acquisition of resistance when exposed to antifungal drugs. Indeed, experimental evolution has produced 30- to more than 500-fold increases in resistance to fluconazole or caspofungin in as few as two or three 48-hour passages [50–52]. To evaluate the ability of *C. auris* to develop resistance to clioquinol, and to assess the resulting determinants of resistance, two independent cultures each for two *C. auris* isolates (AR-384 and AR-390, another South Asian Clade I strain with greater resistance to fluconazole and amphotericin B than AR-387) were serially passaged 30 times (roughly 150-200 generations) in the presence of increasing concentrations of clioquinol, ranging from 0.4-0.75  $\mu$ M at the start to 2-8-4.4  $\mu$ M at the end (Figure 5.1C). One of the two AR-390 cultures is not discussed further due to cross contamination that developed early in the experiment. By the end of the drug selection, the clioquinol IC<sub>50</sub> increased 2.4- and 5.2- fold relative to parental strains (from 0.75  $\mu$ M to 1.80 $\mu$ M and from 0.29  $\mu$ M to 1.48 $\mu$ M) in the AR-384 and AR-390 backgrounds, respectively (Figures 5.3A, 5.3B). These IC<sub>50</sub> increases occurred over multiple steps, had some variation in the

rate of resistance evolution, and plateaued around passage 16 for each parallel strain (Figure 5.3A). Notably, the degree of resistance arising from more than two months of exposure to clioquinol was less than has been observed for fluconazole or caspofungin over shorter time frames. Furthermore, the clioquinol-evolved strains remained sensitive to clioquinol concentrations at least 5-fold below the minimal toxic concentrations observed for human cells.

### *C. auris* mutated *Cap1* and *Cdr1* in response to extended clioquinol exposure

The resistance of the evolved strains persisted even though these strains were regrown for several days in the absence of clioquinol before evaluating sensitivity, suggesting that resistance was linked to one or more genome mutations rather than a short-term transcriptional response to clioquinol. To test this hypothesis and determine the determinant(s) of clioquinol resistance, whole genome sequencing was performed on two single colony isolates from the endpoint of the resistance assay for each culture as well as on populations harvested from selected intermediate points. We observed premature termination mutations in the c-terminal end of the transcriptional regulator *Cap1* (B9J08\_005344 / CJ197\_005427) by the eighth passage in all three cultures (16 days growth or approximately 35 to 40 generations) (Figure 5.3A). Each mutation was distinct (E398\* in AR-390; either E441\* or a 8-bp deletion resulting in T387\* in AR-384) and were in 76 to 98% of the population sample reads at passage eight. The same *Cap1* mutations were in 96 to 98% of population sample reads and in all six single cell samples at the endpoint of the experiment. No *Cap1* mutations were observed in the DMSO treated control samples.

Sometime after the eighth passage (by passage 12 in AR-390 and between passages 8 and 31 in AR-384) distinct mutations arose in the ATP-binding cassette (ABC) drug transporter *Cdr1* (B9J08\_000164 / CJ197\_000167), in several cases in or before the N-terminal six transmembrane

region (E722\* and V704L in AR-390; K909N or Q415\* in one AR-384 culture, and Q548\* or a 8bp deletion whose resulting frame shift affected 34 different amino acids at aa343-376 before a premature stop codon at aa377 in the other AR-384 culture) (Figure 5.3A). These Cdr1 mutations were not as penetrant as the Cap1 mutations, comprising between 25 and 97% of reads in population samples and being observed in only four of the six single cell endpoint samples. No Cdr1 mutations arose in the DMSO treated control samples. We note that the apparent selective pressure to inactivate the Cdr1 drug pump suggests that hydroxyquinolines function against *C. auris*, at least in part, at the cell surface or inside the cell rather than just by chelating iron, copper, or zinc from the media; consistent with a previous report that hydroxyquinolines sequester metals in *S. cerevisiae*'s plasmid membrane [53]. We also note that, in addition to export of antifungal drugs, Cdr1 has been linked to the export of anti-cancer drugs, steroids, and fluorescent dyes as well as being involved in the translocation of phosphoglycerides from the internal to the external plasma membrane [54,55] and, as such, the hydroxyquinolines could be affecting a wide range of Cdr1-associated functions instead of or in addition to exporting drugs from the cell.

To determine whether the Cap1 or Cdr1 mutations were indeed casual for increased clioquinol resistance, the Cap1 E398\* or the Cdr1 E722\* mutations were introduced by Cas9 gene editing into the parental AR-390 or AR-387 strain backgrounds. The Cap1 E398\* mutation caused a increase in resistance of 1.7 to 1.8-fold to clioquinol in both backgrounds (Figure 5.3B). No significant difference in clioquinol IC<sub>50</sub> was observed between evolved and CRISPR engineered Cap1\* mutants in the AR-390 background, indicating a strong recapitulation of the resistance phenotype by the engineered strain. Introduction of the Cdr1 E722\* mutation did not significantly affect clioquinol resistance in AR-387 (nor did deletion of Cdr1) but did increase resistance 1.9-fold in AR-390 (Figure 5.3B). Thus, the Cap1 truncation can explain much of the clioquinol

resistance to that arose during the experimental evolution and the subsequent Cdr1 mutation might explain the smaller resistance increases observed later in the experiment.

#### *Cap1 truncation results in increased Mdr1 expression*

In *C. albicans*, Cap1 promotes expression of the major facilitator superfamily (MFS) drug transporter Mdr1 and it has been reported that C-terminal truncations of Cap1 like we observed cause a hyperactive phenotype which up-regulates Mdr1 expression and increases fluconazole resistance [56–59]. Expression of Cdr1 in both *C. albicans* and *C. auris*, on the other hand, is regulated by the transcriptional regulator Tac1/Tac1b [50,60,61]. In order to determine whether the Cap1 mutants we observed affected Mdr1 expression and whether Cdr1 expression was changing in the evolved strains, we used RT-qPCR to determine Cdr1, Cdr2, and Mdr1 transcript levels. In the AR-384 background, Mdr1 expression was up-regulated more than 50-fold by passage 8 and remained at this level at the end of the experiment (Figure 5.3C). In the AR-390 background, where expression started roughly 30-fold lower than AR-384, Mdr1 expression was up-regulated nearly 300-fold by passage 8 and over 1500-fold by the final selection passage, reaching a similar level to the evolved AR-384 strains (Figure 5.3C). In contrast to Mdr1, expression of Cdr1 and Cdr2 changed minimally during the course of the selection experiment (1.7-fold down and 1.1-fold up in AR-384, 1.4-fold down and 7-fold down in AR-390, respectively) (Figure 5.3C). We note that we profiled transcript levels in the cells in the absence of clioquinol, as such these reflect changes in the basal rather than drug induced expression of the pumps.

Transcript levels were then assessed in the mutant stains constructed in the AR-387 and AR-390 strain backgrounds, again in the absence of clioquinol. Consistent with the results for the



evolved strains, the introduction of the Cap1 E398\* mutation resulted in minimal expression change for either Cdr1 or Cdr2, but significant 150- and 390-fold increases in Mdr1 expression in the AR-387 and AR-390 strain backgrounds, respectively (Figure 5.3C). Truncation of the Cdr1 gene resulted in moderate reductions in Cdr1 expression in both backgrounds (9-fold and 3-fold down in AR-387 and AR-390, respectively), negligible changes to Cdr2 expression, and slight increases in Mdr1 expression (1.7- and 3-fold up in AR-387 and AR-390, respectively) (Figure 5.3C).

#### *Extended clioquinol exposure has modest effects on resistance to traditional antifungal agents*

The rise of Cap1 mutations in response to exposure to clioquinol could plausibly affect resistance to existing antifungal agents. Conversely, given the correlation between Cdr1 expression and azole resistance as well as reports that drugs inhibiting Cdr1 increase azole sensitivity [47,62–66], the Cdr1 mutations suggest that long term exposure to clioquinol could result in increased sensitivity to existing antifungal agents. In order to determine how long term exposure to clioquinol affected sensitivity to other drugs, the sensitivity of the evolved strains was measured with respect to a second hydroxyquinoline, broxyquinoline, as well as to the traditional antifungal agents voriconazole, posaconazole, micafungin, and amphotericin B. As expected, clioquinol resistance was associated with modest resistance to the structurally similar Broxyquinoline (Figure 5.3D). Clioquinol resistance had only subtle, if any, effect on resistance to amphotericin B and modestly increased susceptibility to micafungin (Figure 5.3D). Interestingly, although clioquinol resistance was associated in a subtle increase in resistance to voriconazole, we found that the evolved strain with truncated Cdr1 was in fact more sensitive to posaconazole (Figure 5.3D). These findings were recapitulated using the engineered strains with the Cap1 E398\* truncation (Suppl.

Table 4) (Figure 5.3D). These results suggest that mutations resulting long term exposure to clioquinol will not necessarily result in increased resistance to commonly used antifungal agents.

*Dihalogenated hydroxyquinolines inhibit C. auris via chelation of divalent metal ions.*

Three hydroxyquinolines were identified with sub-micromolar antifungal activity against *C. auris*. To evaluate the structure-activity relationship (SAR) of quinolines, the activity of 32 quinoline derivatives (31 compounds plus clioquinol) was tested against three strains of *C. auris* (AR-387, AR-384, AR-386) (Figure 5.1C). Seventeen of the compounds tested showed activity against *C. auris*. All active compounds except for one [1,10-Phenanthroline monohydrate] were hydroxyquinolines, which have a hydroxide at C8 position (Figure 5.4A). Five compounds had an  $IC_{50}$  less than  $1\mu\text{M}$ ; all five of these compounds were dihalogenated at the C5 and C7 positions; these results suggest that dihalogenated hydroxyquinolines are effective inhibitors of *C. auris* at nanomolar concentrations. Compounds with single halogen or other chemical groups at either the 5- or 7-positions generally had an  $IC_{50}$  in the 2 to 20  $\mu\text{M}$  range while a further 15 compounds without an 8-position hydroxy group lacked activity against *C. auris*. (Figure 5.4A, Supplementary Table 2). We note that these trends are largely consistent with those previously reported for halogenated hydroxyquinoline activity against several fungal species (none of which were *Candida*) [67–69].

Previous studies (including transcriptional profiling, enzyme activity assays, and cellular metal abundance quantification by inductively coupled plasma mass spectrometry) have demonstrated that *Saccharomyces cerevisiae* cells treated with clioquinol behave as if they are starved for iron, copper, and zinc. These metals are sequestered in the plasmid membrane and depleted in the cytosol of *S. cerevisiae* cells exposed to clioquinol [53,70,71]. To investigate this

effect with respect to *C. auris* and clioquinol, drug treated cells were grown in the presence of iron, copper, or zinc (Figure 5.1C). The addition of iron (either  $\text{Fe}^{2+}$  or  $\text{Fe}^{3+}$ ) or, to a lesser extent, copper to clioquinol-treated media abrogated the inhibitory effects of the drug and restored growth (Figures 5.4B, 4C). Increasing concentrations of  $\text{Cu}^{2+}$ ,  $\text{Fe}^{2+}$ , or  $\text{Fe}^{3+}$  strongly correlate with increased clioquinol  $\text{IC}_{50}$ , indicating that metal-mediated rescue of *C. auris* viability is concentration dependent (Figure 5.4C). Increasing concentrations of  $\text{Zn}^{2+}$ , on the other hand, had no effect on clioquinol  $\text{IC}_{50}$  (Figure 5.4C). Addition of iron or copper also restored growth in the presence of several other 8-hydroxyquinolines, suggesting that this family of compounds all inhibit *C. auris* by the same mechanism (Figures 5.4B, 5.4C). These effects were agnostic to the order of addition, either introducing iron to *C. auris* cells that had been pretreated for clioquinol for 21 hours or introducing metals to clioquinol-treated media prior to *C. auris* inoculation permitted growth (Figures 5.4B). While the exact mechanism by which the hydroxyquinolines inhibit *C. auris* growth remains to be determined, these experiments suggest that the inhibitory effects arise from either metal chelation or metal sequestration in the fungal plasma membrane, analogous to what has been observed in *S. cerevisiae* [53].

#### *Clioquinol is fungistatic to C. auris*

Previous reports have reached different conclusions as to whether clioquinol is fungistatic or fungicidal against *Saccharomycotina* species like *S. cerevisiae* or *C. albicans* [72,73]. The metal supplementation assay results, where addition of iron restored growth by cells exposed to clioquinol for 21 hours (Figure S1), could be consistent with either (1) clioquinol having a fungistatic effect on *C. auris* or (2) clioquinol killing only a subset of the cells present with the surviving (possibly resistant) cells growing once the metal was added. Both of these possibilities

are also consistent with the observation that clioquinol-treated *C. auris* cell growth resumed after washing with PBS and subsequent inoculation into fresh media or when clioquinol-treated *C. auris* cells were diluted into fresh media (without washing). To distinguish between these two possibilities, live/dead staining assays were performed with *C. auris* cells that were treated with clioquinol for either 2 or 22 hours. After either incubation period, the population of Clioquinol-treated *C. auris* cells resembled the live DMSO-treated cells rather than the isopropanol-killed cells, consistent with a fungistatic effect (Figure S2). Furthermore, the viability of 22 hour clioquinol-treated *C. auris* cells, as quantified by plating assays, changed little relative to DMSO-treated controls (Figure S2). As such, we conclude that clioquinol is fungistatic, rather than fungicidal, to *C. auris* (at least in the context of the 22 hour time frame examined in these assays).

*Clioquinol does not interact synergistically or antagonistically with members of the three main classes of antifungal drugs*

Several reports have linked increased azole and echinocandin sensitivity of *Candida* species, including *C. auris*, to the availability of or ability to use metals like iron or copper [74–81]. To assess the potential for clioquinol to have sensitizing effects in the context of multidrug combinations, four *C. auris* isolates were grown in the presence of amphotericin B, micafungin, or posaconazole, together with clioquinol.

**Discussion**

*C. auris* represents a growing threat to hospitalized patients due to its robust resistance to one or more of the three major classes of antifungal drugs, the propensity for sensitive *C. auris* strains to rapidly develop resistance, and its ability to spread and resist decontamination in health

care settings. We screened 1990 compounds for the potential to be repurposed as antifungals targeting *C. auris*. Among the most promising hits from this screen were the dihalogenated hydroxyquinolines broxyquinoline, chloroxine, and clioquinol.

The hydroxyquinolines, five of which had IC<sub>50</sub>s less than 1 μM and several more of which had IC<sub>50</sub>s less than 10 μM, are especially interesting candidates for repurposing for several reasons. First, we observed little variation in the IC<sub>50</sub>s of individual hydroxyquinolines across the clinical isolates tested (which included representatives of all five known clades), suggesting it is less likely that any of the known *C. auris* clades contain strains already resistant to hydroxyquinolines. Second, although the dihalogenated hydroxyquinolines were the most efficient hydroxyquinolines in our SAR screen, a wide range of chemical space in this family remain to be explored (e.g. different side groups at C2, replacing a halogen at either C5 or C7 with another active group). Third, several hydroxyquinolines have (or have had) both topical and oral forms (both forms for chloroxine and clioquinol, only an oral form for broxyquinoline) suggesting that hydroxyquinolines might be effective against both internal and skin-based infections. Finally, the hydroxyquinolines are of interest due to the limited degree to which *C. auris* developed resistance despite long term exposure. The roughly 2- to 5-fold increases observed in our experiments remain well below the minimum toxicities observed with human cells and are significantly less than the 30- to 500- fold increases reported for fluconazole or caspofungin experiments [50–52]. Furthermore, the rise of hydroxyquinoline resistance translated to only modest, if any, increases in resistance and in several cases to increased sensitivity to known antifungal agents. Given the repeated correlations observed between Cdr1 expression and resistance to azoles as well as previous studies suggesting that Cdr1 inhibitors increase sensitivity to azoles [47,62–65], the increased posaconazole sensitivity of the evolved Cdr1 truncation strains is unsurprising. The

possibility that a combination treatment involving a hydroxyquinoline and posaconazole might leave *C. auris* trapped between increasing Cdr1 expression to resist posaconazole, becoming more sensitive to the hydroxyquinoline, or decreasing Cdr1 expression to resist the hydroxyquinoline, becoming more sensitive to posaconazole, merits further examination, and, if promising *in vitro*, eventual testing in an animal model. Likewise, it would be prudent to conduct experimental evolution of *C. auris* exposed to clioquinol (or another hydroxyquinoline) in combination with a known antifungal agent (e.g. posaconazole) to make sure the combination does not inadvertently increase resistance to the known agent(s).

When considering repurposing the hydroxyquinolines as a treatment for *C. auris*, it is important to note that the oral version of clioquinol was withdrawn from usage as an anti-parasitic in the early 1970s following a report associating it with an outbreak of sub-acute myelo-optic neuropathy (SMON) in Japan [82–84]. Since that time, however, the data in the report linking SMON and Clioquinol has been questioned [85] and it has been noted that similar associations did not occur in countries with higher clioquinol usage at the time [86]. As such, there has been recent interest in using clioquinol to treat both Alzheimers Disease and cancer [82,83]. Although there might not be a strong link between Clioquinol and neurotoxicity, animal studies to validate clioquinol's effectiveness in an *in vivo* context would be warranted before moving to efficacy testing in humans (at least for internal usage).

## **Methods**

### *Drug Libraries*

Compounds for primary screening were from the Selleck FDA-Approved Drug Library (Selleck Chemical, 1591 compounds) and the Pandemic Drug Library (Medicines for Malaria Venture, 399 compounds).

### *Media*

Cells were allowed to recover from glycerol stocks for at least two days at 30°C on yeast extract peptone dextrose (YEPD) plates (2% Bacto™ peptone, 2% dextrose, 1% yeast extract, 2% Agar). Unless otherwise noted, overnight cultures for assays, recovery dilutions, and assays were performed in RPMI-1640 media (containing L-glutamine and lacking sodium bicarbonate, MP Biomedicals #0910601) supplemented with 34.5g/L MOPS (Sigma, M3183) and adjusted to pH 7.0 with Sodium Hydroxide before sterilizing with a 0.22 µm filter.

### *Strains*

A full list of strains used in this study can be found in (DETAILS). Twelve of the thirteen *C. auris* isolates used in this study were acquired from the Centers for Disease Control and Prevention's Antibiotic Resistance Isolate Bank *Candida auris* panel (<https://wwwn.cdc.gov/ARIsolateBank/Panel/PanelDetail?ID=2>). The remaining *C. auris* isolate was a previously reported isolate from a patient at UCSF, in short this strain is a member of the South Asian clade that has some resistance to fluconazole (MIC 32 µg/mL) and was provided by the UCSF Clinical Laboratories at China Basin [87]. For *C. albicans* (SC5314), *Candida dubliniensis* (CD36), and *Candida glabrata*, we used the sequenced strains SC5314, CD36, and

CBS138/ATCC 2001, respectively. SC5314 was isolated from a patient with disseminated candidiasis prior to 1968 [88–91], CD36 was isolated from the mouth of an Irish HIV patient between 1988 and 1994 [92], and CBS138 is listed as coming from a Fecal Sample (<https://www.atcc.org/products/all/2001.aspx#history>). Unless otherwise noted, assays used the same three *C. auris* isolates (AR-384/MLY1540, Clade III; AR-386/MLY1542, Clade IV; AR-387/MLY1543, Clade I) to ensure representation of the three clades most associated with serious infections as well as wide distribution of sensitivities to fluconazole and caspofungin. A fourth isolate, AR-390/MLY1546 from Clade I, was included in the synergy experiments and as the second strain, in addition to AR-384/MLY1540, in the experimental evolution experiment.

A full list of oligonucleotides and plasmids used in the construction of strains can be found in (Table S5). Strain construction took place in the AR-387 and AR-390 *C. auris* strain backgrounds following previously described methods using the hygromycin B resistance selectable marker [93]. The gRNA was designed using the gRNA selection tool in Benchling with the following parameters: “Single guide”, “Guide Length” of 20, “PAM” of NGG. When deleting genes, a 23bp ADDTAG was inserted at the location of the gene to aid further modifications, if necessary. The gRNA fragments were amplified from pCE41 while the Cas9 construct was prepared by digesting pCE38 with the restriction enzyme MssI. Transformations used a lithium acetate competence / heat shock-based protocol with a 4 hour recovery before plating on YPD+HYG600. Potentially successful transformations were verified by Colony PCR, after which candidates were plated for 48 to 72 hours on SC -Leu plates to select for restoration of the Leu2 reading frame and removal of the hygromycin B marker associated with the Cas9 components. In order to confirm the presence of desired mutations after the LEUpOUT step, DNA for sequencing was extracted using a Quick-DNA Fungal/Bacterial Miniprep Kit (Zymo Research D6005)



coupled with a Mini-BeadBeater 16 (Biospec Products); bead beating consisted of two 4 minute cycles separated by a five minute incubation on ice.

### *Antifungal Susceptibility Testing*

Antifungal susceptibility testing assays were performed according to the 4<sup>th</sup> edition CLSI M27 protocol [94] with the following modifications. Overnight cultures (3 mL, in test tubes) were started in RPMI-1640 media on a roller drum at 30°C from two to three day old colonies grown on YPD Agar Plates. The following morning, the OD<sub>600</sub> of the overnight cultures was determined, cultures were diluted back to OD<sub>600</sub> = 0.25 in fresh RPMI-1640, and the diluted cultures were allowed to recover at 30°C for at least three hours. After the recovery growth step, the OD<sub>600</sub> of the recovery cultures was determined and the cells were diluted to an OD<sub>600</sub> = 0.00357 in fresh RPMI-1640. Adding of 21 µL of the OD<sub>600</sub> = 0.00357 resuspension to 54 µL of media/drug mixture in each well resulted in a starting density of OD<sub>600</sub> = 0.001 or approximately 1 x 10<sup>4</sup> cells / mL.

54 µL of media was dispensed into wells (in two 27 µL steps) using a BioMek FX (Beckman-Coulter). Drugs, DMSO loading controls, and other compounds (e.g. metals) were then dispensed into the wells using a Labcyte Echo 525. The 21 µL of cell solution was then added to the 54 µL of media/drug mixture using a BioMek FX. Assays were performed in transparent, sterile, flat-bottomed, non-tissue culture treated 384-well microtiter plates (Thermo 242765 or 242757) that were sealed with Breathe-Easy® sealing membranes (Diversified Biotech, BEM-1) immediately following inoculation. Plates were then incubated at 35°C in a humidified incubator (with 0.1% CO<sub>2</sub>) for 24 hours. After the 24 hour incubation, the absorbance (OD<sub>600</sub>) was determined on a prewarmed (35°C) Tecan Spark10M, taking one read per well. In all experiments, the percent inhibition was determined by first subtracting the background OD<sub>600</sub> (culture wells

filled with media only) from the test well OD<sub>600</sub>, and then normalizing to the average OD<sub>600</sub> of untreated (vehicle only) control wells cultured side-by-side with the test wells. The percent inhibition was then calculated using the following equation: % inhibition = 100\*(1-(test well OD - background OD)/(untreated control OD – background OD)).

### *Primary Screening*

Initial screening was conducted with the three primary *C. auris* strains. All 1990 screening compounds were evaluated for *in vitro* efficacy at concentrations of 1 and 10 μM. For each of the strains, a single well was evaluated for each compound at each concentration. The efficacy of each compound was determined by comparison to the average of untreated control wells on the same culture plate as the tested compounds. Compounds with greater than 50% inhibition of *C. auris* growth for at least two of the three tested strains were selected as hits for further evaluation (89 compounds total).

### *Secondary drug screening and IC<sub>50</sub> determinations*

The activity of 89 primary hit compounds was validated against the three primary *C. auris* strains with dose-response growth inhibition experiments. Drugs were dispensed into test wells using the Labcyte Echo 525 liquid handler to generate 8-point concentration ranges from 0.3 to 100 μM. All drugs were resuspended in DMSO and compared to appropriate vehicle-only controls. Dose-response experiments were performed with two biological replicates, each consisting of two technical replicates. Half maximal inhibitory concentrations (IC<sub>50</sub>) were calculated from dose-response curves generated in GraphPad Prism 7 using four parameter logistic regression. Subsequent experiments determined the IC<sub>50</sub> of the top 5 hit drugs as well as 4 standard of care drugs against 13 different *C. auris* strains, as well as one strain each of *C. albicans*, *C. glabrata*,

and *C. dubliniensis* with 22-point dose-response ranges (0.05-2600  $\mu$ M for fluconazole; 0.001-133.3  $\mu$ M for caspofungin, miltefosine and triclabendazole; 0.001-20  $\mu$ M for posaconazole, amphotericin B, chloroxine, broxyquinoline, and clioquinol) performed as described above with three biological replicates, each consisting of two technical replicates.

#### *Human cell toxicity measurements*

The human cell lines Hep-G2 (liver), HEK-293 (kidney), and HFF-1 (fibroblast) were cultured in Dulbecco's modified Eagle's medium (Gibco) containing 10% (vol/vol) fetal bovine serum (Gibco), 2 mM l-glutamine, 100 U/mL penicillin/streptomycin (Gibco), and 10 mM HEPES buffer. For toxicity experiments, all human cell lines were seeded into sterile, opaque 384-well culture plates (Corning 3570) one day prior to drug addition. Drugs were added using the Labcyte Echo 525 liquid handler to generate 22-point dose-response concentration ranges. Cells were cultured in the presence of drug for 72 hours prior to addition of CellTiter-Glo 2.0 reagent (Promega) and collection of luminescence values in relative luminescence units (RLU) using the Promega GloMax plate reader. The percent viability of each treated culture was calculated using the following equation: % inhibition =  $100 * (\text{test well RLU}) / (\text{untreated control RLU})$ . IC<sub>50</sub> values for each drug against human cell lines were calculated as described above. Toxicity experiments were performed with three biological replicates, each consisting of two technical replicates.

#### *Drug susceptibility in evolved and genetically engineered C. auris strains*

*C. auris* strains selected for clioquinol resistance or engineered for specific mutations were generated and cultured as described previously and the IC<sub>50</sub> of clioquinol and other drugs was determined as described above using 15-point dose-response ranges (0.1-20  $\mu$ M for clioquinol;

3.3-1333  $\mu\text{M}$  for fluconazole; 0.03-66.7  $\mu\text{M}$  for broxyquinoline and amphotericin B; 0.003-13.3  $\mu\text{M}$  for posaconazole, voriconazole, and micafungin). All strains were tested simultaneously for direct comparison of drug effects and three biological replicates were performed, each consisting of two technical replicates. Fold-changes in  $\text{IC}_{50}$  were calculated relative to the parental strains from which each mutant strain was derived.

#### *Structure activity relationship (SAR) assays*

A group of 32 commercially available drugs or compounds that are structurally related to clioquinol were selected for SAR experiments. All drugs were resuspended in DMSO and tested for inhibition of the three primary *C. auris* strains with 15-point dose-response ranges from 0.01 to 150  $\mu\text{M}$ . Experiments were performed and  $\text{IC}_{50}$  values were calculated as described above with three biological replicates, each consisting of two technical replicates.

#### *Metal supplementation experiments*

Stock 10 mM metal solutions for supplementation experiments were prepared in sterile water as follows:  $\text{Ca}^{2+}$  solution from Calcium chloride (Sigma C79-500);  $\text{Mg}^{2+}$  solution from Magnesium sulfate (Sigma 246972);  $\text{Fe}^{2+}$  solution from Ferrous(II) sulfate (Sigma F8048);  $\text{Fe}^{3+}$  solution from Ferric(III) chloride (Sigma F-2877);  $\text{Cu}^{2+}$  solution from Copper(II) sulfate (Sigma C7631);  $\text{Mn}^{2+}$  solution from Manganese sulfate (Sigma M-1144);  $\text{Zn}^{2+}$  solution from Zinc sulfate (Sigma 96500). For metal supplementation experiments, *C. auris* was grown in RPMI media depleted of divalent metal ions using Chelex 100 resin (Biorad) following the manufacturer's protocol. Drugs and metals were dispensed into culture wells using the Labcyte Echo 525 liquid handler prior to addition of *C. auris* cells. Ethylenediaminetetraacetic acid (EDTA) and *N,N,N',N'*-

tetrakis(2-pyridinylmethyl)-1,2-ethanediamine (TPEN) were used as control chelating agents for comparison to antifungal drugs. The percent inhibition for each drug/metal condition was calculated as described above. For calculation of clioquinol IC<sub>50</sub> in the context of different metal concentrations, 8-point dose-responses ranges from 0.01-10  $\mu$ M. Experiments were performed with three biological replicates, each consisting of two technical replicates.

#### *Viability Determination by Live Dead Staining and Plating*

Viability assays were performed using the AR-384 strain. Live/dead staining was performed using the recommended protocol for Molecular Probes' LIVE/DEAD® *FungaLight*<sup>™</sup> Yeast Viability Kit (#L34952). Flow Cytometry for the live/dead assays was performed on a BD Accuri C6 Plus that used a 488nm laser with a 533/30 bandpass filter. Samples were loaded from 96-well U-bottom plates (Falcon 351177), and normal acquisition was 10  $\mu$ L of sample on the slow setting. In brief, overnight cultures (3 mL, in test tubes) were started in RPMI-1640 media on a roller drum at 30°C from two to three day old colonies grown on YPD Agar Plates. The following morning, the OD<sub>600</sub> of the overnight cultures was determined, cultures were diluted back to OD<sub>600</sub> = 0.7 in 8 mL fresh RPMI-1640, and the diluted cultures were allowed to recover at 30°C for three hours. After three hours, clioquinol (5  $\mu$ M) and DMSO controls were added to the cultures which were then incubated for a further two hours on a roller drum at 30°C. A second set of cultures was prepared using the same protocol the previous day in order to provide sets of cells that were exposed to clioquinol or DMSO for 22 hours. As a positive control for cell death, an independent culture was pelleted and resuspended in 70% isopropanol for one hour at room temperature (roughly 20-22°C) with vortexing every 15 minutes. Samples were PBS washed, resuspended at OD<sub>600</sub> = 0.1 in multiple 1 mL PBS aliquots, and then either not stained (controls), stained with

either SYTO®9 or propidium iodide, or stained with both SYTO9 and propidium iodide. Cells were incubated at room temperature for 15 minutes prior to analysis by Flow Cytometry, 20,000 cells were analyzed for each sample.

As an alternative method to evaluate clioquinol's effect on *C. auris* viability, a plate based assay was conducted in parallel. In brief, aliquots were taken from the 22 hour clioquinol and DMSO treated cultures as well as the 1 hour isopropanol treated cultures. Cells were PBS washed and preliminary 10x stocks of normalized cell density were created based on OD<sub>600</sub>. The cell density of each sample was then determined by flow cytometry; cell counts were based on the number of cells detected in a 10 µL sample. 1x normalized cell density stocks were then created based on these measurements. The exact cell density of these 1x stocks was then determined by flow cytometry of 10 µL of each solution. Next, both high density (1:20 dilution) and low density (1:200 dilution) stocks were made from the 1x stock and plated (50 µL of high density, 60 µL of low density) on YEPD plates at 30°C. Three low density and two high density plates were used for clioquinol and DMSO samples; two low and one high density plate were used for isopropanol samples. After two days, colony numbers were determined using a Protos 3 (Synbiosis) automated colony counter. The input cell density (cells / µL) and detectable colonies (CFU) were both normalized to their respective DMSO treated samples and normalized viability (relative to the DMSO treated samples) was determined by dividing the normalized CFU for each sample by the normalized input cell density.

#### *Iron Supplementation Recovery Assay*

Iron supplementation recovery assays were performed on the AR-384 strain and flow cytometry for the iron supplementation recovery assays was performed on the previously described

BD Accuri C6 Plus. Overnight cultures (3 mL, in test tubes) were started in RPMI-1640 media on a roller drum at 30°C from two to three day old colonies grown on YPD Agar Plates. The following morning, the OD<sub>600</sub> of the overnight cultures was determined, cultures were diluted back to OD<sub>600</sub> = 0.5 in fresh RPMI-1640, and the diluted cultures were allowed to recover at 30°C for three hours at which point 4 μM clioquinol was added to the cultures. Cultures were then incubated a further 21 hours on a roller drum at 30°C. After the 21 hour incubation, two 1 mL aliquots were pulled from each clioquinol treated sample and either iron (2μM each of iron (II) sulfate and iron (III) chloride) or water (equivalent volumes to the iron solutions) was added. The remaining volume of the clioquinol treated samples were pelleted by centrifugation, washed once in PBS, resuspended in PBS, diluted to an OD<sub>600</sub> = 1.0 in PBS, and then diluted 1:10 in fresh RPMI for a final OD<sub>600</sub> = 0.1. Four clioquinol samples were processed in this way. Iron (2 μM each of iron (II) sulfate and iron (III) chloride) and water (equivalent volumes to the iron solutions, used as a loading control) were then added to samples. The density of each culture was then determined by flow cytometry and the strains were incubated on a roller drum at 30°C for 25 hours. At each subsequent time point the cultures were vortexed after which samples were removed and diluted with D-PBS. The cell density of each sample was then determined by flow cytometry; cell counts were based on the number of cells detected in a 10 μL sample.

### *Liquid Resistance Assay*

Two overnights each of AR-384 and AR-390 were started from independent single colonies, the following morning the overnight cultures were diluted back to OD<sub>600</sub> = 0.05 in fresh media and allowed to recover for three hours. At this point, clioquinol was added to the cultures at 0.75 μM (AR-384) or 0.4 μM (AR-390) and were incubated for two days on a roller drum at

30°C. Samples were then diluted back to approximately OD<sub>600</sub>= 0.01 in the presence of fresh media and drug. The four independent cultures were passaged a further 30 times in this manner with passages occurring every three, rather than every two, days after passage 20 (we note that samples were frozen down after passage 20, passage 21 was started from single colonies on plates made from these frozen stocks). Clioquinol concentrations were slowly increased during the course of the experiment in response to increased growth by strains, see File S# for the clioquinol concentration present and estimates of the number of generations for each passage. In parallel to this experiment, eighteen passages were made of two independent control cultures for each strain where equivalent volumes of DMSO were added at each passage.

#### *qRT-PCR methods*

Three independent overnights for each strain were started from independent single colonies on roller drum at 30°C, the following morning the overnight cultures were diluted back to OD<sub>600</sub> = 0.35 in 5 mL fresh media and allowed to recover for six hours. We note that clioquinol was not present in the overnight or recovery cultures and as such these samples reflect the basal, as opposed to clioquinol-induced, expression levels. Cultures were then spun down, decanted, and the pellets flash frozen with liquid nitrogen before storage at -80°C. Pellets were thawed and RNA was extracted using the MasterPure Yeast RNA Purification Kit (Lucigen MPY03100) followed by DNase treatment with the DNase TURBO DNA-free kit (Invitrogen AM1907). RNA was diluted 1:50 for RT-qPCR which was conducted using the Luna Universal One-Step RT-qPCR kit (New England Biolabs E3005E) on a C1000 touch thermal Cycler / CFX384 Real-Time System (Biorad). Reactions were performed in Hard-Shell PCR Plates (384-well, thin-wall, Biorad HSP3805) sealed with Microseal B Adhesive Sealers (Biorad MSB-1001). Two independent



oligonucleotide sets each were used for Cdr1, Cdr2, and Mdr1; one of the Cdr1 oligonucleotide sets was located downstream of the E772\* mutation. One oligonucleotide set each was used for the control genes Ubc4 and Act1. Two technical replicates were performed for each oligonucleotide set for each biological replicate. The C<sub>q</sub> values for the two technical replicates were averaged for each set, after which the averaged C<sub>q</sub> values for the Ubc4 and Act1 sets for each biological replicate were then averaged. The  $\Delta C_t$  was then determined for each primer set versus the averaged Ubc4/Act1 C<sub>q</sub>, after which the  $\Delta\Delta C_t$  was calculated versus the parental strain and the fold change determined by taking  $2^{(-\Delta\Delta C_t)}$ . The average was then calculated for the two probe sets for each gene within each biological replicate, after which the average and standard deviation were calculated for each gene across the three biological replicates.

### *DNA Sequencing*

For endpoint samples of the evolved strains, two cultures were inoculated from independent single colonies (single colony samples) and a third culture was started from the dense portion of the streak on the plate (population samples). For samples from intermediate time points for the evolved strains, single cultures was started from the dense portion of the streak on the plate (population samples). A single culture was inoculated from an independent colonies for the parental strains. One culture was inoculated from an independent colony (single colony samples) and a second culture was started from the dense portion of the streak on the plate (population samples) for the DMSO control cultures. Cultures for whole genome DNA sequencing were grown in 8 mL media overnight on a roller drum at 30°C. Prior to harvesting the following morning, a sample was pulled to freeze as a glycerol stock for future use. 6.2 mL of each culture was spun down, decanted, flash frozen in liquid nitrogen, and stored at -80°C.

DNA was extracted using the Quick-DNA Fungal/Bacterial Miniprep Kit (Zymo Research D6005) with two 5 minute cycles on a TissueLyser II (Qiagen) separated by a 5 minute incubation on ice; final elution was in 60  $\mu$ L water and concentrations were determined on a Nanodrop 2000c (Thermo Scientific). The DNA was diluted to 100  $\mu$ L at a concentration of 10 ng /  $\mu$ L and then sheared using a Biorupter® Pico (diagenode) with 13 cycles of 30 s on followed by 30 s off and quantified using an Agilent D1000 ScreenTape (Agilent Technologies); DNA fragment size after this step averaged 240 bp.

Library preparation was performed using the NEBNext Ultra™ DNA Library Prep Kit for Illumina (E7370), using the 200bp recommended bead volumes for step 3, 5 PCR cycles for step 4, and eluting in water for step 5. See Table S5 for a list of the i7\_index\_RC and i5\_index\_RC oligonucleotides used for each sample. Eluted libraries for sequencing were then quantified via Qubit, pooled, the pooled mixture quantified via Qubit, and then the pooled libraries were quantified using an Agilent High Sensitivity D1000 ScreenTape (Agilent Technologies); DNA fragment size after this step averaged 360 bp.

Sequences were aligned to the reference genomes using Bowtie2 with default settings. AR-390 based strains were aligned to B8441 chromosome fasta and GFF features files from the Candida Genome Database (version s01-m01-r-17, dating from 8/8/2021, downloaded on 9/10/2021). AR-384 based strains were aligned to B11221 chromosome fasta and GFF features files from the Candida Genome Database (no version information, dating from 12/17/2019, downloaded on 9/10/2021). Aligned reads were then filtered using Samtools to remove reads with a Cigar Value of “\*”. Mutations in genes were identified using Minority Report [95] in Python 2 with the parental AR-384 and AR-390 sequencing reads used as the basis for comparison, the analyze Copy Number Variants (CNV) feature enabled, and the codon table changed to reflect the

use of “CTG” as Serine rather than Leucine. For single colony samples, the default settings were used; these settings identified mutations that were present in at least 90 percent of the population. For population samples, copy number variation (CNV) analysis was conducted and the following settings were used: “vp” (minimum\_variant\_proportion) of 0.1, “wp” (maximum\_variant\_proportion) of 0.04, “vc” (minimum\_variant\_counts) of 10, and “wc” (maximum\_wildtype\_variant\_counts) of 50. In other words, a mutation or variant must be present in at least 10 percent of experimental sample reads with a minimum requirement for 10 reads and must be present at no more than four percent of parental sequencing reads with a maximum limit of 50 reads.

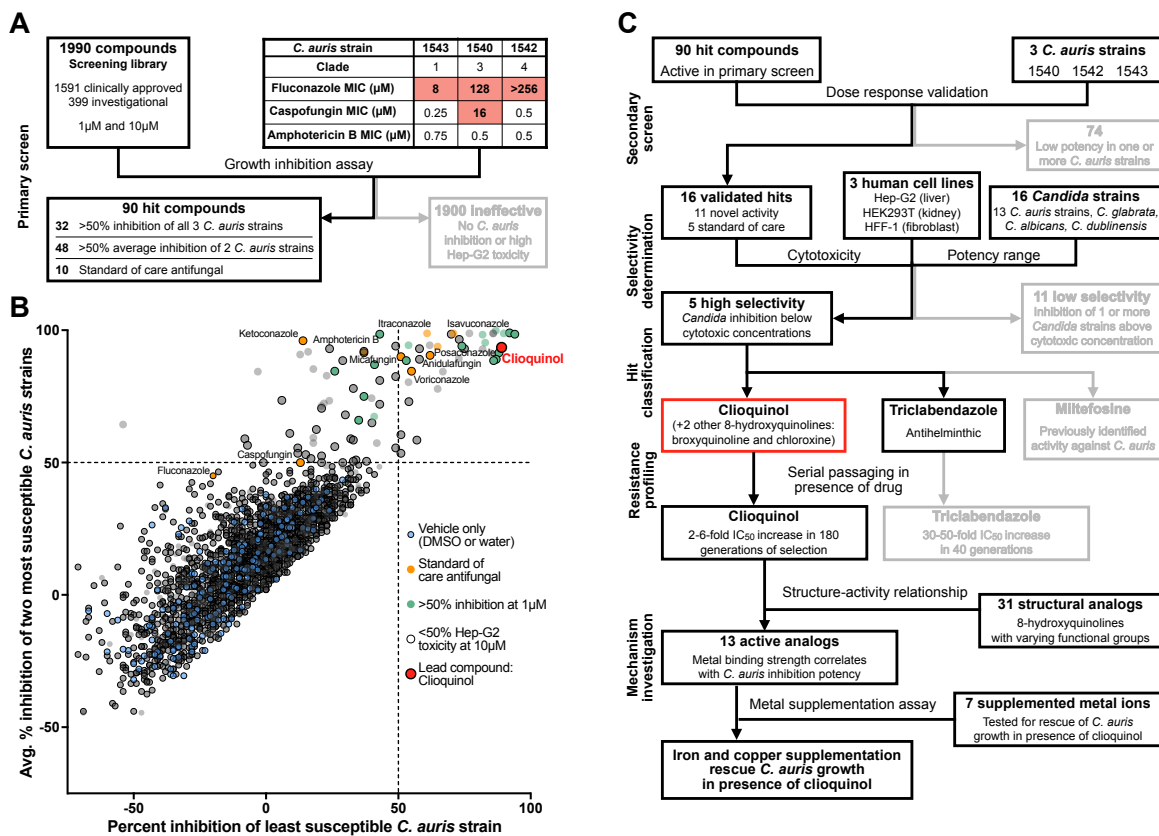


**Figure 5.1. A screen of 1990 clinically approved and investigational compounds for *in vitro* inhibition of *C. auris* identified 89 candidates for further evaluation.** (A) Workflow for the primary screening of 1990 clinically approved and investigational compounds for *in vitro* inhibition of three *C. auris* strains; compounds were screened at both 1  $\mu\text{M}$  and 10  $\mu\text{M}$ . (B) The percent inhibition relative to untreated controls for each compound at 10  $\mu\text{M}$ . For each compound, the lowest percent inhibition achieved against any of the three screened *C. auris* strains is plotted on the x-axis and the average percent inhibition against the other two strains is plotted on the y-axis. Compounds in the upper left quadrant effectively inhibited two of the three *C. auris* strains; compounds in the upper right quadrant effectively inhibited all three strains. (C) The secondary screening pipeline for the 89 hit compounds which inhibited at least two of the three *C. auris* strains by at least 50 percent. Selectivity screening for inhibition of additional *C. auris* strains and lack of toxicity to human cells yielded 5 highly selective candidates (Figure 5.2). Selection for resistance to the lead compound, clioquinol, resulted in 2- to 5-fold increases in  $\text{IC}_{50}$  values after serial passage for 100-200 generations in the presence of clioquinol (Figure 5.3). Structural analogs of clioquinol with potential metal binding activity maintain inhibition of *C. auris* which can be abrogated by supplementation of iron or copper (Figure 5.4).

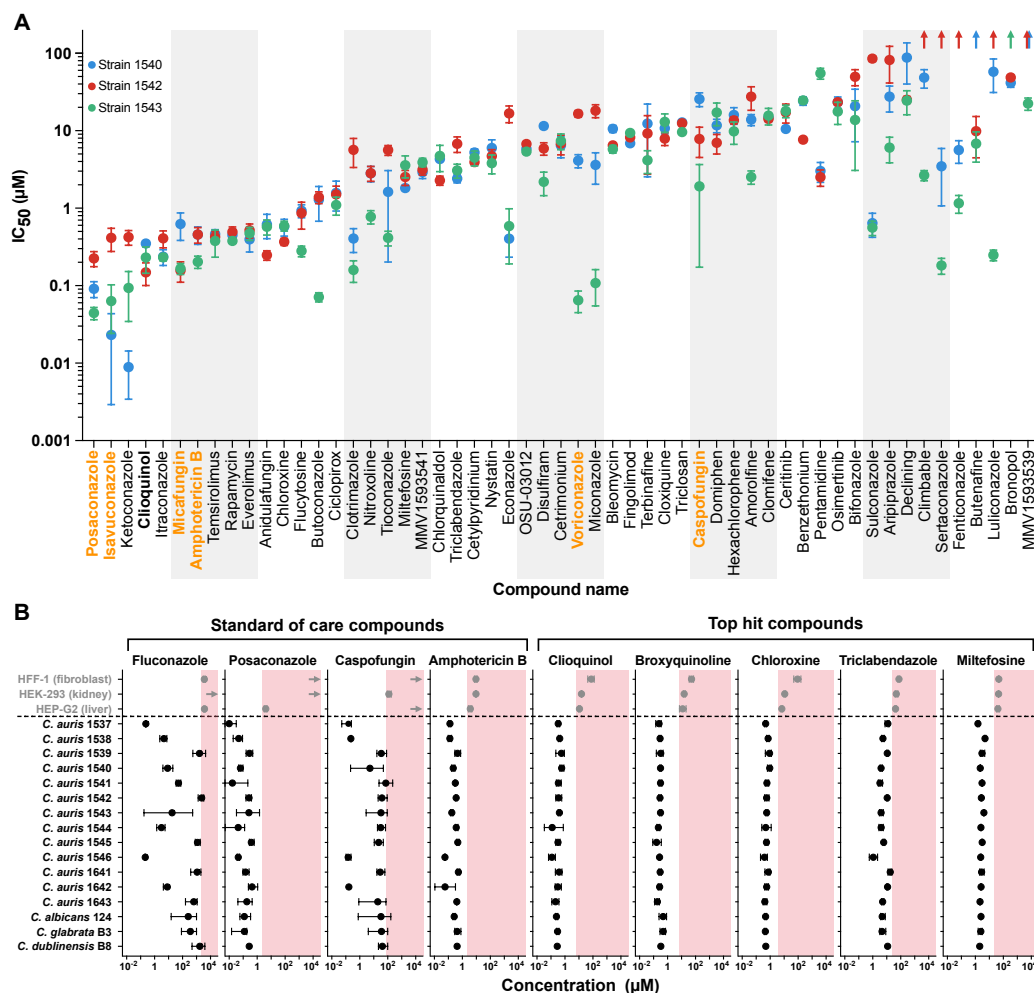


**Figure 5.2. Secondary screening and selectivity measurement identified five promising compounds, including three hydroxyquinolines.** (A) IC<sub>50</sub> values against three *C. auris* strains for 55 compounds calculated from 8-point dose-response curves. Points represent the mean of three biological replicates, error bars represent the standard error of the mean, and upwards arrows indicate IC<sub>50</sub> values greater than the highest concentration tested, 100μM. IC<sub>50</sub> values are not reported for the 34 compounds which had minimal or no activity in dose-response experiments in this screen. Representative standard of care compounds are indicated in orange. (B) IC<sub>50</sub> values for 4 standard of care drugs and 5 top hits against 13 *C. auris* strains, strains from 3 additional *Candida* species, and 3 human cell lines. Pink shaded regions mark concentrations above the lowest observed IC<sub>50</sub> for that compound against a human cell line. Greater differences between *Candida* strain IC<sub>50</sub> and human cell IC<sub>50</sub> indicate higher selectivity. Values represent the mean of three biological replicates, error bars represent the standard error of the mean, and right-pointing arrows indicate IC<sub>50</sub> values greater than 1000 μM.

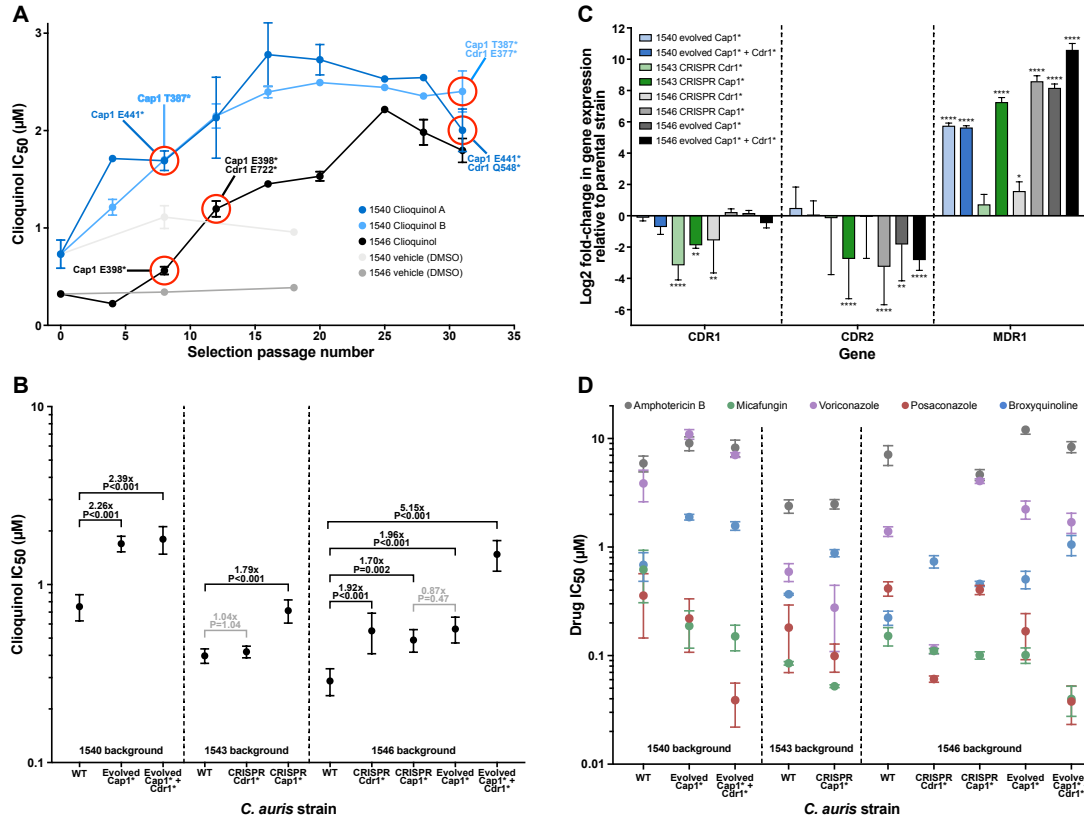


**Figure 5.3. Evolution of clioquinol resistance in a serial passaging selection experiment.** (A) Clioquinol IC<sub>50</sub> against *C. auris* isolates that were selected for clioquinol resistance. Parallel selections were carried out with serial passaging of strains AR-384 (blue) and AR-390 (black) in the presence of clioquinol or vehicle (DMSO; grey). Whole genome sequencing was performed for a subset of *C. auris* passage populations or single cells and the mutations identified are indicated. (B) Comparison of clioquinol's IC<sub>50</sub> against parent, evolved, and CRISPR engineered *C. auris* mutant strains from three different backgrounds. The fold-changes in IC<sub>50</sub> between relevant related strains are shown; the statistical significance of observed differences as determined with unpaired t-tests (two-tailed, equal variance) is indicated. (C) Changes in expression of the *CDR1*, *CDR2*, and *MDR1* drug pump genes in evolved and CRISPR engineered *C. auris* mutant strains from three different backgrounds in the absence of clioquinol. Gene expression changes are shown as the Log<sub>2</sub> fold-change relative to the parental (WT) strain for that background. Statistical significance was determined with unpaired t-tests (two-tailed, equal variance, \* P<.05; \*\* P<.01; \*\*\* P<.001; \*\*\*\* P<.0001). (D) Comparison of IC<sub>50</sub> values for 5 other drugs against parent, evolved, and CRISPR engineered mutant *C. auris* strains. Values represent the mean of three independent experiments; error bars represent the standard error of the mean.

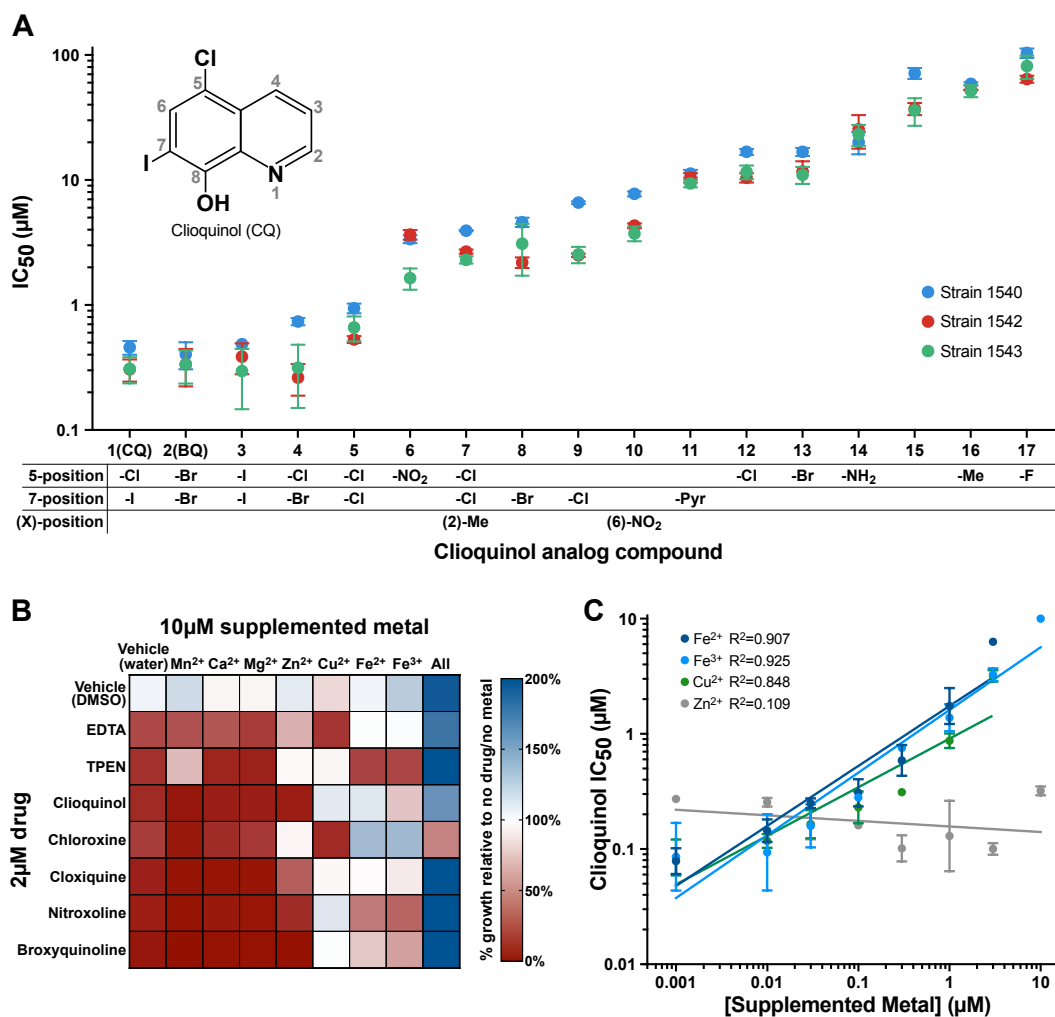


**Figure 5.4. Dihalogenated 8-hydroxyquinolines are the most effective inhibitors of *C. auris* and this activity is abrogated by the presence of Iron or Copper.** (A) IC<sub>50</sub> of clioquinol and 16 structural analogs against three *C. auris* strains. Clioquinol (upper left inset) is comprised of a quinoline core with a 5-position chlorine, 7-position iodine, and 8-position hydroxy group, the functional groups at these and other positions are indicated for each of the structural analogs. A further 15 clioquinol analogs that lacked activity against *C. auris* are not shown. (B) Heat map of *C. auris* growth in the presence of various combinations of metal ion supplementation and 8-hydroxyquinoline drugs or control metal chelators EDTA and TPEN. *C. auris* cultures were grown in metal-depleted media, as a result supplementation of metals enhances growth (blue on heat map) and treatment with 8-hydroxyquinolines or control chelators reduces growth (red on heat map). (C) Relationship between supplemented metal concentration and clioquinol IC<sub>50</sub>. The linear regression is shown for each metal. Data represent the mean of three independent experiments; error bars represent the standard error of the mean.

## Chapter 5 References

1. Fraser, V.J.; Jones, M.; Dunkel, J.; Storfer, S.; Medoff, G.; Dunagan, W.C. Candidemia in a Tertiary Care Hospital: Epidemiology, Risk Factors, and Predictors of Mortality. *Clin. Infect. Dis.* 1992, *15*, 414–421, doi:10.1093/clind/15.3.414.
2. Forsberg, K.; Woodworth, K.; Walters, M.; Berkow, E.L.; Jackson, B.; Chiller, T.; Vallabhaneni, S. *Candida Auris*: The Recent Emergence of a Multidrug-Resistant Fungal Pathogen. *Med Mycol* 2019, *57*, 1–12, doi:10.1093/mmy/myy054.
3. Schelenz, S.; Hagen, F.; Rhodes, J.L.; Abdolrasouli, A.; Chowdhary, A.; Hall, A.; Ryan, L.; Shackleton, J.; Trimlett, R.; Meis, J.F.; et al. First Hospital Outbreak of the Globally Emerging *Candida Auris* in a European Hospital. *Antimicrob Resist Infect Control* 2016, *5*, 35, doi:10.1186/s13756-016-0132-5.
4. Eyre, D.W.; Sheppard, A.E.; Madder, H.; Moir, I.; Moroney, R.; Quan, T.P.; Griffiths, D.; George, S.; Butcher, L.; Morgan, M.; et al. A *Candida Auris* Outbreak and Its Control in an Intensive Care Setting. *N. Engl. J. Med.* 2018, *379*, 1322–1331, doi:10.1056/NEJMoa1714373.
5. Pacilli, M.; Kerins, J.L.; Clegg, W.J.; Walblay, K.A.; Adil, H.; Kemble, S.K.; Xydis, S.; McPherson, T.D.; Lin, M.Y.; Hayden, M.K.; et al. Regional Emergence of *Candida Auris* in Chicago and Lessons Learned from Intensive Follow-Up at One Ventilator-Capable Skilled Nursing Facility. *Clin. Infect. Dis.* 2020, doi:10.1093/cid/ciaa435.
6. Rossow, J.; Ostrowsky, B.; Adams, E.; Greenko, J.; McDonald, R.; Vallabhaneni, S.; Forsberg, K.; Perez, S.; Lucas, T.; Alroy, K.A.; et al. Factors Associated With *Candida Auris* Colonization and Transmission in Skilled Nursing Facilities With Ventilator Units, New York, 2016-2018. *Clin Infect Dis* 2021, *72*, e753–e760, doi:10.1093/cid/ciaa1462.



7. Southwick, K.; Ostrowsky, B.; Greenko, J.; Adams, E.; Lutterloh, E.; NYS *C. auris* Team; Denis, R.J.; Patel, R.; Erazo, R.; Fernandez, R.; et al. A Description of the First *Candida Auris*-Colonized Individuals in New York State, 2016-2017. *Am J Infect Control* 2021, S0196-6553(21)00716-1, doi:10.1016/j.ajic.2021.10.037.
8. Allaw, F.; Kara Zahreddine, N.; Ibrahim, A.; Tannous, J.; Taleb, H.; Bizri, A.R.; Dbaiibo, G.; Kanj, S.S. First *Candida Auris* Outbreak during a COVID-19 Pandemic in a Tertiary-Care Center in Lebanon. *Pathogens* 2021, 10, doi:10.3390/pathogens10020157.
9. Prestel, C.; Anderson, E.; Forsberg, K.; Lyman, M.; de Perio, M.A.; Kuhar, D.; Edwards, K.; Rivera, M.; Shugart, A.; Walters, M.; et al. *Candida Auris* Outbreak in a COVID-19 Specialty Care Unit - Florida, July-August 2020. *MMWR Morb Mortal Wkly Rep* 2021, 70, 56–57, doi:10.15585/mmwr.mm7002e3.
10. Centers for Disease Control and Prevention *Candida Auris* Clinical Update - September 2017 Available online: <https://www.cdc.gov/fungal/candida-auris/c-auris-alert-09-17.html> (accessed on 25 March 2020).
11. Satoh, K.; Makimura, K.; Hasumi, Y.; Nishiyama, Y.; Uchida, K.; Yamaguchi, H. *Candida Auris* Sp. Nov., a Novel Ascomycetous Yeast Isolated from the External Ear Canal of an Inpatient in a Japanese Hospital. *Microbiol. Immunol.* 2009, 53, 41–44, doi:10.1111/j.1348-0421.2008.00083.x.
12. Lockhart, S.R.; Etienne, K.A.; Vallabhaneni, S.; Farooqi, J.; Chowdhary, A.; Govender, N.P.; Colombo, A.L.; Calvo, B.; Cuomo, C.A.; Desjardins, C.A.; et al. Simultaneous Emergence of Multidrug-Resistant *Candida Auris* on 3 Continents Confirmed by Whole-Genome Sequencing and Epidemiological Analyses. *Clin. Infect. Dis.* 2017, 64, 134–140, doi:10.1093/cid/ciw691.

13. Chow, N.A.; de Groot, T.; Badali, H.; Abastabar, M.; Chiller, T.M.; Meis, J.F. Potential Fifth Clade of *Candida Auris*, Iran, 2018. *Emerging Infect. Dis.* 2019, 25, 1780–1781, doi:10.3201/eid2509.190686.
14. Muñoz, J.F.; Gade, L.; Chow, N.A.; Loparev, V.N.; Juieng, P.; Berkow, E.L.; Farrer, R.A.; Litvintseva, A.P.; Cuomo, C.A. Genomic Insights into Multidrug-Resistance, Mating and Virulence in *Candida Auris* and Related Emerging Species. *Nat Commun* 2018, 9, 5346, doi:10.1038/s41467-018-07779-6.
15. Chow, N.A.; Muñoz, J.F.; Gade, L.; Berkow, E.L.; Li, X.; Welsh, R.M.; Forsberg, K.; Lockhart, S.R.; Adam, R.; Alanio, A.; et al. Tracing the Evolutionary History and Global Expansion of *Candida Auris* Using Population Genomic Analyses. *mBio* 2020, 11, doi:10.1128/mBio.03364-19.
16. Kwon, Y.J.; Shin, J.H.; Byun, S.A.; Choi, M.J.; Won, E.J.; Lee, D.; Lee, S.Y.; Chun, S.; Lee, J.H.; Choi, H.J.; et al. *Candida Auris* Clinical Isolates from South Korea: Identification, Antifungal Susceptibility, and Genotyping. *J Clin Microbiol* 2019, 57, doi:10.1128/JCM.01624-18.
17. Welsh, R.M.; Sexton, D.J.; Forsberg, K.; Vallabhaneni, S.; Litvintseva, A. Insights into the Unique Nature of the East Asian Clade of the Emerging Pathogenic Yeast *Candida Auris*. *J Clin Microbiol* 2019, 57, doi:10.1128/JCM.00007-19.
18. Chow, N.A.; Gade, L.; Tsay, S.V.; Forsberg, K.; Greenko, J.A.; Southwick, K.L.; Barrett, P.M.; Kerins, J.L.; Lockhart, S.R.; Chiller, T.M.; et al. Multiple Introductions and Subsequent Transmission of Multidrug-Resistant *Candida Auris* in the USA: A Molecular Epidemiological Survey. *Lancet Infect Dis* 2018, 18, 1377–1384, doi:10.1016/S1473-3099(18)30597-8.

19. Rhodes, J.; Fisher, M.C. Global Epidemiology of Emerging *Candida Auris*. *Curr. Opin. Microbiol.* 2019, *52*, 84–89, doi:10.1016/j.mib.2019.05.008.
20. Borman, A.M.; Johnson, E.M. *Candida Auris* in the UK: Introduction, Dissemination, and Control. *PLoS Pathog* 2020, *16*, e1008563, doi:10.1371/journal.ppat.1008563.
21. Chowdhary, A.; Prakash, A.; Sharma, C.; Kordalewska, M.; Kumar, A.; Sarma, S.; Tarai, B.; Singh, A.; Upadhyaya, G.; Upadhyay, S.; et al. A Multicentre Study of Antifungal Susceptibility Patterns among 350 *Candida Auris* Isolates (2009-17) in India: Role of the *ERG11* and *FKS1* Genes in Azole and Echinocandin Resistance. *J. Antimicrob. Chemother.* 2018, *73*, 891–899, doi:10.1093/jac/dkx480.
22. Ostrowsky, B.; Greenko, J.; Adams, E.; Quinn, M.; O'Brien, B.; Chaturvedi, V.; Berkow, E.; Vallabhaneni, S.; Forsberg, K.; Chaturvedi, S.; et al. *Candida Auris* Isolates Resistant to Three Classes of Antifungal Medications - New York, 2019. *MMWR Morb. Mortal. Wkly. Rep.* 2020, *69*, 6–9, doi:10.15585/mmwr.mm6901a2.
23. Kordalewska, M.; Lee, A.; Park, S.; Berrio, I.; Chowdhary, A.; Zhao, Y.; Perlin, D.S. Understanding Echinocandin Resistance in the Emerging Pathogen *Candida Auris*. *Antimicrob. Agents Chemother.* 2018, *62*, doi:10.1128/AAC.00238-18.
24. Zhu, Y.; O'Brien, B.; Leach, L.; Clarke, A.; Bates, M.; Adams, E.; Ostrowsky, B.; Quinn, M.; Dufort, E.; Southwick, K.; et al. Laboratory Analysis of an Outbreak of *Candida Auris* in New York from 2016 to 2018: Impact and Lessons Learned. *J. Clin. Microbiol.* 2020, *58*, doi:10.1128/JCM.01503-19.
25. Kilburn, S.; Innes, G.; Quinn, M.; Southwick, K.; Ostrowsky, B.; Greenko, J.A.; Lutterloh, E.; Greeley, R.; Magleby, R.; Chaturvedi, V.; et al. Antifungal Resistance Trends of *Candida*

- Auris* Clinical Isolates, New York-New Jersey, 2016-2020. *Antimicrob Agents Chemother* 2022, aac0224221, doi:10.1128/aac.02242-21.
26. Kean, R.; Ramage, G. Combined Antifungal Resistance and Biofilm Tolerance: The Global Threat of *Candida Auris*. *mSphere* 2019, 4, doi:10.1128/mSphere.00458-19.
27. Billamboz, M.; Fatima, Z.; Hameed, S.; Jawhara, S. Promising Drug Candidates and New Strategies for Fighting against the Emerging Superbug *Candida Auris*. *Microorganisms* 2021, 9, doi:10.3390/microorganisms9030634.
28. Seiler, G.T.; Ostrosky-Zeichner, L. Investigational Agents for the Treatment of Resistant Yeasts and Molds. *Curr Fungal Infect Rep* 2021, 1–12, doi:10.1007/s12281-021-00419-5.
29. Aghaei Gharebolagh, S.; Izadi, A.; Talebi, M.; Sadeghi, F.; Zarrinnia, A.; Zarei, F.; Darmiani, K.; Borman, A.M.; Mahmoudi, S. New Weapons to Fight a New Enemy: A Systematic Review of Drug Combinations against the Drug-Resistant Fungus *Candida Auris*. *Mycoses* 2021, doi:10.1111/myc.13277.
30. Bandara, N.; Samaranayake, L. Emerging and Future Strategies in the Management of Recalcitrant *Candida Auris*. *Med Mycol* 2022, myac008, doi:10.1093/mmy/myac008.
31. Lamoth, F.; Lewis, R.E.; Kontoyiannis, D.P. Investigational Antifungal Agents for Invasive Mycoses: A Clinical Perspective. *Clin Infect Dis* 2022, ciab1070, doi:10.1093/cid/ciab1070.
32. Giacobbe, D.R.; Magnasco, L.; Sepulcri, C.; Mikulska, M.; Koehler, P.; Cornely, O.A.; Bassetti, M. Recent Advances and Future Perspectives in the Pharmacological Treatment of *Candida Auris* Infections. *Expert Rev Clin Pharmacol* 2021, 1–16, doi:10.1080/17512433.2021.1949285.

33. Berkow, E.L.; Lockhart, S.R. Activity of CD101, a Long-Acting Echinocandin, against Clinical Isolates of *Candida Auris*. *Diagn Microbiol Infect Dis* 2018, *90*, 196–197, doi:10.1016/j.diagmicrobio.2017.10.021.
34. Kovács, R.; Tóth, Z.; Locke, J.B.; Forgács, L.; Kardos, G.; Nagy, F.; Borman, A.M.; Majoros, L. Comparison of *In Vitro* Killing Activity of Rezafungin, Anidulafungin, Caspofungin, and Micafungin against Four *Candida Auris* Clades in RPMI-1640 in the Absence and Presence of Human Serum. *Microorganisms* 2021, *9*, doi:10.3390/microorganisms9040863.
35. Berkow, E.L.; Lockhart, S.R. Activity of Novel Antifungal Compound APX001A against a Large Collection of *Candida Auris*. *J Antimicrob Chemother* 2018, *73*, 3060–3062, doi:10.1093/jac/dky302.
36. Zhu, Y.; Kilburn, S.; Kapoor, M.; Chaturvedi, S.; Shaw, K.J.; Chaturvedi, V. *In Vitro* Activity of Manogepix against Multidrug-Resistant and Panresistant *Candida Auris* from the New York Outbreak. *Antimicrob Agents Chemother* 2020, *64*, doi:10.1128/AAC.01124-20.
37. Hager, C.L.; Larkin, E.L.; Long, L.; Zohra Abidi, F.; Shaw, K.J.; Ghannoum, M.A. *In Vitro* and *In Vivo* Evaluation of the Antifungal Activity of APX001A/APX001 against *Candida Auris*. *Antimicrob Agents Chemother* 2018, *62*, doi:10.1128/AAC.02319-17.
38. Berkow, E.L.; Angulo, D.; Lockhart, S.R. *In Vitro* Activity of a Novel Glucan Synthase Inhibitor, SCY-078, against Clinical Isolates of *Candida Auris*. *Antimicrob Agents Chemother* 2017, *61*, doi:10.1128/AAC.00435-17.
39. Larkin, E.; Hager, C.; Chandra, J.; Mukherjee, P.K.; Retuerto, M.; Salem, I.; Long, L.; Isham, N.; Kovanda, L.; Borroto-Esoda, K.; et al. The Emerging Pathogen *Candida Auris*: Growth Phenotype, Virulence Factors, Activity of Antifungals, and Effect of SCY-078, a Novel Glucan

- Synthesis Inhibitor, on Growth Morphology and Biofilm Formation. *Antimicrob Agents Chemother* 2017, 61, doi:10.1128/AAC.02396-16.
40. Zhu, Y.C.; Barat, S.A.; Borroto-Esoda, K.; Angulo, D.; Chaturvedi, S.; Chaturvedi, V. Pan-Resistant *Candida Auris* Isolates from the Outbreak in New York Are Susceptible to Ibrexafungerp (a Glucan Synthase Inhibitor). *Int J Antimicrob Agents* 2020, 55, 105922, doi:10.1016/j.ijantimicag.2020.105922.
41. Wiederhold, N.P.; Najvar, L.K.; Olivo, M.; Morris, K.N.; Patterson, H.P.; Catano, G.; Patterson, T.F. Ibrexafungerp Demonstrates *In Vitro* Activity against Fluconazole-Resistant *Candida Auris* and *In Vivo* Efficacy with Delayed Initiation of Therapy in an Experimental Model of Invasive Candidiasis. *Antimicrob Agents Chemother* 2021, 65, doi:10.1128/AAC.02694-20.
42. Chu, S.; Long, L.; Sherif, R.; McCormick, T.S.; Borroto-Esoda, K.; Barat, S.; Ghannoum, M.A. A Second-Generation Fungerp Analog, SCY-247, Shows Potent *In Vitro* Activity against *Candida Auris* and Other Clinically Relevant Fungal Isolates. *Antimicrob Agents Chemother* 2021, 65, doi:10.1128/AAC.01988-20.
43. Wall, G.; Chaturvedi, A.K.; Wormley, F.L.; Wiederhold, N.P.; Patterson, H.P.; Patterson, T.F.; Lopez-Ribot, J.L. Screening a Repurposing Library for Inhibitors of Multidrug-Resistant *Candida Auris* Identifies Ebselen as a Repositionable Candidate for Antifungal Drug Development. *Antimicrob. Agents Chemother.* 2018, 62, doi:10.1128/AAC.01084-18.
44. Mamouei, Z.; Alqarihi, A.; Singh, S.; Xu, S.; Mansour, M.K.; Ibrahim, A.S.; Uppuluri, P. Alexidine Dihydrochloride Has Broad-Spectrum Activities against Diverse Fungal Pathogens. *mSphere* 2018, 3, doi:10.1128/mSphere.00539-18.

45. Wall, G.; Herrera, N.; Lopez-Ribot, J.L. Repositionable Compounds with Antifungal Activity against Multidrug Resistant *Candida Auris* Identified in the Medicines for Malaria Venture's Pathogen Box. *J Fungi (Basel)* 2019, 5, doi:10.3390/jof5040092.
46. de Oliveira, H.C.; Monteiro, M.C.; Rossi, S.A.; Pemán, J.; Ruiz-Gaitán, A.; Mendes-Giannini, M.J.S.; Mellado, E.; Zaragoza, O. Identification of Off-Patent Compounds That Present Antifungal Activity Against the Emerging Fungal Pathogen *Candida Auris*. *Front Cell Infect Microbiol* 2019, 9, 83, doi:10.3389/fcimb.2019.00083.
47. Iyer, K.R.; Camara, K.; Daniel-Ivad, M.; Trilles, R.; Pimentel-Elardo, S.M.; Fossen, J.L.; Marchillo, K.; Liu, Z.; Singh, S.; Muñoz, J.F.; et al. An Oxindole Efflux Inhibitor Potentiates Azoles and Impairs Virulence in the Fungal Pathogen *Candida Auris*. *Nat Commun* 2020, 11, 6429, doi:10.1038/s41467-020-20183-3.
48. Cheng, Y.-S.; Roma, J.S.; Shen, M.; Mota Fernandes, C.; Tsang, P.S.; Forbes, H.E.; Boshoff, H.; Lazzarini, C.; Del Poeta, M.; Zheng, W.; et al. Identification of Antifungal Compounds against Multidrug-Resistant *Candida Auris* Utilizing a High-Throughput Drug-Repurposing Screen. *Antimicrob Agents Chemother* 2021, 65, doi:10.1128/AAC.01305-20.
49. Fuchs, F.; Hof, H.; Hofmann, S.; Kurzai, O.; Meis, J.F.; Hamprecht, A. Antifungal Activity of Nitroxoline against *Candida Auris* Isolates. *Clin Microbiol Infect* 2021, S1198-743X(21)00366-9, doi:10.1016/j.cmi.2021.06.035.
50. Rybak, J.M.; Muñoz, J.F.; Barker, K.S.; Parker, J.E.; Esquivel, B.D.; Berkow, E.L.; Lockhart, S.R.; Gade, L.; Palmer, G.E.; White, T.C.; et al. Mutations in TAC1B: A Novel Genetic Determinant of Clinical Fluconazole Resistance in *Candida Auris*. *mBio* 2020, 11, doi:10.1128/mBio.00365-20.

51. Bing, J.; Hu, T.; Zheng, Q.; Muñoz, J.F.; Cuomo, C.A.; Huang, G. Experimental Evolution Identifies Adaptive Aneuploidy as a Mechanism of Fluconazole Resistance in *Candida Auris*. *Antimicrob Agents Chemother* 2020, *65*, doi:10.1128/AAC.01466-20.
52. Carolus, H.; Pierson, S.; Muñoz, J.F.; Subotić, A.; Cruz, R.B.; Cuomo, C.A.; Van Dijck, P. Genome-Wide Analysis of Experimentally Evolved *Candida Auris* Reveals Multiple Novel Mechanisms of Multidrug Resistance. *mBio* 2021, *12*, doi:10.1128/mBio.03333-20.
53. Li, C.; Wang, J.; Zhou, B. The Metal Chelating and Chaperoning Effects of Clioquinol: Insights from Yeast Studies. *J. Alzheimers Dis.* 2010, *21*, 1249–1262, doi:10.3233/jad-2010-100024.
54. Prasad, R.; Banerjee, A.; Khandelwal, N.K.; Dhamgaye, S. The ABCs of *Candida Albicans* Multidrug Transporter Cdr1. *Eukaryot Cell* 2015, *14*, 1154–1164, doi:10.1128/EC.00137-15.
55. Prasad, R.; Balzi, E.; Banerjee, A.; Khandelwal, N.K. All about CDR Transporters: Past, Present, and Future. *Yeast* 2019, *36*, 223–233, doi:10.1002/yea.3356.
56. Znaidi, S.; Barker, K.S.; Weber, S.; Alarco, A.-M.; Liu, T.T.; Boucher, G.; Rogers, P.D.; Raymond, M. Identification of the *Candida Albicans* Cap1p Regulon. *Eukaryot Cell* 2009, *8*, 806–820, doi:10.1128/EC.00002-09.
57. Feng, W.; Yang, J.; Yang, L.; Li, Q.; Zhu, X.; Xi, Z.; Qiao, Z.; Cen, W. Research of Mrr1, Cap1 and *MDR1* in *Candida Albicans* Resistant to Azole Medications. *Exp Ther Med* 2018, *15*, 1217–1224, doi:10.3892/etm.2017.5518.
58. Sasse, C.; Schillig, R.; Reimund, A.; Merk, J.; Morschhäuser, J. Inducible and Constitutive Activation of Two Polymorphic Promoter Alleles of the *Candida Albicans* Multidrug Efflux Pump *MDR1*. *Antimicrob Agents Chemother* 2012, *56*, 4490–4494, doi:10.1128/AAC.00264-12.



59. Schubert, S.; Barker, K.S.; Znaidi, S.; Schneider, S.; Dierolf, F.; Dunkel, N.; Aïd, M.; Boucher, G.; Rogers, P.D.; Raymond, M.; et al. Regulation of Efflux Pump Expression and Drug Resistance by the Transcription Factors Mrr1, Upc2, and Cap1 in *Candida Albicans*. *Antimicrob Agents Chemother* 2011, 55, 2212–2223, doi:10.1128/AAC.01343-10.
60. Coste, A.T.; Karababa, M.; Ischer, F.; Bille, J.; Sanglard, D. *TAC1*, Transcriptional Activator of CDR Genes, Is a New Transcription Factor Involved in the Regulation of *Candida Albicans* ABC Transporters *CDR1* and *CDR2*. *Eukaryot Cell* 2004, 3, 1639–1652, doi:10.1128/EC.3.6.1639-1652.2004.
61. Liu, T.T.; Znaidi, S.; Barker, K.S.; Xu, L.; Homayouni, R.; Saidane, S.; Morschhäuser, J.; Nantel, A.; Raymond, M.; Rogers, P.D. Genome-Wide Expression and Location Analyses of the *Candida Albicans* Tac1p Regulon. *Eukaryot Cell* 2007, 6, 2122–2138, doi:10.1128/EC.00327-07.
62. Shukla, S.; Sauna, Z.E.; Prasad, R.; Ambudkar, S.V. Disulfiram Is a Potent Modulator of Multidrug Transporter Cdr1p of *Candida Albicans*. *Biochem Biophys Res Commun* 2004, 322, 520–525, doi:10.1016/j.bbrc.2004.07.151.
63. Xu, Y.; Lu, H.; Zhu, S.; Li, W.-Q.; Jiang, Y.-Y.; Berman, J.; Yang, F. Multifactorial Mechanisms of Tolerance to Ketoconazole in *Candida Albicans*. *Microbiol Spectr* 2021, 9, e0032121, doi:10.1128/Spectrum.00321-21.
64. Wasi, M.; Khandelwal, N.K.; Moorhouse, A.J.; Nair, R.; Vishwakarma, P.; Bravo Ruiz, G.; Ross, Z.K.; Lorenz, A.; Rudramurthy, S.M.; Chakrabarti, A.; et al. ABC Transporter Genes Show Upregulated Expression in Drug-Resistant Clinical Isolates of *Candida Auris*: A Genome-Wide Characterization of ATP-Binding Cassette (ABC) Transporter Genes. *Front Microbiol* 2019, 10, 1445, doi:10.3389/fmicb.2019.01445.

65. Zhang, H.; Niu, Y.; Tan, J.; Liu, W.; Sun, M.-A.; Yang, E.; Wang, Q.; Li, R.; Wang, Y.; Liu, W. Global Screening of Genomic and Transcriptomic Factors Associated with Phenotype Differences between Multidrug-Resistant and -Susceptible *Candida Haemulonii* Strains. *mSystems* 2019, 4, e00459-19, doi:10.1128/mSystems.00459-19.
66. Saini, P.; Gaur, N.A.; Prasad, R. Chimeras of the ABC Drug Transporter Cdr1p Reveal Functional Indispensability of Transmembrane Domains and Nucleotide-Binding Domains, but Transmembrane Segment 12 Is Replaceable with the Corresponding Homologous Region of the Non-Drug Transporter Cdr3p. *Microbiology (Reading)* 2006, 152, 1559–1573, doi:10.1099/mic.0.28471-0.
67. Gershon, H.; McNeil, M.W.; Parmegiani, R.; Godfrey, P.K. Antifungal Activity of 7- and 5,7-Substituted 8-Quinolinols. *J Med Chem* 1972, 15, 987–989, doi:10.1021/jm00279a028.
68. Gershon, H.; Parmegiani, R.; Godfrey, P.K. Antifungal Activity of 5-, 7-, and 5,7-Substituted 2-Methyl-8-Quinolinols. *Antimicrob Agents Chemother* 1972, 1, 373–375, doi:10.1128/aac.1.5.373.
69. Gershon, H.; McNeil, M.W.; Parmegiani, R.; Godfrey, P.K. Secondary Mechanisms of Antifungal Action of Substituted 8-Quinolinols. 3. 5,7,8-Substituted Quinolines. *J Med Chem* 1972, 15, 105–106, doi:10.1021/jm00271a033.
70. Treiber, C.; Simons, A.; Strauss, M.; Hafner, M.; Cappai, R.; Bayer, T.A.; Multhaup, G. Clioquinol Mediates Copper Uptake and Counteracts Copper Efflux Activities of the Amyloid Precursor Protein of Alzheimer's Disease. *J. Biol. Chem.* 2004, 279, 51958–51964, doi:10.1074/jbc.M407410200.
71. Tardiff, D.F.; Brown, L.E.; Yan, X.; Trilles, R.; Jui, N.T.; Barrasa, M.I.; Caldwell, K.A.; Caldwell, G.A.; Schaus, S.E.; Lindquist, S. Dihydropyrimidine-Thiones and Clioquinol

- Synergize To Target  $\beta$ -Amyloid Cellular Pathologies through a Metal-Dependent Mechanism. *ACS Chem Neurosci* 2017, 8, 2039–2055, doi:10.1021/acchemneuro.7b00187.
72. Yan, C.; Wang, S.; Wang, J.; Li, H.; Huang, Z.; Sun, J.; Peng, M.; Liu, W.; Shi, P. Clioquinol Induces G2/M Cell Cycle Arrest through the up-Regulation of *TDH3* in *Saccharomyces Cerevisiae*. *Microbiol. Res.* 2018, 214, 1–7, doi:10.1016/j.micres.2018.05.006.
73. You, Z.; Zhang, C.; Ran, Y. The Effects of Clioquinol in Morphogenesis, Cell Membrane and Ion Homeostasis in *Candida Albicans*. *BMC Microbiol* 2020, 20, 165, doi:10.1186/s12866-020-01850-3.
74. Hunsaker, E.W.; Franz, K.J. *Candida Albicans* Reprioritizes Metal Handling during Fluconazole Stress. *Metallomics* 2019, 11, 2020–2032, doi:10.1039/c9mt00228f.
75. Hunsaker, E.W.; Franz, K.J. Copper Potentiates Azole Antifungal Activity in a Way That Does Not Involve Complex Formation. *Dalton Trans* 2019, 48, 9654–9662, doi:10.1039/c9dt00642g.
76. Hunsaker, E.W.; Yu, C.-H.A.; Franz, K.J. Copper Availability Influences the Transcriptomic Response of *Candida Albicans* to Fluconazole Stress. *G3 (Bethesda)* 2021, 11, doi:10.1093/g3journal/jkab065.
77. Eldesouky, H.E.; Lanman, N.A.; Hazbun, T.R.; Seleem, M.N. Aprepitant, an Antiemetic Agent, Interferes with Metal Ion Homeostasis of *Candida Auris* and Displays Potent Synergistic Interactions with Azole Drugs. *Virulence* 2020, 11, 1466–1481, doi:10.1080/21505594.2020.1838741.
78. Savage, K.A.; Parquet, M. del C.; Allan, D.S.; Davidson, R.J.; Holbein, B.E.; Lilly, E.A.; Fidel, P.L. Iron Restriction to Clinical Isolates of *Candida Albicans* by the Novel Chelator DIBI

- Inhibits Growth and Increases Sensitivity to Azoles *In Vitro* and *In Vivo* in a Murine Model of Experimental Vaginitis. *Antimicrob Agents Chemother* 2018, 62, doi:10.1128/AAC.02576-17.
79. Sun, L.; Hang, C.; Liao, K. Synergistic Effect of Caffeic Acid Phenethyl Ester with Caspofungin against *Candida Albicans* Is Mediated by Disrupting Iron Homeostasis. *Food Chem Toxicol* 2018, 116, 51–58, doi:10.1016/j.fct.2018.04.014.
80. Fiori, A.; Van Dijck, P. Potent Synergistic Effect of Doxycycline with Fluconazole against *Candida Albicans* Is Mediated by Interference with Iron Homeostasis. *Antimicrob Agents Chemother* 2012, 56, 3785–3796, doi:10.1128/AAC.06017-11.
81. Polvi, E.J.; Averette, A.F.; Lee, S.C.; Kim, T.; Bahn, Y.-S.; Veri, A.O.; Robbins, N.; Heitman, J.; Cowen, L.E. Metal Chelation as a Powerful Strategy to Probe Cellular Circuitry Governing Fungal Drug Resistance and Morphogenesis. *PLoS Genet* 2016, 12, e1006350, doi:10.1371/journal.pgen.1006350.
82. Mao, X.; Schimmer, A.D. The Toxicology of Clioquinol. *Toxicol Lett* 2008, 182, 1–6, doi:10.1016/j.toxlet.2008.08.015.
83. Perez, D.R.; Sklar, L.A.; Chigaev, A. Clioquinol: To Harm or Heal. *Pharmacol Ther* 2019, 199, 155–163, doi:10.1016/j.pharmthera.2019.03.009.
84. Nakae, K.; Yamamoto, S.; Shigematsu, I.; Kono, R. Relation between Subacute Myelo-Optic Neuropathy (S.M.O.N.) and Clioquinol: Nationwide Survey. *Lancet* 1973, 1, 171–173, doi:10.1016/s0140-6736(73)90004-4.
85. Asao, M. Clioquinol and S.M.O.N.: Reanalysis of Original Data. *Lancet* 1979, 1, 446, doi:10.1016/s0140-6736(79)90928-0.
86. Meade, T.W. Subacute Myelo-Optic Neuropathy and Clioquinol. An Epidemiological Case-History for Diagnosis. *Br J Prev Soc Med* 1975, 29, 157–169, doi:10.1136/jech.29.3.157.

87. Woodworth, M.H.; Dynerman, D.; Crawford, E.D.; Doernberg, S.B.; Ramirez-Avila, L.; Serpa, P.H.; Nichols, A.; Li, L.M.; Lyden, A.; Tato, C.M.; et al. Sentinel Case of *Candida Auris* in the Western United States Following Prolonged Occult Colonization in a Returned Traveler from India. *Microb. Drug Resist.* 2019, *25*, 677–680, doi:10.1089/mdr.2018.0408.
88. Odds, F.C.; Brown, A.J.; Gow, N.A. *Candida Albicans* Genome Sequence: A Platform for Genomics in the Absence of Genetics. *Genome Biol* 2004, *5*, 230.
89. Aszalos, A.; Robison, R.S.; Lemanski, P.; Berk, B. Trienine, an Antitumor Triene Antibiotic. *J Antibiot (Tokyo)*. 1968, *21*, 611–615.
90. Maestrone, G.; Semar, R. Establishment and Treatment of Cutaneous *Candida Albicans* Infection in the Rabbit. *Naturwissenschaften* 1968, *55*, 87–88.
91. Meyers, E.; Miragila, G.J.; Smith, D.A.; Basch, H.I.; Pansy, F.E.; Trejo, W.H.; Donovan, R. Biological Characterization of Prasinomycin, a Phosphorus-Containing Antibiotic. *Appl Microbiol* 1968, *16*, 603–608.
92. Sullivan, D.J.; Westerneng, T.J.; Haynes, K.A.; Bennett, D.E.; Coleman, D.C. *Candida Dubliniensis* Sp. Nov.: Phenotypic and Molecular Characterization of a Novel Species Associated with Oral Candidosis in HIV-Infected Individuals. *Microbiology (Reading, Engl.)* 1995, *141 ( Pt 7)*, 1507–1521, doi:10.1099/13500872-141-7-1507.
93. Ennis, C.L.; Hernday, A.D.; Nobile, C.J. A Markerless CRISPR-Mediated System for Genome Editing in *Candida Auris* Reveals a Conserved Role for Cas5 in the Caspofungin Response. *Microbiol Spectr* 2021, *9*, e0182021, doi:10.1128/Spectrum.01820-21.
94. CLSI *Reference Method for Broth Dilution Antifungal Susceptibility Testing of Yeasts. 4th Edition, CLSI Standard M27*; 4th ed.; Clinical and Laboratory Standards Institute: Wayne, PA, 2017;

95. Horst, J.A.; Wu, W.; DeRisi, J.L. MinorityReport, Software for Generalized Analysis of Causal Genetic Variants. *Malar J* 2017, *16*, 90, doi:10.1186/s12936-017-1730-2.

## Chapter 6:

### Real-world performance testing of a SARS-CoV-2 rapid antigen test in San Francisco, California

This chapter is a reprint of:

Pilarowski G, Lebel P, Sunshine S, Liu J, Crawford E, Marquez C, Rubio L, Chamie G, Martinez J, Peng J, Black D, Wu W, Pak J, Laurie MT, Jones D, Miller S, Jacobo J, Rojas S, Rojas S, Nakamura R, Tulier-Laiwa V, Petersen M, Havlir DV; CLIAHUB Consortium, DeRisi J. Performance Characteristics of a Rapid Severe Acute Respiratory Syndrome Coronavirus 2 Antigen Detection Assay at a Public Plaza Testing Site in San Francisco. *J Infect Dis.* 2021; Apr 8;223(7):1139-1144. doi: 10.1093/infdis/jiaa802.

Supplemental files that are not figures can be found with the original work.

## ***Abstract***

We evaluated the performance of the Abbott BinaxNOW rapid antigen test for coronavirus disease 2019 (Binax-CoV2) to detect virus among persons, regardless of symptoms, at a public plaza site of ongoing community transmission. Titration with cultured severe acute respiratory syndrome coronavirus 2 yielded a human observable threshold between  $1.6 \times 10^4$ - $4.3 \times 10^4$  viral RNA copies (cycle threshold [Ct], 30.3-28.8). Among 878 subjects tested, 3% (26 of 878) were positive by reverse-transcription polymerase chain reaction, of whom 15 of 26 had a Ct <30, indicating high viral load; of these, 40% (6 of 15) were asymptomatic. Using this Ct threshold (<30) for Binax-CoV2 evaluation, the sensitivity of Binax-CoV2 was 93.3% (95% confidence interval, 68.1%-99.8%) (14 of 15) and the specificity was 99.9% (99.4%-99.9%) (855 of 856).

## ***Main Text***

The global pandemic of severe acute respiratory syndrome coronavirus 2 (SARS-CoV-2) infection has spread at an unprecedented pace [1] fueled by efficient transmission of infection by the respiratory route, including by asymptomatic and presymptomatic persons. Instances of successful control make use of masking, social distancing, and aggressive testing, tracing, and quarantine [2].

To date, the cornerstone of testing has been reverse-transcription polymerase chain reaction (RT-PCR) examination of respiratory secretions, which has excellent sensitivity and specificity but is expensive and requires sophisticated equipment and highly trained personnel [3]. In practice, these features have often generated testing delays compromising their utility [4]. As a result, there is interest in rapid and economical assays that circumvent these limitations [5]. However, methods that do not include an amplification step are inherently less sensitive; their proper deployment will



therefore require a rigorous evaluation of performance characteristics in different epidemiologic settings.

Lateral flow antigen detection diagnostics have been deployed for a variety of infectious diseases including malaria, RSV, and influenza. The Abbott BinaxNOW COVID-19 Ag Card (hereafter referred to as Binax-CoV2) is one such assay that detects viral nucleocapsid (N) protein directly from nasal swab samples. The test requires no instrumentation; results are scored visually and returned within 15 minutes. In August 2020, the Food and Drug Administration issued an emergency use authorization for the diagnosis of SARS-CoV-2 infection in symptomatic patients within 7 days of symptom onset [6]. The US Department of Health and Human Services has distributed 150 million test kits. Given the value of a rapid assessment of infectiousness, there is anticipated use in a broad range of subjects, including those who are asymptomatic. Here we present a systematic examination of the performance characteristics of the Binax-CoV2 test in a community screening setting where testing was offered for symptomatic and asymptomatic subjects.

## ***Methods***

### *Study Population and Specimen Collection*

Over 3 days in September 2020, we offered testing in the Mission District, a Latinx-predominant neighborhood, known from prior surveys to have an elevated prevalence of SARS-CoV-2 infection [7, 8]. Walk-up, free testing was conducted at a plaza located at an intersection of the Bay Area-wide subway system (BART) and the San Francisco city bus/streetcar system (MUNI). On the day of testing, participants self-reported symptoms and date of onset, demographics, and contact information, as required by state and federal reporting guidelines. A laboratory technician performed sequential anterior swab (both nares) for the Binax-CoV2 assay

followed by a second swab (both nares) for RT-PCR. Participants were notified of RT-PCR test results. For this study, Binax-CoV2 results were not reported back to study subjects.

#### *Laboratory Testing for SARS-CoV-2*

RT-PCR detection of SARS-CoV-2 was performed at the Clinical Laboratory Improvement Amendments–certified laboratory operated by the University of California, San Francisco (UCSF), and the Chan Zuckerberg Biohub, as described elsewhere [9, 10].

#### *Field Testing Using Binax-CoV2 Assay*

The Binax-CoV2 assay was performed by technicians on site as described by the manufacturer using the supplied swabs. Each assay was read by 2 independent observers, and a site supervisor served as a tiebreaker. Beginning on day 2 of the study, each Binax-CoV2 assay card was scanned onsite using a color document scanner (CanoScan LIDE 400; Canon). Sample bands were retrospectively quantified from image data. Sample and background regions were localized by offset from the control band, and relative mean pixel intensity decreases were calculated from blue and green channels averaged with respect to background.

#### *Titration of in vitro Cultured SARS-CoV-2 on Binax-CoV2 Cards*

SARS-CoV-2 from a UCSF clinical specimen was isolated, propagated and plaqued on Huh7.5.1 cells overexpressing angiotensin-converting enzyme 2 and transmembrane serine protease 2 (TMPRSS2) [11]. Viral titers were determined using standard plaque assays [12]. For titration experiments, SARS-CoV-2 was diluted in Dulbecco phosphate-buffered saline, and 40  $\mu$ L of each dilution was absorbed onto the supplied swab samples. Images of Binax-CoV2 cards

were taken with an Apple iPhone 6. All experiments using cultured SARS-CoV-2 were conducted in a biosafety level 3 laboratory.

### *N Protein Titration Assay*

SARS-CoV-2 N protein (1–419) was expressed in BL21(DE3) *Escherichia coli* and purified by nickel–nitrilotriacetic acid chromatography, incorporating a 1-mol/L sodium chloride, 50-mmol/L imidazole wash to remove bound RNA. Six concentrations of N protein were tested on 10 lots of Binax-CoV2 kits, and 40 µL of N protein was absorbed onto the provided swab sample.

### *Ethics Statement*

The UCSF Committee on Human Research determined that the study met criteria for public health surveillance. All participants provided informed consent for dual testing.

## **Results**

### *Binax-CoV2 Performance Using a Titration of in vitro Cultured SARS-CoV-2*

To explore the relationship of RT-PCR cycle threshold (Ct), viral load, and the corresponding visual Binax-CoV2 result, a dilution series of laboratory-cultured SARS-CoV-2 with known titers was assayed with both RT-PCR and Binax-CoV2 (Figure 6.1). For this stock of virus, the threshold for detectability by human eye on the Binax-CoV2 assay was between 1.6 and  $4.3 \times 10^4$  viral copies (100–250 plaque-forming units), corresponding to t values (average of N and E genes) of 30.3 and 28.8, respectively, in this assay.

### *Community RT-PCR Testing Results*

Of the 878 subjects tested, 54% were male, 77% were 18–50 years of age, 81% self-identified as Latinx, and 84% reported no symptoms in the 14 days before testing. Twenty-six persons (3%) were RT-PCR positive; of these, 15 (58%) had a Ct <30, and 6 of the 15 (40%) were asymptomatic. Among asymptomatic individuals with a Ct <30, 4 of 6 developed symptoms within 2 days after testing. Of the 11 persons RT-PCR–positive with a Ct >30, 4 reported symptom onset  $\geq 7$  days before testing, 1 reported symptom onset 3 days before testing, and the remainder reported no symptoms.

### *Comparison of RT-PCR and Binax-CoV2 Testing Results from Community Testing*

Because the readout of the Binax-CoV2 assay is by visual inspection, results may be subjective, especially when bands are faint or partial. The manufacturer’s instructions suggest scoring any visible band as positive. On day 1 of testing, these reading instructions were used and 217 samples tested, of which 214 yielded valid Binax-CoV2 results: 7 of 214 (3.3%) were RT-PCR positive; using the manufacturer’s proposed criteria, 5 of these 7 were Binax-CoV2 positive. Of 214, a total of 207 were RT-PCR negative, 9 (4.3%) of which were Binax-CoV2 positive. Thus, using the manufacturer’s criteria, 9 of 14 Binax-CoV2–positive tests (64%) in this population of 217 tests had false-positive results (Binax-CoV2 positive/RT-PCR negative). We thought that these initial criteria used on day 1 of testing were insufficient for classifying faint Binax-CoV2 assay bands, resulting in excessive false-positive calls.

On subsequent testing days, we evaluated additional criteria for classifying a band as positive, in consultation with experts from the manufacturer’s research staff. Optimal performance occurred when the bands were scored as positive, if they extended across the full width of the strip,

irrespective of the intensity of the band. Updated scoring criteria were implemented by the third day of testing, when a total of 292 tests were administered. Of this total, 283 were RT-PCR negative, all of which scored Binax-CoV2 negative, demonstrating these updated reading criteria markedly alleviated false-positive readings. Of the 292 total day 3 tests, 9 were RT-PCR positive, of which 5 were Binax-CoV2 positive for antigen with these updated scoring criteria. Of the 9 RT-PCR-positive samples, the 4 that were Binax-CoV2 negative had a Ct >30, consistent with our laboratory-observed limit of detection for Binax-CoV2. We find that scoring a test as positive if bands extend across the full width of the strip, irrespective of band intensity, is the least subjective and easiest method to implement in the field, and we have developed a training tool (<https://unitedinhealth.org/binax-training>).

The results of the 26 RT-PCR-positive individuals identified throughout the 3-day study were stratified by RT-PCR test Ct value and categorized according to Binax-CoV2 result (Figure 6.2). The rapid antigen detection test performed well in samples with higher viral loads: 15 of 16 samples with a Ct <32 were Binax-CoV2 positive (Figure 6.2A). By contrast, none of the 10 samples with a Ct  $\geq$ 34 were positive by Binax-CoV2 antigen detection. Retrospective image quantification of Binax-CoV2 sample band intensity is correlated with RT-PCR Ct values for those individuals (Figure 6.2B). In each case, the corresponding image is shown to demonstrate the correspondence between RT-PCR and the visual result (Figure 6.2C).

### *Sensitivity and Specificity*

RT-PCR is considered a reference standard [3] and, in the RT-PCR assay used in this study, has a limit of detection of 100 viral RNA copies/mL. Direct antigen assays are inherently not as sensitive as RT-PCR. In the context of community based testing, we defined a threshold for high

virus levels corresponding to the range of highest probability of transmissibility: a Ct of 30, which corresponds to a viral RNA copy number of approximately  $1.9 \times 10^4$  in this assay [10, 13]. Using this Ct <30 case definition and 95% confidence intervals (CIs), the sensitivity of the Binax-CoV2 was 93.3% (95% CI, 68.1%–99.8%) (14 of 15), and the specificity was 99.9% (99.4%–99.9%) (855 of 856). Adjusting the threshold to a more conservative Ct value of 33 ( $2.6 \times 10^3$  viral RNA copies), the sensitivity was 93.8% (95% CI, 69.8%–99.8%) (15 of 16), and the specificity was 100% (99.6%–100%) (855 of 855). Without a Ct threshold, the sensitivity of the Binax-CoV2 assay was (57.7%; 95% CI, 36.9%–76.6%) (15 of 26), and the specificity was (100%; 99.6%–100%) (845 of 845). Given that the Binax-CoV2 assay detects infected individuals with high levels of virus ( $>10^4$ ), the sensitivity of the assay in the absence of a threshold will largely depend on the viral kinetics within the testing population. Sensitivity and specificity calculations were completed with the final scoring criteria, using retroactive Binax-CoV2 scores from images covering all 3 study days.

#### *Evaluation of Binax-CoV2 Lot-to-Lot Variation*

We quantified lot-to-lot variability in 10 different lots of Binax-CoV2 card tests using a dilution series of N protein. (Figure 6.3). At protein concentrations of  $\geq 17.2$  ng/mL, a sample band was detected in all lots and thus would not affect the outcome of this binary assay (Figure 6.3A).

#### ***Discussion***

The data reported here describe the performance characteristics of the Binax-CoV2 antigen detection kit in the context of community testing including asymptomatic subjects. These results indicate a clear relationship between relative viral load and test positivity and provide a practical,

real-world criterion to assist calling results in this setting. We found that small training modifications reduced the presence of false-positives, a legitimate concern for the rollout of these tests.

The currently approved emergency use authorization for the Binax-CoV2 assay specifies use only in symptomatic individuals. The results presented here suggest that the Binax-CoV2 test should not be limited to symptomatic testing alone. Many asymptomatic individuals have high viral loads (corresponding to low Ct values) and, therefore, have a high probability of being infectious and transmitting the virus, a feature and likely driver of the pandemic that we and others have observed previously [7, 14]. Limiting use of Binax-CoV2 to symptomatic individuals would have missed nearly half of the SARS-CoV-2 infections in the current study.

Furthermore, the impact of testing on forward transmission is hampered by long wait times. Our group reported previously that in the community setting, by the time a person is tested, counseled, and situated under isolation conditions, the effective isolation period is often nearly over [8]. This is particularly true for many communities of color, where reported delays in accessing tests and results are even longer [4, 15]. Rapid tests could reduce these delays and maximize the time of effective isolation. Limitations of our study include its cross-sectional design and the overall small number of RT-PCR positive cases. Additional field performance of this assay is needed and will help inform optimal use strategies. We recommend evaluating the Binax-CoV2 assay side by side with RT-PCR in each context where it will be used before using Binax-CoV2 without RT-PCR.

During the early stages of infection, viral load may be too low to detect by direct antigen assays such as Binax-CoV2. This inherent lower sensitivity may be offset by faster turn-around and higher frequency of testing, with overall lower cost, relative to RT-PCR methods. That said,

for persons who present with a high index of suspicion of coronavirus disease 2019 and a negative Binax-CoV2 result, the test should be complemented with RT-PCR or a repeated Binax-CoV2 test at a later time to make sure cases are not missed.

In summary, under field conditions with supplementary technician training, the Binax-CoV2 assay accurately detected SARS-CoV-2 infection with high viral loads in both asymptomatic and symptomatic individuals. The Binax-CoV2 test could be a valuable asset in an arsenal of testing tools for the mitigation of SARS-CoV-2 spread, as rapid identification of highly infectious individuals is critical.

### ***Supplementary Data***

Supplementary materials are available at *The Journal of Infectious Diseases* online. Consisting of data provided by the authors to benefit the reader, the posted materials are not copyedited and are the sole responsibility of the authors, so questions or comments should be addressed to the corresponding author.



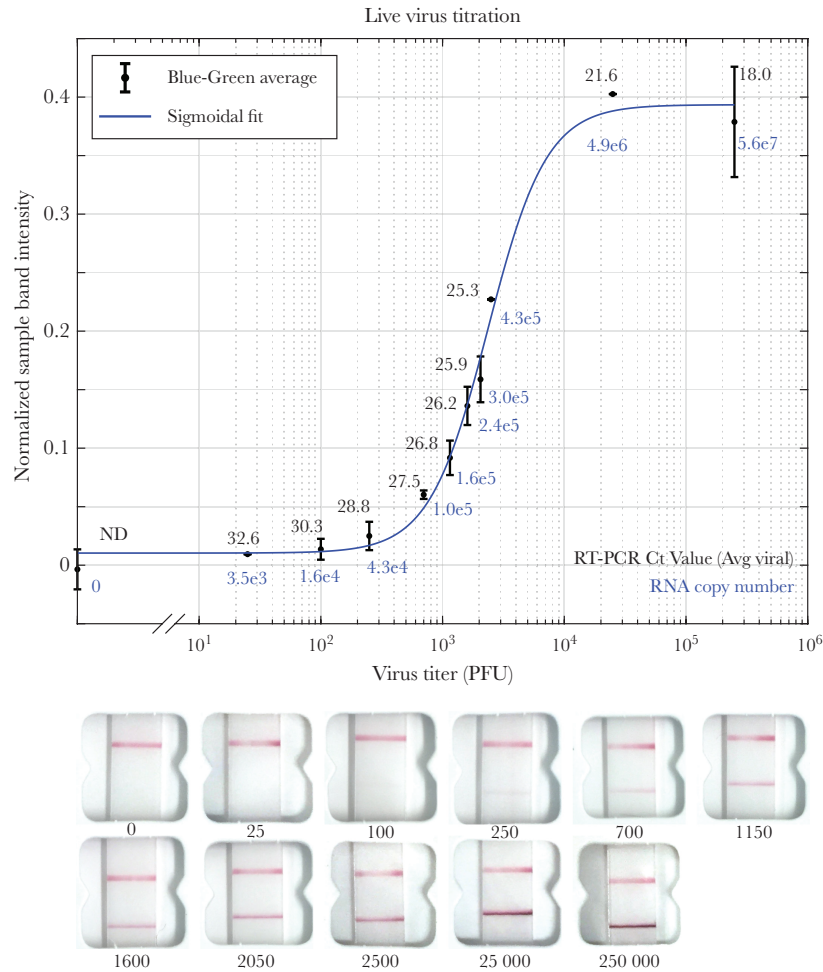


**Figure 6.1. Titration of in vitro grown severe acute respiratory syndrome coronavirus 2 and detection with Binax-CoV2 assay.** *Top*, Normalized Binax-CoV2 sample band intensity (blue-green average) for cards loaded with a known amount of virus. Error bars represent standard deviation of sample band intensity of technical replicates. Reverse-transcription polymerase chain reaction (RT-PCR) testing was performed at the CLIAHUB consortium [10]. Corresponding RT-PCR cycle threshold (Ct) values (average of N and E gene probes) are shown in black, and the corresponding RNA copy numbers in blue. Note that Ct and genome copy number correlation varies by RT-PCR platform. *Bottom*, Representative card images from each data point. Abbreviation: PFUs, plaque-forming units.

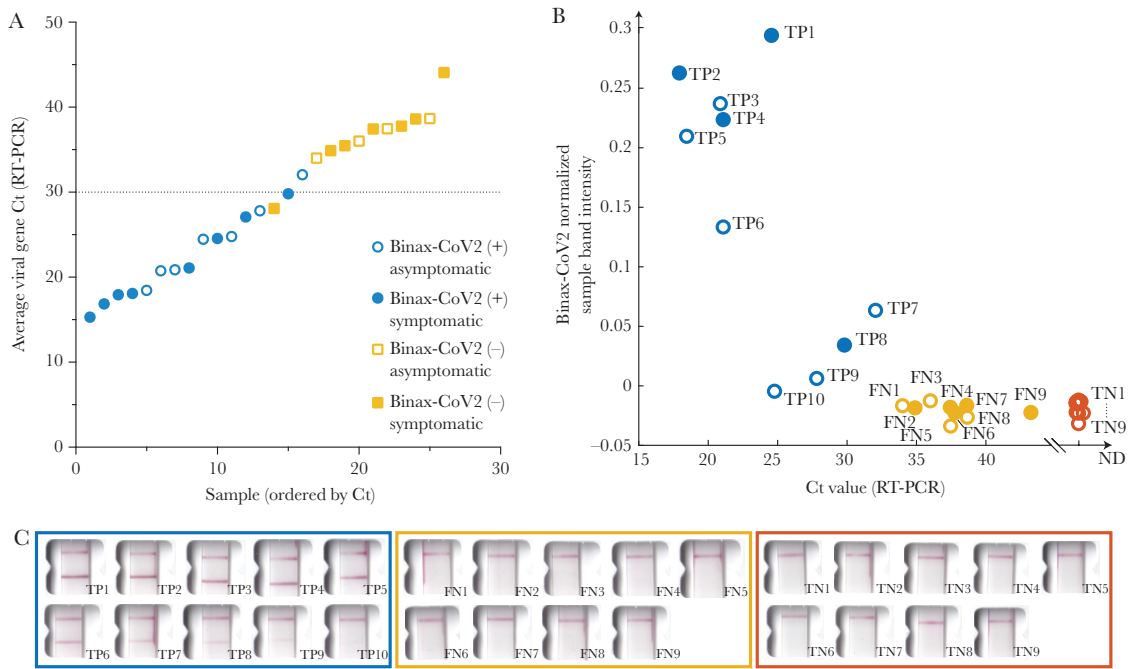


**Figure 6.2. Comparison of Binax-CoV2 test with quantitative reverse-transcription polymerase chain reaction (RT-PCR) test.** *A*, Average viral cycle threshold (Ct) values from all 26 RT-PCR–positive individuals from the community study, plotted in ascending order. Blue circles indicate Binax-CoV2–positive samples; yellow squares, Binax-CoV2–negative samples. Open symbols represent individuals who were asymptomatic on the day of the test and filled symbols, those who reported symptoms on that day. *B*, Normalized sample band signal from retrospective image analysis of Binax-CoV2 cards was plotted as a function of Ct value for all available scanner images (19 of 26 RT-PCR–positive samples and a random subset of RT-PCR–negative samples). Binax-CoV2 true-positives are shown in blue and labeled TP; false-negatives, shown in yellow and labeled FN; and true-negatives, shown in red and labeled TN. *C*, Corresponding Binax-CoV2 card images from the data in *B*.

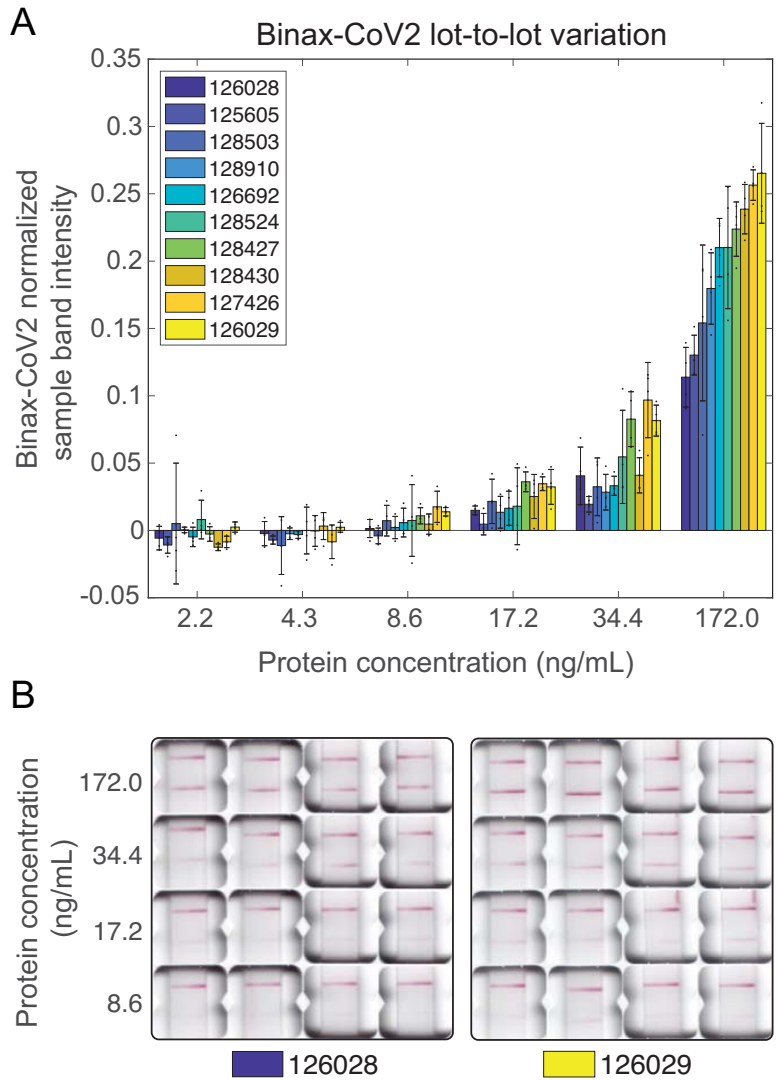


**Figure 6.3. Variability of signal intensity in Binax-CoV2 card lots.** (A) Normalized sample band signal intensity of Binax-CoV2 cards from different lots run with a dilution series of purified SARS-CoV-2 N protein with known concentration. N=4 cards per lot per concentration. Each point represents one card. (B) Images of each card test for the highest (126029) and lowest (126028) performing lots.

## Chapter 6 References

1. Johns Hopkins Coronavirus Resource Center. COVID-19 dashboard by the Center for Systems Science and Engineering (CSSE) at Johns Hopkins University (JHU). <https://coronavirus.jhu.edu/map.html>. Accessed 23 October 2020.
2. Baker MG, Wilson N, Anglemeyer A. Successful elimination of Covid-19 transmission in New Zealand. *N Engl J Med* 2020; 383:e56.
3. Esbin MN, Whitney ON, Chong S, Maurer A, Darzacq X, Tjian R. Overcoming the bottleneck to widespread testing: a rapid review of nucleic acid testing approaches for COVID-19 detection. *RNA* 2020; 26:771–83.
4. Chwe H, Quintana A, Lazer D, et al. . The state of the nation: a 50-state COVID-19 survey. Report #17: COVID-19 test result times. October 2020. <http://www.kateto.net/covid19/COVID19%20CONSORTIUM%20REPORT%2017%20TESTING%20OCT%202020.pdf>. Accessed 23 October 2020.
5. Mina MJ, Parker R, Larremore DB. Rethinking Covid-19 test sensitivity—a strategy for containment. *N Engl J Med* 2020; 383:e120.
6. Abbott Diagnostics. Abbott BinaxNOW COVID-19 Ag package insert, version 1.6. 2020. <https://www.fda.gov/media/141570/download>. Accessed 20 October 2020.
7. Chamie G, Marquez C, Crawford E, et al. . SARS-CoV-2 community transmission disproportionately affects Latinx population during shelter-in-place in San Francisco [published online ahead of print August 21, 2020]. *Clin Infect Dis* 2020; doi:10.1093/cid/ciaa1234
8. Kerkhoff AD, Sachdev D, Mizany S, et al. . Evaluation of a novel community-based COVID-19 ‘Test-to-Care’ model for low-income populations. *PLoS One* 2020; 15:e0239400.

9. Crawford ED, Acosta I, Ahyong V, et al. . Rapid deployment of SARS-CoV-2 testing: the CLIAHUB. *PLoS Pathog* 2020; 16:e1008966.
10. Vanaerschot M, Mann SA, Webber JT, et al. . Identification of a polymorphism in the N gene of SARS-CoV-2 that adversely impacts detection by RT-PCR. *J Clin Microbiol* 2020; 59:e02369-20.
11. Wang R, Simoneau CR, Kulsuptrakul J, et al. . Functional genomic screens identify human host factors for SARS-CoV-2 and common cold coronaviruses. *bioRxiv* [Preprint: not peer reviewed]. 24 September 2020. Available from: <https://www.biorxiv.org/content/10.1101/2020.09.24.312298v1>. [Google Scholar]
12. Honko AN, Storm N, Bean DJ, Vasquez JH, Downs SN, Griffiths A. Rapid quantification and neutralization assays for novel coronavirus SARS-CoV-2 using Avicel R RC-591 semi-solid overlay. 2020. <https://www.preprints.org/manuscript/202005.0264/v1>. Accessed 23 October 2020.
13. Wölfel R, Corman VM, Guggemos W, et al. . Virological assessment of hospitalized patients with COVID-2019. *Nature* 2020; 581:465–9.
14. Oran DP, Topol EJ. Prevalence of asymptomatic SARS-CoV-2 infection: a narrative review. *Ann Intern Med* 2020:362–7.
15. Kim HN, Lan KF, Nkyekyer E, et al. . Assessment of disparities in COVID-19 testing and infection across language groups in Seattle, Washington. *JAMA Netw Open* 2020; 3:e2021213.

## Chapter 7:

### Differential secondary attack rates of SARS-CoV-2 variants measured by local viral genomic surveillance

This chapter is a reprint of:

Peng J\*, Liu J\*, Mann SA\*, Mitchell AM\*, Laurie MT\*, Sunshine S\*, Pilarowski G\*, Ayscue P\*, Kistler A, Vanaerschot M, Li LM, McGeever A, Chow ED, Marquez C, Nakamura R, Rubio L, Chamie G, Jones D, Jacobo J, Rojas S, Rojas S, Tulier-Laiwa V, Black D, Martinez J, Naso J, Schwab J, Petersen M, Havlir D, DeRisi J; IDseq Team. Estimation of Secondary Household Attack Rates for Emergent Spike L452R Severe Acute Respiratory Syndrome Coronavirus 2 (SARS-CoV-2) Variants Detected by Genomic Surveillance at a Community-Based Testing Site in San Francisco. *Clin Infect Dis.* 2022; Jan 7;74(1):32-39. doi: 10.1093/cid/ciab283.

\*These authors contributed equally to this work

Supplemental files that are not figures can be found with the original work.

## ***Abstract***

### *Background*

Sequencing of the severe acute respiratory syndrome coronavirus 2 (SARS-CoV-2) viral genome from patient samples is an important epidemiological tool for monitoring and responding to the pandemic, including the emergence of new mutations in specific communities.

### *Methods*

SARS-CoV-2 genomic sequences were generated from positive samples collected, along with epidemiological meta- data, at a walk-up, rapid testing site in the Mission District of San Francisco, California during 22 November to 1 December, 2020, and 10–29 January 2021. Secondary household attack rates and mean sample viral load were estimated and compared across observed variants.

### *Results*

A total of 12 124 tests were performed yielding 1099 positives. From these, 928 high-quality genomes were generated. Certain viral lineages bearing spike mutations, defined in part by L452R, S13I, and W152C, comprised 54.4% of the total sequences from January, compared to 15.7% in November. Household contacts exposed to the “California” or “West Coast” variants (B.1.427 and B.1.429) were at higher risk of infection compared to household contacts exposed to lineages lacking these variants (0.36 vs 0.29, risk ratio [RR] = 1.28; 95% confidence interval [CI]: 1.00–1.64). The reproductive number was estimated to be modestly higher than other lineages spreading in California during the second half of 2020. Viral loads were similar among persons infected with West Coast versus non-West Coast strains, as was the proportion of individuals with symptoms (60.9% vs 64.3%).

## *Conclusions*

The increase in prevalence, relative household attack rates, and reproductive number are consistent with a modest transmissibility increase of the West Coast variants.

## *Main Text*

Genomic surveillance during the severe acute respiratory syndrome coronavirus 2 (SARS-CoV-2) pandemic is a critical source of situational intelligence for epidemiological control measures, including outbreak investigations and detection of emergent variants [1]. Countries with robust, unified public health systems and systematic genomic surveillance have been able to rapidly detect SARS-CoV-2 variants with increased transmission characteristics, and mutations that potentially subvert both naturally acquired or vaccination-based immunity (eg, COVID-19 Genomics UK Consortium). Examples include the rapidly spreading B.1.1.7 lineage documented in the United Kingdom and the B.1.351 lineage described from South Africa, or the P.1/P.2 lineages that harbor the spike E484K mutation that is associated with reduced neutralization in laboratory experiments [2–5].

In the United States, genomic surveillance is sparse relative to the number of confirmed cases (27.8 million as of 20 February 2021), with 123 672 genomes deposited in the GISAID database, representing only 0.4% of the total reported cases. Despite the low rates of US genomic surveillance, independent local programs and efforts have contributed to our understanding of variant emergence and spread [6–8]. The appearance of new nonsynonymous mutations highlight the utility of this approach in the United States [9].

Genomic sequencing of SARS-CoV-2 in California has predominantly been conducted by academic researchers and non-profit biomedical research institutions (eg, the Chan Zuckerberg Biohub and the Andersen Lab at the Scripps Research Institute) in conjunction with state and local



public health partners. These efforts identified an apparent increase in the prevalence of lineages B.1.427 and B.1.429 (“California” or “West Coast” variant), which share S gene nonsynonymous mutations at sites 13, 152, 452, and 614, during December 2020 to February 2021 when California was experiencing the largest peak of cases observed during the pandemic. Although the cluster of mutations was first observed in a sample from May 2020, these variants rose from representing <1% of the consensus genomes recovered from California samples collected in October 2020 (5/546; 0.91%) to over 50% of those collected during January 2021 (2309/4305; 53.6%; GISAID accessed 20 February 2021).

The majority of sequencing efforts in the United States utilize samples from symptomatic individuals or out- breaks, introducing selection bias making interpretation of trends, such as the rise in lineage prevalence, complex. Furthermore, clinical remnant samples are most often de-linked from case information, thus eliminating the possibility of evaluating genotypes with detailed household information, and other metadata useful for investigation of transmission dynamics.

Sequencing cases identified during intensive, longitudinal community-based testing may help address both limitations. Here we describe an investigation of the prevalence of the West Coast variants as well as other variants among persons tested at a community testing site situated in the Mission District of San Francisco, a neighborhood with high coronavirus disease 2019 (COVID-19) incidence, during 2 periods: 22 November to 1 December 2020 and 10–29 January 2021. Using metadata collected at the testing site and supplementary household testing, we estimated secondary household attack rate with respect to viral genotype to evaluate relative transmissibility of identified variants.

## ***Methods***

### *Study Setting and Population*

Over 22 November to 1 December 2020 and 10–29 January 2021, BinaxNOW<sup>TM</sup> rapid antigen tests were performed at the 24th & Mission BART (public transit) station in the Mission District of San Francisco, a setting of ongoing community transmission, predominantly among Latinx persons [10, 11]. Tests for SARS-CoV-2 were performed free of charge on a walk-up, no-appointment basis, including persons  $\geq 1$  year of age and regardless of symptoms, through “Unidos en Salud,” an academic, community (Latino Task Force) and city partnership. Certified lab assistants collected 2 bilateral anterior nasal swabs. The first was tested with BinaxNOW<sup>TM</sup>, immediately followed by a separate bilateral swab for SARS-CoV-2 genomic sequencing [11, 12]. Results were reported to participants within 2 hours, and all persons in a household (regardless of symptom status) corresponding to a positive BinaxNOW case were offered BinaxNOW testing. All persons testing BinaxNOW positive were offered participation in longitudinal Community Wellness Team support program [13, 14].

### *SARS-CoV-2 Genomic Sequence Recovery and Consensus Genome Generation*

SARS-CoV-2 genomes were recovered using ARTIC Network V3 primers [15] and sequenced on an Illumina NovaSeq platform. Consensus genomes generated from the resulting raw. fastq files using IDseq [16] were used for subsequent analysis. Full details are included in Supplementary materials.

### *Household Attack Rate Analyses*

Households ( $n = 328$ ) tested in January and meeting the following inclusion criteria were eligible for secondary attack rate analyses: 1)  $\geq 1$  adult (aged  $\geq 18$  years) with a positive BinaxNOW result; 2)  $\geq 1$  case in household sequenced; and 3)  $\geq 2$  persons tested with BinaxNOW during the study period. Households in which sequences represented both West Coast and non-West Coast variants were excluded ( $n = 9$ ). The index was defined as the first adult to test positive. Crude household attack rates, stratified by variant classification, were calculated as i) the proportion of positive BinaxNOW results among tested household contacts; and ii) the mean of the household-specific secondary attack rate, with 95% confidence interval (CI) based on cluster-level bootstrap. Generalized estimating equations were used to fit Poisson regressions, with cluster-robust standard errors and an exchangeable working covariance matrix. Because symptoms and disease severity may be affected by strain, these factors were not included in the a priori adjustment set. We evaluated for overdispersion [17] and conducted sensitivity analyses using targeted maximum likelihood estimation (TMLE) combined with Super Learning to relax parametric model assumptions; influence curve-based standard error estimates used household as the unit of independence [18].

### *Bayesian Phylogenetic Analysis*

We compared the growth rates of B.1.427 and B.1.429 Phylogenetic Assignment of Named Global Outbreak (PANGO) lineages against 2 other lineages, B.1.232 and B.1.243, that had been circulating in California during the latter half of 2020. To do this, we built a Bayesian phylogeny for each lineage in BEAST v.1.10.4 and estimated the effective population size over time using the Bayesian SkyGrid model. We fit an exponential model to the median SkyGrid curve and

inferred the reproductive numbers based on the exponential growth rates and generation time estimates from literature. Full analysis details are included in Supplementary materials.

### *Ethics Statement*

The UCSF Committee on Human Research determined that the study met criteria for public health surveillance. All participants provided informed consent for dual testing.

### **Results**

#### *Low-Barrier SARS-CoV-2 Testing and Sequencing*

From 22 November to 1 December 2020, 3302 rapid direct antigen tests were performed on 3122 unique individuals; sample characteristics from this testing have been previously described [11]. From 10–29 January, using identical methods, 8822 rapid direct antigen tests were performed on 7696 unique individuals, representing 5239 households; household attack rate analyses were restricted to January samples, described here (Supplementary Table 1).

Test subjects originated from addresses in 8 Bay Area counties, indicating a wide catchment area (Figure 7.1). During this time period, there were 885 (10.0%) samples from 863 unique persons that were BinaxNOW positive for SARS-CoV-2 infection. From this set, a total of 80 samples were sequenced for the S gene only, of which 58 had S gene coverage over 92%. In addition, full SARS-CoV-2 genome sequencing was attempted on a total of 775 samples, of which 737 (95%) samples resulted in a genome coverage over 92% (Supplementary Table 2, sequences deposited in GISAID). These 986 samples, together with an additional 191 SARS-CoV-2 genome sequences generated from the same testing site during the period of 22 November to 1 December 2020 [11, 19] had adequate coverage of the full genome or spike protein for further analysis based

on S gene sequence (Supplementary Table 3). Classification as either a West Coast variant or a non-West Coast variant was determined for 846 of all samples sequenced.

Similar to previous observations in San Francisco [20], full length sequences were distributed among the major clades (Supplementary Figure 1) [21]. Notably, mutations at spike position 501 were not observed, and thus no instances of the B.1.1.7 strain or any other strain bearing the N501Y mutation were detected in any sample during this period in January 2021. A single individual was found to have been infected with the P.2 strain, which carries the spike E484K mutation and was described in Brazil from a reinfection case [5]. This mutation has been associated with decreased neutralization in laboratory experiments [2, 4].

We observed SARS-CoV-2 genome sequences that belonged to PANGO lineages B.1.427 and B.1.429, both of which share a trio of recent mutations in the spike protein (S13I, W152C, and L452R) (Figure 7.2). These lineages are separated by differing mutations ORF1a and ORF1b, including ORF1b:P976L and ORF1a:I4205V, respectively. Sequencing of 191 viral genomes from 22 November to 1 December 2020 revealed that sequences carrying this trio of mutations represented only 15.7% of the total. A trend of increasing frequency was observed on a daily basis during the January testing period (Figure 7.2A), and the frequency of these lineages were observed to have increased to 54.4% of the total, representing an increase of more than 3-fold in approximately 1.5 months (Figure 7.2B, 7.2C). This increase in frequency is consistent with an expansion of viruses more broadly in California carrying these same mutations [23].

Additional nonsynonymous mutations were observed throughout the genome, including 108 unique non-synonymous mutations in the spike gene, several within functionally-significant regions of the protein (Figure 7.2C, Supplementary Table 3). Twelve unique mutations were observed in the receptor binding domain, most of which have yet to be investigated for functional

effects. Additionally, 8 unique mutations were found adjacent to the polybasic furin cleavage site at the S1/S2 junction, which is reported to have a potential role in determination of virulence and host cell tropism [24–27]. Moderately prevalent mutations were observed at spike position 681 (P681H, n = 34 and P681R, n = 1), which is within the furin recognition site, and at spike position 677, where 2 different amino acid substitutions were observed in this cohort (Q677H, n = 22 and Q677P, n = 11). Multiple mutations at both of these sites have been previously observed [9].

### *Disease Severity*

The SARS-CoV-2 reverse transcription polymerase chain reaction (RT-PCR) cycle thresholds (Ct) for nasal swab samples from which whole genomes corresponding to the West Coast variant were recovered were compared to parallel non-West Coast variant samples. Mean Ct values did not differ significantly between persons infected with West Coast (mean Ct 23.56; interquartile range [IQR] 6.4) versus non-West Coast (mean Ct 23.67; IQR 7.8) strains (95% CI:  $-.77$  to  $.50$ ,  $P$ -value =  $.67$ ) (Supplementary Figure 2, Supplementary Table 2). The proportion of individuals with symptoms was similar among persons infected with West Coast (273/448, 60.9%) versus non-West Coast (250/389, 64.3%) strains. Among 364 sequenced cases with longitudinal follow-up by the Community Wellness Team, 4 (1.1%) were hospitalized (3/183, and 1/181, for West Coast and non-West Coast, respectively).

### *Household Secondary Attack Rate*

A total of 328 households met inclusion criteria for evaluation of secondary attack rate; of these, 9 households had individuals with mixed strains and thus were excluded from analyses. Among the remaining 319 households, characteristics including race/ethnicity, ages of other

household members, household size, density, and location were similar, regardless of whether the members were positive for West Coast or non-West Coast variants. (Table 1, Supplementary Table 4).

The 319 index cases had a total of 1241 nonindex household members; of these, 867 (69.9%) had a BinaxNOW test result available (452/658 [68.7%] for West Coast variant households; 415/583 [71.2%] of non-West Coast variant households). A total of 35.6% (161/452) of household contacts exposed to the West Coast variant tested BinaxNOW positive (33.2%, 78/235 for B.1.427; 40.3%, 79/196 for B.1.429), whereas 29.4% (122/415) of contacts exposed to non-West Coast variant tested positive (Table 2). Secondary cases were identified a median of 1 day after index cases (IQR 0–4).

Based on unadjusted Poisson regression with cluster-robust standard errors, household contacts exposed to the West Coast variant had an estimated 28% higher risk of secondary infection, compared to household contacts exposed to a non-West Coast variant (RR: 1.28, 95% CI: 1.00–1.64,  $P$ -value = .05). When exposure to West Coast variants was disaggregated by B.1.427 and B.1.429, corresponding risks of secondary infections relative to exposure to non-West Coast variants were 1.19 (95% CI: .89–1.59,  $P$ -value = .20) and 1.43 (95% CI: 1.07–1.91,  $P$ -value = .02), respectively. Dispersion ratios were  $>0.9$  in all regression analyses. Estimated relative risks of infection after household exposure to West Coast versus non-West Coast variants were similar after adjustment for household and individual-level characteristics of secondary contacts (adjusted risk ratio [aRR]: 1.25, 95% CI: .98–1.59,  $P$ -value: .07 for West Coast vs non-West Coast variants; aRR: 1.19, 95% CI: .90–1.59,  $P$ -value = .20 and aRR: 1.36, 95% CI: 1.01–1.83,  $P$ -value = .04 for B.1.427 and B.1.429, respectively). Relative attack rates were generally similar when stratified by household characteristics and by the characteristics of secondary contacts (Table 3);

secondary attack rates among children aged <12 years were 51.9% (41/79) and 39.7% (31/78) when exposed to West Coast and non-West Coast strains, respectively. Sensitivity analyses in which parametric assumptions were relaxed using TMLE and Super Learning yielded similar estimates (Supplementary Table 5).

### *Estimation of Reproductive Number*

Using Bayesian phylogenetic analysis, we estimated the reproductive number to be 1.27 (95% CI: 1.10–1.46) for B.1.427 and 1.18 (95% CI: 1.05–1.32) for B.1.429 during the second half of 2020. These values were slightly higher than 2 other lineages spreading in California during the same time period: 1.12 (95% CI: 1.10–1.14) for B.1.232, and 1.02 (95% CI: .98–1.05) for B.1.243. As the reproductive numbers are very similar and were calculated from the median SkyGrid estimates, we cannot conclude any statistically significant differences between the lineages.

### *Discussion*

We monitored SARS-CoV-2 viral variants by genomic sequencing and integration of metadata from households at a community based “test-and-respond” program. We found that the West Coast variants (PANGO lineages B.1.427 and B.1.429) increased in prevalence relative to wild type from November to January in the San Francisco Bay Area among persons tested in the same community-based location. These data extend and confirm prior observations from convenience, outbreak, and clinical samples reporting apparent increases in relative prevalence of the West Coast variants [23].

Household secondary attack rates of the West Coast variants were modestly higher than for non-West Coast variants, suggesting the potential for increased transmissibility. The West



Coast variants comprise two closely related lineages (B.1.427 and B.1.429) that share identical sets of mutations in the spike protein but differ by additional synonymous and nonsynonymous mutations in other genes. Although the frequency of both lineages increased in this study and in California more widely [23], and the estimated increase in risk of secondary household infection relative to non-West Coast variants was fairly consistent across lineages, the point estimate was somewhat higher for B.1.429. Although moderate compared to increased transmissibility of other previously identified variants, even small increases in transmissibility could contribute to a substantial increase in cases, particularly in the context of reproductive numbers just below 1. Although this finding may be due to chance, future work should continue to monitor individual lineages.

The household attack rate observed here was higher than that reported in a recent global meta-analysis [28], even for the non- West Coast variants. It was similar to, or lower than, attack rates reported in other US settings. Prior US reports, however, were based on substantially smaller sample sizes.

Our findings that the West Coast variants increased in relative prevalence and had higher household secondary attack rates potentially suggest higher transmissibility. However, the West Coast variant has been detected in multiple locations and has been detected since May 2020 in California without relative expansion until the peak associated with the holiday season of November–January. Using Bayesian phylogenetic analysis, the estimated reproductive number for both West Coast lineages was found to be modestly higher than other circulating lineages.

We found no significant differences in viral load (using Ct) between West Coast and non-West Coast variants (Supplementary Figure 2), and recorded hospitalizations ( $n = 5/388$ ) remained rare, despite the West Coast variant representing 54.4% of positive cases. This highlights the

importance of studying walk-up populations, whether they are symptomatic or asymptomatic, as hospitalized populations often are confounded by comorbidities and subject to selection bias.

At the time of this sampling, no instances of B.1.1.7, or independent N501Y mutations were detected in our sample population of 830, despite sporadic observations elsewhere in CA (approximately 3% [69/2423] of genomes reported in California during the January study period; accessed from GISAID 24 February 2021), suggesting that introductions of B.1.1.7 have been rare in this catchment area, despite high SARS-CoV-2 incidence [29]. A single case of the P.2 variant, which carries the E484K mutation [2], was detected in this study. Surprisingly, this case did not have a travel history, highlighting the risk of cryptic transmission.

In addition to the mutations associated with spike L452R in the West Coast variants, we observed, at lower frequencies, other mutations of interest, such as those at spike positions 677 and 681, both of which have been reported previously on their own [9].

This study has several limitations. First, testing was conducted at a walk-up testing site, and thus these are inherently convenience samples; however, this would not be expected to impose a differential selection bias for those with or without any particular variant. Second, clear classification of the index case was not always possible, particularly when multiple adults from a household tested positive on the same date; furthermore, secondary household attack rate calculations do not account for potential external sources of infection other than the index case. However, the relative risk of secondary infection from household exposure to West Coast versus non-West Coast variants was similar among children, a group less likely to have been misclassified as non-index or to be exposed to external infection. Third, household testing coverage was incomplete and, in some cases, consisted of only a single follow-up test; this might contribute to

an underestimate (or overestimate) of secondary attack rate, and although we again have no reason to suspect differential ascertainment by strain, this could bias estimates of relative risk.

The occurrence of variants in SARS-CoV-2 was always expected; however, it is often difficult to understand the clinical and epidemiological importance of any given single or set of co-occurring mutations. Although further epidemiological and laboratory experiments will be required to fully understand the community impact and mechanistic underpinnings of each variant, it is clear that enhanced genomic surveillance paired with community engagement, testing, and response capacity is an important tool in the arsenal against this pandemic.

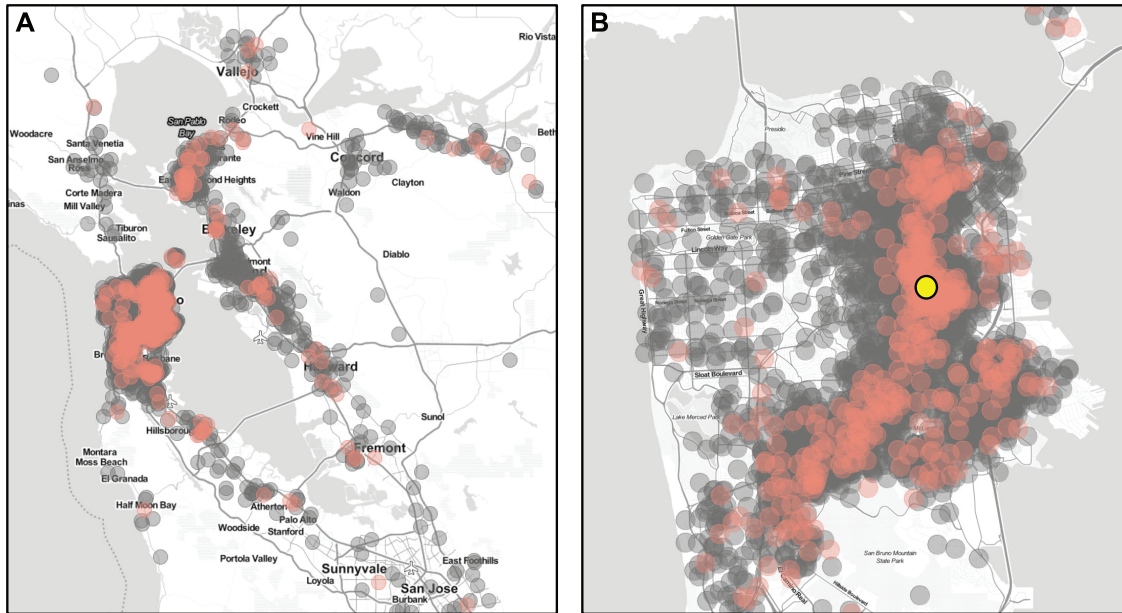


**Figure 7.1. Testing catchment area.** The location of the 24th & Mission testing site is denoted by the yellow symbol. Negative tests are in gray, and positive tests are shown in red. Household locations shown have a random offset of up to 750 meters to obfuscate the precise addresses of individuals. The testing catchment area encompasses a substantial number of individuals in the surrounding 8 Bay Area counties (A). The greatest concentration of individuals reside within San Francisco county (B), Map tiles by Stamen Design and data by OpenStreetMap.

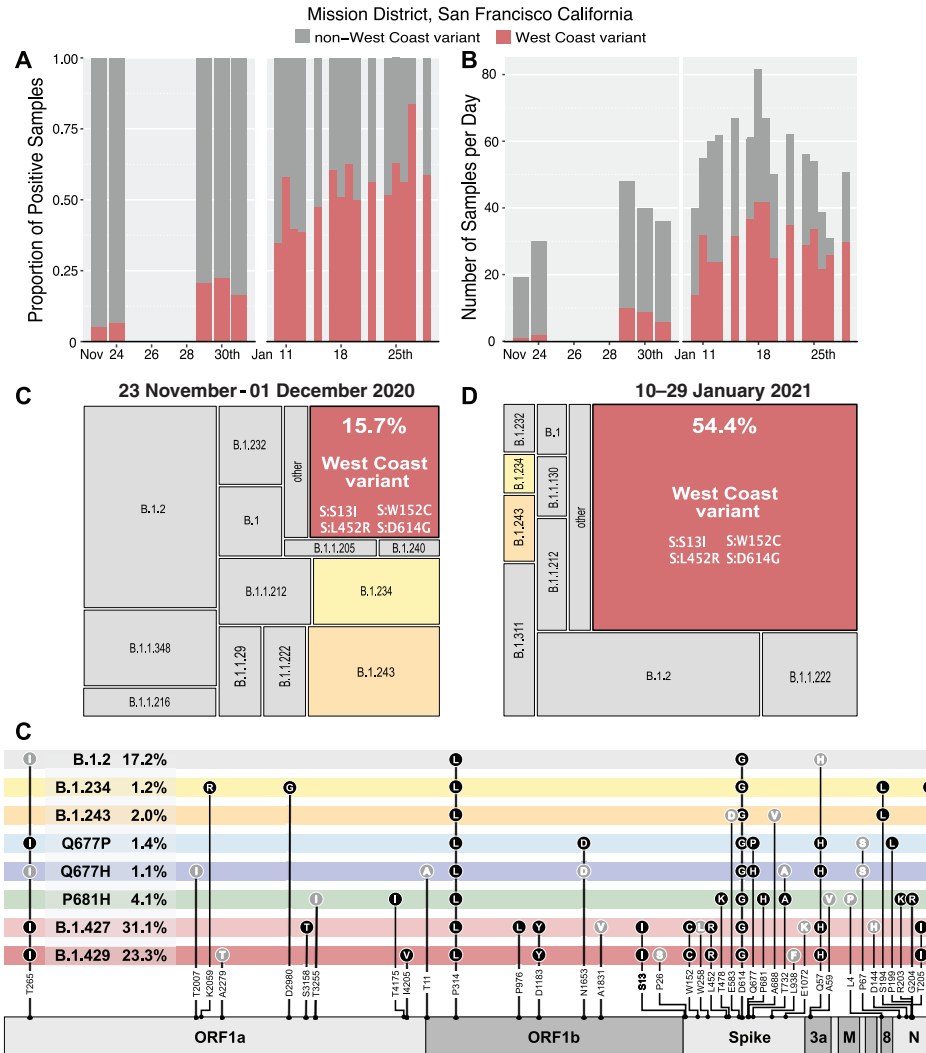


**Figure 7.2. Variants observed at 24th & Mission.** *A*, Proportion of daily cases belonging to West Coast and non-West Coast variants. *B*, Total number of samples per day. *C*, *D*, Area maps [22] showing the relative proportion of PANGO lineages acquired from full length genomes from the November (N = 191) and January (N = 737) time periods, respectively. *E*, Genome maps for variants detected in this study. Dominant mutations (*filled black circles*), and nonsynonymous mutations detected at lower frequency in combination with existing lineages (*filled gray circles*) are shown in gray. Abbreviation: PANGO, Phylogenetic Assignment of Named Global Outbreak.

**Table 7.1. Characteristics of households included in the household attack rate analysis, stratified by strain.**

	Non-West Coast (N = 156)	West Coast			Total (N = 319)
		B.1.427 (N = 90)	B.1.429 (N = 65)	All West Coast (N = 163) <sup>a</sup>	
<b>Race/Ethnicity (most common in household)</b>					
Hispanic/Latinx	143 (91.7%)	78 (86.7%)	62 (95.4%)	146 (89.6%)	289 (90.6%)
Asian	5 (3.2%)	5 (5.6%)	1 (1.5%)	8 (4.9%)	13 (4.1%)
White/Caucasian	4 (2.6%)	3 (3.3%)	0 (0%)	3 (1.8%)	7 (2.2%)
Black or African American	2 (1.3%)	2 (2.2%)	2 (3.1%)	4 (2.5%)	6 (1.9%)
Other	2 (1.3%)	2 (2.2%)	0 (0%)	2 (1.2%)	4 (1.3%)
<b>Has children</b>					
Does not have children	105 (67.3%)	69 (76.7%)	35 (53.8%)	110 (67.5%)	215 (67.4%)
Has children	51 (32.7%)	21 (23.3%)	30 (46.2%)	53 (32.5%)	104 (32.6%)
<b>Location</b>					
San Francisco	118 (75.6%)	71 (78.9%)	39 (60.0%)	115 (70.6%)	233 (73.0%)
Outside San Francisco	38 (24.4%)	19 (21.1%)	26 (40.0%)	48 (29.4%)	86 (27.0%)
<b>Household size</b>					
2 persons	14 (9.0%)	12 (13.3%)	5 (7.7%)	20 (12.3%)	34 (10.7%)
3–4 persons	63 (40.4%)	33 (36.7%)	22 (33.8%)	57 (35.0%)	120 (37.6%)
5+ persons	79 (50.6%)	45 (50.0%)	38 (58.5%)	86 (52.8%)	165 (51.7%)
<b>Household density<sup>b</sup></b>					
Mean (SD)	1.86 (0.858)	1.91 (0.881)	2.27 (1.22)	2.04 (1.03)	1.95 (0.955)
Median [min, max]	1.88 [0.250, 7.00]	1.67 [0.444, 5.00]	2.00 [0.714, 6.00]	1.69 [0.444, 6.00]	1.75 [0.250, 7.00]

<sup>a</sup>8 households with S gene only sequence available.

<sup>b</sup>Household density missing for 17 households.

**Table 7.2. Secondary household attack rates for West Coast Variants, combined and disaggregated by B.1.427 and B.1.429.**

Class	Positives Among Tested Contacts (%)	Mean Household Attack Rate (95% CI)	Unadjusted		Adjusted	
			RR (95% CI)	P-value	aRR	P-value
Non-West Coast	122/415 (29.4%)	25.6% (20.3–31)	...	...	...	...
West Coast	161/452 (35.6%)	35.9% (30.1–41.9)	1.28 (1.00–1.64)	.05	1.25 (.98–1.59)	.07
<b>Lineage</b>						
B.1.427	78/235 (33.2%)	32.9% (25.4–40.6)	1.19 (0.89–1.59)	.20	1.19 (.90–1.59)	.20
B.1.429	79/196 (40.3%)	40.9% (31.5–50.5)	1.43 (1.07–1.91)	.02	1.36 (1.01–1.83)	.04

Relative risks estimated based on Poisson regression using generalized estimating equations and cluster-robust standard errors. Adjustment variables included age group, Latinx/Hispanic race, household size, and household density.

Abbreviations: aRR, adjusted risk ratio; CI, confidence interval; RR, risk ratio.

**Table 7.3. Secondary attack rate disaggregated by covariates.**

	Non-West Coast Strain		West Coast Strain	
	Positives Among Tested Contacts (%)	Mean Household Attack Rate (95% CI)	Positives Among Tested Contacts (%)	Mean Household Attack Rate (95% CI)
<b>Location</b>				
San Francisco	88/321 (27.4%)	22.9% (17.2–28.8)	113/316 (35.8%)	37.5% (30.2–44.9)
Outside of San Francisco	34/94 (36.2%)	34% (22.1–46.2)	48/136 (35.3%)	32.1% (22.2–42.1)
<b>Age group</b>				
Age ≤ 12	31/78 (39.7%)	...	41/79 (51.9%)	...
Age > 12	91/337 (27%)	...	120/373 (32.2%)	...
<b>Race/Ethnicity</b>				
Latinx/Hispanic	107/372 (28.8%)	...	136/379 (35.9%)	...
Not Latinx/Hispanic	15/43 (34.9%)	...	25/73 (34.2%)	...
<b>Household size</b>				
2 persons	1/14 (7.1%)	7.1% (0–21.4)	12/20 (60%)	60% (40–80)
3–4 persons	30/115 (26.1%)	26.5% (17.7–35.7)	35/102 (34.3%)	33.3% (23.7–43.6)
5+ persons	91/286 (31.8%)	28.1% (21.1–35.4)	114/330 (34.5%)	32% (25.1–39.2)
<b>Household density</b>				
Bottom half	43/159 (27%)	23.8% (15.7–32.2)	52/176 (29.5%)	33% (24.2–42.3)
Top half	76/243 (31.3%)	27.4% (20.1–35)	101/262 (38.5%)	35.7% (27.9–43.6)

Mean household secondary attack rate only reported disaggregated by household level characteristics.

Abbreviation: CI, confidence interval.

## Chapter 7 References

1. Grubaugh ND, Hodcroft EB, Fauver JR, Phelan AL, Cevik M. Public health actions to control new SARS-CoV-2 variants. *Cell* 2021; 184:1127–32.
2. Liu Z, VanBlargan LA, Bloyet L-M, et al. Identification of SARS-CoV-2 spike mutations that attenuate monoclonal and serum antibody neutralization. *Cell Host & Microbe* 2021; 29:477–488.e4.
3. Voloch CM, Francisco R da S, Almeida LGP de, et al. Genomic characterization of a novel SARS-CoV-2 lineage from Rio de Janeiro, Brazil. *J Virol* 2021; 95. Available at: <https://jvi.asm.org/content/95/10/e00119-21>. Accessed 17 May 2021.
4. Weisblum Y, Schmidt F, Zhang F, et al. Escape from neutralizing antibodies by SARS-CoV-2 spike protein variants. *eLife* 2020;9:e61312.
5. Ferrareze PAG, Franceschi VB, Mayer A de M, et al. E484K as an innovative phylogenetic event for viral evolution: genomic analysis of the E484K spike mutation in SARS-CoV-2 lineages from Brazil. *bioRxiv* 2021;2021.01.27.426895.
6. Zeller M, Gangavarapu K, Anderson C, et al. Emergence of an early SARS-CoV-2 epidemic in the United States. *medRxiv* 2021;2021.02.05.21251235.
7. Fauver JR, Petrone ME, Hodcroft EB, et al. Coast-to-coast spread of SARS-CoV-2 during the early epidemic in the United States. *Cell* 2020; 181:990–996.e5.
8. Kalinich CC, Jensen CG, Neugebauer P, et al. Real-time public health communication of local SARS-CoV-2 genomic epidemiology. *PLoS Biol* 2020; 18:e3000869. 9.
9. Hodcroft EB, Domman DB, Oguntuyo K, et al. Emergence in late 2020 of multiple lineages of SARS-CoV-2 spike protein variants affecting amino acid position 677. *medRxiv* 2021;2021.02.12.21251658.



10. COVID Testing Pop-up site Established at 24th & Mission to Help Combat Surge in the City's Most Impacted Community During this Holiday Season. 2020. Available at: [https://www.sfdph.org/dph/alerts/files/12.20.20\\_CCSF\\_Press\\_Release.pdf](https://www.sfdph.org/dph/alerts/files/12.20.20_CCSF_Press_Release.pdf).
11. Pilarowski G, Marquez C, Rubio L, et al. Field performance and public health response using the BinaxNOW™ rapid severe acute respiratory syndrome coronavirus 2 (SARS-CoV-2) Antigen Detection Assay During Community-Based Testing. *Clin Infect Dis* 2021; 73:e3098–101.
12. Pilarowski G, Lebel P, Sunshine S, et al. Performance characteristics of a rapid severe acute respiratory syndrome coronavirus 2 antigen detection assay at a public plaza testing site in San Francisco. *J Infect Dis* 2021; 223:1139–1144.
13. Rubio LA, Peng J, Rojas S, et al. The COVID-19 symptom to isolation cascade in a Latinx community: a call to action. *Open Forum Infect Dis* 2021; 8:ofab023. 14.
14. Kerkhoff AD, Sachdev D, Mizany S, et al. Evaluation of a novel community-based COVID-19 'test-to-care' model for low-income populations. *PLoS One* 2020; 15:e0239400.
15. ARTIC Project. hCoV-2019/nCoV-2019 version 3 amplicon set. Available at: <https://artic.network/resources/ncov/ncov-amplicon-v3.pdf>. Accessed 25 February 2021.
16. Kalantar KL, Carvalho T, de Bourcy CFA, et al. IDseq—an open source cloud-based pipeline and analysis service for metagenomic pathogen detection and monitoring. *GigaScience* 2020; 9. doi:10.1093/gigascience/giaa111.
17. Gelman A, Hill J. *Data analysis using regression and multilevel/hierarchical models*. New York: Cambridge University Press, 2007.

18. Laan MJ van der, Rose S. Targeted learning in data science: causal inference for complex longitudinal studies. London: Springer International Publishing, 2018. Available at: <https://www.springer.com/gp/book/9783319653037>. Accessed 24 February 2021.
19. Elbe S, Buckland-Merrett G. Data, disease and diplomacy: GISAID's innovative contribution to global health. *Glob Chall* 2017; 1:33–46.
20. Chamie G, Marquez C, Crawford E, et al. Community transmission of severe acute respiratory syndrome coronavirus 2 disproportionately affects the Latinx population during Shelter-in-Place in San Francisco. *Clin Infect Dis* 2021; 73(Suppl. 2):S127–35.
21. Hadfield J, Megill C, Bell SM, et al. Nextstrain: real-time tracking of pathogen evolution. *Bioinformatics* 2018; 34:4121–3.
22. Laserson U. *laserson/squarify*. 2021. Available at: <https://github.com/laserson/squarify>. Accessed 26 February 2021.
23. Zhang W, Davis BD, Chen SS, Martinez JMS, Plummer JT, Vail E. Emergence of a novel SARS-CoV-2 strain in Southern California, USA. *medRxiv* 2021;2021.01.18.21249786.
24. Hoffmann M, Kleine-Weber H, Pöhlmann S. A Multibasic cleavage site in the spike protein of SARS-CoV-2 is essential for infection of human lung cells. *Mol Cell* 2020; 78:779–784.e5.
25. Örd M, Faustova I, Loog M. The sequence at spike S1/S2 site enables cleavage by furin and phospho-regulation in SARS-CoV2 but not in SARS-CoV1 or MERS- CoV. *Sci Rep* 2020; 10:16944.
26. Johnson BA, Xie X, Bailey AL, et al. Loss of furin cleavage site attenuates SARS- CoV-2 pathogenesis. *Nature* 2021; 591:293–299.
27. Jaimes JA, Millet JK, Whittaker GR. Proteolytic cleavage of the SARS-CoV-2 spike protein and the role of the novel S1/S2 site. *iScience* 2020; 23:101212.

28. Madewell ZJ, Yang Y, Longini IM Jr, Halloran ME, Dean NE. Household Transmission of SARS-CoV-2: a systematic review and meta-analysis. *JAMA Netw Open* 2020; 3:e2031756.
29. Volz E, Mishra S, Chand M, et al. Assessing transmissibility of SARS-CoV-2 lineage B.1.1.7 in England. *Nature* 2021; 593:266–269.

## Chapter 8:

### **Neutralizing antibody responses to SARS-CoV-2 vaccination in Multiple Sclerosis patients**

This chapter is a reprint of:

Sabatino JJ Jr, Mittl K, Rowles WM, McPolin K, Rajan JV, Laurie MT, Zamecnik CR, Dandekar R, Alvarenga BD, Loudermilk RP, Gerungan C, Spencer CM, Sagan SA, Augusto DG, Alexander JR, DeRisi JL, Hollenbach JA, Wilson MR, Zamvil SS, Bove R.

Multiple sclerosis therapies differentially affect SARS-CoV-2 vaccine-induced antibody and T cell immunity and function. *JCI Insight*. 2022; Feb 22;7(4):e156978.

doi:10.1172/jci.insight.156978.

Supplemental files that are not figures can be found with the original work.

## ***Abstract***

### *Background*

Vaccine-elicited adaptive immunity is a prerequisite for control of SARS-CoV-2 infection. Multiple sclerosis (MS) disease-modifying therapies (DMTs) differentially target humoral and cellular immunity. A comprehensive comparison of the effects of MS DMTs on SARS-CoV-2 vaccine-specific immunity is needed, including quantitative and functional B and T cell responses.

### *Methods*

Spike-specific Ab and T cell responses were measured before and following SARSCoV-2 vaccination in a cohort of 80 study participants, including healthy controls and patients with MS in 6 DMT groups: untreated and treated with glatiramer acetate (GA), dimethyl fumarate (DMF), natalizumab (NTZ), sphingosine-1-phosphate (S1P) receptor modulators, and anti-CD20 mAbs. Anti-spike-Ab responses were assessed by Luminex assay, VirScan, and pseudovirus neutralization. Spike-specific CD4<sup>+</sup> and CD8<sup>+</sup> T cell responses were characterized by activation-induced marker and cytokine expression and tetramer.

### *Results*

Anti-spike IgG levels were similar between healthy control participants and patients with untreated MS and those receiving GA, DMF, or NTZ but were reduced in anti-CD20 mAb- and S1P-treated patients. Anti-spike seropositivity in anti-CD20 mAb-treated patients was correlated with CD19<sup>+</sup> B cell levels and inversely correlated with cumulative treatment duration. Spike epitope reactivity and pseudovirus neutralization were reduced in anti-CD20 mAb- and S1P-treated patients. Spike-specific CD4<sup>+</sup> and CD8<sup>+</sup> T cell reactivity remained robust across all

groups, except in S1P-treated patients, in whom postvaccine CD4+ T cell responses were attenuated.

### *Conclusion*

These findings from a large cohort of patients with MS exposed to a wide spectrum of MS immunotherapies have important implications for treatment-specific COVID-19 clinical guidelines. FUNDING. NIH grants 1K08NS107619, K08NS096117, R01AI159260, R01NS092835, R01AI131624, and R21NS108159; NMSS grants TA-1903-33713 and RG1701-26628; Westridge Foundation; Chan Zuckerberg Biohub; Maisin Foundation.

### *Introduction*

Multiple sclerosis (MS) is an inflammatory demyelinating condition of the central nervous system that is treated with more than 20 different, approved disease modifying therapies (DMTs) (1). MS DMTs differ considerably in their mechanisms of action, with variable impacts on humoral and cellular immune functions that can lead to associated risks of certain infections (2). COVID-19 is an infectious disease caused by SARS-CoV-2, which has resulted in a pandemic that has been ongoing since early 2020. Control of SARS-Cov-2 infection involves mobilization of Ab- and T cell-mediated immunity (3–5). Evidence suggests that patients with MS who receive anti-CD20 mAb therapies are at higher risk for hospitalization due to COVID-19 infection (6, 7). Recent reports have demonstrated that patients with MS treated with an anti-CD20 mAb or S1P receptor modulators have reduced or undetectable spike antigen-specific IgG following COVID-19 infection (8–12).

Vaccines based on the SARS-CoV-2 spike protein have proven to be highly effective in preventing serious sequelae of COVID-19, in which protective immunity involves a combination of robust Ab and CD4<sup>+</sup> and CD8<sup>+</sup> T cell responses (13–16). Given the variable effects of different classes of MS DMTs on humoral and cellular immunity, there is much concern that SARS-CoV-2 vaccine immunity may be blunted by certain MS treatments and thus result in increased risk of serious complications from COVID-19. Indeed, most MS DMTs have been reported to at least partially affect vaccine-elicited Ab and/or T cell immunity (17, 18). To date, the majority of studies evaluating SARS-CoV-2 vaccine responses in patients with MS have been limited to measuring Ab titers, demonstrating reduced spike antigen-specific Ab responses in patients with MS treated with anti-CD20 mAbs and S1P receptor modulators (8, 19–22). No studies to date, to our knowledge, have investigated how MS DMTs affect the functional reactivity against the spike protein, which is vital for Ab-mediated protection against COVID-19 (4, 23). Although several reports have also indicated largely intact spike antigen-specific T cell responses in vaccinated patients with MS treated with anti-CD20 mAbs (19, 24), there currently are no available data comparing SARS-CoV-2 vaccine-specific CD4<sup>+</sup> and CD8<sup>+</sup> T cell reactivity across patients treated with different DMTs. This represents an important gap in our understanding of COVID-19 susceptibility in at-risk patient populations.

The goal of this study was to systematically analyze SARS-CoV-2 vaccine-induced humoral and cellular immune responses in patients with MS treated with an array of different immunotherapies. Spike antigen-specific IgG and CD4<sup>+</sup> and CD8<sup>+</sup> T cell responses were measured before and after SARS-CoV-2 vaccination in a cohort of healthy control individuals (HCs; n = 13) and patients with MS (n = 67) across 6 different types of treatment: untreated, glatiramer acetate (GA), dimethyl fumarate (DMF), natalizumab (NTZ), S1P receptor modulators,

and anti-CD20 mAbs. Patients with MS treated with anti-CD20 mAbs or S1P receptor modulators had substantially reduced levels of total spike IgG and spike receptor-binding domain–specific (RBD-specific) IgG with binding to a restricted array of spike immune determinants. Spike-Ab seropositivity in anti-CD20 mAb–treated patients was associated with higher CD19+ B cell levels and was inversely correlated with cumulative duration of anti-CD20 mAb therapy. In patients treated with anti-CD20 mAbs and S1P receptor modulators who had detectable anti–spike Abs, pseudovirus neutralization was markedly blunted and directly correlated with reduced levels of spike RBD IgG levels. In contrast to the humoral response, spike antigen–specific CD4+ and CD8+ T cell responses were similar overall in frequency in all MS-treatment groups and had similar cytokine and memory profiles. However, spike-specific CD4+ T cell frequencies did not significantly increase in patients treated with S1P receptor modulators following vaccination. These findings, therefore, provide new critical insights into the differential effects of MS DMTs on SARS-CoV-2 vaccine–elicited adaptive immunity with important consequences for clinical decision-making in vulnerable immunosuppressed patients.

## ***Results***

### *Study overview*

To study the effects of different MS DMTs on SARS-CoV-2 vaccine–induced immune responses, we recruited a cohort of 80 participants comprising HCs (n = 13) and patients with MS who were receiving no treatment (n = 9) or were treated with GA (n = 5), DMF (n = 5), NTZ (n = 6), S1P receptor modulators (n = 7), or anti-CD20 mAbs, including rituximab (RTX; n = 13) or ocrelizumab (OCR; n = 22) (Table 1). Baseline samples were collected prior to SARS-CoV-2 vaccination (mean 7.2 days, range 0–34 days before first vaccine) and postvaccination samples



were collected approximately 2 weeks following the second mRNA COVID-19 vaccination (BNT162b2 or mRNA-1273; mean 15.7 days, range 11–40 days) or 4 weeks following adenoviral vaccination (Ad26.COV2.S; mean 28.5 days, range 28–29 days).

#### *Overview of basic immune cell subsets*

The percentages of immune cell subsets, including CD4<sup>+</sup> and CD8<sup>+</sup> T cells, CD19<sup>+</sup> B cells, CD14<sup>+</sup>, CD14<sup>+</sup> CD16<sup>+</sup>, and CD16<sup>+</sup> cells, were evaluated in all participants before and after SARS-CoV-2 vaccination, using the gating strategy shown in Supplemental Figure 1A (supplemental material available online with this article; <https://doi.org/10.1172/jci.insight.156978DS1>). Except for CD14<sup>+</sup> CD16<sup>+</sup> cells in GA-treated patients ( $P = 0.0425$ ), no significant differences were observed in any of the immune cell subsets before and after SARS-CoV-2 vaccination in all other cohorts (Supplemental Figure 1, B–G). Although the percentage of CD8<sup>+</sup> T cells was not significantly affected by treatment status, the percentage of CD4<sup>+</sup> T cells was significantly reduced before ( $P < 0.0001$ ) and after ( $P < 0.0001$ ) vaccination in S1P receptor modulator–treated patients compared with patients in the untreated group, consistent with the known mechanism of action of S1P receptor modulators (25) (Supplemental Figure 1B). As expected, the percentages of CD19<sup>+</sup> B cells were also significantly reduced at both collection time points in patients treated with S1P receptor modulators ( $P < 0.0001$ ), RTX ( $P < 0.0001$ ), and OCR ( $P < 0.0001$ ) compared with patients with untreated MS (Supplemental Figure 1D).

#### *Semiquantitative analysis of anti–spike Abs by MS treatment type*

Total spike IgG and spike RBD IgG levels were measured as net MFI after normalization to a background BSA control (26). HCs, patients with untreated MS, and patients with MS treated

with GA, DMF, or NTZ demonstrated significantly increased total spike IgG (Figure 8.1A) and spike RBD IgG (Figure 8.1B) levels following SARS-CoV-2 vaccination, compared with their respective prevaccination time points. Of note, the one patient with untreated MS who received the single-injection Ad26.COVS vaccine also had the lowest total spike and spike RBD IgG Ab levels. In contrast, vaccine-elicited total spike and spike RBD IgG levels were variable among patients treated with S1P receptor modulators, RTX, and OCR, with undetectable Ab levels in some patients and near-normal IgG levels in others (Figure 8.1, A and B). Overall, patients treated with S1P receptor modulators and RTX had no significant increase in postvaccination total spike IgG compared with prevaccination levels, whereas spike RBD IgG levels in the S1P receptor modulator, RTX, and OCR groups were not significantly increased following COVID-19 vaccination (Figure 8.1, A and B). Postvaccination total spike IgG levels in HCs and patients with MS treated with GA, DMF, or NTZ were similar to those in patients with untreated MS, but spike RBD IgG levels were significantly higher in the DMF ( $P = 0.038$ ) and NTZ ( $P < 0.0001$ ) groups. In contrast, postvaccination total spike and spike RBD IgG levels were significantly reduced in patients with MS treated with S1P receptor modulators ( $P = 0.02$  and  $P = 0.01$ , respectively), RTX ( $P = 0.001$  and  $P = 0.002$ , respectively), and OCR ( $P = 0.005$  and  $P = 0.0004$ , respectively) (Figure 8.1, A and B). IgG seropositivity to total spike protein and spike RBD following SARS-CoV-2 vaccination was also compared between patients in the untreated MS group and all other cohorts. Only patients treated with RTX had a significant decrease in total spike IgG seropositivity ( $23.1\% \pm 12.2\%$  SEM;  $P < 0.0001$ ), whereas those treated with S1P receptor modulators, RTX, and OCR had significant reductions in spike RBD IgG seropositivity ( $42.9 \pm 20.2\%$  SEM,  $P = 0.01$ ;  $7.7 \pm 7.7\%$  SEM,  $P < 0.0001$ ; and  $36.4 \pm 10.5\%$  SEM,  $P = 0.0002$ , respectively) (Figure 8.1C). These findings are consistent with recent reports indicating reductions in SARS-CoV-2 spike-specific

Abs in SARS-CoV-2 vaccinated patients with MS treated with S1P receptor modulators and anti-CD20 mAbs (8, 19, 20).

*Factors associated with anti-spike IgG seropositivity in patients with MS treated with anti-CD20 mAbs and S1P receptor modulators*

Given the variations in total spike and spike RBD IgG levels in patients with MS receiving anti-CD20 mAbs, we investigated factors associated with SARS-CoV-2 vaccine-elicited Ab responses. Within the anti-CD20 mAb cohorts (i.e., RTX and OCR), we conducted a univariate analysis of anti-spike-Ab responses by age, sex, vaccine type, cumulative treatment duration prior to vaccination, total IgG levels, interval between last anti-CD20 infusion and first vaccine dose, lymphocyte subsets before and after vaccination, and HLA-DRB1\*15:01 status, given its well-established association with MS susceptibility (27).

There was no significant association between total spike or spike RBD IgG seropositivity and age, sex, mRNA-vaccine type, last measured total IgG levels, percentages of CD4+ and CD8+ T cells, or HLADRB1\*15:01 status (Supplemental Table 1). Although there was not a significant difference between the percentage of prevaccination CD19+ B cells and total spike and spike RBD serostatus, there was a significant increase in patients seropositive for postvaccination CD19+ B cells and total spike ( $P = 0.0021$ ) and spike RBD ( $P = 0.0158$ ) compared with those who were seronegative (Figure 8.1, D and E, and Supplemental Table 1). Similarly, although there was no significant correlation with total spike and spike RBD IgG levels and percentages of CD19+ B cells prior to vaccination (Supplemental Figure 2, A and B), there was a strong positive correlation between the percentage of postvaccination CD19+ B cells and total spike IgG ( $r = 0.6084$ ;  $P = 0.0001$ ) and spike RBD IgG ( $r = 0.4166$ ;  $P = 0.0128$ ) levels (Supplemental Figure 2, C and D).

The mean interval between blood sample collection at prevaccination and postvaccination in patients receiving anti-CD20 mAb treatment was 6.6 weeks; therefore, we reasoned a potential difference for the discrepancy in correlations of CD19+ B cell levels at the 2 time points was possible interim B cell reconstitution during the vaccination period. We calculated the differences in percentages of CD19+ B cells between the postvaccine and prevaccine time points and observed a significant correlation between CD19+ B cell changes and total spike ( $r = 0.4903$ ;  $P = 0.0028$ ) and spike RBD ( $r = 0.4005$ ;  $P = 0.0171$ ) IgG levels (Supplemental Figure 2, E and F), providing support for this hypothesis.

Given variability in the timing of anti-CD20 mAb infusions caused by the ongoing SARS-CoV-2 pandemic, we also assessed whether differences in the interval between the last prior anti-CD20 mAb infusion and first SARS-CoV-2 vaccination could be related to vaccine-induced IgG responses, which have been reported previously (19, 20). In the combined anti-CD20 mAb cohorts, we did not observe any significant association of infusion to vaccination interval and total spike and spike RBD IgG levels (Supplemental Figure 2, G and H, and Supplemental Table 1). We also assessed the cumulative duration of anti-CD20 mAb treatment (i.e., time from start of anti-CD20 mAb treatment until first SARS-CoV-2 vaccination). Longer cumulative duration of anti-CD20 mAb treatment was significantly inversely correlated with total spike IgG and spike RBD IgG levels (Figure 8.1, F and G) and was significantly associated with serostatus (Supplemental Table 1). Although there was no significant difference between the last infusion to vaccination interval in patients treated with RTX and OCR (median 5.0 months and 4.3 months, respectively;  $P = 0.90$ ), the significant reduction in total spike IgG seropositivity in the RTX group compared with the OCR group (Figure 8.1C) was explained by a significantly increased cumulative duration of therapy in the RTX group compared with the OCR cohort (median 56.4 months and 36.4 months,

respectively;  $P = 0.0017$ ) (Figure 8.1H). We did not find a significant correlation between cumulative duration of anti-CD20 mAb therapy and the percentages of CD19+ B cells before or after vaccination ( $P = 0.99$  and  $P = 0.29$ , respectively).

Given reports of variable anti-spike seropositivity among patients treated with S1P receptor modulators (8, 22), we also assessed factors contributing to differences in Ab outcomes. Although S1P receptor modulator–treated patients composed a smaller cohort, we observed a nonsignificant trend between longer cumulative duration of S1P receptor modulator therapy and lower total spike and spike RBD IgG levels (Figure 8.1, I and J). There was no significant relationship between total spike and spike RBD IgG levels and absolute lymphocyte count and numbers of CD19+ B cells, CD4+ T cells, or CD8+ T cells.

#### *Identification of anti-spike protein IgG determinants by coronavirus VirScan*

We further explored the immune determinants of SARS-CoV-2 vaccine–induced IgG using VirScan analysis (<https://www.virscan.org/>) of patient sera from pre- and postvaccination time points. Sera samples were probed against a library of overlapping peptides ( $n = 38$  amino acids each) spanning the entire proteomes of 9 different human coronaviruses (including SARS-CoV-2) as well as a peptide library of the spike protein of SARS-CoV-1 and SARS-CoV-2, as previously demonstrated in patients with COVID-19 (26).

No signal was detected against spike peptide sequences from any of the sera samples from individuals before they were vaccinated, indicating that all measured spike-specific IgG responses resulted from SARS-CoV-2 vaccination rather than preexisting cross-reactive immunity against other coronaviruses. Multiple Ab-binding determinants were revealed throughout the spike protein, including against the N-terminal domain, regions flanking the RBD, the S1/S2 cleavage site, the fusion site, as well as the C-terminal region, in HCs and untreated patients with MS (Figure

8.2). Of note, neutralizing Abs targeting RBD epitopes are largely conformation dependent (28), which is generally not well represented by phage-displayed linear peptides. Anti-spike-Ab reactivity was slightly more narrowed in patients treated with GA, DMF, or NTZ, with some loss of reactivity in subdominant N-terminal domain and C-terminal regions. In patients treated with anti-CD20 mAbs and S1P receptor modulators, however, seroreactivity against the spike protein was primarily restricted to determinants flanking the RBD and the C-terminal regions (Figure 8.2, signal-intensity column). In addition, several in the OCR group also had detectable reactivity to portions of the S2 subunit. These findings, therefore, highlight that anti-CD20 mAb and S1P receptor modulator treatments may lead to qualitative changes in the breadth of anti-spike IgG epitopes in addition to quantitative changes in the overall spike IgG titer.

#### *Functional assessment of anti-SARS-CoV-2 Abs by pseudoviral neutralization*

Given the reduction in anti-spike levels and binding determinants in patients treated with anti-CD20 mAbs and S1P receptor modulators, we investigated whether virus neutralization might be consequently affected. Using a pseudovirus neutralization assay (see Methods), we compared neutralization in patients treated with anti-CD20 mAbs (n = 5) and S1P receptor modulators (n = 3) who were seropositive by VirScan with neutralization in representative HCs (n = 5) and untreated patients with MS (n = 5) from our cohort. Although pseudovirus neutralization was robust among HCs and untreated patients with MS, neutralization was significantly reduced in patients treated with anti-CD20 mAbs and S1P receptor modulators (Figure 8.3A). Consistent with prior reports (29), pseudovirus neutralization was significantly correlated with spike RBD IgG levels (Figure 8.3B). A weaker but still significant correlation was found between total spike IgG

levels and neutralization ( $r = 0.5604$ ;  $P = 0.0156$ ), providing support that not all anti-spike Abs are capable of neutralization.

Overall, we found that the reduced pseudovirus neutralization in patients treated with anti-CD20 mAbs and S1P receptor modulators was highly correlated with reduced spike RBD IgG levels (Figures 8.3C). These findings, therefore, indicate that SARS-CoV-2 neutralization appears to be compromised among the subset of patients treated anti-CD20 mAbs and S1P receptor modulators who had detectable anti-spike Abs (i.e., seropositive patients).

#### *Evaluation of spike antigen-specific CD4+ and CD8+ T cells*

We investigated the frequency and phenotype of spike antigen-specific CD4+ and CD8+ T cells, using pools of spike peptides spanning the entire spike protein by activation-induced marker (AIM) expression and intracellular cytokine stimulation (ICS) (see gating strategies in Supplemental Figure 3). In the AIM assay, antigen reactivity was assessed by CD137 and OX-40 co-expression in CD4+ T cells and CD137 and CD69 co-expression by CD8+ T cells (Figure 8.4, A and D), as previously demonstrated (30). Cytokine analysis included IFN- $\gamma$ , TNF- $\alpha$ , and IL-2, the dominant cytokines produced by spike-specific T cells (30, 31), as well as IL-4 and IL-10, which can be upregulated by certain MS DMTs (32).

A significant increase in spike-specific CD4+ T cells was observed by AIM in all postvaccination groups apart from the S1P receptor modulators cohort (Figure 8.4B), likely due to the pronounced S1P-mediated CD4+ T cell lymphopenia. Importantly, none of the postvaccination MS treatment groups showed a significant reduction in spike-specific CD4+ T cells compared with untreated patients with MS (Figure 8.4B). CD4+ T cells from all postvaccination cohorts produced similar frequencies of IFN- $\gamma$ , TNF- $\alpha$ , and IL-2, indicating broad polyfunctionality regardless of

MS treatment status (Figure 8.4C). In contrast, frequencies of IL-4<sup>-</sup> and IL-10<sup>-</sup> producing CD4<sup>+</sup> T cells were minimal with no changes in any of the DMT MS cohorts. The numbers of spike antigen-specific CD8<sup>+</sup> T cells were significantly increased in all postvaccination MS cohorts except the GA-treated group (Figure 8.4E), which was likely influenced by the smaller sample size of that group. Moreover, none of the postvaccination MS treatment groups had a significant reduction of spike-specific CD8<sup>+</sup> T cells measured by AIM, compared with untreated patients with MS (Figure 8.4E).

Cytokine production by postvaccination spike antigen-specific CD8<sup>+</sup> T cells revealed similar polyfunctionality, with significant production of IFN- $\gamma$ , TNF- $\alpha$ , and IL-2, but minimal IL-4 and IL-10 production (Figure 8.4F). Although cytokine responses were similar overall among all MS treatment cohorts, a significant increase in IFN- $\gamma$ <sup>+</sup> CD8<sup>+</sup> T cells was observed in patients receiving RTX and OCR and in TNF- $\alpha$ <sup>+</sup> CD8<sup>+</sup> T cells in patients treated with S1P receptor modulators and RTX, compared with HCs (Figure 8.4F). In addition, no significant relationship was found between the frequencies of spike-specific CD4<sup>+</sup> and CD8<sup>+</sup> T cells measured by AIM and total spike and spike RBD IgG levels or serostatus in anti-CD20 mAb-treated patients.

#### *Ex vivo evaluation of spike antigen-specific CD8<sup>+</sup> T cells by peptide MHC tetramers*

Having demonstrated robust expansion of spike-specific T cells following SARS-CoV-2 vaccination, we sought to further characterize the individual SARS-CoV-2 vaccine-elicited CD8<sup>+</sup> T cell response at the individual epitope level. Ex vivo analysis of spike-specific CD8<sup>+</sup> T cells by peptide MHC (pMHC) tetramers was performed in a subset of postvaccination participants from the HCs and each MS cohort (Supplemental Table 2). Several panels of pMHC tetramers were generated using previously published spike epitopes (16, 31, 33–35). Combinatorial tetramer



staining (Supplemental Table 3) and enrichment were performed as previously described (36, 37). Spike-specific CD8<sup>+</sup> T cells identified by tetramer enrichment were subsequently assessed for memory status by CCR7 and CD45RA expression (Figure 8.5A).

The proportion of samples with detectable spike tetramer-positive CD8<sup>+</sup>T cells was similar across all MS cohorts, ranging from 27% to 56% tetramer positivity (Figure 8.5B). The mean frequencies of spike tetramer-positive CD8<sup>+</sup> T cells did not significantly differ between MS cohorts (Figure 8.5C), although there were variations in spike-specific CD8<sup>+</sup> T cell population sizes, which was at least partially related to differences in the HLA genotypes available for tetramer analysis across the different patient cohorts (Supplemental Table 2). Consistent with a postvaccination response measured in peripheral blood samples, spike-specific CD8<sup>+</sup> T cells were predominantly effector memory (Tem), which were significantly higher than corresponding naive T cell (Tn) populations in all cohorts (Figure 8.5D). In addition, the proportion of Tn, T central memory (Tcm), Tem, and Tem cells reexpressing CD45RA (Temra) spike-specific CD8<sup>+</sup> T cells did not significantly differ across any of the MS cohorts. Overall, these findings indicate that the magnitude and activation state of SARS-CoV-2 vaccine-elicited T cell responses are not substantially changed by the various MS immunotherapies evaluated in this study.

## ***Discussion***

MS DMTs differentially affect humoral and cell-mediated immunity, both of which are essential for protection against COVID-19 (3, 5). In support of this, recently reported data indicate that unvaccinated patients with MS receiving anti-CD20 mAb treatments are at higher risk for severe COVID-19 (6, 7). To date, the majority of studies evaluating SARS-CoV-2 vaccine responses in patients with MS have been limited to measuring Ab levels (9–12, 22), and those that

have explored T cell reactivity have primarily focused on anti-CD20 mAb-treated patients (19, 24, 38). Moreover, no MS studies to date, to our knowledge, have investigated how DMTs affect neutralization against SARS-CoV-2, a key correlate of immune protection (4). Thus, there is a significant need to comprehensively investigate how different MS DMTs affect SARSCoV-2 vaccine-elicited Ab and CD4+ and CD8+ T cell immunity

Following vaccination, untreated patients with MS and those treated with GA, DMF, or NTZ mounted similar total spike and spike RBD IgG responses, compared with HCs. In contrast, patients treated with S1P receptor modulators or anti-CD20 mAbs had significantly reduced levels of total spike and spike RBD IgG, consistent with findings in recent reports (9–12). We did not observe a clear relationship between spike-Ab seropositivity and anti-CD20-mAb infusion interval and SARS-CoV-2 vaccination, in contrast to findings of several other studies (8, 19, 20, 22, 24). This disparity could be due to differences in patient populations or methodology. Our finding that the percentage of CD19+ B cells following vaccination, but not prior to vaccination, was significantly associated with spike-Ab seropositivity suggests that interval B cell reconstitution occurring in lymphoid tissue prior to circulation in the blood may be sufficient for Ab generation. Indeed, this idea is supported by a recent finding that spike-IgG seropositivity is present in a portion of anti-CD20 mAb-treated patients with MS despite the absence of circulating spike-specific B cells (19). Furthermore, the negative effect of cumulative anti-CD20 mAb treatment duration on spike-IgG seropositivity suggests that although essentially all circulating B cells are rapidly depleted following anti-CD20 mAb treatment, B cells may initially persist in smaller numbers in secondary lymphoid tissue (39) but are ultimately depleted with long-term treatment. It is also interesting to note that certain S1P receptor modulator-treated patients had near-normal total spike and spike RBD IgG levels, while other patients did not seroconvert. S1P

receptor modulators sequester B cells and T cells in secondary lymphoid tissues and disrupt germinal center formation (40), which is an important part of humoral reactivity following SARS-CoV-2 mRNA vaccination (41). It is possible the differences in Ab outcomes are related to S1P receptor modulator treatment duration; however, this conclusion is limited by lower patient numbers in the S1P receptor modulators cohort.

A strength of our study was the ability to assess high-resolution Ab reactivity across the entire spike protein using programmable phage display (VirScan) and to assess functional reactivity by pseudovirus neutralization. Ab reactivity against a broad range of spike determinants was observed among HCs and untreated patients with MS, including regions vital for SARS-CoV-2 entry into cells. In contrast, Ab reactivity was restricted to a narrower range of spike epitopes in seropositive patients with MS treated with S1P receptor modulators and anti-CD20 mAbs. Moreover, pseudovirus neutralization was significantly attenuated in patients receiving anti-CD20 mAb and S1P receptor modulator therapies, which directly correlated with reduced spike RBD IgG titers. These findings are clinically important because they highlight the limited applicability of using anti-spike seropositivity alone as a marker of immune protection. Rather, these data emphasize the importance of achieving high-titer spike RBD seroreactivity to infer adequate viral neutralization ability in patients with MS who are receiving certain immunotherapies. The SARS-CoV-2 sequences used in the VirScan (ancestral Wuhan-1) and neutralization assays (B.1 D614G) did not assess reactivity to more recent variants that harbor multiple mutations in the spike protein, such as B.1.617.2 (Delta) and B.1.1.529 (Omicron). Given the impacts of anti-CD20 mAbs and S1P receptor modulators on spike reactivity and neutralization, our findings raise the concern that protective Ab immunity will be further compromised against spike protein mutants.

We also performed an extensive analysis of spike-specific CD4<sup>+</sup> and CD8<sup>+</sup> T cells in all participants before and after SARS-CoV-2 vaccination. In contrast to the humoral response, spike-specific CD4<sup>+</sup> and CD8<sup>+</sup> T cell responses were largely intact across all MS cohorts irrespective of DMT status. Vaccine-elicited CD4<sup>+</sup> T cell responses were diminished in patients treated with S1P receptor modulators, which is consistent with the preferential reduction of circulating CD4<sup>+</sup> T cells by S1P receptor modulators (25). In addition, spike-specific CD4<sup>+</sup> and CD8<sup>+</sup> T cells from all MS treatment groups produced multiple effector cytokines, suggesting DMT exposure did not alter T cell polyfunctionality. Interestingly, we observed a trend toward increased CD8<sup>+</sup> T cell cytokine production in anti-CD20 mAb-treated patients compared with untreated patients with MS, which was significantly increased in the case of IFN- $\gamma$ <sup>+</sup> CD8<sup>+</sup> T cells in both anti-CD20 mAb cohorts. These findings support those in recent similar reports of increased SARS-CoV-2-specific CD8<sup>+</sup> T cell activation in anti-CD20 mAb-treated patients with MS (19, 24) and suggest that B cell depletion may result in compensatory changes in certain aspects of cellular immunity. However, the mechanism of such T cell-mediated changes and whether this has a protective effect against COVID-19 remain unknown.

A limitation of our study was the relatively smaller number of patients in certain MS treatment groups. Nonetheless, the results of our study have important potential implications for clinical guidance about treatment of patients with MS and other autoimmune conditions with similar immunotherapies. Our findings support similar findings of impaired SARS-CoV-2 vaccine-elicited humoral immunity in a variety of vulnerable, immunocompromised patient populations (42, 43). The finding that certain MS immunotherapies preferentially disrupt SARS-CoV-2 vaccine-induced humoral immune responses both quantitatively and functionally raises the concern that patients receiving such therapies may be at higher risk of contracting vaccine-

breakthrough COVID-19 (44). In addition, our data highlight the cumulative negative impact of prolonged anti-CD20 mAb treatment on the generation of de novo humoral immunity. On the other hand, the preservation of cell-mediated immunity provides reassurance that most immunosuppressed patients with MS will obtain at least partial protection from more severe COVID-19 outcomes. An outstanding question is whether immunosuppressed patients with MS will benefit from booster SARS-CoV-2 vaccinations, either by Ab seroconversion and/or augmentation of cell-mediated immunity. The data from our study, therefore, provide important insights regarding COVID-19 risk assessment and SARS-CoV-2 vaccination practices for immunosuppressed patient populations.

## ***Methods***

### *Study design*

In this prospective observational study, participants included patients with clinically definite MS (by 2017 McDonald criteria) (45) and HCs (i.e., not immunocompromised or receiving immunosuppressive therapy) aged 18 to 75 years. MS cohorts included patients not receiving any treatment (no DMT in the prior 6 months) or treated with GA, DMF, NTZ, any S1P receptor modulator, or i.v. anti-CD20 mAb therapy (i.e., RTX or OCR). No patients were treated with chronic daily steroids or high-dose steroids within 3 months of sample collection; however, most anti-CD20 mAb-treated patients received steroids as part of their preinfusion treatment regimen. Only participants with no history of COVID-19 and not previously vaccinated against SARS-CoV-2 prior to enrollment were included. All study participants completed full SARS-CoV-2 vaccination with one of the FDA-approved or authorized vaccines (i.e., Comiranty/BNT162b2 from Pfizer/BioNTech, mRNA-1273 from Moderna, or Ad26.COV2 from Johnson & Johnson). Blood samples were collected from all individuals before and 2 weeks (for

Comirnaty/BNT162b2 and mRNA-1273) or 4 weeks (for Ad26. COV2) after final SARS-CoV-2 vaccination. Basic participant characteristics and vaccine-related variables are outlined in Supplementary Table 1. Treatment-specific characteristics were recorded from the medical record for anti-CD20 mAb- and S1P receptor modulator-treated patients with MS. For patients receiving anti-CD20 mAb therapy, total IgG (last measured prior to vaccine), total cumulative treatment duration (i.e., time from start of antiCD20 mAb treatment until first vaccine dose), and treatment interval between last anti-CD20 mAb infusion and first vaccine dose were recorded. Absolute lymphocyte count (last measured prior to vaccine) and total cumulative treatment duration were also recorded for patients treated with S1P receptor modulators.

#### *Sample collection and processing*

Blood samples were collected from consented participants at the Neurosciences Clinical Research Unit at the University of California, San Francisco, or the patient's residence through ExamOne (a Quest Diagnostics company). At each time point, 90 mL of whole blood was collected in heparinized tubes and an additional 10 mL of blood was collected in serum separator tubes. All samples were processed within 24 hours of collection. Blood samples were spun at 500g for 10 minutes and plasma and serum were removed and frozen at  $-80^{\circ}\text{C}$  until ready for use. Whole-blood pellets were resuspended in  $1\times$  Dulbecco's PBS and PBMCs were isolated over Ficoll gradient. PBMCs were frozen in freezing medium (10% DMSO and 90% FBS) and stored in liquid nitrogen until the day of experimentation.

### *Semiquantitative spike-Ab analysis by Luminex assay*

Spectrally distinct Luminex beads were conjugated with trimeric spike protein (residues 1–1213), spike RBD (residues 328–533) (provided by John Pak, Chan Zuckerberg Biohub), or BSA fraction V (Sigma-Aldrich, catalog 10735094001) at a concentration of 5 µg of protein per 1 million beads. Conjugation was done via an EDC/sulfo-N-hydroxysuccinimide coupling strategy to terminal amines using Ab coupling kit following manufacturer’s instructions (Luminex, catalog 40-50016), as performed previously (26). All serological analyses were performed in duplicate, and beads were pooled on the day of use. Thawed serum samples were diluted in PBS + 0.05% Tween 20 (PBST) containing 1% nonfat milk and mixed with pooled protein-coated beads (2000–2500 beads per protein) at a final serum dilution of 1:500. Samples were incubated for 1 hour at room temperature, washed, and stained with 1:2000 anti-human IgG Fc Ab PE (BioLegend, catalog 637310) in PBST for 30 minutes at room temperature. Beads were washed with PBST and analyzed in a 96-well format on a Luminex LX 200 cytometer. The net MFI was recorded for each set of beads. The mean net MFI for total spike and spike RBD for each sample was divided by the net MFI for the corresponding BSA negative control. A net MFI  $\geq 5.0$  was used as a cutoff for total spike and spike RBD seropositivity, which has been previously demonstrated to be highly sensitive and specific (46).

### *Ab analysis by CoV VirScan*

Coronaphage library design and construction, immunoprecipitation, and generation of peptide count tables were performed as previously described (26). All peptide counts were converted to reads/100,000 reads (rp100k). For each vaccinated individual, peptide enrichment was calculated relative to the corresponding prevaccination sample as

rp100kpostvaccination/rp100kprevaccination. For each sample, enrichments were log transformed, and a z score calculated for each peptide in each sample. Peptides with z scores > 3 in postvaccination samples were considered significantly enriched over prevaccination. Seroreactivity maps were generated for each sample by aligning each significantly enriched peptide to the concatenated ORFs of SARS-CoV-2, focusing on the spike protein. Signal intensity at each position in the spike protein was the sum of signal for all peptides covering each position and was used to generate heatmaps as well as plots depicting the proportion of individuals with seroreactivity at each position in each treatment group.

#### *SARS-CoV-2 pseudovirus neutralization assay*

SARS-CoV-2 pseudoviruses were generated using a previously described recombinant vesicular stomatitis virus expressing GFP in place of the VSV glycoprotein (47). The SARS-CoV-2 spike gene bearing the D614G mutation was cloned in a CMV-driven expression vector and used to produce SARS-CoV-2 spike reporter pseudoviruses. Pseudoviruses were titered on Huh7.5.1 cells overexpressing ACE2 and TMPRSS2 (a gift from Andreas Puschnik, Chan Zuckerberg Biohub) using GFP expression to measure the concentration of focus-forming units (ffu), as recently described (48). Huh7.5.1-ACE2-TMPRSS2 cells were seeded in 96-well plates at a density of 7000 cells/well 1 day prior to pseudovirus inoculation. Cells were verified to be free of mycoplasma contamination with the MycoAlert Mycoplasma Detection Kit (Lonza). Serum samples (heat inactivated at 56°C for 30 minutes prior to neutralization) were diluted into complete culture media (DMEM with 10% FBS, 10 mM HEPES, 1× Pen-Strep-Glutamine) using the LabCyte Echo 525 liquid handler. To each well we added 1500 ffu of SARS-CoV-2 pseudovirus to reach final dilutions ranging from 1:20 to 1:2560, including no-serum and no-pseudovirus



controls. Serum/pseudovirus mixtures were incubated at 37°C for 1 hour before being added directly to cells. Cells inoculated with serum/pseudovirus mixtures were incubated at 37°C and 5% CO<sub>2</sub> for 24 hours, resuspended using 10× TrypLE Select (Gibco), and cell fluorescence was measured with the BD Celesta flow cytometer. All neutralization assays were repeated for a total of 3 independent experiments, with each experiment containing 2 technical replicates for each condition. Flow cytometry data were analyzed with FlowJo to determine the percentage of cells transduced with pseudovirus (i.e., GFP positive). Percent neutralization for each serum dilution was calculated by normalizing GFP-positive cell percentage to no-serum control wells. Fifty percent neutralization titers (NT<sub>50</sub>) were calculated from 8-point response curves generated in GraphPad Prism 7 using 4-parameter logistic regression.

*Flow cytometry analysis of basic immune cell subsets.*

PBMCs were thawed, washed, and equilibrated in RPMI medium with 10% FBS for 2 hours at 37°C and stained with the indicated cell-surface panel for identifying immune cell subsets, as shown in Supplemental Table 4. All samples were collected on an LSR Fortessa (BD). The gating strategy used is shown in Supplemental Figure 1A. Flow cytometry analysis was completed using FlowJo (BD).

*T cell analysis by AIM expression and ICS*

PBMCs were thawed, washed, and equilibrated in RPMI medium with 10% FBS for 2 hours at 37°C prior to initiation of functional T cell studies. PBMCs were washed and resuspended in serum-free RPMI medium for AIM studies or resuspended in serum-free RPMI medium containing 1:500 GolgiStop (BD), 1:500 GolgiPlug (BD), and 1:200 FastImmune (BD) for ICS

studies. For all studies, PBMCs were plated at  $1 \times 10^6$  cells/well in 96-well round-bottom plates. PBMCs were stimulated in parallel with spike peptide pools (n = 2 pools of 157 and 158 peptides; JPT Peptide Technologies) at a final concentration of 1  $\mu\text{g}/\text{mL}/\text{peptide}$ . In all assays, 0.2% DMSO vehicle control was used for no stimulation. PBMCs were stimulated for 24 hours for AIM assays and 16 hours for ICS assays. Cells were washed with FACS wash buffer (1 $\times$  Dulbecco's PBS without calcium or magnesium, 0.1% sodium azide, 2 mM EDTA, 1% FBS) and stained with the Ab panels for AIM and ICS listed in Supplemental Table 4.

In the case of AIM assays, cells were washed with FACS wash buffer, fixed with 2% paraformaldehyde (BD), and stored in FACS wash buffer in the dark at 4°C until ready for flow cytometry analysis, as described in the preceding sentence. For ICS assays, cells were washed after cell-surface staining and stained with a cocktail of intracellular cytokine Abs (see Supplemental Table 4 for Ab panel) in permeabilization buffer for 1 to 2 hours at 4°C. ICS samples were then fixed, washed, and stored as done for AIM samples until ready for flow cytometry analysis.

The gating strategy for AIM and ICS is shown in Supplemental Figure 3, A and B. The frequencies of spike-specific T cells were calculated by subtracting the no-stimulation background from the corresponding S1 and S2 pool-stimulated samples, which were then summed together.

#### *HLA genotyping*

Genomic DNA was isolated using the QiaAmp DNA Blood Mini Kit (Qiagen). A total of 100 ng of high-quality DNA was fragmented using the KAPA HyperPlus Kit (Roche). Subsequently, the ends of the fragmented DNA were repaired, poly-A tail was added and ligated through PCR to Illumina-compatible dual index adapters that were uniquely barcoded. After ligation, fragments were purified with 0.8 $\times$  ratio AMPure XP magnetic beads, followed by double-

size selection (0.42× and 0.15× ratios) to select libraries of approximately 800 bp. Finally, libraries were amplified and purified with magnetic beads.

After fluorometric quantification, 30 ng of each sample was precisely pooled using ultrasonic acoustic energy, and the targeted capture was performed with HyperCap kit (Roche). Briefly, the volumes were reduced using magnetic beads, and the DNA libraries were bound to 1394 biotinylated probes specific to the HLA region, covering all exons, introns, and regulatory regions of HLA-A, HLA-B, HLA-C, HLADRB1, HLA-DRA, HLA-DQB1, HLA-DQA1, HLA-DPB1, and HLA-DPA1. Fragments targeted by the probes were captured with streptavidin magnetic beads and then amplified and purified. Enriched libraries were analyzed in BioAnalyzer (Agilent) and quantified by digital-droplet PCR. Finally, enriched libraries were sequenced with the HiSeq4000 platform (Illumina) with a paired-end 150 bp sequencing protocol. After sequencing, data were analyzed with HLA Explorer software (Omixon).

#### *Spike antigen-specific CD8<sup>+</sup> T cell analysis by pMHC tetramer*

pMHC I tetramers loaded with spike peptides and labeled with the fluorophores (Supplemental Table 2) were generated from UV-photolabile monomers for HLA-A\*01:01, HLA-A\*02:01, HLA-A\*03:01, HLA-A\*11:01, and HLA-B\*07:02 monomers (NIH Tetramer Core) by UV peptide exchange, as previously described (36, 49). To each tetramer, 500 μM d-biotin was added, and tetramers were pooled as indicated in Supplemental Table 2 on the day of use. All tetramer experiments were completed within 3 weeks of tetramer generation. For each tested sample, 2–3 × 10<sup>7</sup> PBMCs were thawed, washed, and equilibrated in RPMI medium with 10% FBS for 1 hour at 37°C. The frequencies of spike antigen-specific CD8<sup>+</sup> T cells were calculated as previously described (36, 50). In brief, an aliquot of PBMCs was used for cell-surface staining

(Supplemental Table 1) and counted with 123count eBeads (Invitrogen) prior to tetramer enrichment. The remainder of PBMCs were stained with the indicated tetramer pools for 30 minutes at room temperature, washed, and enriched using anti-PE magnetic microbeads (Miltenyi) over a magnetic column. Tetramer-enriched cells were cell surface-stained and counted as done for pre-enrichment.

The gating strategy is outlined in Supplemental Figure 3C. A stringent tetramer gating strategy was used whereby CD8<sup>+</sup> T cells labeled with only 2 fluorophores were considered antigen specific (i.e., cells that stained positive with  $\pm 2$  fluorophores were excluded from the analysis). Spike tetramer-positive CD8<sup>+</sup> T cells with frequencies greater than  $1 \times 10^{-5}$  per total CD8<sup>+</sup> T cells were considered positive.

### *Statistics*

Prevaccine and postvaccine Ab and T cell responses were compared by multiple paired 2-way, 2-tailed t tests. Univariate analysis by serostatus was performed by Mann-Whitney test. Kruskal-Wallis with multiple comparisons was used to analyze postvaccination Ab and T cell responses across different groups; untreated patients with MS were used as the comparison group for statistical significance, unless stated otherwise. Simple linear regression was to analyze IgG levels with the indicated independent variables, and Spearman's rank was used for correlation analysis. The level of significance was set at  $P < 0.05$ .

### *Study approval*

All enrolled participants provided written, informed consent for this study, which was approved by the University of California, San Francisco, Committee on Human Research (IRB no. 21-33240)

### *Author contributions*

JJS, RB, SSZ, and MRW designed and supervised the study. WMR, K Mcpolin, and JRA performed clinical recruitment and sample acquisition. Patient data were collected and managed by JJS, WR, and K Mcpolin. JJS, K. Mittl, WR, CG, CMS, and SAS carried out sample processing. Luminex analysis was completed by JJS, K Mittl, CRZ, RPL, and CG. BDA completed VirScan library preparation immunoprecipitations and JVR and RD performed VirScan analysis. MTL and JLD performed pseudovirus neutralization and analysis. JJS and K Mittl performed all T cell studies. DGA and JAH performed HLA genotyping. Statistical analysis was completed by JJS and JAH. JJS wrote the initial draft of the manuscript. All authors contributed to data interpretation and manuscript review.

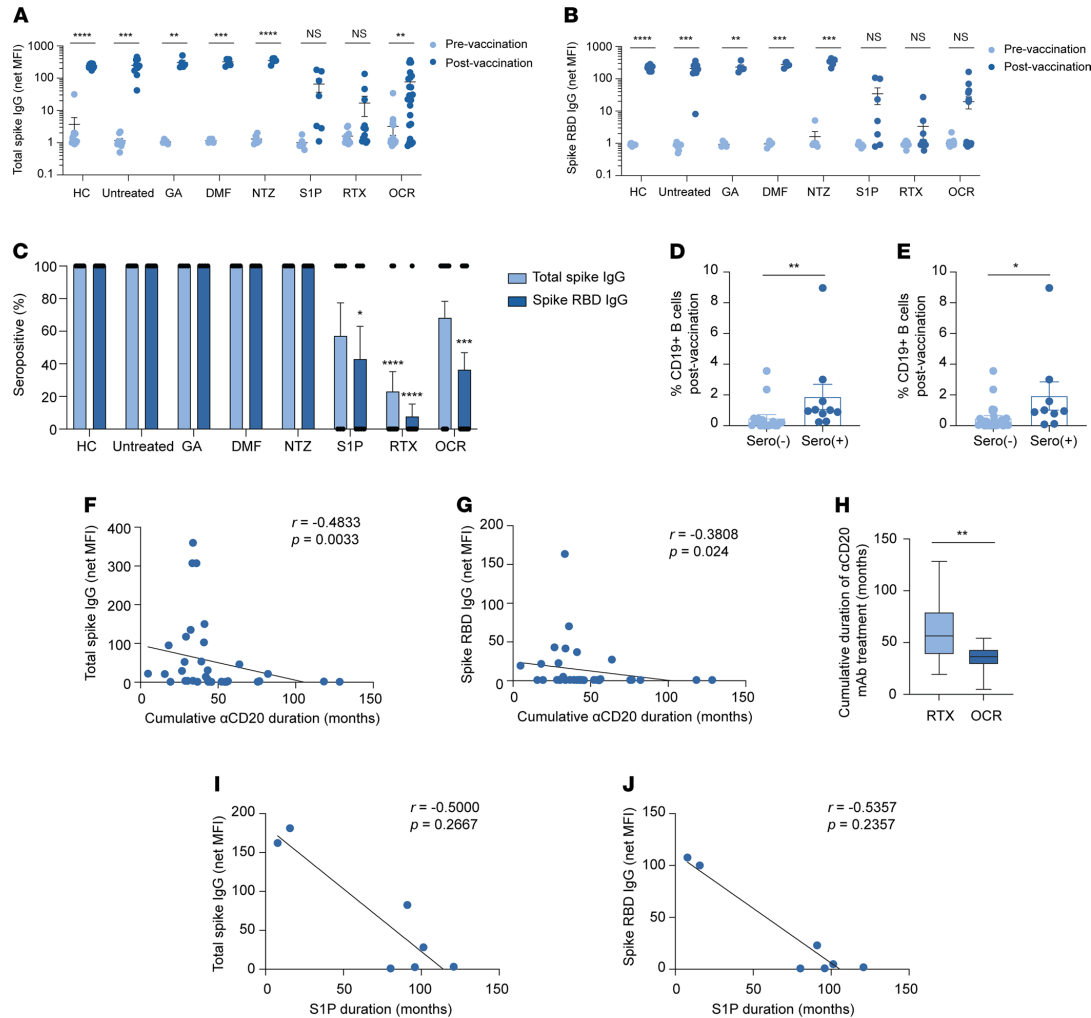


**Figure 8.1. Analysis of total spike and spike RBD IgG before and after SARS-CoV-2 vaccination of patients with MS receiving different DMTs.** (A and B) Mean net MFI ( $\pm$  SEM) of total spike IgG (A) and spike RBD IgG (B) at pre- and postvaccination time points (multiple paired  $t$  tests). (C) Percent seropositivity of total spike IgG and spike RBD IgG following vaccination for each cohort (Kruskal-Wallis test with multiple comparisons; significance was based on comparison between untreated MS and other MS treatment groups). (D and E) Percent CD19<sup>+</sup> B cells following vaccination in total spike IgG (D) and spike RBD (E) seronegative and seropositive patients treated with anti-CD20 mAbs (Mann-Whitney test). (F and G) Simple linear regression of cumulative duration of anti-CD20 mAb treatment prior to SARS-CoV-2 vaccination total spike IgG (F) and spike RBD (G) (correlation by Spearman's rank). (H) Comparison of cumulative duration of therapy by type of anti-CD20 mAb treatment (Mann-Whitney test). (I and J) Simple linear regression of net MFI of total spike IgG (I) and spike RBD IgG (J) by duration of S1P receptor modulator duration (correlation by Spearman's rank). NS,  $P > 0.05$ ; \* $P < 0.05$ ; \*\* $P < 0.01$ ; \*\*\* $P < 0.001$ ; \*\*\*\* $P < 0.0001$ .

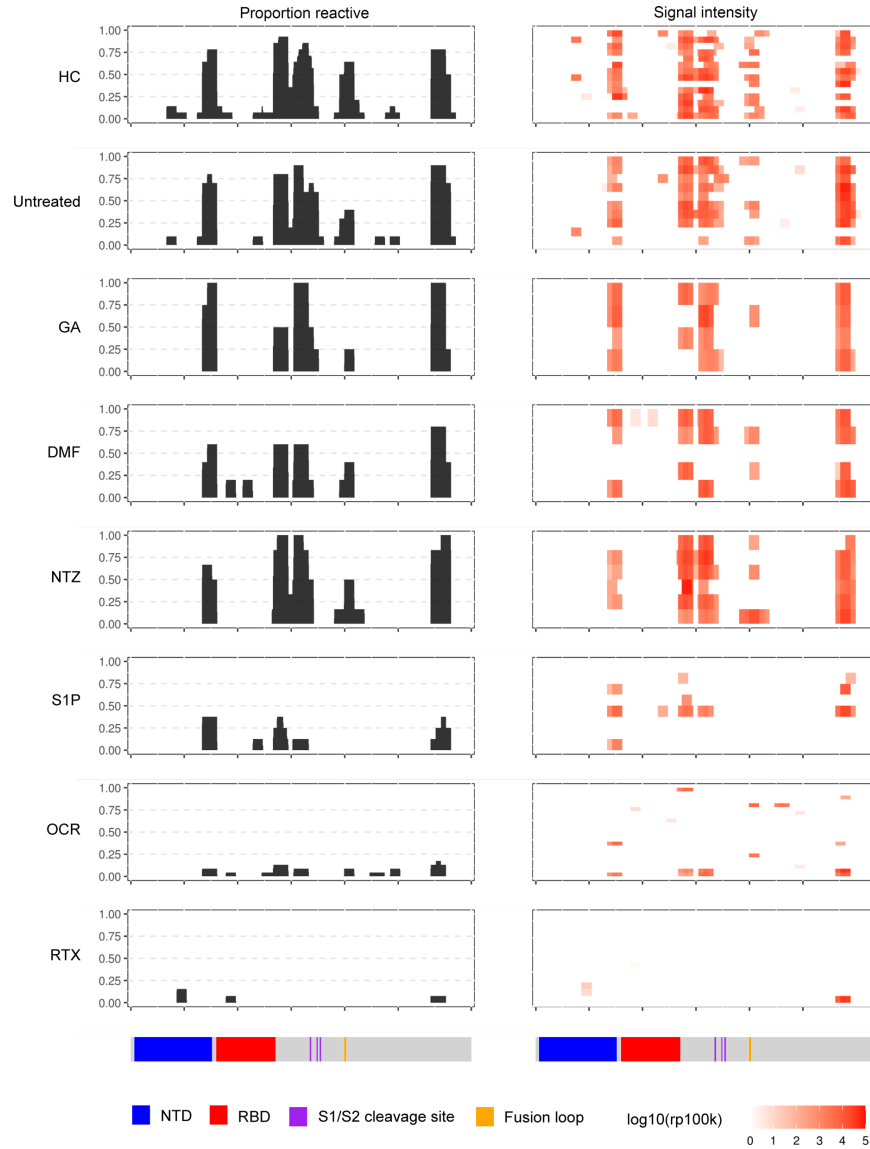


**Figure 8.2. VirScan analysis of postvaccination Ab reactivity against the SARS-CoV-2 spike proteome by MS DMT status.** The left column indicates the proportion of individuals seroreactive against the different regions of the spike protein, and the right column indicates the relative signal intensity of Ab binding, with each individual separated by row. The corresponding regions of the spike protein are indicated below the plots.

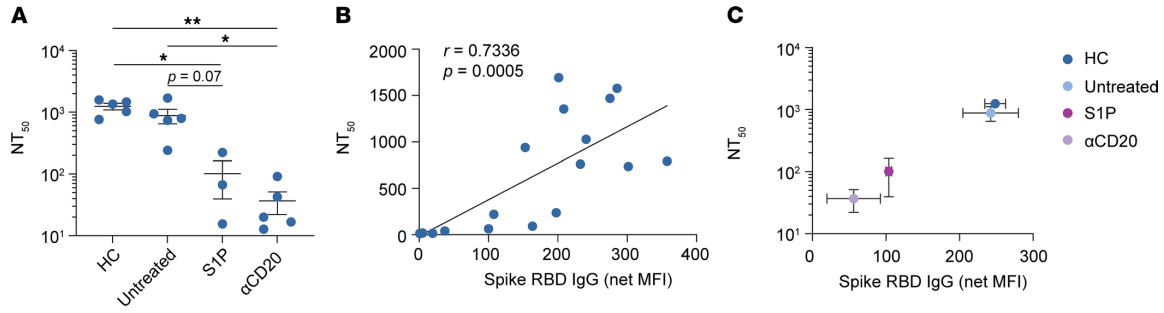


**Figure 8.3. SARS-CoV-2 pseudovirus neutralization in seropositive patients treated with S1P receptor modulators or anti-CD20 mAbs.** (A) Mean 50% pseudovirus neutralization titer reciprocal dilution ( $NT_{50} \pm SEM$ ) of serum from anti-spike seropositive HCs ( $n = 5$ ), untreated patients with MS ( $n = 5$ ), patients treated with S1P receptor modulators ( $n = 3$ ), and those treated with anti-CD20 mAbs ( $n = 5$ ) (Kruskal-Wallis test with multiple comparisons). (B) Nonlinear regression of spike RBD IgG (net MFI) of all samples by  $NT_{50}$  (correlation by Spearman's rank). (C) Spike RBD IgG (mean net MFI  $\pm SEM$ ) versus 50% neutralization titer ( $NT_{50} \pm SEM$ ) by the indicated treatment groups.



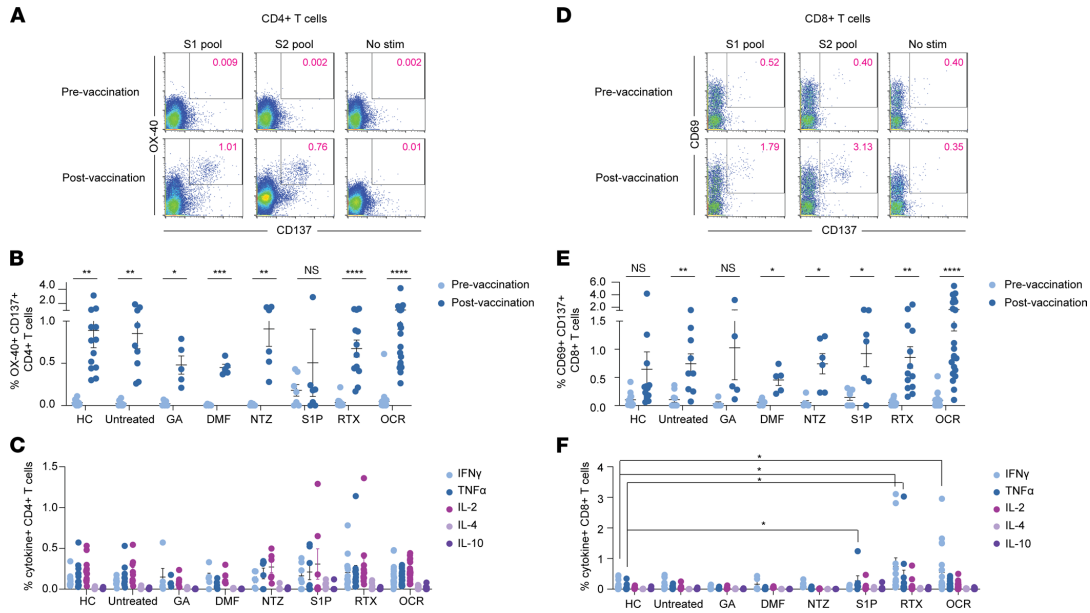


**Figure 8.4. Evaluation of spike antigen–specific CD4<sup>+</sup> and CD8<sup>+</sup> T cells in patients with MS treated with different DMTs.** (A and D) AIM analysis of CD4<sup>+</sup> (A) and CD8<sup>+</sup> (D) T cells from a representative patient with MS before and after SARS-CoV-2 vaccination. Summarized AIM and ICS analysis of CD4<sup>+</sup> (B and C) and CD8<sup>+</sup> T cells (E and F) across all cohorts. AIM data are shown for pre- and postvaccination time points (multiple paired *t* tests); ICS data depict post-vaccination analysis only (Kruskal-Willis test with multiple comparisons). Stim, stimulation.

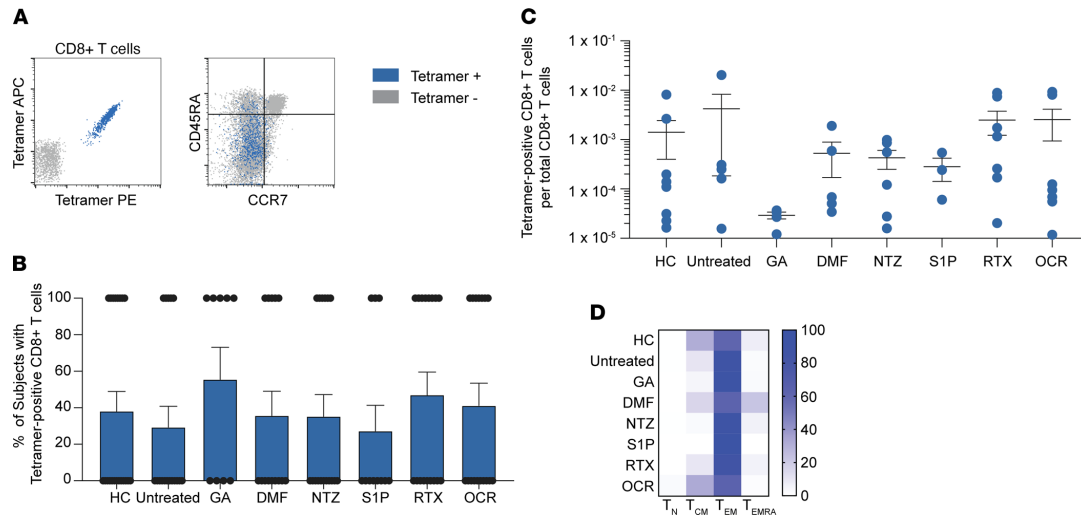


**Figure 8.5. Ex vivo analysis of postvaccination spike-specific CD8<sup>+</sup> T cells of patients with MS treated with different DMTs, by pMHC I tetramer.** (A) Representative analysis of enriched spike peptide tetramer-positive CD8<sup>+</sup> T cells (left panel) and memory analysis by tetramer status (right panel). (B and C) The proportion of tested participants in each cohort with detectable spike tetramer-positive CD8<sup>+</sup> T cells (B) and their frequencies (C) are shown. (D) Heatmap analysis of memory subsets of spike tetramer-positive CD8<sup>+</sup> T cells in each cohort. APC, allophycocyanin; PE, phycoerythrin.

## Chapter 8 References

1. McGinley MP, et al. Diagnosis and treatment of multiple sclerosis: a review. *JAMA*. 2021;325(8):765–779.
2. Luna G, et al. Infection risks among patients with multiple sclerosis treated with fingolimod, natalizumab, rituximab, and injectable therapies. *JAMA Neurol*. 2020;77(2):184–191.
3. Sette A, Crotty S. Adaptive immunity to SARS-CoV-2 and COVID-19. *Cell*. 2021;184(4):861–880.
4. Khoury DS, et al. Neutralizing antibody levels are highly predictive of immune protection from symptomatic SARS-CoV-2 infection. *Nat Med*. 2021;27(7):1205–1211.
5. Goldman-Israelow B, et al. Adaptive immune determinants of viral clearance and protection in mouse models of SARS-CoV-2. *Sci Immunol*. 2021;6(64):eabl4509.
6. Salter A, et al. Outcomes and risk factors associated with SARS-CoV-2 infection in a North American registry of patients with multiple sclerosis. *JAMA Neurol*. 2021;78(6):699–708.
7. Sormani MP, et al. Disease-modifying therapies and Coronavirus disease 2019 severity in multiple sclerosis. *Ann Neurol*. 2021;89(4):780–789.
8. Achiron A, et al. Humoral immune response to COVID-19 mRNA vaccine in patients with multiple sclerosis treated with high-efficacy disease-modifying therapies. *Ther Adv Neurol Disord*. 2021;14:17562864211012835.
9. van Kempen ZLE, et al. SARS-CoV-2 antibodies in adult patients with multiple sclerosis in the Amsterdam MS cohort. *JAMA Neurol*. 2021;78(7):880–882.
10. Louapre C, et al. Anti-CD20 therapies decrease humoral immune response to SARS-CoV-2 in patients with multiple sclerosis or neuromyelitis optica spectrum disorders. *J Neurol Neurosurg Psychiatry*. 2021;93(1):24–31.

11. Sormani MP, et al. SARS-CoV-2 serology after COVID-19 in multiple sclerosis: an international cohort study [published online July 30, 2021]. *Mult Scler*. <https://doi.org/10.1177/13524585211035318>.
12. Bigaut K, et al. Impact of disease-modifying treatments of multiple sclerosis on anti-SARS-CoV-2 antibodies. *Neurol Neuroimmunol Neuroinflamm*. 2021;8(5):e1055.
13. Widge AT, et al. Durability of responses after SARS-CoV-2 mRNA-1273 vaccination. *N Engl J Med*. 2020;384(1):80–82.
14. Walsh EE, et al. Safety and immunogenicity of two RNA-based Covid-19 vaccine candidates. *N Engl J Med*. 2020;383(25):2439–2450.
15. Anderson EJ, et al. Safety and immunogenicity of SARS-CoV-2 mRNA-1273 vaccine in older adults. *N Engl J Med*. 2020;383(25):2427–2438.
16. Sahin U, et al. BNT162b2 vaccine induces neutralizing antibodies and poly-specific T cells in humans. *Nature*. 2021;595(7868):572–577.
17. Ciotti JR, et al. Effects of MS disease-modifying therapies on responses to vaccinations: a review. *Mult Scler Relat Disord*. 2020;45:102439.
18. Bar-Or A, et al. Effect of ocrelizumab on vaccine responses in patients with multiple sclerosis: the VELOCE study. *Neurology*. 2020;95(14):e1999–e2008.
19. Apostolidis SA, et al. Altered cellular and humoral immune responses following SARS-CoV-2 mRNA vaccination in patients with multiple sclerosis on anti-CD20 therapy. *Nat Med*. 2021;27(11):1990–2001.
20. Tallantyre EC, et al. COVID-19 vaccine response in people with multiple sclerosis. *Ann Neurol*. 2022;91(1):89–100.

21. Novak F, et al. Humoral immune response following SARS-CoV-2 mRNA vaccination concomitant to anti-CD20 therapy in multiple sclerosis. *Mult Scler Relat Disord*. 2021;56:103251.
22. Disanto G, et al. Association of disease-modifying treatment and anti-CD20 infusion timing with humoral response to 2 SARSCoV-2 vaccines in patients with multiple sclerosis. *JAMA Neurol*. 2021;78(12):1529–1531.
23. Cao Y, et al. Potent neutralizing antibodies against SARS-CoV-2 identified by high-throughput single-cell sequencing of convalescent patients' B cells. *Cell*. 2020;182(1):73–84.
24. Gadani SP, et al. Discordant humoral and T cell immune responses to SARS-CoV-2 vaccination in people with multiple sclerosis on anti-CD20 therapy. *EBioMedicine*. 2021;73:103636.
25. Mehling M, et al. FTY720 therapy exerts differential effects on T cell subsets in multiple sclerosis. *Neurology*. 2008;71(16):1261–1267.
26. Zamecnik CR, et al. ReScan, a multiplex diagnostic pipeline, pans human sera for SARS-CoV-2 antigens. *Cell Rep Med*. 2020;1(7):100123.
27. Sawcer S, et al. Genetic risk and a primary role for cell-mediated immune mechanisms in multiple sclerosis. *Nature*. 2011;476(7359):214–219.
28. Barnes CO, et al. SARS-CoV-2 neutralizing antibody structures inform therapeutic strategies. *Nature*. 2020;588(7839):682–687.
29. Premkumar L, et al. The receptor binding domain of the viral spike protein is an immunodominant and highly specific target of antibodies in SARS-CoV-2 patients. *Sci Immunol*. 2020;5(48):eabc8413.

30. Grifoni A, et al. Targets of T cell responses to SARS-CoV-2 Coronavirus in humans with COVID-19 disease and unexposed individuals. *Cell*. 2020;181(7):1489–1501.
31. Nelde A, et al. SARS-CoV-2-derived peptides define heterologous and COVID-19-induced T cell recognition. *Nat Immunol*. 2021;22(1):74–85.
32. Rommer PS, et al. Immunological aspects of approved MS therapeutics. *Front Immunol*. 2019;10:1564.
33. Schulien I, et al. Characterization of pre-existing and induced SARS-CoV-2-specific CD8<sup>+</sup> T cells. *Nat Med*. 2021;27(1):78–85.
34. Kared H, et al. SARS-CoV-2-specific CD8<sup>+</sup> T cell responses in convalescent COVID-19 individuals. *J Clin Invest*. 2021;131(5):145476.
35. Ferretti AP, et al. Unbiased screens show CD8<sup>+</sup> T cells of COVID-19 patients recognize shared epitopes in SARS-CoV-2 that largely reside outside the spike protein. *Immunity*. 2020;53(5):1095–1107.
36. Sabatino JJ, et al. Anti-CD20 therapy depletes activated myelin-specific CD8<sup>+</sup> T cells in multiple sclerosis. *Proc Natl Acad Sci U S A*. 2019;116(51):25800–25807.
37. Oberhardt V, et al. Rapid and stable mobilization of CD8<sup>+</sup> T cells by SARS-CoV-2 mRNA vaccine. *Nature*. 2021;597(7875):268–273.
38. Brill L, et al. Humoral and T-cell response to SARS-CoV-2 vaccination in patients with multiple sclerosis treated with ocrelizumab. *JAMA Neurol*. 2021;78(12):1510–1514.
39. Häusler D, et al. Functional characterization of reappearing B cells after anti-CD20 treatment of CNS autoimmune disease. *Proc Natl Acad Sci U S A*. 2018;115(39):9773–9778.
40. Han S, et al. FTY720 suppresses humoral immunity by inhibiting germinal center reaction. *Blood*. 2004;104(13):4129–4133.

41. Turner JS, et al. SARS-CoV-2 mRNA vaccines induce persistent human germinal centre responses. *Nature*. 2021;596(7870):109–113.
42. Marinaki S, et al. Immunogenicity of SARS-CoV-2 BNT162b2 vaccine in solid organ transplant recipients. *Am J Transplant*. 2021;21(8):2913–2915.
43. Deepak P, et al. Effect of immunosuppression on the immunogenicity of mRNA vaccines to SARS-CoV-2: a prospective cohort study. *Ann Intern Med*. 2021;174(11):1572–1585.
44. Brosh-Nissimov T, et al. BNT162b2 vaccine breakthrough: clinical characteristics of 152 fully vaccinated hospitalized COVID-19 patients in Israel. *Clin Microbiol Infect*. 2021;27(11):1652–1657.
45. Thompson AJ, et al. Diagnosis of multiple sclerosis: 2017 revisions of the McDonald criteria. *Lancet Neurol*. 2018;17(2):162–173.
46. Fenwick C, et al. Changes in SARS-CoV-2 spike versus nucleoprotein antibody responses impact the estimates of infections in population-based seroprevalence studies. *J Virol*. 2021;95(3):e01828–20.
47. Hoffmann M, et al. A multibasic cleavage site in the spike protein of SARS-CoV-2 is essential for infection of human lung cells. *Mol Cell*. 2020;78(4):779–784.
48. Laurie MT, et al. SARS-CoV-2 variant exposures elicit antibody responses with differential cross-neutralization of established and emerging strains including Delta and Omicron [published online January 3, 2022]. *J Infect Dis*. <https://doi.org/10.1093/infdis/jiab635>.
49. Rodenko B, et al. Generation of peptide-MHC class I complexes through UV-mediated ligand exchange. *Nat Protoc*. 2006;1(3):1120–1132.
50. Moon JJ, et al. Tracking epitope-specific T cells. *Nat Protoc*. 2009;4(4):565–581.

## **Chapter 9:**

### **Transmission dynamics of SARS-CoV-2 among vaccinated household members and related immune responses**

This chapter is a reprint of:

Liu J, Laurie MT, Rubio L, Vazquez SE, Sunshine S, Mitchell AM, Hapte-Selassie M, Mann SA, Pilarowski G, Black D, Marquez C, Rojas S, Lionakis MS, Petersen M, Whitman JD, Jain V, Anderson M, Havlir D, DeRisi J. SARS-CoV-2 transmission dynamics and immune responses in a household of vaccinated persons. *Clin Infect Dis.* 2022; Jan 17:ciac029. doi: 10.1093/cid/ciac029.

Supplemental files that are not figures can be found with the original work.



## ***Abstract***

While SARS-CoV-2 vaccines prevent severe disease effectively, post-vaccination ‘breakthrough’ COVID-19 infections and transmission among vaccinated individuals remain ongoing concerns. We present an in-depth characterization of transmission and immunity among vaccinated individuals in a household, revealing complex dynamics and unappreciated comorbidities, including autoimmunity to type1 interferon in the presumptive index case.

## ***Introduction***

COVID-19 has caused over 230 million cases of infection worldwide, leading to more than 4.7 million deaths due to coronavirus disease (COVID-19) [1]. Global vaccination efforts have so far administered 6.1 billion vaccine doses [2]. In the United States, three FDA-authorized vaccines have been widely distributed: BNT162b2 by Pfizer/BioNTech, mRNA-1273 by Moderna, and JNJ-78436735 by J&J/Janssen. Each has demonstrated, through clinical trials and retrospective studies, the capacity to prevent symptomatic infection and severe disease [3].

Approximately 50% of the United States population is considered fully vaccinated. Many households have mixed populations of adults and children with variable completion of COVID-19 vaccination [2]. Furthermore, most SARS-CoV-2 lineages have been outcompeted and replaced by newer variants of concern including the Delta and Gamma variants. Further, many spike protein mutations associated with neutralizing antibody escape (K417N/T, R346K, L452R, T478K, E484K/Q, N501Y) have emerged [4,5]. Given these factors, COVID-19 infections in fully vaccinated people (i.e., breakthrough) are well documented [6]. However, there have been relatively few detailed studies to date of household transmission trajectories, especially in

households with individuals who received different vaccines, or who have different vaccine completion statuses.

Here, we describe a household cluster of Gamma variant COVID-19 cases occurring in vaccinated family members living in co-residence that resulted in mixed clinical outcomes. A detailed inspection of the epidemiological and clinical features of these cases, together with serology testing and genomic sequencing, suggest complex factors including partial immunity and unrecognized underlying autoimmunity, as potential contributors to breakthrough infections. Our data add to rapidly emerging literature on SARS-CoV-2 transmission dynamics within households of vaccinated persons.

### ***Description of individuals in the study household***

Individuals 1-5 lived together in the same residence, where they ate, slept, and socialized with one another in an unmasked setting. Individual 6 lived separately but frequented the home of Individuals 1-5. Together, these individuals also attended weekly community events, such as religious services, together as one large group. Each individual was thus exposed to one another either through co-residence or frequent visitation.

Individual 1 is an 80-year-old man with diabetes and asthma who received BNT162b2/Pfizer vaccine on April 20 and May 10, 2021. On May 13, malaise, myalgia and diarrhea developed. On May 19, a SARS-CoV-2 PCR test was positive and on May 20, he presented to a local hospital, had hypoxia, and was admitted for inpatient management. Due to severe COVID-19, acute respiratory distress syndrome (ARDS), and respiratory failure, he required mechanical ventilation. He received remdesivir, dexamethasone and tocilizumab and improved, was weaned from ventilator, and was discharged home on June 2.

Individual 2 is a 36-year-old woman who received JNJ-78436735/Janssen vaccine on April 10, 2021. On May 16, she had onset of fever, cough, rhinorrhea, and headache. On May 19, a PCR test was positive. On May 23, a BinaxNOW (Abbott) rapid antigen test was positive. She did not require care at a health facility and improved with self-monitoring at home.

Individual 3 is a 60-year-old woman who received mRNA-1273/Moderna vaccine on March 9 and April 6, 2021. On May 19, she had onset of fever, chills, cough and rhinorrhea. On May 20, a SARS-CoV-2 PCR test was positive and on May 23, a BinaxNOW test was positive. She also did not require care at a health facility and improved with self-monitoring at home.

Individual 4 is an 84-year-old woman who received mRNA-1273/Moderna vaccine on February 25 and March 26, 2021. After members of her family tested positive for COVID-19, she began home-based quarantine on May 20th. On May 23, a BinaxNOW test was negative.

Individual 5 is a 40-year-old man who had tested positive for SARS-CoV-2 the previous year on July 24, 2020. At that time, he isolated with Individual 6. Individual 5 received the JNJ-78436735/Janssen vaccine on April 10, 2021. Although he did not quarantine separately from family members who tested positive, a SARS-CoV-2 PCR test on May 22 was negative.

Individual 6 is a 60-year-old woman who directly cared for Individual 5 when he tested positive for SARS-CoV-2 in July 2020. Despite being unable to quarantine, she tested negative for SARS-CoV-2 and did not develop any COVID-like symptoms. On May 17, 2021, she received the first dose of BNT162b2/Pfizer vaccine. Although she lived apart from Individuals 1-5, she visited their home frequently and attended community events with them. When her BinaxNOW test was negative on May 23, she had not yet received a second dose of the vaccine.

Timelines of vaccination, COVID-19 symptom onset, and testing history are summarized in Figure 9.1A and Supplementary Table 1.

## ***Results***

SARS-CoV-2 positivity as determined by qPCR amplification of the nasal swab samples corroborated the BinaxNOW results for each household member. Viral genome sequences were recovered from the three individuals who tested positive. Sequences consistent with the Gamma variant were recovered from Individual 2 (90% genome coverage; GISAID: EPI\_ISL\_2508365) and Individual 3 (98% genome coverage; GISAID: EPI\_ISL\_2508366). (Figure 9.2, BioProject PRJNA790937) Despite incomplete recovery, the partial sequence from Individual 1 (17%) contained mutations consistent with the Gamma variant (Supplementary Table 2). Characteristic mutations of concern (K417T, E484K, and N501Y) were observed [4,5]. Analysis of the consensus genomes from Individuals 2 and 3 revealed only a single nucleotide difference (G17122T, leading to a ORF1b:A1219S amino acid substitution).

Serum samples from the five household members were analyzed for SARS-CoV-2 neutralizing antibodies using a pseudovirus neutralization assay [7]. Sera from members of this household demonstrated a wide range of neutralization (Figure 9.1B). Individual 1 had a much lower neutralizing antibody titer compared to the fully vaccinated individuals (D614G NT<sub>50</sub>=4.4x lower, Gamma NT<sub>50</sub>=6.3x lower), despite being measured 14 days post-symptom onset, and 17 days after his second vaccine dose. Conversely, despite only partial vaccination, Individual 6 had a very high neutralizing antibody titer (D614G NT<sub>50</sub>=4.5x higher, Gamma NT<sub>50</sub>=5.0x higher) versus the healthy vaccinated cohort. Although this may have been related to caring for Individual 5 a year prior, Individual 6 had negative serology on the anti-SARS-CoV-2-N IgG Abbott Architect test. Finally, while Individuals 2, 3, and 4 had neutralizing antibody titers in the typical range of fully vaccinated individuals, Individuals 2 and 3 ultimately tested positive for COVID-19. Taken together, our observations indicate that fully vaccinated individuals may be at risk of

breakthrough infection when living in households with sustained close contact with infected individuals.

The neutralization efficacy of patients' sera against the Gamma variant pseudotype was approximately 2-fold lower than the measured NT<sub>50</sub> against wild-type virus (D614G spike mutation only). This observation is consistent with previously described decreases in neutralization against variants, especially those harboring mutations at E484K [4,5,8].

Additionally, we tested for anti-IFN- $\alpha$ 2 auto-antibodies, a marker correlated with severe COVID-19 and poor patient outcomes [9,10]. Using serum from patients with Autoimmune Polyglandular Syndrome Type 1 (APS1), an autoimmune syndrome where patients frequently develop an abundance of anti-IFN- $\alpha$ 2 antibodies, as a benchmark for verified interferon autoimmunity, we measured for anti-IFN- $\alpha$ 2 antibody presence using a radioligand binding assay (RLBA) [9]. Serum from Individual 1, who had the most severe response to infection, exhibited positive anti-IFN- $\alpha$ 2 antibody signal while the other family members had negative titers (Figure 9.1C).

## ***Discussion***

We describe a family of mixed vaccination statuses who experienced various clinical trajectories after a Gamma variant COVID-19 exposure in the household. Although coverage of the recovered SARS-CoV-2 genome from Individual 1 is incomplete, and Individuals 2 and 3 differ by one amino acid substitution, the rarity of the Gamma variant (6.5% of all sequences submitted to GISAID from San Francisco County from April to June) supports the conjecture that infection of this household is derived from a common source. Furthermore, all other Gamma variant sequences from this time period had 3-32 (mean=13; median=14) nucleotide substitutions

compared to this household, strongly suggesting direct transmission between household individuals as opposed to coincidental, simultaneous infection outside the home.

Clinical trajectories experienced by household individuals ranged from severe illness requiring hospitalization to mild symptomatic illness to avoiding COVID-19 infection altogether. Individual 1, who had low titers of neutralizing antibodies following vaccination, still developed severe COVID-19 infection. Testing for anti-IFN- $\alpha$ 2 auto-antibodies revealed that serum from Individual 1 contained high levels of antibodies against IFN- $\alpha$ 2, a trait enriched among patients with life-threatening COVID-19 pneumonia [10]. Although the presence of such auto-antibodies can be clinically silent, they appear to play an influential role in patient outcomes for SARS-CoV-2 infection [12].

Comorbidities such as autoimmune caused by anti-IFN auto-antibodies can lead to decreased protection against circulating variants with spike mutations conferring neutralization escape and thus raise the risk of breakthrough infections [10]. With household exposure to COVID-19, even fully vaccinated individuals with typical levels of neutralizing antibodies are at risk of infection. This data is strongly consistent with intrahousehold transmission amongst three vaccinated household members in this study, and this data highlights the inherent complexities of individuals, including unrealized underlying autoimmunity, that may contribute to transmission dynamics. This data supports the urgency for continued vaccination, boosters, and next-generation vaccines that contain mutations known to confer immune escape potential.

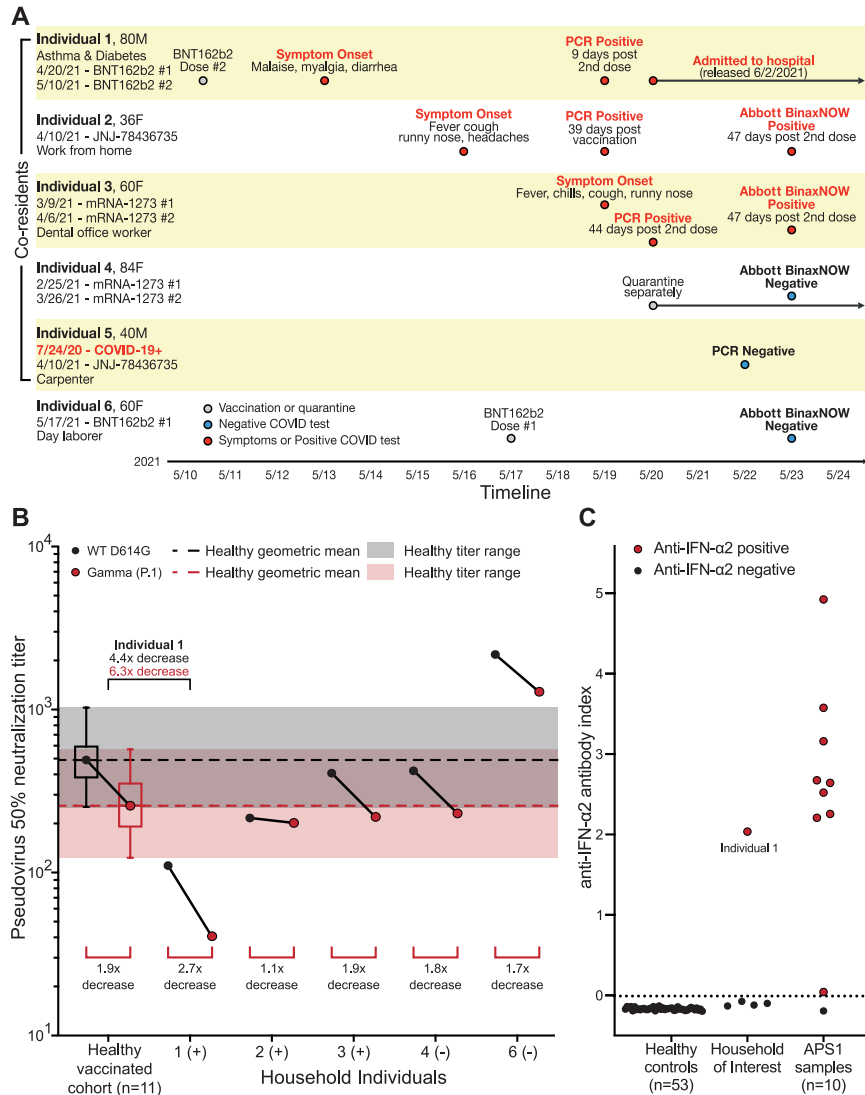


**Figure 9.1. Serum samples from household individuals reveal diverse neutralization capabilities as well as presence of anti-IFN- $\alpha$ 2 auto-antibodies in Individual 1. (A)** Timeline illustrating the order of events experienced by individuals in the study household, including vaccination, symptom onset, and test results. Additional details are available in Supplementary Table 1. **(B)** Plot of 50% pseudo-virus neutralization titers ( $NT_{50}$ ) of serum samples from healthy vaccinated controls ( $n = 11$ ) collected 12–60 days post-second dose (average = 26.4 days; details of serum collection timing relative to vaccination and positive COVID-19 tests are described in Supplementary Table 3). For the healthy vaccinated donor cohort, geometric mean titer (dashed lines), interquartile range (boxes), and full range (shaded region) are shown for D614G (black) and Gamma (red) pseudo-viruses.  $NT_{50}$  values for Gamma variant pseudo-virus were approximately 2-fold lower than D614G pseudo-virus for the healthy vaccinated cohort and most household members sera, apart from Individual 2. All household member serum neutralization titers were within or above the range of healthy donor titers, except for Individual 1, whose

neutralization titers for D614G and Gamma were 4.4-fold and 6.3-fold lower than those in healthy controls, respectively. (C) Detection by radioligand binding assay reveals that anti-IFN- $\alpha$ 2 autoantibodies are absent from all assayed prepandemic healthy controls (n = 42) and vaccinated healthy controls (n = 11) [7]. In this household, only Individual 1 demonstrated the presence of anti-IFN- $\alpha$ 2 auto-antibodies. Autoimmune polyglandular syndrome type 1 (APS1) patient sera are used as positive controls [8]; negative controls are from pre-COVID healthy blood donor plasma or the healthy vaccinated donor cohort. Abbreviations: COVID-19, coronavirus disease 2019; F, female; IFN, interferon; M, male; PCR, polymerase chain reaction.

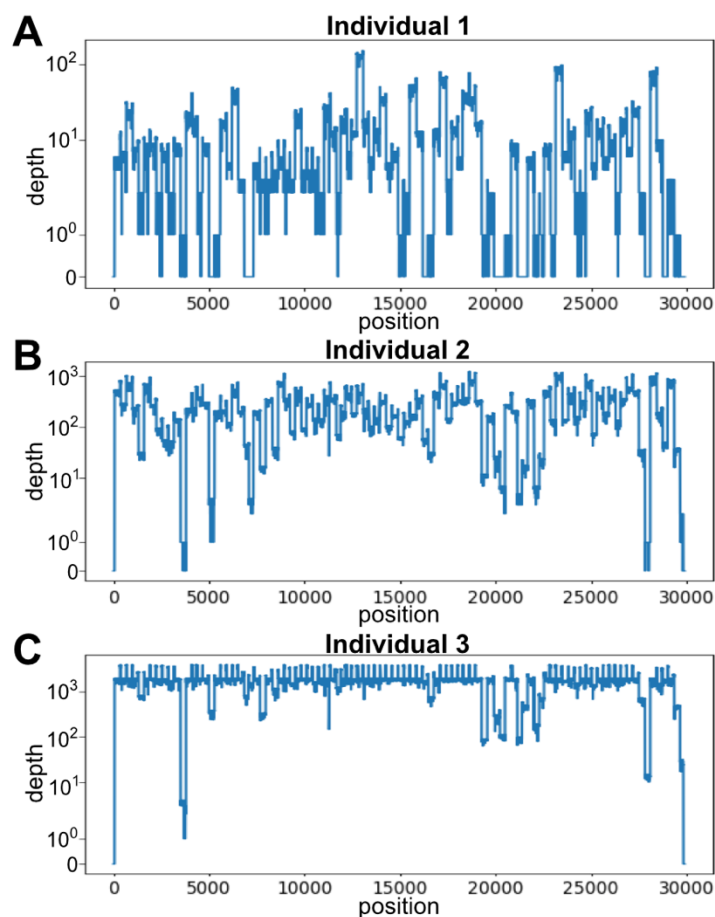


**Figure 9.2. Sequencing depth and coverage of recovered SARS-CoV-2 genomes.** Genome depth and coverage of SARS-CoV-2 Gamma variant recovered from (A) Individual 1, (B) Individual 2, and (C) Individual 3.



## Chapter 9 References

1. COVID-19 Dashboard. Available at: <https://coronavirus.jhu.edu/map.html>. Accessed 11 September 2021.
2. Ritchie H, Mathieu E, Rodés-Guirao L, et al. Our World in Data: Coronavirus Pandemic (COVID-19). Our World in Data 2020; Available at: <https://ourworldindata.org/covid-vaccinations>. Accessed 11 September 2021.
3. Moline HL, Whitaker M, Deng L, et al. Effectiveness of COVID-19 Vaccines in Preventing Hospitalization Among Adults Aged  $\geq 65$  Years - COVID-NET, 13 States, February-April 2021. *MMWR Morb Mortal Wkly Rep* 2021; 70:1088–1093.
4. Garcia-Beltran WF, Lam EC, St Denis K, et al. Multiple SARS-CoV-2 variants escape neutralization by vaccine-induced humoral immunity. *Cell* 2021; 184:2372-2383.e9.
5. Wang Z, Schmidt F, Weisblum Y, et al. mRNA vaccine-elicited antibodies to SARS-CoV-2 and circulating variants. *Nature* 2021; 592:616–622.
6. Vignier N, Bérot V, Bonnave N, et al. Breakthrough Infections of SARS-CoV-2 Gamma Variant in Fully Vaccinated Gold Miners, French Guiana, 2021. *Emerg Infect Dis* 2021; 27:2673–2676.
7. Hoffmann M, Kleine-Weber H, Pöhlmann S. A Multibasic Cleavage Site in the Spike Protein of SARS-CoV-2 Is Essential for Infection of Human Lung Cells. *Mol Cell* 2020; 78:779-784.e5.
8. Laurie MT, Liu J, Sunshine S, et al. Exposures to different SARS-CoV-2 spike variants elicit neutralizing antibody responses with differential specificity towards established and emerging strains. *medRxiv* 2021; :2021.09.08.21263095.

9. van der Wijst MGP, Vazquez SE, Hartoularos GC, et al. Type I interferon autoantibodies are associated with systemic immune alterations in patients with COVID-19. *Sci Transl Med* 2021; 13:eabh2624.
10. Bastard P, Rosen LB, Zhang Q, et al. Autoantibodies against type I IFNs in patients with life-threatening COVID-19. *Science* 2020; 370:eabd4585.
11. Ferre EMN, Rose SR, Rosenzweig SD, et al. Redefined clinical features and diagnostic criteria in autoimmune polyendocrinopathy-candidiasis-ectodermal dystrophy. *JCI Insight* 2016; 1:e88782.
12. Bastard P, Gervais A, Le Voyer T, et al. Autoantibodies neutralizing type I IFNs are present in ~4% of uninfected individuals over 70 years old and account for ~20% of COVID-19 deaths. *Sci Immunol* 2021; 6:eabl4340.

## Chapter 10:

### **Cross-neutralization of SARS-CoV-2 variants by immune sera elicited by a range of infection and vaccination exposures**

This chapter is a reprint of:

Laurie MT, Liu J, Sunshine S, Peng J, Black D, Mitchell AM, Mann SA, Pilarowski G, Zorn KC, Rubio L, Bravo S, Marquez C, Sabatino JJ Jr, Mittl K, Petersen M, Havlir D, DeRisi J. SARS-CoV-2 variant exposures elicit antibody responses with differential cross-neutralization of established and emerging strains including Delta and Omicron.

*J Infect Dis.* 2022; Jan 3:jiab635. doi: 10.1093/infdis/jiab635.

Supplemental files that are not figures can be found with the original work.

## ***Abstract***

The wide spectrum of SARS-CoV-2 variants with phenotypes impacting transmission and antibody sensitivity necessitates investigation of the immune response to different spike protein versions. Here, we compare the neutralization of variants of concern, including B.1.617.2 (Delta) and B.1.1.529 (Omicron) in sera from individuals exposed to variant infection, vaccination, or both. We demonstrate that neutralizing antibody responses are strongest against variants sharing certain spike mutations with the immunizing exposure. We also observe that exposure to multiple spike variants increases the breadth of variant cross- neutralization. These findings contribute to understanding relationships between exposures and antibody responses and may inform booster vaccination strategies.

## ***Background***

Genomic surveillance of SARS-CoV-2 continues to identify a diverse spectrum of emerging variants possessing mutations in the spike gene, the main viral determinant of cellular entry and primary target of neutralizing antibodies [1]. Many spike mutations likely result from selective pressure which improves viral fitness through increased transmissibility or evasion of host immunity [2,3]. Studies have demonstrated that sera from vaccinated and naturally infected individuals yield diminished neutralizing activity against certain variants, including the globally dominant Delta variant [4]. Because serum neutralization titer is an important correlate of real-world protective immunity, these findings suggest that antibody responses elicited by exposure to ancestral spike versions (Wuhan or D614G) will be less effective at preventing future infection by certain variants [5]. However, the diversity and prevalence of variants have fluctuated greatly throughout the pandemic, creating a complex population of individuals that may have inherently

different capacity to neutralize certain variants depending on the specific genotype of their previous exposures, including vaccination [6].

In this study, we address the question of variant-elicited immune specificity by determining the breadth of neutralizing activity elicited by exposure to specific SARS-CoV-2 variants, vaccines, or both. To accomplish this, we collected serum from subjects with prior infections by variants B.1 (D614G mutation only), B.1.429 (Epsilon), P.2 (Zeta), B.1.1.519, and B.1.617.2 (Delta), which were identified by viral sequencing. We also collected serum from mRNA vaccine recipients who were infected with the B.1 ancestral spike lineage prior to vaccination, infected with B.1.429 prior to vaccination, or had no prior infection. We measured and compared the neutralization titer of each serum cohort against a panel of pseudoviruses representing each different exposure variant plus the variants of concern B.1.351 (Beta), P.1 (Gamma), B.1.617, B.1.617.2 (Delta), and B.1.1.529 (Omicron), which have one or more spike mutations of interest in common with one of the exposure variants. Our results provide a quantitative comparison of the degree of neutralization specificity produced by different exposures. We also demonstrate the effect of serial exposure to different spike versions in broadening the cross-reactivity of neutralizing antibody responses. Together, these findings describe correlates of protective immunity within the rapidly evolving landscape of SARS-CoV-2 variants and are highly relevant to the design of future vaccination strategies targeting spike antigens.

## ***Methods***

### *Serum collection*

Samples for laboratory studies were obtained under informed consent from participants in an ongoing community program —Unidos en Salud, which provides SARS-CoV-2 testing,

genomic surveillance, and vaccination services in San Francisco, California [7]. Subjects with and without symptoms of COVID-19 were screened with the BinaxNOW rapid antigen assay (supplied by California Department of Public Health). Positive rapid tests were followed by immediate disclosure and outreach to household members for testing, supportive community services, and academic partnership for research studies. All samples were sequenced using ARTIC Network V3 primers on an Illumina NovaSeq platform and consensus genomes generated from the resulting raw .fastq files using IDseq [8].

Convalescent serum donors were selected based on sequence-confirmed infection with the following variants of interest: B.1 (D614G mutation only; n=10 donors), B.1.429 (Epsilon; n=15), B.1.1.519 (n=6), P.2 (Zeta; n=1), B.1.526 (Iota; n=1), B.1.617.2 (Delta; n=3), D614G infection with subsequent BNT162b2 vaccination (n=8), and B.1.429 infection with subsequent BNT162b2 vaccination (n=17). Serum was also collected from healthy recipients of two (n=11) or three (n=7) doses of BNT162b2 or mRNA-1273 vaccines who were confirmed to have no prior SARS-CoV-2 infection by anti-SARS-CoV-2 nucleocapsid IgG assay [9]. All serum was collected from donors an average of 34 days (standard deviation 16.6 days) after exposure to either SARS-CoV-2 or the most recent dose of mRNA vaccine. For pooled serum experiments, samples from the same exposure group were pooled at equal volumes. Serum samples from the closely related exposures P.2 and B.1.526 were pooled together for the —E484K exposure pool, and samples from BNT162b2 and mRNA-1273 exposures were pooled together for the —vaccine exposure pool because of the very similar neutralization specificity observed in individual tests of these sera. Serum samples were heat inactivated at 56°C for 30 minutes prior to experimentation. Relevant serum sample metadata and exposure grouping is shown in Table S1.

### *Pseudovirus production*

SARS-CoV-2 pseudoviruses bearing spike proteins of variants of interest were generated using a recombinant vesicular stomatitis virus expressing GFP in place of the VSV glycoprotein (rVSV $\Delta$ G-GFP) described previously [10]. The following mutations representative of specific spike variants were cloned in a CMV-driven expression vector and used to produce SARS-CoV-2 spike pseudoviruses: B.1 (D614G), B.1.429/Epsilon (S13I, W152C, L452R, D614G), P.2/Zeta (E484K, D614G), B.1.351/Beta (D80A, D215G,  $\Delta$ 242-244, K417N, E484K, N501Y, D614G, A701V), P.1/Gamma (L18F, T20N, P26S, D138Y, R190S, K417T, E484K, N501Y, D614G, H655Y, T1027I, V1176F), B.1.1.519 (T478K, D614G, P681H, T732A), B.1.617 (L452R, E484Q, D614G, P681R), B.1.617.2/Delta (T19R, T95I, G142D,  $\Delta$ 157-158, L452R, T478K, P681R, D614G, D950N), and B.1.1.529/Omicron (32 spike mutations). All pseudovirus spike mutations are listed in Table S2. Pseudoviruses were titered on Huh7.5.1 cells overexpressing ACE2 and TMPRSS2 (gift of Andreas Puschnik) using GFP expression to measure the concentration of focus forming units (ffu).

### *Pseudovirus neutralization experiments*

Huh7.5.1-ACE2-TMPRSS2 cells were seeded in 96-well plates at a density of 7000 cells/well one day prior to pseudovirus inoculation. Serum samples were diluted into complete culture media (DMEM with 10% FBS, 10mM HEPES, 1x Pen-Strep-Glutamine) using the LabCyte Echo 525 liquid handler and 1500 ffu of each pseudovirus was added to the diluted serum to reach final dilutions ranging from 1:40-1:5120, including no-serum and no-pseudovirus controls. Serum/pseudovirus mixtures were incubated at 37°C for 1h before being added directly to cells. Cells inoculated with serum/pseudovirus mixtures were incubated at 37°C and 5% CO<sub>2</sub>

for 24h, resuspended using 10x TrypLE Select (Gibco), and cells were assessed with the BD Celesta flow cytometer. The WHO International Reference Standard 20/150 was used to validate the pseudovirus assay and compare serum neutralization titers (Table S3) [11]. All neutralization assays were repeated in a total of three independent experiments with each experiment containing two technical replicates for each condition. Cells were verified to be free of mycoplasma contamination with the MycoAlert Mycoplasma detection kit (Lonza).

### *Data Analysis*

Pseudovirus flow cytometry data was analyzed with FlowJo to determine the percentage of GFP-positive cells, indicating pseudovirus transduction. Percent neutralization for each condition was calculated by normalizing GFP-positive cell percentage to no-serum control wells. Neutralization titers (NT<sub>50</sub> and NT<sub>90</sub>) were calculated from eight-point response curves generated in GraphPad Prism 7 using four-parameter logistic regression. The fold-change in pseudovirus neutralization titer in each serum group was calculated by normalizing each variant NT<sub>50</sub> and NT<sub>90</sub> value to D614G pseudovirus NT<sub>50</sub> and NT<sub>90</sub> values in the same serum group. To compare neutralization titer across a panel of different pseudoviruses and serum groups, the Log<sub>2</sub> fold-change compared to D614G pseudovirus was reported.

### *Results*

We compared the 50% and 90% neutralization titers (NT<sub>50</sub> and NT<sub>90</sub>) of D614G and B.1.429 (Epsilon) pseudoviruses in individual serum samples from subjects exposed to D614G infection, B.1.429 infection, mRNA vaccination, D614G infection with subsequent mRNA vaccination, and B.1.429 infection with subsequent mRNA vaccination (Figure 10.1). Fold-



changes in both NT<sub>50</sub> and NT<sub>90</sub> are reported since these values often differ in magnitude due to differences in neutralization curve slope between different variants and sera. In D614G- exposed and vaccine-exposed serum, we observed approximately 2 to 3-fold decreases in average neutralization titer against B.1.429 pseudovirus compared to D614G pseudovirus. As expected, B.1.429-exposed serum neutralized B.1.429 pseudovirus more efficiently than D614G pseudovirus. Of note, previous infection with either D614G or B.1.429 followed by vaccination led to substantially higher neutralization titers against both pseudoviruses. In contrast to other exposure groups, serum from vaccine recipients previously infected by B.1.429 neutralized D614G and B.1.429 at similar titers, with only a 1.3-fold difference in NT<sub>90</sub>, indicating that exposure to multiple spike variants elicits a potent response with specificity toward the breadth of prior exposures.

We next investigated how exposure impacts neutralization specificity by crossing a panel of eight different spike variants against serum pools elicited by nine different prior exposures. (Figure 10.2; Table S3). A range of reductions in neutralization titer relative to D614G pseudovirus were observed, with B.1.617.2 (Delta), B.1.351 (Beta), and B.1.1.529 (Omicron) exhibiting the greatest resistance to neutralization in serum from vaccinated or D614G- exposed individuals with up to 4-fold, 12-fold, and 65-fold reductions in NT<sub>90</sub>, respectively. However, for most variants, reductions in neutralization titer were considerably smaller or absent in serum from subjects previously exposed to a variant bearing some or all of the same spike mutations as the variant being tested. Specifically, prior exposure to the E484K mutation in the spike receptor binding domain (RBD) produced the greatest neutralization of four tested variants with mutations at the E484 position: B.1.617, P.1 (Gamma), P.2 (Zeta), and B.1.351 (Beta). Similarly, B.1.617.2 (Delta) was neutralized more effectively by serum elicited by partially homologous exposures B.1.1.519

and B.1.429 and was neutralized most effectively by serum elicited by fully homologous B.1.617.2 exposure. Conversely, in B.1.617.2-exposed serum we observed the least efficient neutralization of the highly divergent spike variants P.1 and B.1.351. Interestingly, although B.1.1.529 (Omicron) substantially escaped neutralization in all convalescent sera and serum from recipients of two vaccine doses, a much more modest 4 to 8-fold reduction in neutralization titer was observed in sera from individuals with previous infection plus vaccination or three vaccine doses.

### ***Discussion***

In this study, we observe that vaccination and natural SARS-CoV-2 infection elicit neutralizing antibody responses that are most potent against variants that bear spike mutations present in the immunizing exposure. This trend is exemplified by variants with mutations at the spike E484 position, which were neutralized more effectively by E484K- exposed serum than other serum types. Importantly, we also show that B.1.617.2 (Delta) is neutralized more effectively by serum elicited by prior exposure to three different variants — B.1.429, B.1.1.519, and B.1.617.2 — which have separate sets of spike mutations partially or fully overlapping with mutations in B.1.617.2. These effects are presumably due to the shared L452R RBD mutation in B.1.429 and B.1.617.2, and the shared T478K RBD mutation and P681 furin cleavage site mutation found in both B.1.1.519 and B.1.617.2. The poor neutralization of P.1 and B.1.351 by Delta-exposed serum further reinforces the notion that cross-neutralization is heavily impacted by antigenic distance between variants [12]. Together, these results demonstrate that serum neutralization specificity is strongest against variants fully homologous to the exposure, but even single shared spike mutations, particularly those in highly antigenic regions such as the RBD, can enhance cross-neutralization as supported in other studies [3,6,13].

This study also demonstrates the effect of serial exposure to repeated or novel versions of spike on neutralizing antibody response. Infection with B.1.429 (Epsilon) followed by vaccination led to greater cross-neutralization of B.1.429 and B.1.617.2 (Delta) compared to vaccination alone or D614G infection plus vaccination, supporting the notion that exposure to multiple spike variants expands neutralization breadth. Repeated immunizing exposures from infection plus vaccination or booster vaccination led to both an overall increase in neutralization titers and generally broadened neutralization specificity, particularly towards B.1.1.529 (Omicron), which was neutralized most effectively by serum from recipients of three vaccine doses. A limitation of this study is the relatively small number of serum samples, however the shift in neutralization titer between D614G and variant pseudoviruses shows strong consistency between samples.

These serology data leverage human exposures to an array of naturally occurring spike mutations, including those relevant to the globally dominant B.1.617.2 and recently ascendant B.1.1.529 variants, providing a real-world complement to previous animal studies investigating heterologous boosting or multivalent vaccination strategies [14,15]. Our findings suggest that immunity acquired through natural infection will differ significantly between populations in different regions of the world due to highly variable prevalence of different SARS-CoV-2 variants throughout the course of the ongoing pandemic. These results also reinforce the urgent need for widespread booster vaccination and contribute additional evidence suggesting that heterologous or multivalent boosting strategies may be important and effective measures to address newly emergent variants such as the highly immune evasive B.1.1.529 (Omicron). Future studies investigating immune responses to additional emerging variants in vaccinated and unvaccinated individuals will contribute to identifying spike antigen versions that elicit broadly neutralizing antibody responses.

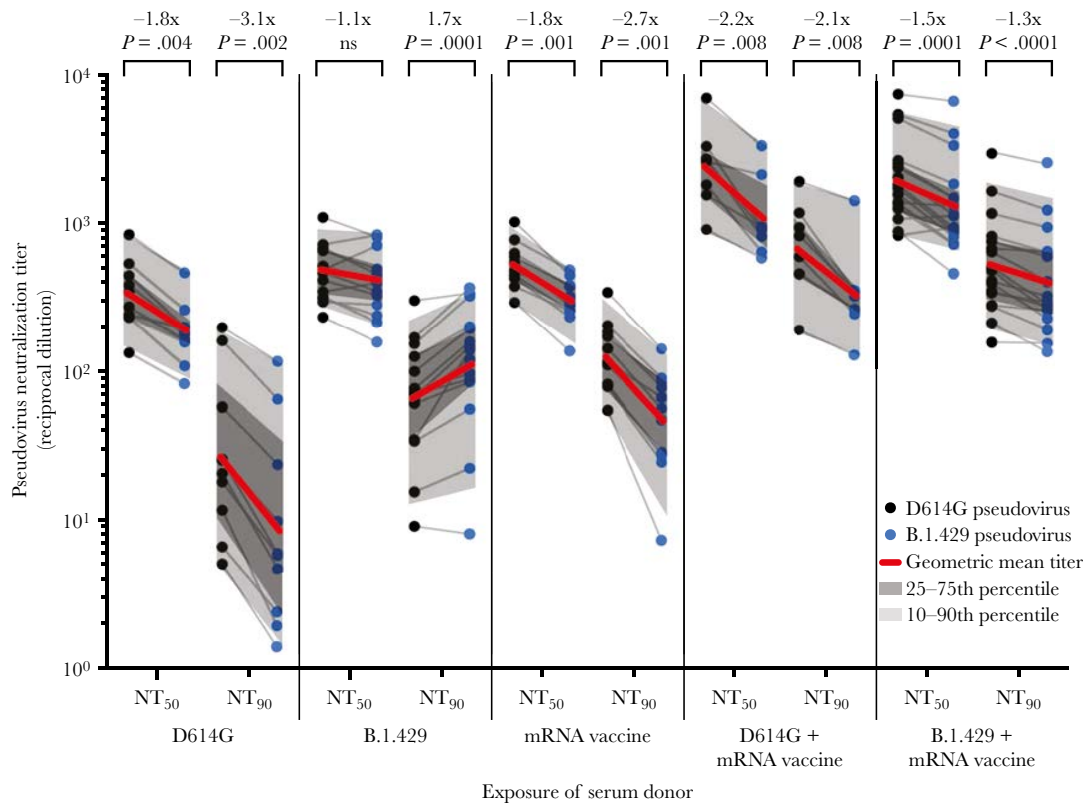


**Figure 10.1. Neutralization of D614G and B.1.429 pseudoviruses by serum from individuals with different exposures.** Plot of 50% and 90% pseudovirus neutralization titers (NT<sub>50</sub> and NT<sub>90</sub>) of serum samples obtained from donors with the indicated infection and/or vaccination exposures. Grey lines connect neutralization titer values for D614G (black dots) and B.1.429 (blue dots) pseudoviruses within each individual serum sample. Geometric mean neutralization titers for each serum group are marked with red lines and fold-change in NT<sub>50</sub> and NT<sub>90</sub> between D614G and B.1.429 pseudoviruses is shown along with  $P$  value. Dark grey shading marks the interquartile range of titer values in each group and light grey shading marks the 10th–90th percentile of the range.  $P$  values were calculated with a Wilcoxon matched-pairs signed-rank test.

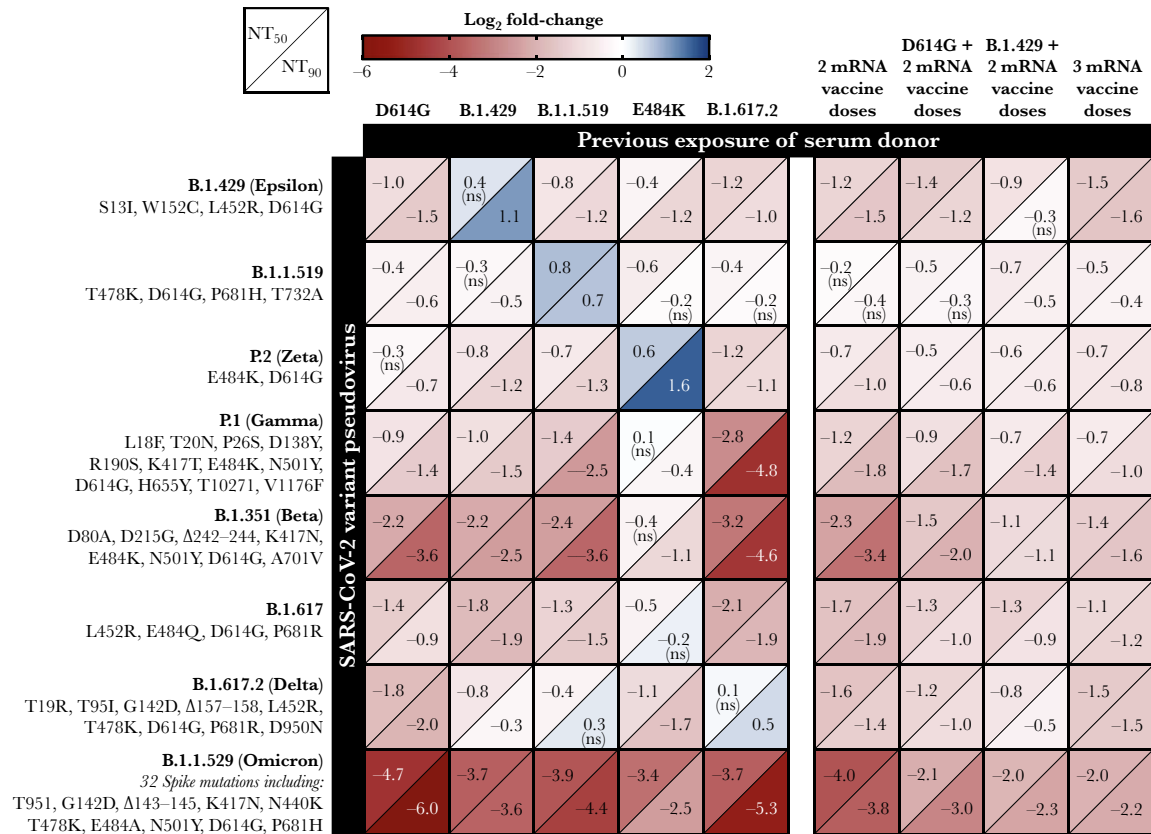


**Figure 10.2. Change in variant pseudovirus neutralization titer relative to D614G.** Matrix of normalized neutralization titers for 8 different variant pseudoviruses (rows) neutralized by 9 different pools of individual sera grouped by exposure (columns). Data are represented as a heat map of the log<sub>2</sub> fold-change in NT<sub>50</sub> (top left of each box) and NT<sub>90</sub> (bottom right of each box) of each variant relative to D614G pseudovirus. All serum samples were collected at least 14 days after the date of the subject's positive COVID-19 test or date of most recent vaccine dose. All titer measurements are the mean of at least 3 independent experiments, each performed with 2 technical replicates. Positive log<sub>2</sub> fold-change (blue) indicates an increase in neutralization titer for that variant relative to D614G pseudovirus, while negative log<sub>2</sub> fold-change (red) indicates a decrease relative to D614G. Statistical significance was determined with unpaired *t* tests. All values are statistically significant (*P* value < .05) except where noted with ns to indicate the difference in variant neutralization titer is not significantly different from D614G pseudovirus neutralization titer in that serum pool. Abbreviations: COVID-19, coronavirus disease 2019; NT<sub>50</sub> and NT<sub>90</sub>, 50% and 90% neutralization titer.

## Chapter 10 References

1. CDC. Coronavirus Disease 2019 (COVID-19) [Internet]. Centers for Disease Control and Prevention. 2020 [cited 2021 Sep 1]. Available from: <https://www.cdc.gov/coronavirus/2019-ncov/variants/variant-info.html>
2. Teyssou E, Delagrèverie H, Visseaux B, et al. The Delta SARS-CoV-2 variant has a higher viral load than the Beta and the historical variants in nasopharyngeal samples from newly diagnosed COVID-19 patients. *J Infect.* 2021; :S0163-4453(21)00416–3.
3. Greaney AJ, Starr TN, Barnes CO, et al. Mapping mutations to the SARS-CoV-2 RBD that escape binding by different classes of antibodies. *Nat Commun.* 2021; 12(1):4196.
4. Liu J, Liu Y, Xia H, et al. BNT162b2-elicited neutralization of B.1.617 and other SARS-CoV-2 variants. *Nature.* 2021; 596(7871):273–275.
5. Corbett KS, Nason MC, Flach B, et al. Immune correlates of protection by mRNA- 1273 vaccine against SARS-CoV-2 in nonhuman primates. *Science* [Internet]. American Association for the Advancement of Science; 2021 [cited 2021 Sep 1]; . Available from: <https://www.science.org/doi/abs/10.1126/science.abj0299>
6. Liu C, Ginn HM, Dejnirattisai W, et al. Reduced neutralization of SARS-CoV-2 B.1.617 by vaccine and convalescent serum. *Cell.* 2021; 184(16):4220-4236.e13.
7. Peng J, Liu J, Mann SA, et al. Estimation of secondary household attack rates for emergent spike L452R SARS-CoV-2 variants detected by genomic surveillance at a community-based testing site in San Francisco. *Clin Infect Dis.* 2021; :ciab283.
8. Kalantar KL, Carvalho T, de Bourcy CFA, et al. IDseq—An open source cloud-based pipeline and analysis service for metagenomic pathogen detection and monitoring. *GigaScience*

[Internet]. 2020 [cited 2021 Jul 14]; 9(10). Available from: <https://doi.org/10.1093/gigascience/giaa111>

9. Elledge SK, Zhou XX, Byrnes JR, et al. Engineering luminescent biosensors for point-of-care SARS-CoV-2 antibody detection. *Nat Biotechnol.* 2021; :1–8.
10. Hoffmann M, Kleine-Weber H, Pöhlmann S. A Multibasic Cleavage Site in the Spike Protein of SARS-CoV-2 Is Essential for Infection of Human Lung Cells. *Mol Cell.* 2020; 78(4):779-784.e5.
11. Mattiuzzo G, Bentley EM, Hassall M, et al. Establishment of the WHO International Standard and Reference Panel for anti-SARS-CoV-2 antibody. *World Health Organization.* 2020; :60.
12. Liu C, Zhou D, Nutalai R, et al. The antibody response to SARS-CoV-2 Beta underscores the antigenic distance to other variants. *Cell Host Microbe.* 2021; :S1931- 3128(21)00519–9.
13. McCallum M, Walls AC, Sprouse KR, et al. Molecular basis of immune evasion by the Delta and Kappa SARS-CoV-2 variants. *Science.* 2021; :eab18506.
14. Wu K, Choi A, Koch M, et al. Variant SARS-CoV-2 mRNA vaccines confer broad neutralization as primary or booster series in mice. *Vaccine.* 2021; 39(51):7394–7400.
15. Corbett KS, Gagne M, Wagner DA, et al. Protection against SARS-CoV-2 Beta variant in mRNA-1273 vaccine-boosted nonhuman primates. *Science.* 2021; 374(6573):1343–1353.

## Publishing Agreement

It is the policy of the University to encourage open access and broad distribution of all theses, dissertations, and manuscripts. The Graduate Division will facilitate the distribution of UCSF theses, dissertations, and manuscripts to the UCSF Library for open access and distribution. UCSF will make such theses, dissertations, and manuscripts accessible to the public and will take reasonable steps to preserve these works in perpetuity.

I hereby grant the non-exclusive, perpetual right to The Regents of the University of California to reproduce, publicly display, distribute, preserve, and publish copies of my thesis, dissertation, or manuscript in any form or media, now existing or later derived, including access online for teaching, research, and public service purposes.

DocuSigned by:

*Matthew Laurie*

8929B2606BB64C2...

Author Signature

4/20/2022

Date